ALMA MATER STUDIORUM
UNIVERSITÀ DI BOLOGNA

DOTTORATO DI RICERCA IN

FISICA

Ciclo 37

Settore Concorsuale: 02/A1 - FISICA SPERIMENTALE DELLE INTERAZIONI FONDAMENTALI

Settore Scientifico Disciplinare: FIS/01 - FISICA SPERIMENTALE

STUDY AND DEVELOPMENT OF NEW SILICON TECHNOLOGIES FOR THE ALICE 3 TIME-OF-FLIGHT DETECTOR

Presentata da: Sofia Strazzi

Coordinatore Dottorato

Alessandro Gabrielli

Supervisore

Andrea Alici

Co-supervisore

Gilda Scioli

Esame finale anno 2025

To my parents

Abstract

In preparation for the future ALICE 3 experiment proposed to be installed at the LHC at CERN in 2036, an extensive R&D program is actively addressing the challenge of developing a 20-picosecond technology for the Time-Of-Flight (TOF) detector. Various silicon technologies are under investigation to achieve this goal. Among those, Low Gain Avalanche Detectors (LGADs) constitute a promising solution. In this thesis, comprehensive R&D efforts focused on state-of-the-art LGADs are presented. A wide range of LGADs, both single channel sensors and matrices, including different thickness, area, doping and inter-pad design have been fully characterized with laboratory measurements and studied first with a laser setup and subsequently using particle beams at CERN facilities. First tests of 25 µm and 35 µm LGADs compared to 50 µm-thick sensors highlighted the potential of a thinner design for improved time resolution. This prompted further investigations into progressively thinner sensors, arriving to test the first 15 µm-thick LGADs ever produced by FBK. Additionally, the innovative double-LGAD concept was introduced to address the challenge of small input signals in the electronics. Notably, this new concept not only yields the significant benefit of an enhancement of the charge at the input of electronics which allows for reduced power consumption, but also translates into an improvement in overall time resolution. Finally, a dedicated study has been performed to determine the impact of particle incidence angles on the time resolution, a crucial aspect to be taken into account in the ALICE 3 experiment. Overall, this R&D campaign on LGAD detectors, finally resulted in sensors that meet the time resolution requirements of ALICE 3 Time-Of-Flight detector, establishing them also as strong candidates for future-generation experiments. This thesis is structured as follows: an outline of the future ALICE 3 experiment is presented in Chapter 1, including a description of the detector concept and main physics objectives. A detailed description of silicon detectors is provided in Chapter 2, with a focus on LGADs working principles and main characteristics in Chapter 3. Chapter 4 discusses the R&D efforts on LGADs and all the measurements conducted in the laboratory, followed by the results from beam test campaigns in Chapter 5.

Contents

Introduction

In recent years, in the dynamic realm of silicon detector advancements, the pursuit of consistently improved timing precision has witnessed remarkable progress. However, unlocking the full potential to achieve large-area systems with the extraordinary time resolution required by future experiments remains a challenge.

The ALICE Collaboration has proposed a next-generation heavy-ion experiment, called ALICE 3, which will be installed at the LHC during the Long Shutdown 4, in preparation for Run 5 (2036) and beyond. The experiment will be completely realized using cutting-edge silicon technologies to study heavy-ion collisions and collect significantly higher luminosities than the current detector (during Run 3 and 4), in a pseudorapidity region up to $|\eta| < 4$. This kind of experimental apparatus will be able to measure the electromagnetic radiation produced by the Quark Gluon Plasma (QGP) in a multi-differential way, in order to probe its early stages of evolution and characterize the production of hadrons with heavy flavors up to extremely low momenta. To achieve this goal, a dedicated system of detectors for Particle IDentification (PID) will be employed. In particular, the Time-Of-Flight (TOF) system will play a key role in PID and it requires an outstanding time resolution of 20 ps. Various silicon-based devices are currently under evaluation for this purpose. This thesis presents the comprehensive research and development efforts focused on state-of-the-art Low Gain Avalanche Detectors (LGADs).

LGADs are a new kind of avalanche silicon detectors optimized for timing. It has been proven that standard LGAD with a thickness of 50 µm combined with a gain of 20-30 can provide a time resolution around 30 ps. In light of their impressive timing performance, this technology is already earmarked for numerous detector upgrades. The stringent

20 ps timing resolution required by ALICE 3, however, has driven a substantial R&D effort aimed at further refining LGAD technology. Achieving this level of time precision would not only meet ALICE 3's needs but could also significantly enhance detector performance in a range of future experiments [1]. A large variety of LGADs, both single channel sensors and matrices, including different thickness, area, doping and inter-pad design, have been fully characterized and tested through laboratory measurements by also using a laser setup to obtain preliminary performances and subsequently deeply investigates using particle beams at CERN facilities in numerous beam tests between 2021 and 2024.

These studies have steered R&D in the direction of producing first very thin LGAD by FBK (Fondazione Bruno Kessler, Italy), including sensors of 15, 20, 25 and 35 µm of thickness, which were deeply investigated together with standard 50 µm-thick sensors used for comparison purposes. Several results on this new generation of LGADs will be shown, including many extracted characteristics, such as drift electric field, noise and charge distributions together with a comprehensive analysis of the timing performance.

In addition, the new concept of "double LGAD", in which two similar sensors are connected to the same board, was introduced and tested for the first time, considering couples of LGADs with all the aforementioned thicknesses. With both of them being connected to the same amplifier, a higher signal is generated at the input, allowing for less power-consuming electronics and also resulting in a benefit in improved time resolution. Results for this innovative implementation will be presented, followed by a comparison with single sensors.

Considering potential experimental conditions, studies were done to investigate the response of LGADs placed at the edge of the barrel layer of the TOF detector, traversed by particles with inclined tracks or that are not fully traversed by low momentum particles. Tests were performed on an LGAD rotated with respect to the beam's orthogonal axis to understand the dependence of the time resolution on the track incidence angle.

This thesis is organized as following: an outline of the future ALICE 3 experiment is presented in Chapter 1, with a description of the detector concept and a summary of the main physics objectives. A detailed description of silicon detectors is reported in Chapter 2, with a focus on LGAD's working principles and main characteristics in

Chapter 3. Finally, a detailed overview of the R&D efforts on LGADs, reporting the characterization measurements and the tests with the laser setup are reported in Chapter 4, followed by the results from beam test measurements in Chapter 5.

In the appendices additional activities are reported, including some very recent measurements performed on the sensors connected to a full front-end and readout chain C, an application of LGADs for particle identification in tests with Silicon PhotoMultipliers B, and regarding the construction of an ALTAI tracking telescope to better investigate possible edge effects, different inter-pad configurations and efficiency D.

Finally, the results of an analysis to extract the performances of the ALICE TOF detector in LHC Run 3 is reported in Appendix A.

Chapter 1

ALICE 3 Experiment

1.1 Introduction and Planning

ALICE (A Large Ion Collider Experiment) [2] is an experiment at the CERN Large Hadron Collider (LHC), designed to study the physics of strongly interacting matter at extreme energy densities and temperatures, where a state of matter called Quark-Gluon Plasma (QGP) is formed. The experiment leverages collisions provided by the LHC with beams of heavy ions or protons. In particular, ultra-relativistic heavy-ion collisions allow the recreation of conditions similar to those in the early universe.

During LHC Run 1 (2009–2013) and Run 2 (2015–2018), ALICE pursued a rich program in Quantum Chromodynamics (QCD) physics, achieving precise measurements that enhanced our understanding of QGP properties. These efforts led to the discovery of new phenomena, such as the evolution of strangeness enhancement from low-multiplicity pp to high-multiplicity Pb–Pb events and the regeneration of the J/Ψ meson via coalescence of independently produced charm and anti-charm quarks.

To fully exploit the scientific potential of the LHC, the experiment underwent major detector upgrades during Long Shutdown 2 (LS2). These upgrades, coupled with a new continuous readout system (see Appendix A), enable the experiment to handle the high interaction rates of Run 3 and Run 4, expecting an integrated luminosity for Pb–Pb collisions of $\sim$13 nb^{-1} [3].

In addition, preparations are already ongoing for further detector upgrades during

the next Long Shutdown (2026–2029). Research and Development (R&D) programs for future detectors been essentially completed and the construction of two new detectors, the ITS3 and the Focal, is starting. The improved ALICE detector will enable key measurements in heavy-ion collisions, such as the production of multi-charmed baryons, the elliptic flow of electron-positron pairs, and photon production at very low momentum.

However, despite the wide-ranging capabilities of the upgraded apparatus, several open physics questions will remain to be addressed.

Promising opportunities to extend the heavy-ion program are the substantial increase in nucleon-nucleon luminosity at the LHC after LS4 (around 2025) and the use intermediate-mass nuclei, such as Ar–Ar or Kr–Kr (see Section 1.2.3 for further details), which would provide novel probes of the QGP and open a new era of precision measurements for rare probes in the Pb–Pb system. However, since ALICE tracking system relies on a large TPC detector, such luminosities would saturate the maximum interaction rate that the current ALICE experiment can handle. Therefore, a faster and different technology is required to replace the current tracking based on a TPC.

To handle the increased interaction rates, a next-generation heavy-ion experiment, ALICE 3 [4], has been proposed for installation at the LHC Interaction Point 2 during Long Shutdown 4 (LS4). In this chapter, after a short summary of the present status of Heavy-Ion (HI) physics, the physics motivations of the ALICE 3 experiment will be outlined, followed by an overview of the system apparatus, with a focus on the Time-Of-Flight (TOF) detector.

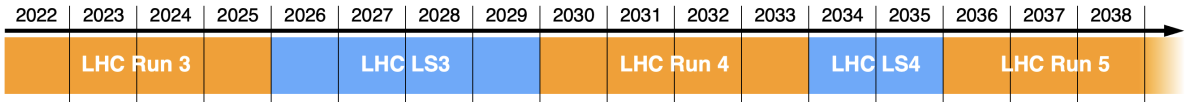

Figure 1.1: LHC schedule with the main phases toward the ALICE 3 installation during LS4 and operation from Run 5.

ALICE 3 will be an all-silicon detector, exploiting technological advances in novel silicon technologies with unprecedented low mass. This design will allow exploration of an ultra-soft region of phase space, enabling the measurement of very low transverse momentum lepton pairs, photons, and hadrons at the LHC.

The start of data-taking with ALICE 3 is planned for LHC Run 5, currently scheduled

to begin in 2036 (see Figure 1.1). Detector construction and pre-commissioning are planned for 2028–2031, allowing one year of contingency before the installation. The dismantling of the current ALICE detector, followed by the installation of ALICE 3, is expected to require a shutdown of two years, consistent with the current LHC schedule.

1.2 Physics motivations

The Standard Model (SM) of particle physics describes the fundamental constituents of matter and the laws governing their interactions, explaining also how collective phenomena and equilibrium properties emerge. Theoretical predictions provide quantitative insights into the equation of state for SM matter, the nature of electroweak and strong phase transitions, and fundamental properties such as transport coefficients and relaxation times.

Collisions of nuclei at ultra-relativistic energies offer a unique opportunity to test key aspects of high-temperature thermodynamics in controlled, laboratory-based experiments. These collisions can reproduce the temperature, pressure and energy density conditions necessary to have the transition of the strongly interacting matter from the hadronic phase to the colour-deconfined QGP, allowing for direct access to the dynamics of partonic matter and providing insight into the properties of the high-temperature phase of QCD.

1.2.1 Introduction to QGP

Heavy-ion collisions at ultra-relativistic energies are used to create the QGP in the laboratory. Before they interact, the nuclei at the LHC are highly Lorentz contracted, with the impact parameter b representing the distance in the transverse plane between the centers of the colliding nuclei. This parameter is closely related to the number of nucleons (N_{part}) in the nuclei that undergo at least one inelastic collision with a nucleon of the other nucleus during the collision (so called "participants"). It also controls the initial volume of the collision region. The total number of binary inelastic nucleon–nucleon collisions is referred to as N_{coll}. When b is small, both N_{part} and N_{coll} are large, and vice versa.

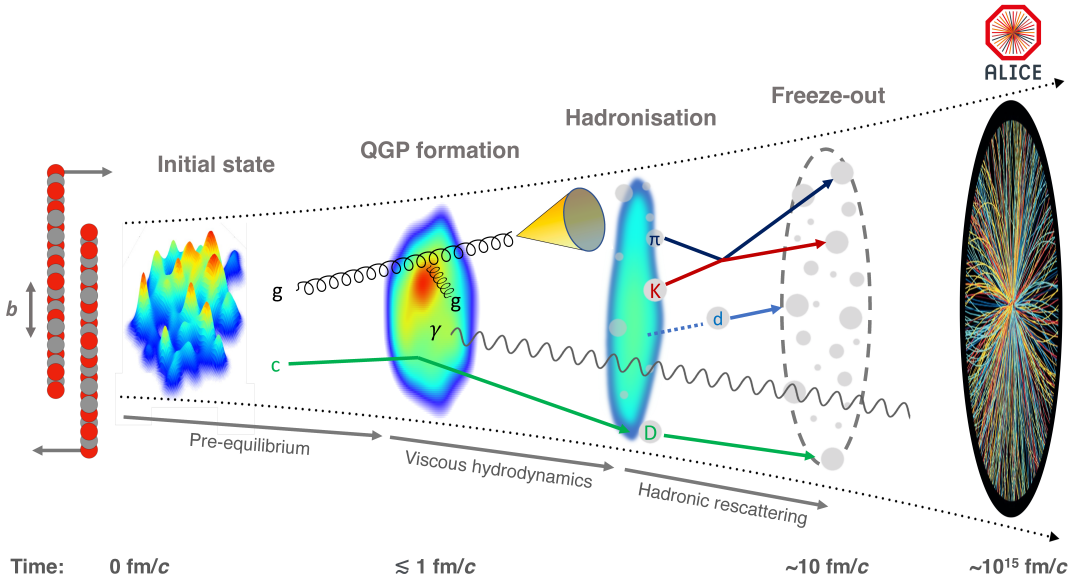

Figure 1.2: Evolution phases of heavy-ion collisions at the LHC [5].

From the time $t = 0$ fm/c in which the collision starts, the evolution of the collision can be divided into different stages [5], schematically shown in Figure 1.2:

- Immediately after the collision, the small momentum exchange (soft) interactions take place during a weakly-coupled **pre-equilibrium phase** ($t < 0.1$ fm/c). This is followed by the creation of softer partons, which enable the formation of a strongly coupled QGP phase. During this phase, the production of direct photons is expected, and additionally, some hard processes occur, resulting in the production of partons and particles with either large masses or large transverse momenta.

- The soft partons produced in the initial collisions continue to interact, leading to the formation of a region with matter at high energy density evolving towards thermal equilibrium. This stage is known as **thermalisation** (0.1–0.3 fm/c) and is the phase in which the QGP is actually produced and the relative abundances of gluons, as well as of u, d, and s quarks, change. Due to internal pressure, the thermalised system starts a rapid expansion and the energy density starts to decrease.

- When the system reaches the critical energy density $\epsilon_c \sim 1$ GeV/fm^3, the process of

hadronisation (when the partons combine to form the hardons) begins, while the system continues to gradually expand and cool down, evolving into an interacting hadron resonance gas. During this phase, both elastic and inelastic interactions take place among the hadrons.

- Inelastic interactions continue, modifying the relative aboundances of hadron species until a point called **chemical freeze-out**, after which the relative aboundances become fixed, but the elastic interactions still persist, continuing to modify the kinetic properties of the hadrons.

- Finally, when the distances between hadrons become larger than the range of the interactions, elastic collisions also stop, reaching the **kinetic freeze-out**. At this stage, the kinematic distributions of the hadrons are fixed.

These particles then travel to the ALICE detector, where they are measured approximately 10^{15} fm/c after the initial collision. The produced QGP has an extremely short lifetime of approximately 10 fm/c (10^{-23} s), making its direct study impossible. As a result, information can only be inferred from the final state of the collision. However there are various experimental probes used to investigate all the evolution steps of heavy-ion collisions. Each of these probes has a different sensitivity to each phase:

- **Hard probes** are produced in high-momentum-transfer scatterings during the early stages of the collision. These include high p_T particles and jets, as well as particles containing heavy-flavour quarks (charm and beauty), produced in the form of open charm and beauty hadrons or quarkonia states ($q\bar{q}$).

- **Electromagnetic probes** consist of photons emitted both before, during and after the thermalisation phase of the collision. These can be identified by detecting the lepton pairs they produce in the final state. However, isolating their signal from the background of photons produced in the later stages of medium evolution poses a significant challenge.

- **Soft probes** consist of particles produced in soft processes that occur during the later stages of the fireball evolution. These probes carry indirect information about

the phase transition properties of the QGP. They are predominantly composed of hadrons containing light quarks with momenta below 2 GeV/c.

More details about the different stages can be found in Reference [5].

1.2.2 Current insight and near-term prospects in heavy-ion physics at the LHC

The first Heavy-Ion experiments started in the 1980s at the Super Proton Synchrotron (SPS) [6] at CERN and at the Alternating Gradient Synchrotron (AGS) [7]. From the first signals of colour deconfinement and the discovery some years later of a strongly-coupled QCD medium that quenches hard partons [8], HI physics has made significant progress.

In particular, nuclear collisions at the LHC provide a unique environment for an extensive program of characterisation of the QGP. During LHC Runs 1 and 2 (from 2010 till 2018), the LHC experiments, and in particular ALICE, specifically designed for this purpose, provided access to the highest-temperature, longest-lived experimentally accessible QCD medium, enabling the possibility of many new observations. As an example, heavy-flavour measurements revealed a mass-dependent energy loss of quarks in the QGP, paving the way for systematic studies of the medium's properties using charm and beauty quarks as calibrated probes; furthermore, significant progress was made in understanding J/ψ production, providing evidence for production mechanisms involving recombination of deconfined charm and anti-charm quarks.

After the first set of results, during LS2 (2019-2021), ALICE underwent a major upgrade [9], with additional upgrades planned for the third long shutdown. The upgraded apparatus is presently taking data and will allow precise measurements of baryon-to-meson ratios in the charm sector and improve constraints on the transport coefficients of charm quarks in the QGP. The expectations are to perform the first measurements of beauty hadrons, providing a valuable test of heavy-quark transport and hadronisation processes in non-equilibrium conditions. However, the precision of beauty-sector measurements in Runs 3 and 4 will be limited, necessitating further improvements in pointing resolution, acceptance, and event rate capability.

Another important objective for Runs 3 and 4 is the first measurement of thermal dilepton emission at the LHC, which will probe the temperature in the early phase of collisions and study mechanisms related to chiral symmetry restoration at vanishing baryon density. However, background from correlated dileptons from heavy-flavour decays will continue to limit precision in the mass range needed.

As also seen from some listed examples, despite the ambitious scientific program for Runs 3 and 4, important questions will remain unanswered, highlighting the need for future detector upgrades.

1.2.3 Ion collisions at the LHC beyond Run 4

The LHC HI program will continue even after LS4 in Runs 5 and 6. However, to address the remaining open questions in heavy-ion physics, it is crucial to fully exploit the LHC potential as a heavy-ion collider. While Pb ions provide the largest collision system and the strongest QGP effects, the luminosity is limited. Indeed, lighter ions are also planned to be used. Due to their lower charge, they can be injected into the LHC with higher bunch intensities, resulting in higher nucleon-nucleon luminosity, thus enhancing the rate of hard processes.

Based on current projections, Runs 5 and 6 will enable studies with more than five times the nucleon-nucleon luminosity achieved with Pb–Pb collisions in Runs 3 and 4. Several measurements will benefit from or only become possible with this increase in luminosity combined with vastly improved detector capabilities.

System	$\mathcal{L}^{\text{month}}$	$\mathcal{L}^{\text{Run5+6}}$
pp	$0.5\,\text{fb}^{-1}$	$18\,\text{fb}^{-1}$
pp reference	$100\,\text{pb}^{-1}$	$200\,\text{pb}^{-1}$
Xe–Xe	$26\,\text{nb}^{-1}$	$156\,\text{nb}^{-1}$
Pb–Pb	$5.6\,\text{nb}^{-1}$	$33.6\,\text{nb}^{-1}$

Table 1.1: Integrated luminosities for different collision systems.

Table 1.1 shows the expected integrated luminosity for various collision systems under consideration. The detector optimisation for the heavy-ion program [4], will be

specifically optimised to totally exploit these luminosities.

1.2.4 ALICE 3 physics

ALICE 3, with its ability to measure the production of leptons, photons, and identified hadrons down to p_T scales of the order of a few tens of MeV/c, would provide significant advances in several areas. This will enable a rich physics program, ranging from measurements with electromagnetic probes at ultra-low transverse momenta to precision physics in the charm and beauty sector.

1.2.4.1 Heavy Quarks: hadronisation and propagation

Heavy Flavour (HF) production

One of the most interesting physics topics that will be addressed by ALICE 3 concerns the heavy flavour measurements. HF production in heavy-ion collisions provides a unique tool to investigate the mechanisms of in-medium energy loss and the hadronisation of heavy quarks from the QGP.

In studies of heavy-ion collisions at high energies, partons produced in hard scatterings serve as powerful probes of the deconfined medium [10]. High-p_T partons and heavy quarks are produced in processes with large momentum transfer, which can be described by perturbative QCD calculations and occur on short time scales compared to QGP formation. Once created, these partons interact with the medium via inelastic (gluon radiation) and elastic (collisional) processes, leading to energy loss and momentum broadening perpendicular to the direction of propagation. By measuring the effect of the QCD medium on the propagation of such partons, it is possible to study the fundamental properties of the QGP and characterise its constituents. For these reasons, HF hadrons provide direct information on all stages of system evolution [11, 12].

The unique tracking and vertexing capabilities of the proposed apparatus, together with the high luminosity provided by the LHC after LS4, will open a new precision era for measurements of the production of open and hidden heavy flavour particles in nuclear collisions.

As an example, two observables widely used for studying the interactions of heavy

quarks with the QGP are the nuclear modification factor R_{AA} and the elliptic flow v_2. The nuclear modification factor is defined as the ratio between the measured yields in nucleus-nucleus (AA) and pp collisions, normalised to the average number of binary collisions, $\langle N_{\mathrm{coll}} \rangle$, in the considered AA centrality interval:

$$R_{AA}(p_{\mathrm{T}}) = \frac{1}{\langle N_{coll} \rangle} \times \frac{dN_{AA}/dp_{\mathrm{T}}}{dN_{pp}/dp_{\mathrm{T}}} \tag{1.1}$$

The anisotropic flow coefficients v_n are the coefficients of the Fourier expansion of the particle azimuthal distribution with respect to the corresponding symmetry planes of the participant distribution Ψ_n:

$$v_n = \langle \cos[n(\varphi - \Psi_n)] \rangle \tag{1.2}$$

The second harmonic coefficient, v_2, is the elliptic flow, and the corresponding symmetry plane is the reaction plane, i.e., the plane defined by the impact parameter of the colliding nuclei and the beam direction.

Precise measurements of the R_{AA} could provide insights into the momentum dependence of heavy quark energy loss, particularly regarding the suppression of high-p_T HF hadrons in nucleon-nucleon collisions with respect to pp collisions. These measurements also offer important tests of QCD predictions regarding the expected flavour and mass dependence of energy loss processes. In this regime, a hierarchy in energy loss is expected, with higher-mass quarks losing less energy compared to lower-mass quarks. At low p_{T}, the production rate of heavy-flavour hadrons in heavy-ion collisions is predominantly governed by the elastic energy loss due to collisional processes. In this regime, heavy quarks undergo Brownian motion as they diffuse within the QGP, subsequently recombining with light quarks during the hadronisation stage. Consequently, exploring the properties of the QGP across various scales necessitates measurements down to very low p_{T}.

HF Hadronization

The new detector system will also be able to tackle another important topic, particularly in light of recent measurements in both AA and pp collisions: HF hadronisation.

Fragmentation is one of the most common approaches for calculating inclusive hadron production, particularly for high-momentum partons emerging from initial hard pro-

cesses, where high-momentum quarks fragment directly and independently into high-momentum hadrons. However, recent measurements of the Λ_c/D^0 ratio at the LHC indicate that fragmentation via single-string breaking (breaking of the force which connects quarks and gluons, resulting in quark-antiquark pairs) may not be sufficient to describe heavy-flavour hadronisation at low momentum in *pp* and p–Pb collisions, particularly regarding baryon production [13].

To explain these experimental data, other mechanisms are taken into account, such as coalescence, which is expected to dominate in the low-momentum regime in nucleus–nucleus collisions. In this regime, partons are abundant, and heavy quarks can hadronise by recombining with light quarks [14]. Other models have been introduced, including new topologies (such as junctions) connecting quarks created in different Multi-Parton Interaction (MPI) systems or production via feed-down from yet-unobserved charm-baryon states.

Since these different mechanisms are expected to be important at low-intermediate p_T, the ability to reach very low momentum measurements with the new apparatus is of essential importance.

Multi-charm Baryons and Exotic States

Measurements of multi-charm hadrons, such as the Ξ_{cc}^{+} (ccd), Ξ_{cc}^{++} (ccu), Ω_{cc}^{+} (ccs), Ω_{ccc}^{++} (ccc), and exotic states such as the newly-discovered T_{cc}^{+} (ccud) [15], would provide a direct window into hadron formation from a deconfined QGP, offering more experimental constraints to models. Multi-charm state production in the same hard scattering is very rare, so these states can be considered as "pure" coalescence particles. The yields of multi-charm baryons relative to the number of produced charm quarks are predicted to be significantly enhanced in *AA* compared to *pp* collisions.

Enhancements of up to a factor of 10^2 are expected for the recently observed Ξ_{cc} baryon [16], and even up to 10^3 for the yet-undiscovered Ω_{ccc} baryon [17].

The measurements enabled by ALICE 3 would open a crucial new window on hadron formation from deconfined matter. Impressive results on the reconstruction of complex cascades of weak decays are expected for Multiply Heavy Flavoured (MHF) baryons. The precise quantification of their production enhancement in *AA* collisions relative to *pp* ones will allow, for the first time, a test of coalescence and statistical hadronisation

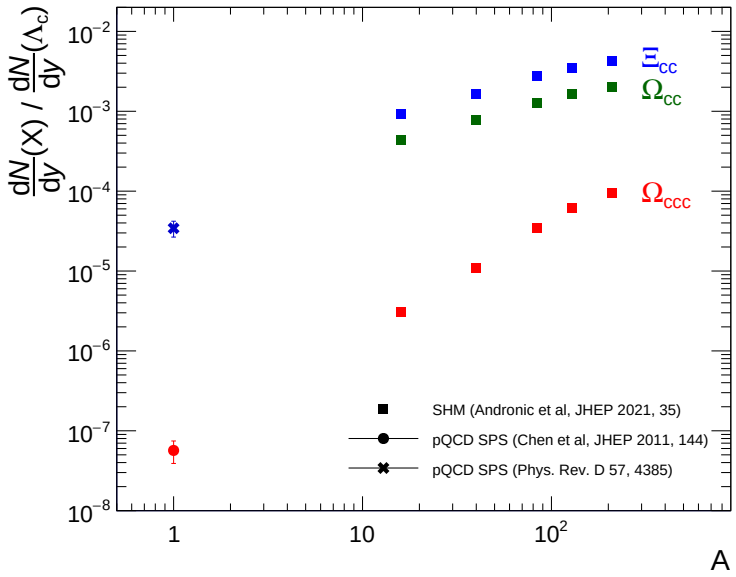

Figure 1.3: Simulation's expectations of multi-charm baryon to single-charm baryon (Λ_c) yield as a function of mass number, using single parton scattering (SPS) calculations [18] at $\sqrt{s} = 14$ TeV (shown at $A = 1$), and a statistical hadronisation model calculation [19] for AA collisions at $\sqrt{s_{\mathrm{NN}}} = 5.02$ TeV with $A \neq 1$.

models for this kind of particle. This will provide a key confirmation of the current interpretation of the LHC quarkonium results and offer additional knowledge about the properties of the QGP.

Figure 1.3 shows the wide span between the single parton scattering expectation and the statistical hadronisation model prediction for the ratio between the yields of multi-charm baryons and that of the Λ_c as a function of the colliding system size. This indicates the large sensitivity of these yields to the underlying production mechanisms.

Quarkonium physics

Quarkonia have represented one of the most valuable probes of the QGP since the very first experimental studies with ultra-relativistic heavy-ion collisions [20]. A remarkable discovery from Pb-Pb collisions at the LHC was the significantly reduced suppression of J/Ψ compared to lower energies, with a much greater reduction observed at low p_T [21]. These measurements are compatible with predictions of the quarkonium pro-

duction mechanism called regeneration [22]. Alternatively, a mechanism of continuous creation and destruction of charmonia in the QGP has been proposed, occurring near the QCD phase boundary [23].

Disentangling the contributions of prompt J/Ψ, particularly those originating from B decays and the production yields of low transverse momentum χ_c states, as well as non-prompt J/Ψ, and considering path-length dependent energy loss, is essential to understanding the systematics of charmonium production. The proposed apparatus will offer excellent separation of prompt charmonia from secondary ones.

1.2.4.2 Electromagnetic radiation: chiral symmetry restoration and temperature of QGP

While hadrons are produced mostly in the late stages, electromagnetic radiation is expected to be emitted during a significant part of the QGP lifetime. Photons and dileptons, i.e., lepton-antilepton pairs produced by the internal conversion of virtual photons, are unique tools to study the space-time evolution of the hot and dense matter created in ultra-relativistic heavy-ion collisions. These electromagnetic probes are continuously produced by various sources throughout the entire evolution of the QGP. In particular, intermediate- and high-p_T probes traverse the medium and couple directly to quarks, escaping the collision without being affected by the strong interaction, thus carrying undistorted information about their production source. Different intervals of the dielectron invariant mass spectrum are sensitive to different stages of the collision and their related physical processes.

The nearly massless detector would allow measurements at very low transverse momentum, approaching the natural scale determined by the inverse radius of the system (about 100 MeV/c in *pp* collisions and 10 MeV/c in Pb-Pb collisions). This capability enables an entirely new approach based on precision measurements of photons and thermal dileptons, providing unique sensitivity to the early stages of the deconfined system. The very low mass and p_T cutoff will allow testing theoretical predictions in the phase space region, currently beyond reach, where most of the radiation is emitted.

Dilepton production from the medium in the vicinity of the transition temperature is sensitive to the effects of chiral symmetry restoration via the spectral functions of

the vector mesons, which mediate interactions in the hot hadron gas. This intermediate invariant mass region of the dielectron spectrum contains contributions from low-mass vector meson decays and thermal radiation from both the partonic and hadronic phases. In this mass range, dielectron production is largely mediated by the ρ^0, ω, and φ mesons. Among these, the contribution of the $\rho(770)$ is by far the most important, making it a prime probe for in-medium modifications of hadron properties. Its strong coupling to the $\pi^+\pi^-$ channel ($\pi^+\pi^- \to \rho^0 \to \gamma^* \to e^+e^-$) and its lifetime of only 1.3 fm/c make it subject to regeneration in the longer-lived fireball at the LHC. The study of the dielectron spectrum in Pb–Pb collisions, where higher energies are delivered, will be particularly interesting to further investigate the ρ^0 broadening effect near the phase transition, connected to chiral symmetry restoration.

The expected dielectron mass distribution in heavy-ion collisions at the LHC is shown in Figure 1.4. The solid black line shows the expected total dilepton mass spectrum. Two different processes are indicated in the plot: thermal production from both the plasma and the hadron gas, and hadronic production via vector mesons. Since only the hadronic production channels are sensitive to chiral symmetry restoration, the comparison between these and production without medium effects provides a crucial test of this phenomenon in the hot and dense phase of the collision, for which no direct experimental evidence currently exists.

With the nearly zero-mass detector proposed for ALICE 3, it will be possible to make very precise measurements of the thermal dilepton continuum in the mass range from the ρ meson to 1.6 GeV, in pp, p-Pb, and Pb-Pb collisions. This will allow, for example, testing whether the minimum at 1.26 GeV found in e^+e^- collisions, corresponding to the mass of the a_1 meson (considered the chiral partner of the ρ), fills in as we go from minimum bias pp to central Pb-Pb collisions, providing a test of chiral symmetry restoration in the $\rho - a_1$ sector.

Moreover, the study of thermal dielectrons, facilitated by the dramatic improvement in the apparatus, will also provide precise information on the temperature of the system in the 1.8–3 GeV region of the mass spectrum, leading to a better understanding of its thermodynamic properties.

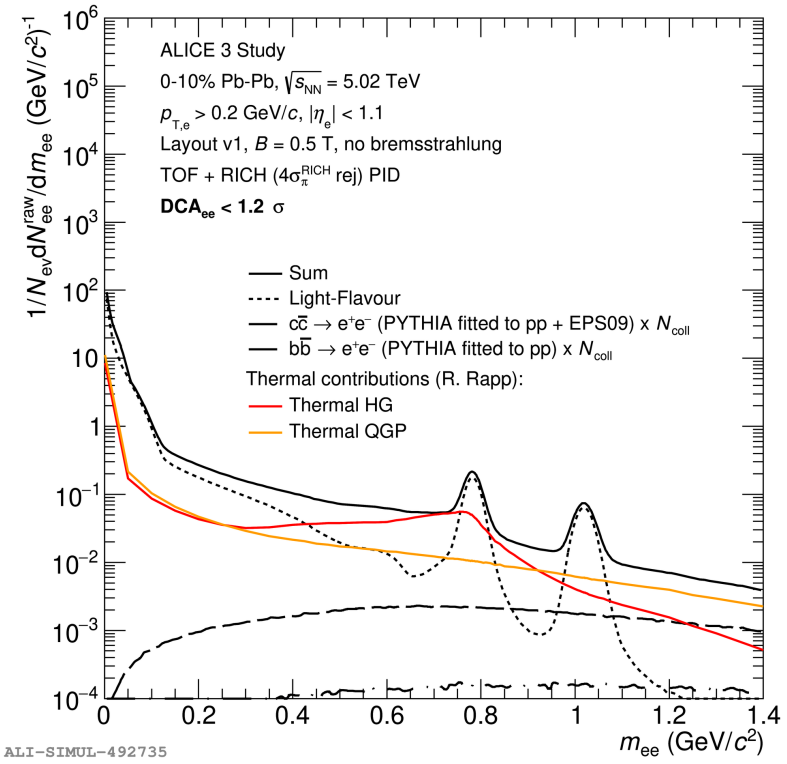

Figure 1.4: Expected raw dielectron yield after a maximum DCA$_{ee}$ cut at 1.2 sigma, in 0-10% Pb-Pb collisions, with the ALICE 3 setup and B = 0.5 T. The different contributions from thermal emission from the hadron gas (red line) and from the QGP (orange line) are shown separately and compared to hadronic production. The solid black line shows the expected total dilepton mass spectrum.

1.2.4.3 Soft and Ultra-Soft Photons: tests of Quantum Field Theories

Photons are particularly valuable for studying the hot QCD medium, as they, like dileptons, escape without interacting with the medium, carrying direct information from the early stages of heavy-ion collisions. At low transverse momentum, the direct photon spectrum is primarily fed by the thermal emission of the hadron gas and, to a larger extent, the QGP expected in ultra-relativistic heavy-ion collisions. The production of these thermal photons is highly sensitive to the properties of the hot medium, offering insight into its spatial expansion and temperature, and thus contributing to our understanding of the hadronic matter phase diagram. However, studying real soft photons in the low-p$_T$

region in a collider environment is challenging due to the substantial background from hadron decays (mainly π^0), electron bremsstrahlung in detector material, and ultra-peripheral collisions. Currently, measurements in heavy-ion collisions extend down to approximately 1 GeV/c [24]. ALICE 3 aims to push these boundaries significantly. A dedicated forward tracker, in the range $3.5 < |\eta| < 5$, designed to reconstruct photon conversions at ultra-low transverse momenta, will allow measurements from 1 MeV/c to 100 MeV/c, enabling state-of-the-art measurements to test Low's theorem, thereby probing the infrared limit of Quantum Electrodynamics (QED) as a gauge theory. The ultra-low mass tracker in ALICE 3 will extend the photon transverse momentum range to 50–100 MeV/c, providing an unprecedented opportunity to test current predictions for QGP radiation in previously unexplored regions of phase space. In high-energy hadronic collisions, bremsstrahlung photons are emitted during the production of prompt charged hadrons that are stable against strong decays. For photon transverse momentum (k_T) approaching zero with respect to the emitting hadron, i.e., in the ultra-soft regime, the bremsstrahlung spectrum can be computed model- and process-independent. This results in the characteristic $1/k_T$ dependence of the photon spectrum, a direct consequence of electric charge conservation. Low's theorem provides a framework for quantitatively testing the infrared limits of quantum field theories such as QED, QCD, and quantum gravity. In these theories, the production of ultra-soft photons is linked to the charged final state through fundamental "soft theorems" [25, 26]. Specifically, Low's theorem relates the momenta of hadrons produced in high-energy collisions to the number of soft photons emitted. Although Low's theorem has not yet been conclusively verified, any violation would signal a significant issue in theoretical understanding. Most experimental tests of the theorem have observed significant excesses of soft photons beyond predictions by factors of four to eight. Achieving the experimental sensitivity to detect photons in this p_T region is crucial for testing these predictions.

1.2.4.4 Searches Beyond the Standard Model

The search for physics Beyond the Standard Model (BSM) is one of the primary objectives of the LHC. Heavy-ion collisions provide complementary, and in some cases better, opportunities compared to *pp* collisions for investigating new phenomena not accounted

for by the Standard Model. In particular, ultra-peripheral collisions (UPCs) of heavy ions offer ideal conditions for studying photon-mediated processes, such as light-by-light scattering ($\gamma\gamma \rightarrow \gamma\gamma$), axion-like particle searches, and τ lepton anomalous magnetic moment measurements. ALICE 3 offers the potential to extend these studies to low-p_{T} photons for axion-like particle searches in $\gamma\gamma \rightarrow \gamma\gamma$, using photons reconstructed in the electromagnetic calorimeter as well as those detected through conversions. Additionally, ALICE 3 will enable searches involving low-p_{T} electrons or muons from τ decays. This opens up access to kinematic regions that are inaccessible to other LHC experiments. The wide pseudorapidity coverage of the ALICE 3 detector offers a significant advantage in selecting exclusive final states in UPCs, further enhancing the sensitivity of such BSM searches.

1.3 Detector System

The physics goals outlined in the previous section rely on a series of observables, which are summarised in Table 1.2.

Observables	**Kinematic Range**
Heavy-flavour hadrons	$p_{\mathrm{T}} \rightarrow 0$, $\lvert\eta\rvert < 4$
Dielectrons	$p_{\mathrm{T}} \approx 0.05$ to $3\,\mathrm{GeV}/c$, $M_{ee} \approx 0.05$ to $4\,\mathrm{GeV}/c^2$
Photons	$p_{\mathrm{T}} \approx 0.1$ to $50\,\mathrm{GeV}/c$, $-2 < \eta < 4$
Quarkonia and exotica	$p_{\mathrm{T}} \rightarrow 0$, $\lvert\eta\rvert < 1.75$
Ultrasoft photons	$p_{\mathrm{T}} \approx 1$ to $50\,\mathrm{MeV}/c$, $3 < \eta < 5$
Nuclei	$p_{\mathrm{T}} \rightarrow 0$, $\lvert\eta\rvert < 4$

Table 1.2: Overview of key physics observables and the respective kinematic ranges of interest for ALICE 3.

These observables determine the requirements for the detector design, with also the additional requirement that the apparatus has to fully exploit the expected delivered

luminosities. This has led to the detector concept shown in Figure 1.5.

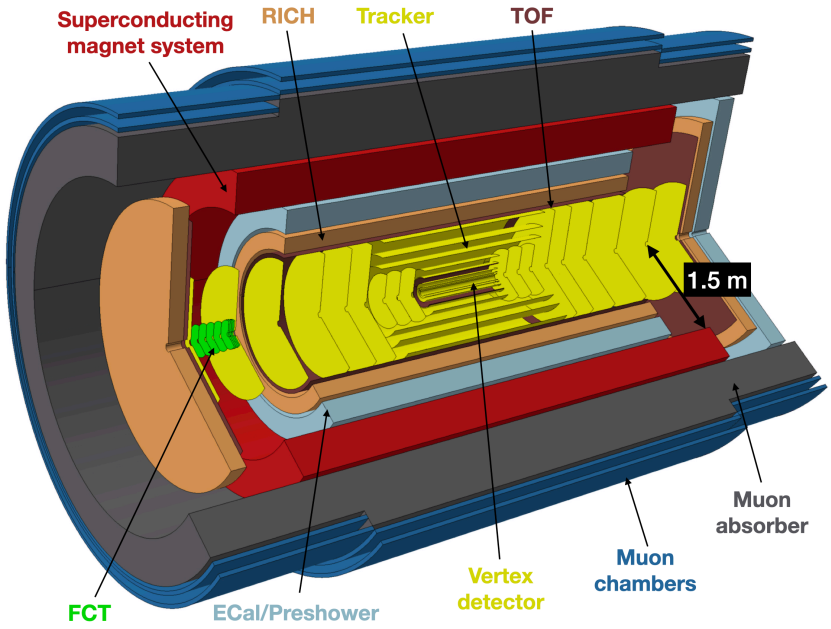

Figure 1.5: ALICE 3 detector layout: a silicon tracker composed of cylinders and disks serves for track reconstruction in the magnetic field provided by a superconducting magnet system. The vertex tracker is housed within the beam pipe. For particle identification, a time-of-flight detector, RICH detector, photon detector, and a muon system are employed. The forward conversion tracker is housed in a dedicated dipole magnet [4].

An all-silicon, nearly massless detector, capable of tracking over a wide momentum range with excellent decay vertex resolution, particle identification, and high-speed capabilities, based on state-of-the-art technologies and innovative approaches, has been proposed. The detector has a very compact layout in both the radial and longitudinal dimensions and covers a pseudorapidity region of $|\eta| < 4$ over the full azimuth. The whole system is placed within a superconducting solenoidal magnet providing a field of B = 2T. The schematic longitudinal cross-section of the reference version of the detector is shown in Figure 1.6.

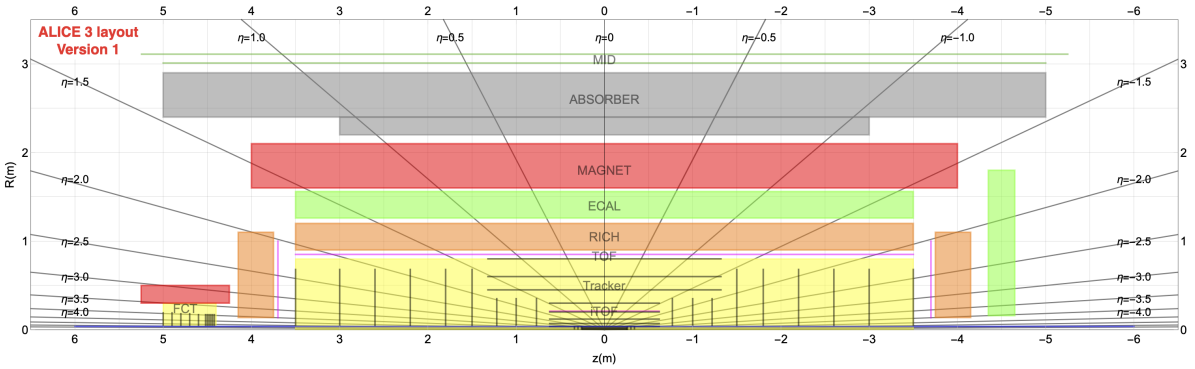

Figure 1.6: ALICE 3 detector layout version 1: longitudinal cross-section. The MAPS-based Inner and Outer Trackers are complemented by PID detectors (inner and outer TOF, RICH), all housed within a superconducting magnet system. In addition, the electromagnetic calorimeter (ECal), the muon identifier (MID) with a hadron absorber, and the Forward Conversion Tracker (FCT) within a small dipole magnet are shown. The Forward Detectors (FD) at $z \approx \pm 18$ m are not shown.

1.3.1 Tracking Detectors

The apparatus is centered on an ultra-low-mass, all-silicon tracker arranged in truly cylindrical layers to achieve the best possible impact parameter resolution for decay vertex reconstruction, complemented by endcap disks to cover a large pseudorapidity range. The core detector component is a large silicon tracker consisting of CMOS Monolithic Active Pixel Sensors (MAPS), arranged in 11 barrel layers and 12 forward and 12 backward disks, covering a total area of about 60 m^2.

The **Inner Tracker (IT)** includes the three innermost layers and disks (Vertex Detector), followed by four Middle Layers up to a radius of 20 cm, and six small disks at longitudinal distances z ranging from ± 77 cm to ± 122 cm.

The **Vertex Detector** will be located inside the beam pipe, thanks to the IRIS tracker concept, shown in Figure 1.7. The retractable design allows for a 16 mm beam aperture during the LHC injection phase to ensure beam stability and vacuum preservation, which can be reduced when the system closes during stable beams. The IRIS tracker closes to an innermost radius of 5 mm, providing a track pointing resolution better than 10 µm for $p_T > 250$ MeV/c over the full η acceptance. Thanks to the unprecedented

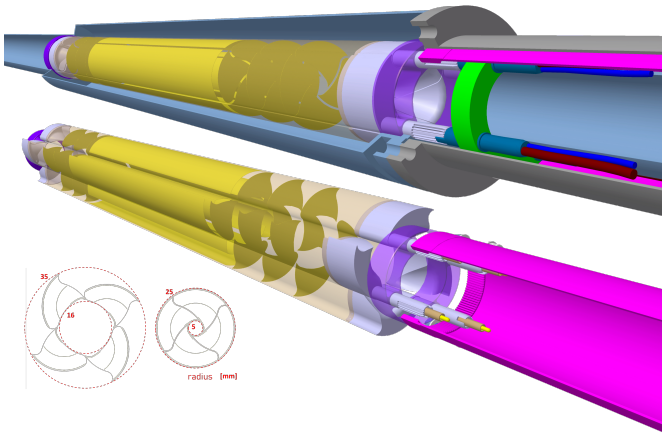

Figure 1.7: Movable IRIS tracker, which can be opened (down) during the accelerator startup and closed (up) during operations.

low material budget of 0.05% X_0 per layer and pixel sizes of about 5 µm × 5 µm, this ultra-low-mass movable vertex tracker delivers outstanding vertexing performance.

The **Outer Tracker (OT)** consists of the four outermost layers, located at radii between 30 cm and 80 cm, and twelve large disks at longitudinal distances z ranging from ±150 cm to ±350 cm.

1.3.2 Particle Identification Detectors

Charged-hadron and electron identification is achieved over a large p_T range, from 15-60 MeV/c (depending on the magnetic field value) to several GeV/c, by complementing Time-Of-Flight (TOF) detector measurements with Ring Imaging Cherenkov (RICH) detection. Figure 1.8 summarises the PID capabilities of the proposed detector, highlighting the $\eta - p_{\mathrm{T}}$ regions where particle identification with better than 3σ separation is possible.

The **TOF system** consists of an Inner TOF barrel (iTOF) located at $r = 19$ cm, adjacent to the sixth tracker layer, and an Outer TOF barrel (oTOF) and forward disks (fTOF) located outside the last tracker layer, at $r = 85$ cm, and the last tracker disk, at $|z| = 370$ cm, respectively. The fTOF disks can also determine the collision time and provide the time zero for single-particle timing measurements. More details on the various technologies considered are provided in Section 1.4.

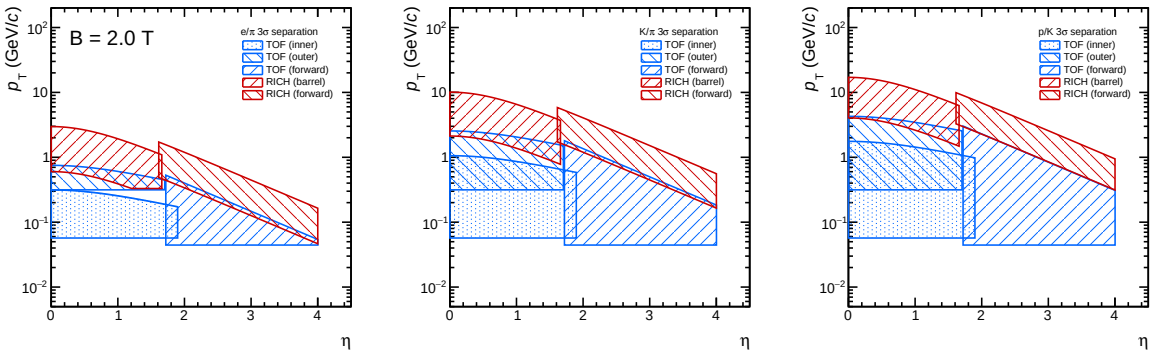

Figure 1.8: Analytical calculations of the $\eta - p_{\mathrm{T}}$ regions where charged particles can be separated by at least 3σ by the ALICE 3 particle-identification subsystems in a 2.0 T magnetic field. Electron/pion, pion/kaon, and kaon/proton separation plots are shown from left to right.

The **RICH detector** consists of aerogel radiator tiles coupled to SiPM photodetectors via a proximity gap (distance between the photosensor and the radiator) of about 20 cm, arranged in a barrel with inner radius $r = 90$ cm (bRICH), and forward disks (fRICH) positioned at $|z| = 380$ cm. The barrel RICH geometry has been optimised with a projective layout (Figure 1.9), which enhances the PID performance at $|\eta| > 1.5$ by avoiding acceptance losses for Cherenkov photons and reduces the active area to 28 m^2, allowing pseudorapidity coverage up to $|\eta| < 2$.

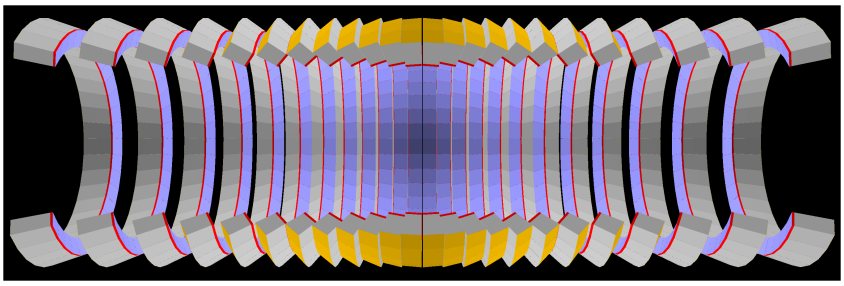

Figure 1.9: Projective layout of the bRICH detector.

The **Electromagnetic Calorimeter (ECal)**, the outermost system inside the solenoid, consists of Pb-scintillator sampling modules in both the barrel and endcap. A central barrel covering $|\eta| < 0.45$ and full azimuth will be instrumented with $PbWO_4$ crystals providing an energy resolution below 1 GeV, enabling, for example, separation of the

states χ_{c1} and χ_{c2} in the decay channel $J/\psi\gamma$. SiPM-based readout is considered for both the Pb-scintillator and crystal sections of the ECal.

A **Muon Identification Detector (MID)** is located outside the magnet and consists of a hadron absorber followed by sensor planes made of plastic scintillator bars coupled to SiPMs or alternatively by resistive plate chambers or multiwire proportional chambers. Iron is used as an absorber material.

Finally, a **Forward Conversion Tracker (FCT)** for ultrasoft photon detection is under consideration; however, feasibility studies are still ongoing.

1.4 Time-Of-Flight Detector

The Time-Of-Flight (TOF) system provides particle identification across the full detector acceptance ($|\eta| < 4$). It consists of inner and outer TOF layers in the central barrel and forward disks on both sides of the experiment, covering a total area of 45 m^2.

1.4.1 Specifications

The specifications and dimensions of the TOF system are summarised in Table 1.3. The system is expected to have a time resolution of 20 ps (r.m.s.) with a low material budget of 1–3% of X_0 and a power density of 50 mW/cm^2.

Despite recent breakthroughs in the timing performance of silicon sensors [27, 28, 29], which make them the preferred candidates for this detector, a large-area system like the one required for ALICE 3 has yet to be realised. Therefore, a focused R&D program is underway.

Compared to general-purpose LHC detectors, the requirements for hit rate and radiation hardness are moderate, which opened opportunities to explore various technologies. For efficient track matching, the cell size can be as large as 1 mm $\times$ 1 mm for the inner TOF and 5 mm $\times$ 5 mm for the outer TOF. The choice of the effective sensor's cell size will be mainly determined by sensor capacitance and noise, in order to maximise the time resolution; multiple cells will then be grouped within the front-end electronics to achieve the desired granularity for processing. To minimize the material budget and costs, efforts are being made to implement each TOF system using a single sensor layer.

	Inner TOF	Outer TOF	Forward TOF Disks
Radius (m)	0.19	0.85	0.15 to 1.0
z range (m)	-0.62 to 0.62	-3.50 to 3.50	± 3.70
Area (m^2)	1.5	37	6
Acceptance	$\lvert\eta\rvert < 1.9$	$\lvert\eta\rvert < 2$	$2 < \lvert\eta\rvert < 4$
Granularity (mm^2)	1×1	5×5	1×1 to 5×5
Hit rate (kHz/cm^2)	200	15	280
Material thickness ($\%X_0$)	1 to 3	1 to 3	1 to 3
Power density (mW/cm^2)	50	50	50
Time resolution (ps)	20	20	20

Table 1.3: TOF specifications, with values updated in respect to to [4].

For the TOF system, while the sensors and front-end solutions will be discussed in the next section, the general requirements for the readout are:

- **Time-to-Digital Converter (TDC):** Current TDCs with sampling rates in the tens of MHz and power consumption below 10 mW per channel can achieve a bin size of 10 ps, resulting in negligible r.m.s. quantization noise of 2.9 ps, far below the system time resolution requirement of 20 ps [30].
- **Clock Management:** Recent advances in clock management have produced very low-jitter clocks required for high-speed serialisers, which can now achieve data rates exceeding 10 Gbit/s.
- **Readout:** The readout will employ an asynchronous communication scheme between the pixels and the periphery, reducing the power dissipation that would result from clock distribution across the full matrix.

Despite the progress made in recent years and the state-of-art technologies currently available, designing a TDC and a clock management for such a large-scale system remains

challenging; anyway, these tasks are independent of the sensor and front-end electronics choices.

The readout architecture, including the power network and the pixel-to-periphery data path, will be designed modularly using a digital-on-top approach, allowing straightforward scalability. Data generated by the matrix will be collected at the chip periphery, serialised, and transmitted off-chip via high-speed serial links. Time-over-Threshold (ToT) will be employed to correct for time-walk. The calibration strategy will be modeled on the basis of the scheme used by the current ALICE TOF detector [31].

Regarding the mechanical support structure, the design will closely follow the approach used for the outer layer of the tracking systems. The idea is to finalise the choice of sensor technology by early 2026, following the conclusion of the current R&D phase and have the first prototypes of mechanical components, modules, and cooling systems available by the end of 2026 in order to start the production phase in 2029 and the integration in 2031.

1.4.2 Main considered sensor's technologies

Three sensor technologies have been identified as candidates for dedicated R&D, which is already underway: Low Gain Avalanche Detectors (LGADs), fully depleted CMOS LGAD sensors, and Single Photon Avalanche Diodes (SPADs).

1.4.3 Low Gain Avalanche Detectors (LGADs)

Conventional Low Gain Avalanche Detectors are currently the most cutting-edge devices for timing silicon sensors and actually the only technology capable of meeting the stringent requirement of a time resolution of less than 20 ps for the ALICE 3 TOF detector. The present state-of-the-art in LGAD technology and ongoing R&D efforts to further improve their performance are extensively discussed in Chapter 4.

In the LGAD scenario, the sensors and the front-end electronics are fabricated on separate wafers. LGADs are produced on sensor-grade silicon wafers and require dedicated readout electronics, resulting in higher production costs and more complex assembly procedures compared to CMOS sensors (Section 1.4.4).

Two interconnection methods between the sensor and the front-end electronics are being considered. The first option is to use traditional hybrid pixel detector techniques, where the front-end ASIC layout matches the pixel pattern of the sensor, and they are connected via bump-bonding. This method minimises parasitic capacitance and inductance. However, the best timing performance achieved with LGADs to date has been through standard ultrasonic bonding wires between the sensor and the front-end ASICs.

A well-designed fan-out may allow large pixel sensors to be connected to much smaller front-end chips without compromising the system's time resolution.

1.4.4 Fully depleted CMOS LGADs

Fully depleted CMOS sensors offer a promising solution, as they could provide full coverage with a single layer and allow for a true 2D monolithic sensor design. This would significantly reduce production costs and simplify assembly compared to traditional hybrid designs.

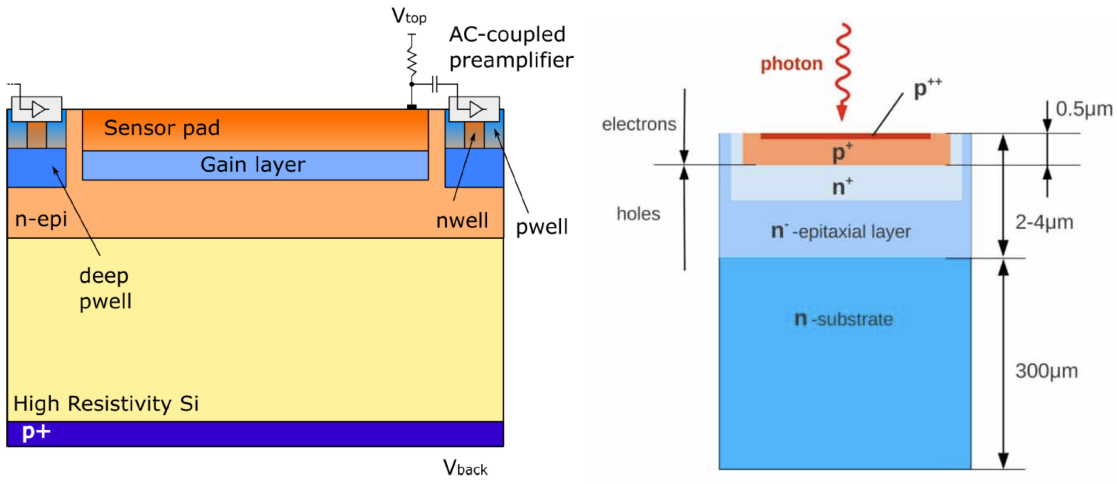

Figure 1.10: Schematic view of a thin fully depleted CMOS LGADs sensor with an added gain layer (left) and of a SPAD (right).

Currently, CMOS sensors are unable to provide the required time resolution of 20 ps. Significant R&D is already ongoing to push their timing capability beyond current levels. To reduce the effects of electronic noise, dedicated studies are underway to implement a

thin gain layer (Figure 1.10), similar to the one used in standard LGADs. This concept, combined with improved designs, is expected to enable CMOS sensors to achieve the required timing resolution while maintaining reasonable power consumption.

One of the main challenges with monolithic timing sensors is that the collection electrode occupies a large portion of each pixel. Therefore, the pixel size must strike a balance between minimising sensor capacitance and being large enough to allow for more uniform electric fields and, therefore, more consistent signal collection times. The idea is to equip each sensing diode with a dedicated front-end amplifier and discriminator. Larger macro-pixels would then be composed by combining signals from small pixels into a single data line, with time-tagging and data processing circuits handling the full data stream from each macro-pixel. This approach helps to manage both power consumption and space constraints.

1.4.5 Single Photon Avalanche Diodes (SPADs)

A Single Photon Avalanche Diode (SPAD) is a reverse-biased diode held in a meta-stable state. A single carrier can trigger avalanche multiplication, making the device inherently binary. A quenching circuit halts the avalanche, returning the SPAD to its sensitive state.

The use of SPADs has been thoroughly explored through several beam tests on different Silicon Photomultiplier (SiPM) sensors [32, 33, 34], of which SPADs constitute the individual cells. For charged particles traversing the sensors, the newly observed Cherenkov effect in the protective layer has resulted in an efficiency close to 100% and a time resolution of 20–25 ps, which approaches the ALICE 3 TOF requirements.

However, estimates of the radiation doses expected in the areas where the two TOF layers and disks will be located suggest that SPADs are not a viable option for the inner TOF or the two disks. Consequently, this solution will only be further pursued for the outer TOF layer. Additionally, the use of SiPMs in combination with the RICH detector for the outer TOF is under investigation. Indeed, a SPAD-based system could potentially merge the TOF and RICH readouts, so this option will be considered only if the integration of the two systems is viable.

SPADs fabricated using CMOS technology could offer a monolithic solution, though

the use of a single layer faces challenges, such as dark count rates (random sensor firings without any crossing particle) and fill-factor limitations (the fraction of sensitive area).

One notable advantage of using SPADs is their reduced capacitance, which lowers the load on the front-end electronics. To retain this advantage, only a few SPADs should be grouped together [35].

Chapter 2

Solid State Detectors

Since thirty years, solid state detectors, especially silicon-based ones, are used in high-energy physics (HEP). They have undergone constant improvements and have made significant advances in the last decades to satisfy challenging demands and to overcome limitations. Though based on a concept of detection, a multitude of silicon sensor designs have been introduced, attaining exceptional performance levels, providing very accurate position and time resolution and gaining curiosity in a range of physics experiments and external applications, where they are used for various purposes depending on the need for excellent spatial, temporal, or energy resolutions. In this chapter, an introduction to semiconductor materials and particle interactions with them is presented, followed by an overview of the fundamental characteristics and key elements of these detectors.

2.1 Radiation interaction

The way in which solid state detectors work, is strictly related to the different interaction mechanisms of particles with the materials of the various layers of which the detector is composed. When a particle passes through a device, it can interact with the medium, transferring the totality or a part of its energy to the electrons or nuclei of the atoms constituting the medium. In the two cases the particle is, respectively absorbed or scattered, being deflected by its incident direction.

The loss of energy happens in many different steps, with the particle decreasing its velocity at each interaction until it is totally absorbed or escapes the detector. The **maximum possible energy transfer W_{max}** of charged particle with mass $M > m_e$ to an electron in a single collision is

$$W_{max} = \frac{2m_e\beta^2c^2\gamma^2}{1 + \frac{2\gamma m_e}{M} + \left(\frac{m_e}{M}\right)^2} \tag{2.1}$$

that for heavy-charged particles, satisfying the condition $M >> 2m_e\gamma$, becomes

$$W_{max} \simeq 2m_e\beta^2c^2\gamma^2. \tag{2.2}$$

In particular, when an heavy-charged particle enters in a material with a velocity $v = \beta c$, it interacts with the atoms of the medium through Coulomb scatterings with the orbital electrons. The energy lost in this interactions can cause the excitation of electrons up to higher energy levels or ionization. In the second case subsequent secondary ionization (δ rays) close to the primary track is possible. Specifically, the mean energy loss for unit path length and unity density is called **mass stopping power**; it can be well described in the range $0.1 < \beta\gamma < 1000$ by the **Bethe-Bloch formula** [36]:

$$\left\langle -\frac{dE}{dx} \right\rangle \frac{1}{\rho} = Kz^2\frac{Z}{A}\frac{1}{\beta^2}\left(\frac{1}{2}\ln\frac{2m_ec^2\beta^2\gamma^2W_{max}}{I^2} - \beta^2 - \frac{\delta(\beta\gamma)}{2}\right)[MeVcm^2/g] \tag{2.3}$$

with $\mathrm{K} = 4\pi\mathrm{N}_A\mathrm{r}_e^2\mathrm{m}_e\mathrm{c}^2$ where N_A is the Avogadro's number, r_e is the classical electron radius, m_e is the rest mass of the electron, Z and A are the atomic number and the atomic mass, respectively, and I is the mean ionization energy of the medium. The behavior of the mass stopping power is shown in Figure 2.1 for positive muons.

Outside the mentioned range, at $\beta\gamma \sim 0.1$ the projectile speed is comparable to atomic electron speed and at $\beta\gamma \sim 1000$ radiative effects begin to be important [36].

As shown in the plot, in the very low energy range the curve is governed by a factor $1/\beta^\alpha$, where $\alpha \approx 1.4 - 1.7$, decreasing with increasing Z, and reaches a broad minimum. Considering particles with the same charge, for all the materials, the minimum is reached at $\beta\gamma \sim$ 3-4. A particle whose energy loss is at the minimum of the Bethe-Bloch function is usually called **Minimum Ionizing Particle (MIP)**. These particles, loosing a small

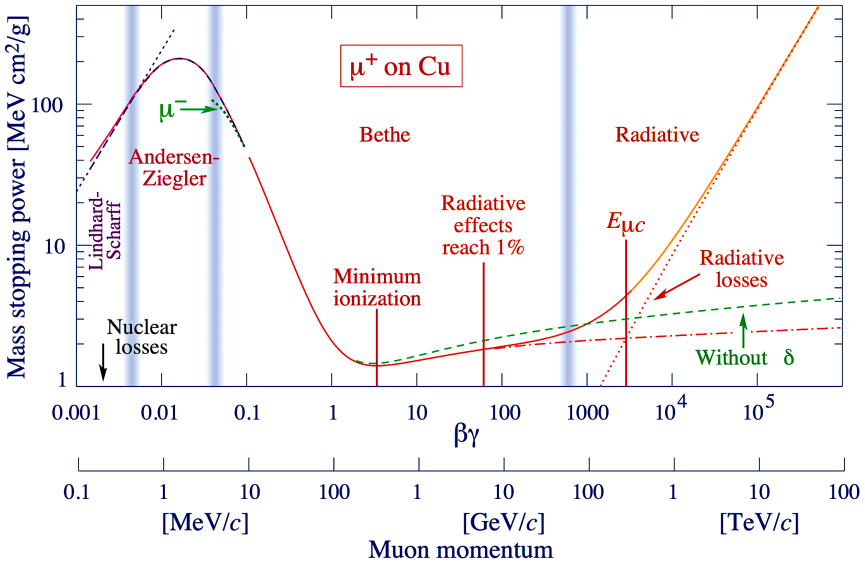

Figure 2.1: Mass stopping power as a function of $\beta\gamma = p/Mc$, for positive muons in copper; a conversion to the momentum is reported below the plot. The total stopping power is indicated with the solid line in red. Values at $\beta\gamma \sim 0.1$ and at the high energies are calculated assuming only β dependence [37, 38]. and the vertical light blue bands indicate the ranges of the boundaries of the different approximations discussed in the text. μ^- shows the dependence of stopping power on projectile charge at very low energies, called Barkas effect [39].

fraction of their energy during their path in the material, can be considered as MIP during all the whole interaction and their average stopping power in silicon is of about 1.66 MeV·cm^2/g.

After the minimum, the curve is characterized by a logarithmic rise and and for $\beta\gamma$ >4 radiating effects starts to be important. In this range, two independent mechanisms have to be taken into account: the rise due to the relativistic flattening ($\beta^2\gamma^2$ dependence) and extension of the particle's electric field in the transverse plane and the density correction $\delta(\beta\gamma)$ which, partially cancel the high energy rising, since at greater distances, rather than producing ionization, the field polarizes the medium along the particle's path and shield the long-range interactions. In addition, in this range, hard collision events increasingly extend the tail of the energy loss distribution, increasing the mean but with little effect on the position of the maximum, representing the most probable energy loss.

Taking into account the energy lost by a charged particle after a given path inside the detector ΔE, obtained by multiplying the Equation (2.3) for the thickness and the density of the detector, it is simple to obtain the **number of pairs generated** in a given material:

$$n = \frac{\Delta E}{W} \tag{2.4}$$

In particular, considering the mean energy needed to remove one electron from the atom creating a pair for silicon is $W_{Si} \sim 3.6$ eV at room temperature, each traversing MIP creates $\sim 1.1 \cdot 10^2$ pairs per µm inside it.

2.2 General properties of semiconductor materials

In order to work effectively as particle detectors, semiconductor materials must be in the form of high-purity crystals. These crystals exhibit a lattice structure where atoms are arranged in a predictable, periodic pattern. Although individual atoms possess distinct energy levels, when arranged within a lattice structure, the allowed energy levels overlap so that two bands, known as the valence and conduction bands forms, separated by a forbidden energy gap (E_g).

The magnitude of this gap is related to the chemical bonding characteristics of each material. For silicon, this energy gap typically measures $E_g \sim 1.12$ eV at 300 K. This is the minimum energy required to break a covalent bond and excite an electron from the valence to the conduction band.

At low temperature (T = 0 K), for an intrinsic semiconductor (without impurities) the valence band is completely occupied, while the conduction band is empty. In this equilibrium condition, the semiconductor behaves like an insulator, showing no electrical conductivity. At higher temperature instead, thermal vibrations can break the covalent bond, allowing a valence electron to move into the conduction band, creating a vacancy in the valence band, known as a hole. The electron-hole pair is so available for conduction. The concentration of electrons n in the conduction band and holes p in the valence band are both equal to the **intrinsic concentration** of charges $n_i = n = p$.

Both electrons and holes are subjected to the **Fermi-Dirac statistics**, so taking into account the Pauli principle, at thermal equilibrium, the probability of occupancy of one state at energy E at a temperature T is given by:

$$f(E,T) = \frac{1}{1 + e^{(E-E_F)/k_B T}} \tag{2.5}$$

where k_B is the Boltzmann constant and E_F is the **Fermi energy**. When $E = E_F$:

$$f(E = E_F) = \frac{1}{2} \tag{2.6}$$

so E_F can be seen as the energy at which exactly half of the available levels are occupied.

So, in thermal equilibrium, the final concentration of free charge carriers is given by the sum of the number of electrons n in the conduction band and holes p in the valence band, calculated respectively as:

$$n = \int_{E_C}^{\infty} g_e(E) f(E) dE \tag{2.7}$$

$$p = \int_{0}^{E_V} g_h(E) f(E) dE \tag{2.8}$$

being $g_e(E)$ and $g_h(E)$, the density of the states in the conduction and valence bands, and E_C and E_V their minimum and maximum energy levels, respectively.

Considering the effective density of states in the conduction N_C and valence N_V bands, from the integration of the equations (2.7) and (2.8), the concentration for electrons and holes results

$$n = 2\left(\frac{m_e kT}{\hbar}\right)^{3/2} e^{-\frac{E_C - E_F}{k_B T}} = N_C e^{-\frac{E_C - E_F}{k_B T}} \tag{2.9}$$

$$p = 2\left(\frac{m_h kT}{\hbar}\right)^{3/2} e^{-\frac{E_F - E_V}{k_B T}} = N_V e^{-\frac{E_F - E_V}{k_B T}} \tag{2.10}$$

with m_e and m_h the effective masses of electrons and holes and $\hbar$ the reduced Plank constant; the factor 2 derives from the two possible spin states of the electrons.

Also in this condition of high temperature, due to charge conservation, the densities of electrons and holes are equal and the charge neutrality still holds. Consequently, the intrinsic charge carrier density n_i is directly related to them by the mass-action law:

$$n_i{}^2 = n \cdot p = N_C N_V e^{-E_g/kT} \tag{2.11}$$

depending only on the **band gap** $E_g = E_C - E_V$, not on the Fermi level E_F. For intrinsic pure silicon, at room temperature ($T = 300$ K), the concentration is $n_i = 1.45 \cdot 10^{10}$ cm^{-3}.

Silicon is one of the main materials used for particle detection also because of its conductive properties. A really important parameter to be carefully tuned in the design of detectors is indeed the **conductivity** σ, defined as

$$\sigma = \frac{1}{\rho} = e n_i (\mu_e + \mu_h) \tag{2.12}$$

where ρ is the resistivity, e is the electron charge, and μ_e and μ_h are the **mobilities** of electrons and holes. The mobilities in silicon are relatively high, with values, at room temperature, of $\mu_e = 1350$ cm^{2}V^{-1}s^{-1} and $\mu_h = 480$ cm^{2}V^{-1}s^{-1}, resulting from Equation (2.12) in a resistivity of about 230 KΩcm [40]. This low value of resistivity at room temperature makes this material one of the only few suitable to be operated without cooling and deeply used in HEP detectors.

Considering the concentration of charge carriers at room temperature, for a detector with a thickness $d = 300$ µm and area $A = 1$ cm^2, the total amount of free carriers due to thermal effects, results

$$n_i dA \sim 4.35 \cdot 10^8 \; e^- h^+ pairs \tag{2.13}$$

which constitute the noise of the detector. Although, comparing this value with the signal expected from a MIP, considering an energy loss for path length unit $dE/dx = 3.87$ MeV/cm and a mean energy to produce an electron-hole pair $\mathrm{I}_0 = 3.62$ eV, in silicon

$$\frac{dE/dx \cdot d}{I_0} \sim 3.2 \cdot 10^4 \; e^- h^+ pairs \tag{2.14}$$

the resulting signal is four orders of magnitude lower than the number of free charge carriers, making intrinsic silicon unsuitable for particle detection. In order to detect crossing charged particles, it is fundamental that the charge deposited in the silicon by ionization is sufficiently higher than the amount of free carriers originating from thermal effects, so, to use silicon as a particle detector the free charge carriers must be reduced by several order of magnitudes. Cooling down the silicon volume at very low temperatures can be a solution for small implementations, but less straightforward for large detectors applications. In order to overcome this problem, instead of pure silicon crystals, doped crystals are used to create junction of semiconductor materials with different doping, called **p-n junction**.

2.2.1 Doped semiconductors and p-n junction

A p-n junction forms when an n-type and p-type semiconductors are put in contact. The main goal is to create a **space-charge region (SCR)**, or **depletion region**, where the free charge carriers are highly suppressed on either side of the junction.

Doped semiconductors are materials in which controlled impurities are artificially inserted into the lattice (Figure 2.2). This technique, called doping, allow to create additional levels in the energy gap, altering the free charge carriers concentrations and consequently changing the electrical characteristics of the crystal.

In particular, for group-IV elements, constituted by atoms with 4 valence electrons, like silicon, the most common doping materials are either group-V or group-III elements. Group-V elements, such as phosphorus, having a quasi-free valence electron easily excitable, remain as positive ions, acting as donor impurities and creating additional levels close to the conduction band. Group-III elements, as boron, instead, act as acceptors, adding levels close to the valence band. In the two cases, the material is respectively referred to as n-type silicon, with an excess of electrons as majority charge carriers, and p-type silicon, with an excess of holes.

As in the previous case, also for doped semiconductors an equilibrium between the charges is maintained, but now there are additional charge carriers balanced by dopant nuclei:

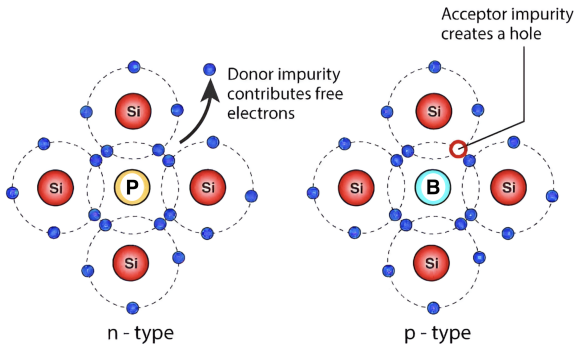

Figure 2.2: An n-type semiconductor on the left, formed by doping silicon with group-V atoms (e.g. Arsenic and Phosphorus): four electrons form covalent bonds with silicon, and the fifth becomes a free electron, increasing conductivity. A p-type semiconductors on the right, obtained by doping silicon with trivalent atoms (e.g., Boron, Aluminum, and Indium): due to the missing fourth electron needed for bonding with silicon, these atoms create holes acting as positive charge carriers.

$$N_D + p = N_A + n \tag{2.15}$$

where N_A and N_D are the acceptors and donors concentrations, respectively.

In materials dominated by one type of impurities, the dopant density is much larger than the intrinsic charge carrier concentration; taking this into account, from Equations (2.11) and (2.15), the final charge carrier density can be expressed in terms of dopant concentration obtaining for a **n-type semiconductor** ($n \gg p$ and $N_A \simeq 0$):

$$n \simeq N_D, \;\; p \simeq \frac{n_i^2}{N_D} \tag{2.16}$$

and analogously for a **p-type semiconductor** ($p \gg n$ and $N_D \simeq 0$):

$$p \simeq N_A, \;\; n \simeq \frac{n_i^2}{N_A}. \tag{2.17}$$

As the semiconductor concentration of majority charge carriers aligns closely with the dopant concentration, the contribution of minority carriers to the current becomes

negligible. From equations (2.17) and (2.16), the resistivity ρ can be rewritten in the two cases as

$$\rho_{n-type} = \frac{1}{eN_D\mu_e} \tag{2.18}$$

$$\rho_{p-type} = \frac{1}{eN_A\mu_h}. \tag{2.19}$$

In general, employing a doped semiconductor as a particle detector is not sufficient to overcome the problem given by the high number of free charge carriers. Also in this scenario, the signal would be inevitably lost under the noise. However, through the integration of semiconductors with opposite doping, a region free from charge carriers can be created and exploited to detect charged particles.

The main operating principle is based on the fact that, for a semiconductor in thermal equilibrium, the Fermi energy must be constant. Thus, when two semiconductors with different doping are joined together, a diffusion movement of free majority charge carriers to the opposite regions takes place, due to the different concentrations. A visualization of the different phases that happen when two types of semiconductors are put together is shown in Figure 2.3: electrons start to move to the lower Fermi levels, towards the p-side and holes to the higher, going in the opposite direction, leaving behind ionized charged dopant atoms. Once crossed the junction, these mobile charges become minority carriers and combine with the majority carriers present in that region, cancel each other out. The result is a region across the junction with a net charge provided by the uncovered fixed ions. The diffusion proceeds until the equilibrium condition, having the Fermi energy constant in the whole volume, is reached. The current density due to diffusion $\vec{J}_{diff}$ for both electrons and holes, described by the **Fick's first law** is proportional to the gradients of their densities $\vec{\nabla}(n,p) = \pm\frac{d\vec{n}_{n,p}}{dx}$ and can be written as:

$$\vec{J}_{diff} = qD_{n,p}\vec{\nabla}(n,p) \tag{2.20}$$

where q is the elementary charge and $D_{n,p}$ are the diffusion constants of electrons and holes, respectively.

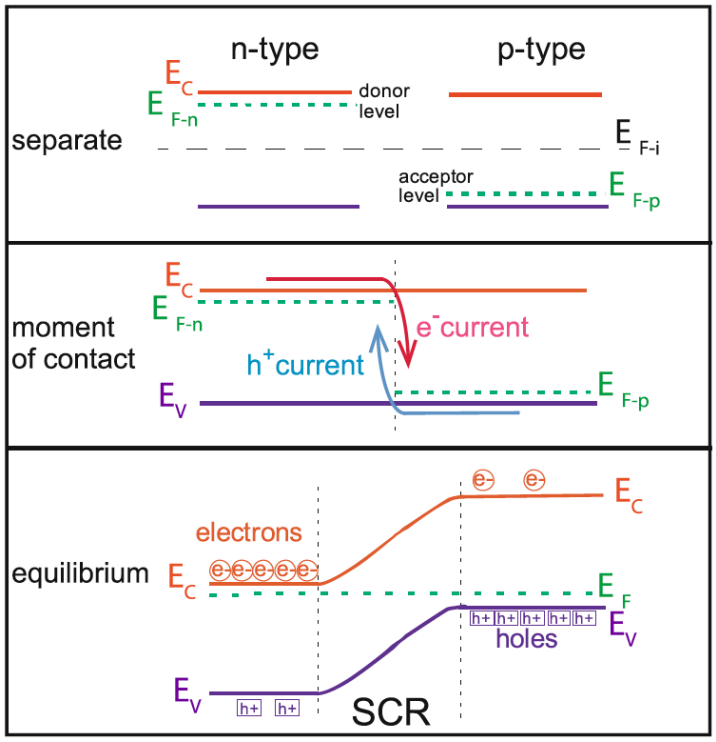

Figure 2.3: Representation of the different phases that follow the brought in contact of two semiconductors with different doping: in the first diagram, the initial Fermi levels E_{F-p} and E_{F-n} are reported respectively for the separated p-type and n-type semiconductors. The dotted line represents where the Fermi level E_{F-i} would lie in an intrinsic sensor. In the middle is shown the moment in which the two materials are joined together: electrons migrate towards the area with the lower Fermi energy, while holes move towards the region with the higher Fermi energy. Finally, the equilibrium condition in which a spatial charge is established is shown with the resulting shifts in potentials. Throughout this process, the Fermi energy reaches a constant value across the entire junction.

Due to the diffusion and accumulation of the charge carriers, a difference of potential, called **built-in voltage** V_0 is created where the SCR forms, causing an electric field $\vec{E}$, which prevent further diffusion. The charge carriers start to drift under the influence of this electric field in the opposite direction of diffusion. When the current produced by the electric field compensates the one due to diffusion a dynamic equilibrium is created and the total current density for electrons and holes results:

$$\vec{J} = \vec{J}_{diff} + \vec{J}_{drift} = qD_{n,p}\vec{\nabla}n(p) + q\mu_{n,p}(n,p)\vec{E} \tag{2.21}$$

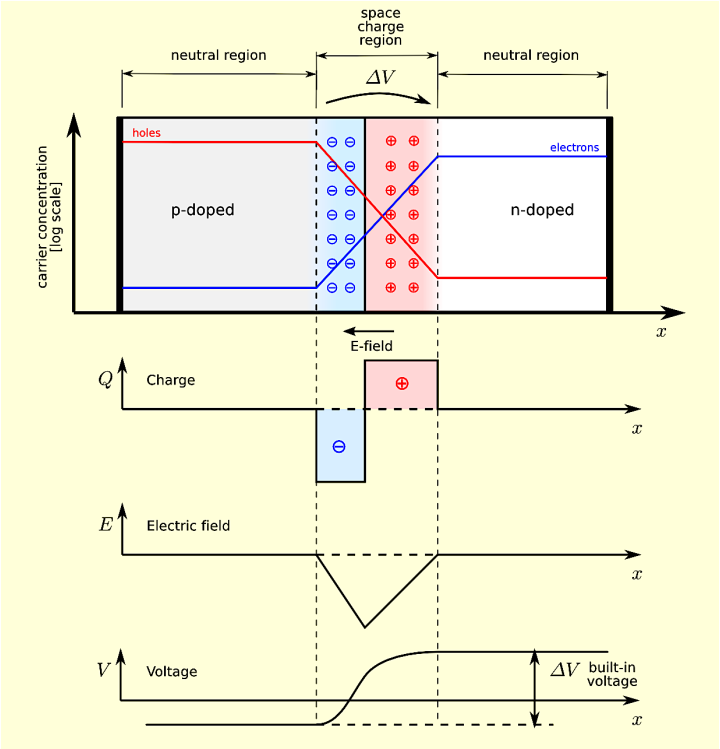

Figure 2.4: Shape of the charge density (Q), electric field (E) and voltage (V) of a p–n junction in thermal equilibrium.

In this dynamic equilibrium, the total current is 0 and the whole system is completely defined by the energy barriers related only to the doping concentration of the two sides of the junction (Figure 2.4). The volume across the p-n junction with a net charge and essentially depleted of all mobile charge carriers, is called depletion region. The size of that region can be altered by means of an external electric field applying a voltage difference to the edges of the junction; on the basis of the polarity of such applied voltage, it is possible to increase or decrease the width of this region.

When an external voltage is applied, the depletion width w increases or decreases accordingly to the following equation [41]

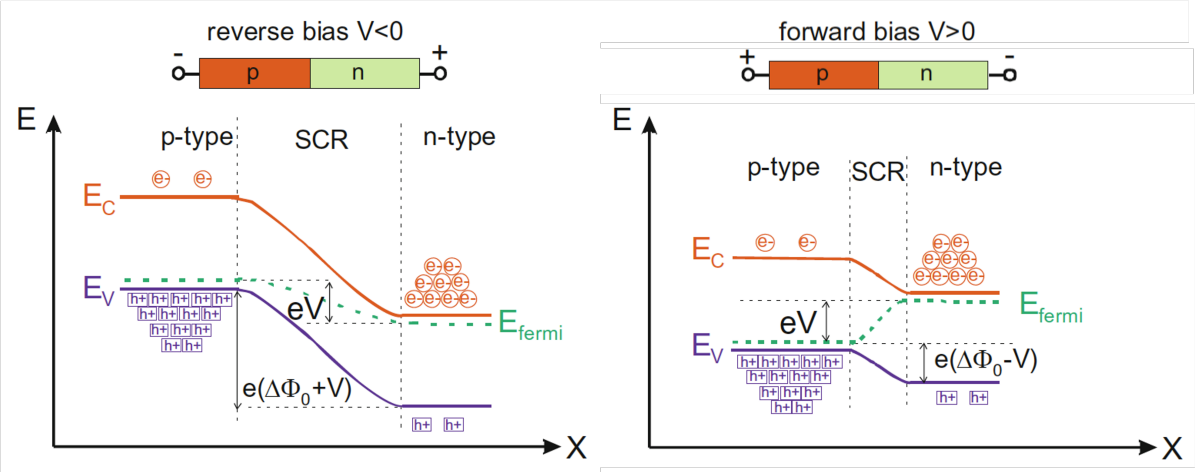

Figure 2.5: In the reverse biased case (left), both the potential barrier and the depletion width increase. In forward bias case (right), the barrier significantly reduces, allowing majority carriers to move freely through the junction.

$$w = \sqrt{\frac{2\epsilon_0\epsilon_{Si}}{e}}\sqrt{\frac{N_A + N_D}{N_A N_D}(V_0 - V)} = \sqrt{2\epsilon\mu\rho V} \tag{2.22}$$

where V is the external applied voltage and ϵ_{Si} the permittivity of silicon.
The two possible biasing conditions are depicted in Figure 2.5:

- **Forward bias:** when a positive (negative) voltage is applied to the p-side (n-side) of the *pn*-junction, the built-in voltage decreases, causing the depletion zone to shrink.

- **Reverse bias:** when a negative (positive) voltage is applied to the p-side (n-side) of the *pn*-junction, the built-in voltage increases, leading to the enlargement of the depletion zone.

Silicon detectors are operated in reverse bias mode. In this condition, in absence of an incident radiation the leakage current across the junction is dominated by thermally generated e-h pairs and is very small. The bias voltage V_{FD} required to fully deplete a sensor is found equalizing the width of the depletion region to the thickness of the detector $w = d$ in the equation (2.22)

$$V_{FD} = \frac{d^2}{2\epsilon\mu\rho}. \tag{2.23}$$

This parameter has to be taken into account in the design of the sensors. Indeed for many applications, it is important to work with a full depleted sensor, i.e. V_{FD} should be lower than the sensor breakdown voltage. This value is related also to the full depletion capacitance of the sensor which depends only on the sensor thickness and area:

$$C_{FD} = \frac{\varepsilon_{\mathrm{Si}}\varepsilon_0 A}{w} \tag{2.24}$$

where $\varepsilon_{\mathrm{Si}}$ is the dielectric constant of silicon, ε_0 is the dielectric constant of vacuum, A is the area of the detector, and w is its thickness.

2.3 Basic principles of silicon detectors

A silicon detector is basically a solid state ionization chamber which exploits the properties of a semiconductor to detect radiation. Silicon detectors used in particle physics are usually based on a **reverse-biased p-n junction**, featuring a heavily doped p^+ electrode connected to a negative voltage and a heavily doped n^+ connected to a positive voltage. The two electrodes are usually separated by a lightly doped n^- epitaxial layer, which serves as the detector's active region. A basic diagram of a silicon detector is shown in Figure 2.6.

When an ionising particle passes through the depleted region, it interacts with the atoms in the material. As it travels, it transfers some or all of its energy to the electrons in the atoms, that can excite the electrons, causing them to break free from their atomic bonds and move into the conduction band, so that electron-hole pairs are created. These pairs drift towards their respective electrodes, following the electric field lines created by the bias voltage. The generated holes drift towards the p^+, while the electrons drift to the n^+ back-plane. The movement of these charges induces a current on the electrodes 2.26, producing a measurable signal proportional to the number of pairs generated and, consequently, to the energy lost by the particle in the material. The charge induced on the doped electrode can be capacitatively (AC) coupled to the aluminum readout, in turn connected to a charge pre-amplifier of the readout chip. Once all charge carriers

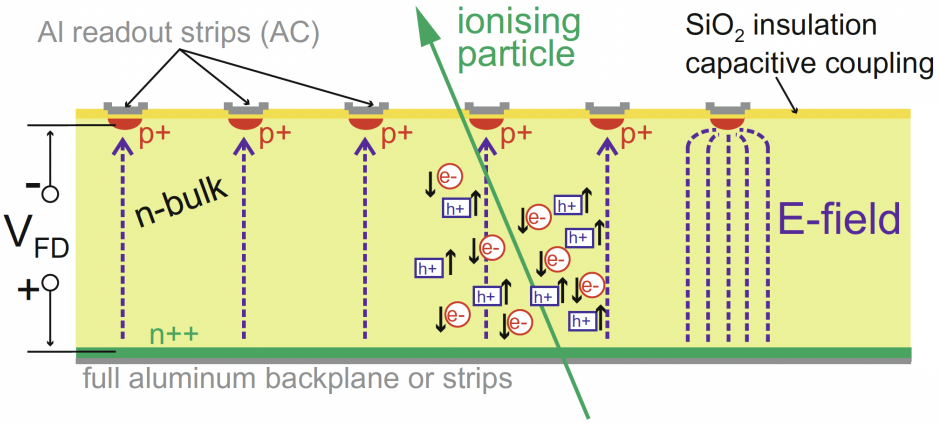

Figure 2.6: Principle of operation of a p-in-n AC-coupled silicon micro-strip detector. Electron-hole pairs generated by the ionization due to the passage of the ionizing particle, are driven by the electric field towards the electrodes on the sensor planes. In this picture a segmentation of the p-n junction is present, enabling charge collection on individual strips capacitively coupled to some aluminum readout strips. These are in turn connected to the readout electronics, where the signals are shaped and amplified.

have reached the collection electrodes the signal ends.

Although the working principle is the same of many radiation detectors, as the ones based on ionization in gas, if compared with others, semiconductors have unique properties which make them very suitable for this purpose. The average energy needed to create an electron-hole pair in silicon is $\sim$ 3.6 eV, one order of magnitude smaller than the ionization energy of gases ($\sim$ 30 eV) [42]. Thanks to the very low energy gap, a larger number of charge carriers is created per unit energy loss of the ionizing particle to be detected. Moreover, semiconductors feature a high material density ($\sim$ 2.33 g/cm^3 for silicon) that leads to a large energy loss dE/dx of a MIP, of the order of 390 eV/µm, allowing the construction of thin detectors that can still produce measurable signals. It is important to note that despite the higher material density, electrons and holes can move almost freely in semiconductors, leading to a very fast charge collection of around 10 ns making these detectors really suitable also in high-intensity environments. Thanks to the combination of all these advantages, solid state detectors, and in particular silicon

based ones are being used and scheduled in a wide range of applications.

2.3.1 Signal formation

As already introduced, charged particles, crossing a detector, release energy inside it, causing excitation or ionization of atoms, creating e-h pairs. When an external bias voltage is applied, charge carriers begin to drift, inducing a current on the electrodes, which depends on the position where the pairs have been created, thus producing a measurable signal [43, 44].

When all the carriers reach the collecting electrodes the induced signal stops and the pulse is fully developed. The **total collected charge** in the time t_c (of the order of ns for silicon) is

$$Q_{tot} = \int_0^{t_c} i(t)dt. \tag{2.25}$$

The signal induced by on each electrode is described by the Shockley-Ramo's theorem [45, 46, 47]. The **instantaneous charge** $Q(t)$ and **current** $i(t)$ generated on a given electrode, by a carrier with charge q which is moving with a velocity $\vec{v}$ is calculated as:

$$Q(t) = -qV_w(x) \tag{2.26}$$

$$i(t) = -q\vec{v} \cdot \vec{E}_w(x) \tag{2.27}$$

where the **weighting potential** $V_w(x)$ and the **weighting field** $\vec{E}_w(x)$ represents the interaction between the charge q and the considered electrode. In the case of a single $e-h$ pair inside the active area of the sensor, the charge q is the integral of the currents generated by both electrons and holes.

$$q = \int (i_e(t) + i_h(t))\ dt \tag{2.28}$$

In fact, the drift of the electrons towards the cathode and the one of the holes in the opposite direction induce on an electrode two currents with the same sign. Moreover, the relative contribution of $i_e(t)$ and $i_h(t)$ is proportional to either the weighting field and the geometry. Since $V_w(x)$ and $\vec{E}_w(x)$ are assumed as they would be calculated in an instantaneous position x, having a readout electrode set to 1 V and all others to 0 V,

the weighting field exhibits the same geometric dependence as an electric field, scaling as a function of the distant d as $1/d$ for a linear electrode, as $1/d^2$ for a punctiform one and remaining constant between two large electrodes.

So, in a simple configuration of a parallel plate detector, like for example a standard PIN (p-on-n) diode with a pixel size larger than the sensor thickness, where the cathode and the anode, at a relative distance of d, represent the plates, the weighting field becomes

$$\vec{E}_w(x) = -\frac{1}{d}\vec{e}_x. \tag{2.29}$$

Having a constant weighting field, the induced signal depends uniquely upon the velocity of the carriers and not on their position.

2.3.2 Diffusion and drift velocity

The motion of the charge carriers inside semiconductors influence many operating characteristics of the detector. In particular, diffusion and drift velocity have a significant effect on the signal length and shape.

For the most part, this motion is described by the classical kinetic theory of ionization detectors.

In absence of an electric field, electrons and holes released by the passage of a particle diffuse uniformly, undergo multiple collisions inside the material, loosing their energy until they reach a condition of thermal equilibrium and eventually recombine. At thermal energy T, the velocities of the charges are described by the Maxwell-Boltzmann distribution, resulting in a mean diffusion velocity v_{diff} of

$$v_{\text{diff}} = \sqrt{\frac{8kT}{\pi m_e}} \tag{2.30}$$

where k is the Boltzmann constant and m_e is the electron mass. At room temperature, v_{diff} is of the order of 10^6 cm/s for electrons and 10^4 cm/s for holes.

The fraction of particles at a given position and time, $\frac{1}{N_0}\frac{dN}{dx}$, with N_0 the total number of charges, follows a Gaussian distribution. Defining the diffusion coefficient as $D = \frac{1}{3}v_{\text{diff}}\lambda$, where λ is the mean free path, the standard deviation σ of this distribution results:

$$\sigma = \sqrt{2Dt} \tag{2.31}$$

When an electric field E is present instead, electrons and ions start to drift along the field lines with an average **drift velocity**:

$$v_{\text{drift}} = \mu E \tag{2.32}$$

where is the mobility as defined in Equation (2.12).

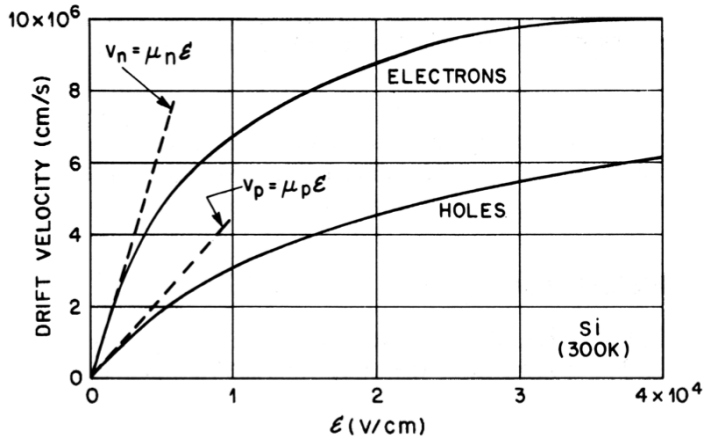

Figure 2.7: Drift velocity as a function of electric field for electrons and holes in silicon [29].

The drift velocity is different for electrons and holes. At higher electric fields, the drift velocity of electrons increases until it saturates due to collisions with the detector atoms at around $E_w = 30$ kV/cm at room temperature. The drift velocity for the holes is usually not saturated inside detectors, since in this case an extremely high value of electric field is required ($E_w > 100$ kV/cm).

The relationship between drift velocity and electric field for electrons and holes in silicon is shown in Figure 2.7.

2.4 Time resolution of silicon sensors

In addition to the sensors, other elements must be taken into account when performing a timing measurement. The key components can be modeled as schematized in Figure

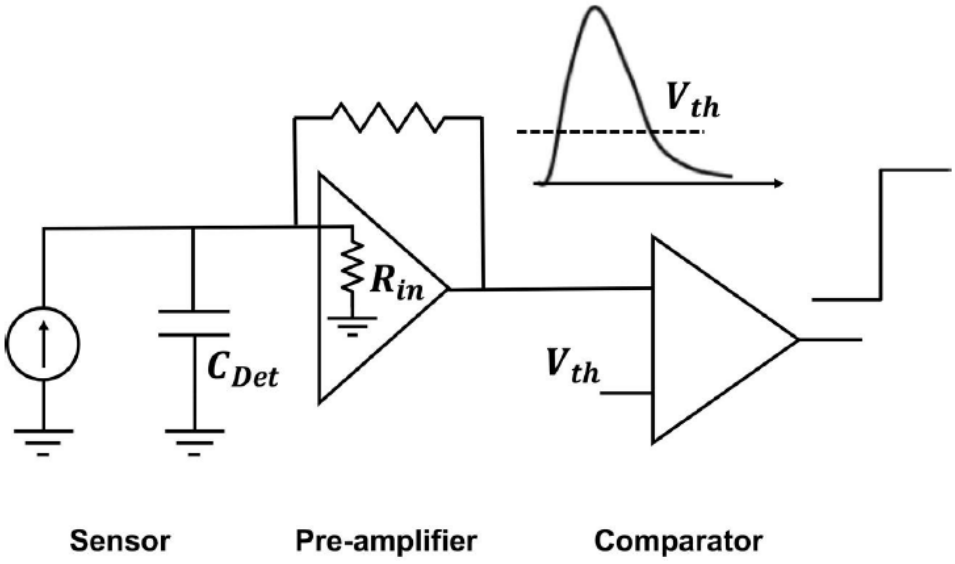

Figure 2.8: Scheme of the elements composing a timing detector. The time measurement corresponds to the passage of the signal above the threshold V_{th} inside the comparator.

2.8. The sensor can be represented by a capacitance (C_{det}) in parallel to a current generator (I_{in}), followed by a pre-amplifier, which amplifies and shapes the signal, before it arrives to the comparator. At this stage, the amplified signal is compared to a reference voltage level (V_{th}) and discriminated, i.e. converted in a logical signal when exceeding this threshold. Finally, a Time-to-Digital Converter (TDC) measures the time interval between two events, as the particle crossing time and a reference signal (start) and converts this time measurement into a digital value. Any effect in this whole readout chain that might impact the shape of the signal and thus influence the time at which the signal amplitude exceeds the comparator threshold, will affect the precision of the measurement of the time of the hit.

In order to perform a very precise timing measurements both the sensor and the front-end electronics have to be carefully chosen. The sensor must provide a large and fast signal, while the electronics has to decide with the minimum uncertainty a given point of the waveform to be associate to the time of arrival of the particle.

Taking into account all the described elements, the total time resolution can be expressed as the quadratic sum of the contributions related to each of them:

$$\sigma^2_{tot} = \sigma^2_{Landau} + \sigma^2_{TimeSlewing} + \sigma^2_{Jitter} + \sigma^2_{Distortions} + \sigma^2_{TDC}. \tag{2.33}$$

The first two terms are related to the non uniform energy deposition of the impinging particles. The jitter contribution is due to the electronic noise, while the distortion is connected to the non-uniformities of the electric field or a non-saturated drift velocity. The last one is due to the finite size of the TDC bin. More details are provided in the next paragraphs.

2.4.1 Landau noise

Landau noise is related to the stochastic nature of the energy deposition and number of pairs produced. As shown in the Shockley-Ramo theorem (2.26), a non uniform ionization, i.e. a difference in the induced current, reflects in irregularities in the shape of the signal. Indeed, large amplitude signals are generated by large localized clusters of charge, resulting in a non uniform charge deposition. This variability degrades the achievable temporal resolution and constitute the physical limit of how uniform the sensor signal can be. If the detector is well designed, the Landau noise should be the dominant factor in the total time resolution.

This effect can be mitigated integrating the output current over a long period of time in order to overcome the spike length, smoothing the signal ramp, or considering thinner sensor layouts. In thin sensors, the signal, having a faster rising edge, is less sensitive to Landau fluctuations. More details are present in Section 3.3.1.

2.4.2 Time Slewing

Like for the Landau noise, time slewing (also called time walk) is a consequence of the non-uniform ionization of particles and, more specifically, it is related to the number of pairs produced. Indeed, identical particles can produce a different number of e-h pairs traversing the same material thickness due to the stochastic nature of the creation process, resulting in changes of the signal amplitude. In particular this contribution arises when comparing the signal to a fixed threshold V_{th} in the analog-to-digital conversion.

Indeed, signals with different amplitudes cross the same threshold level V_{th} at a different times. As shown in Figure 2.9, larger signals cross the threshold earlier than smaller ones.

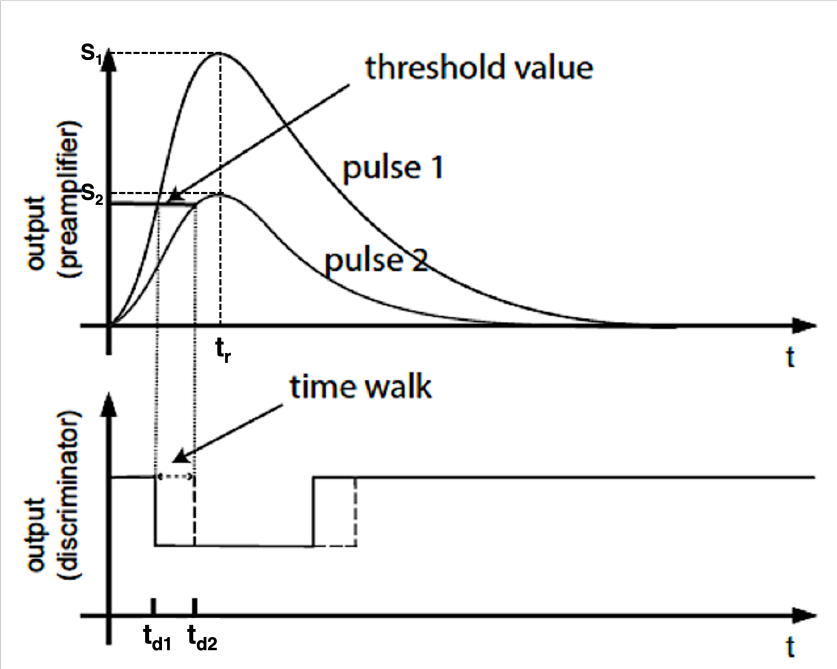

Figure 2.9: Analog signals (pulse 1 and 2) with different amplitudes cross the threshold value at different times (t_{d1} and t_{d2}), generating discriminated signals with a time walk delay proportional to their amplitude.

Given a signal with **amplitude** S and **rise time** t_r and using the geometrical relation $t_d/t_r = V_{th}/S$, the time t_d at which a fixed threshold V_{th} is crossed is proportional to

$$t_d \propto \frac{t_r V_{th}}{S} = \frac{V_{th}}{dV/dt} \tag{2.34}$$

where the second equality comes from the fact that $S/t_r = dV/dt$. The **Time Slewing contribution** to the time resolution is defined as the RMS of t_d

$$\sigma_{TimeSlewing} = [t_d]_{RMS} \propto \left[\frac{V_{th}}{S/t_r}\right]_{RMS} = \left[\frac{N}{dV/dt}\right]_{RMS}. \tag{2.35}$$

The choice of V_{th} is made to ensure the exclusion of the **noise amplitude** N, and

therefore it is set a certain number of times above it ($V_{\text{th}} = n \times N$), where n depends on the amount of noise contamination one is willing to tolerate.

2.4.2.1 Time Slewing correction

The time slewing effect can't be avoided in systems whose front-end electronics consists in a discriminator with a fixed threshold, introducing a significant degradation in the total temporal resolution. However, it is possible to correct this effect using appropriate electronic circuits and/or time slewing corrections. Two common approaches used to correct for this effect are the **measurement of the charge** and **Constant Fraction Discriminator (CFD)**. Indeed, the measured charge is related to the Time-Over-Threshold (ToT), i.e. the time during which the signal remains above the threshold. In particular, the arrival time, t_{d1}, defined as the moment when the signal exceeds the threshold, can be corrected using the ToT, given by $\text{ToT} = t_{d2} - t_{d1}$, where t_{d2} is the instant when the signal falls back below the threshold. By analyzing the correlation between the initial arrival time t_{d1} and ToT, the correction is performed as follows: the ToT spectrum is divided into bins, each containing a similar number of events. For each bin, the Gaussian mean of the arrival times is extracted along with its dispersion. These mean values are then fitted with a function $f(\text{ToT})$ that accurately represents their trend, typically a polynomial or a spline function. Finally, each measured arrival time t_{d1} is corrected by subtracting the value or the function evaluated at the corresponding ToT, as $t_{d1_{corr}} = t_{d1} - f(\text{ToT})$. The CFD method instead consists in determine the particle arrival time at a fixed fraction of the signal amplitude (usually referred to as the CFD percentage), rather than when it crosses a fixed threshold. CFD is a very good compromise between accuracy and fast timing and works well in conditions in which the signals amplitude scaling is not affected by distortions. A schematics of the electronic implementation is reported in Figure 2.10. The incoming signal is divided into three parts. One part is directly sent to another comparator (1). The other two parts are instead sent to the two amplifiers of the same comparator (2): one is scaled by a given factor C of the signal amplitude (3) and sent to the inverting input (4), the other is delayed by a time t_d lower than the rising time t_r (5) and these two signal are then summed (6). The output signal (7) is a bipolar pulse which crosses the time axis (zero-crossing time) at constant fraction of the height of the

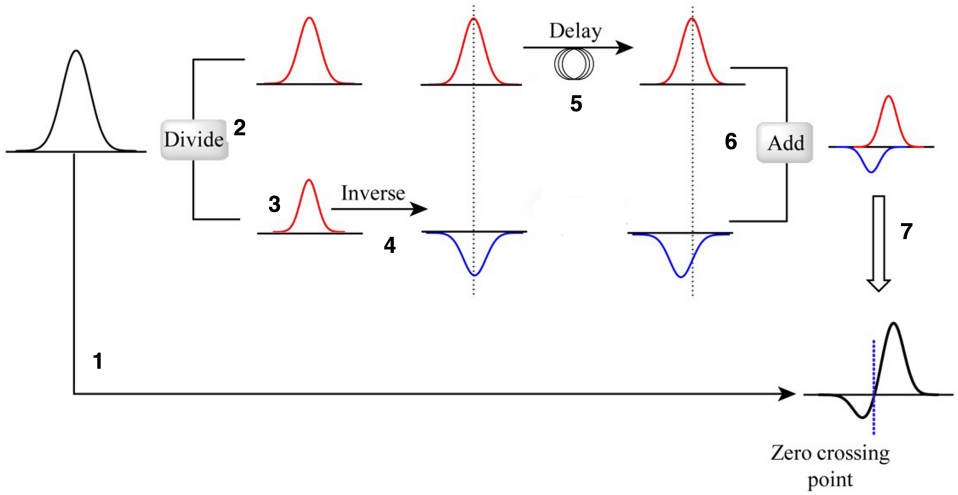

Figure 2.10: Principle of the digital constant fraction discriminator algorithm.

original pulse.

2.4.3 Jitter

Jitter contribution is related to the noise on the signal coming from either the detector connected to the pre-amplifier, or from the discriminator. The effect of this noise is making the signal passing the threshold at an earlier or later time. Looking at this effect near the threshold V_{th}, it is directly proportional to the RMS of the noise voltage N and inversely proportional to the slope of the signal. The signal level in fact, also for a fixed amplitude, is affected by the detector and electronic noise, as shown in Figure 2.11. Considering then a constant slope, the slew rate dV/dt can be approximated by the ratio of the signal amplitude S over the rising time t_r. The jitter can be written as

$$\sigma_{Jitter} = \frac{N}{|dV/dt|_{V_{th}}} \sim \frac{t_r}{S/N} \tag{2.36}$$

2.4.4 Distortions

In order to design a sensor aiming to achieve a very good time resolution, it is necessary to generate very uniform current signals $i(t)$ across the whole sensor volume. As derived

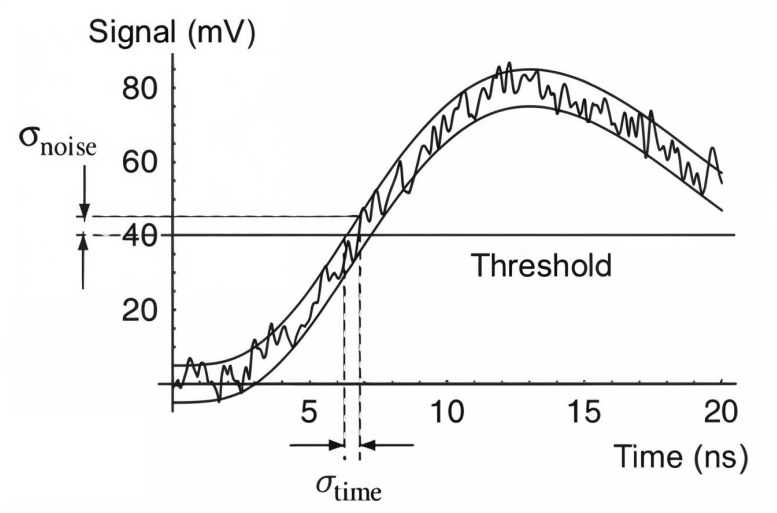

Figure 2.11: Jitter contribution: the noise of the system results in a variation of the time at which the signal crosses the threshold.

in Section 2.3.1 the signal shape is determined by the Shockley-Ramo's Theorem ($i(t) = -q\vec{v} \cdot \vec{E}_w(x)$) 2.27. From this relation, the critical elements to be taken into account are the drift velocity $\vec{v}$ and the weighting field $\vec{E}_w(x)$:

- the main requirement for the charge carriers **drift velocity** $\vec{v}$ is the uniformity along the whole active area of the sensor, to avoid any variation in the signal shape, related to its impact position. In order to reach this condition, the simplest way is to saturate the drift velocity of the charge carriers, by having in the whole sensor a sufficiently high electric field. Specifically for electrons, an electric field of $\sim$ 30 kV/cm is required, while for holes this condition is never reached. This means that higher fields always generate sharper signals.

- For the **weighting field** $E_w(x)$ the requirement is to be as uniform as possible along the whole sensor surface. This parameter represents the coupling between the readout electrode and a carrier with charge q positioned in a given location, meaning that if in this location a weighting field $E_w(x)$ is present, than a charge $q \cdot E_w(x)$ is induced. For a non-uniform $E_w(x)$ along the pitch implant, the shape of the generated signal is dependent on the particle impinging point. As shown in Figure 2.12, for a narrow strip implant this value largely depends on the position,

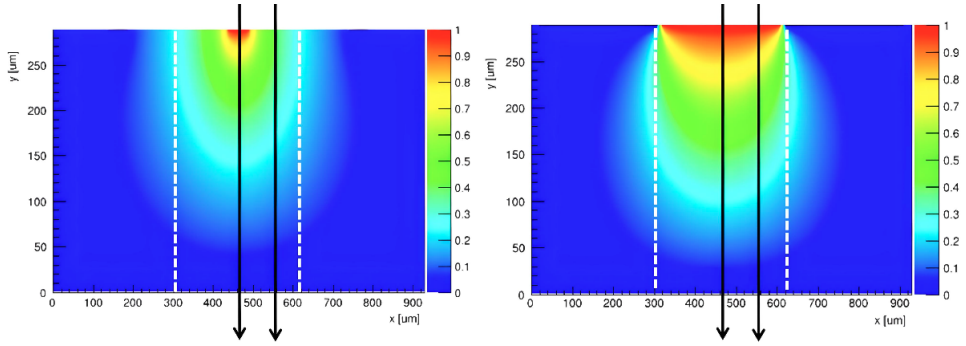

Figure 2.12: Weighting field E_w for a narrow (left) and a more wide pitch implant (right). For the narrow implant, the weighting field is less uniform along the x-axis, and there is a clear difference between the current $i(t)$ generated in the two showed particle impinging points, increasing the time resolution uncertainty.

while if the implant is comparable to the pitch, a more uniform E_w is obtained.

From the two previous considerations, it is immediate to concluded that the best sensor geometry to obtain an electric and weighting fields as uniform as possible, is in a simple approximation a parallel plate capacitor with a pitch larger than the sensor thickness, assuring in the whole active volume, a constant drift velocity and coupling between the charge carriers and the readout electrode.

2.4.5 TDC

TDC contribution is connected to the digitization of the signal made by the Time-to-Digital Converter (TDC). The TDC saves the threshold crossing time in a time bin of finite width, corresponding to its **internal clock cycle of duration** Δt. The period from the start to the end of the signal is given by the **number of clock cycles** n, between the two events in the counter: $n\Delta$t. As a consequence this conversion adds a contribution to the time resolution equal to

$$\sigma_{TDC} = \frac{\Delta t}{\sqrt{12}}. \tag{2.37}$$

TDC which are used in high energy physics experiments have usually a very fine binning, that can arrive to the order of few ps, so that this contribution results really small and in some cases almost negligible.

2.4.6 Final considerations

All the different contributions detailed in this section make it clear that the base to obtain a better time resolution requires both a high slew rate (fast signal) and a large S/N ratio. In principle, to achieve this condition the best strategy seems to use a thicker detector, and be in the conditions in which the velocity of the charge carriers is as high as possible and the electric field inside the sensor is highly uniform, however:

- while the thickness of the detector may seem like a straightforward approach to increase the signal, from Equation (2.26) it can be derived that the maximum current is independent of the detector thickness. Indeed, assuming an electric field high enough to saturate the drift velocity v_{sat}, the value of the **maximum current** for a sensor of thickness d can be expressed as:

$$i_{sat} \propto Nq\frac{1}{d}v_{sat} = (n_{e-h}d)\frac{1}{d}qv_{sat} = n_{e-h}qv_{sat} \tag{2.38}$$

  where n_{e-h} is the number of e-h pairs generated per unit length, assuming a uniform ionization. Since the **total number of pairs generated** N is proportional to the thickness d, in thicker sensors more charges are created, but each of these contributes less to the induced current i_{sat}, being the weighting field lower ($E_w \propto \frac{1}{d}$). In particular, for $N \sim 10^2 \mu\text{m}^{-1}$ and $v_{\text{sat}} = 10^7\,\text{cm/s}$, the maximum current that can be reached is approximately $1 - 2\,\mu\text{A}$.

- increasing the velocity of the charge carries does not help as well, since as seen in Section 2.3.2, this is constrained by the saturation velocity (v_{sat}).

- having a uniform electric field across the detector can be obtained using a p-n diode explained in Section 2.2.1. This effectively ensures a uniform charge collection and helps improving time resolution; nevertheless, standard silicon detectors still face limitations in time resolution, and alternative techniques are required to push beyond these limits.

In conclusion further advancements in detectors time resolution requires innovative techniques beyond conventional silicon detector configurations.

Exploiting the Impact Ionization mechanism could be the solution as discussed in the next section.

2.5 The Impact Ionization mechanism

The multiplication process starts when the charge carriers drift in a region with a sufficiently high electric field. Indeed, primary electrons can gain sufficient energy to cause inelastic collisions, leading to excitation and ionization of nearby atoms. If the electron's energy is larger then the ionization potential of the atom, it can further ionize, generating secondary electrons and triggering a chain reaction. This effect is called **Impact Ionization mechanism** and, if kept under control, by having an electric field under a certain threshold or using a quenching mechanism that stops it in a relatively short time, it does not creates damages in the sensors. As described in details in Section 3.3 it can even been exploited in the optimization of sensors for timing, being the base of Avalanche PhotoDiodes (APDs), SiPMs and, as discussed in Chapter 3, of LGADs. The principle is the same as for gaseous detectors, based on the **Townsend avalanche**: under the effect of an electric field high enough, the primary carriers, both electrons and holes, are accelerated to energies high enough to knock other bounded electrons in the silicon and create secondary electron-holes pairs. These are in turn accelerated and are capable to free additional electrons, so that the avalanche multiplication starts.

It is possible to model the multiplication of initial h and e drifting through a silicon path length d, considering that the the **total number of e-h pairs generated** $[N_{e-h}]_d$ at the end of the avalanche exponentially depends on the distance traveled by the carriers in the high electric field and on the ionization rate, i.e. number of electron-hole pairs n generated by a carrier per unit distance α_n and α_p, respectively for electrons and holes. In particular, considering the **generation rate** $\frac{d(n,p)}{dt}$ in silicon, i.e the number of e-h pairs produced per cm^3 per unit time, is the same for electrons and holes, in a uniform electric field we have that:

$$\frac{dn}{dt} = \frac{dp}{dt} = \alpha_n n v_n + \alpha_p p v_p \tag{2.39}$$

where $v_{n,p}$ are the carrier velocity of electrons and holes, respectively. As a conse-

quence, the charge multiplication factor, namely **gain** G for both types of charges, can be defined as:

$$G = \frac{[N_{e-h}]_d}{[N_{e-h}]_0} = e^{\alpha_{n,p} d} \tag{2.40}$$

$\alpha_{n,p}$ are called **ionization coefficients** and are the inverse of the **mean free path** between two subsequent scattering events producing the secondaries, $\lambda_{n,p} = 1/\alpha_{n,p}$. On average, impact ionization occurs when charge carriers travel in the high electric field a distance d long enough to acquire a kinetic energy larger than the ionization energy E_i. As described before, that in silicon is of the order of 1.5 times the energy gap E_g of the semiconductor, shown in the previous chapter to be 1.12 eV for silicon at 300 K. This is related to the indirect band-gap structure of silicon [48]; indeed, when a valence electron is excited to the conduction band, phonons are needed for momentum conservation, so the energy required to create an electron-hole pair becomes $\sim$ 3.6 eV. Considering the same electric field this distance is larger for holes (λ_p) with respect to the electrons (λ_n), so that it is possible to choose a value at which only the electrons start the multiplication process. This feature is fundamental to maintain a low multiplication factor, preventing the avalanche from developing without control.

One of the most commonly used local avalanche generation model in silicon, similar to the one used in gasses, is called **Chynoweth model** [49], which infers a relation between the $\alpha_{n,p}$ and the electric field:

$$\alpha_{n,p}(E) = \left[\alpha_{n,p}\right]_\infty e^{-\frac{\beta_{n,p}}{|E|}}. \tag{2.41}$$

$\left[\alpha_{n,p}\right]_\infty$ is the maximum number of e-h pairs that can be generated in a strong enough electric field, while $\beta_{n,p}$ is a coefficient derived from experimental fits different for electrons and holes and depending on the temperature. As a consequence, this introduces a relation between the impact ionization coefficients and temperature and specifically, the mean distance necessary to achieve multiplication is shorter at a lower temperature, yielding an increasing of the multiplication at the same electric field.

The dependence of the impact ionization factors can be inferred by many different models, among which the most commons are **Massey** [50], **Van Overstraeten-De**

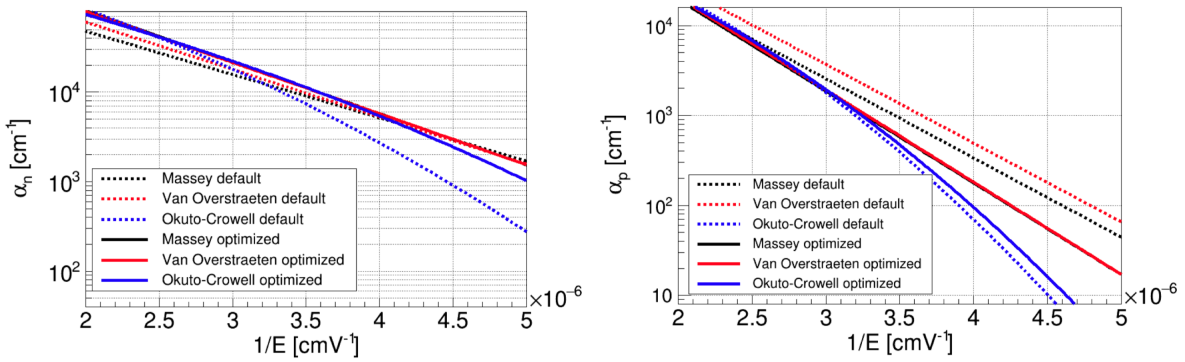

Figure 2.13: Electrons (left) and holes (right) impact ionization factors as a function of the electric field for a fixed temperature of 20°C for three common models. The original models are presented in dashed lines, while a more recent optimization of the value is shown in solid lines. [51]

Man [52] and **Okuto-Crowell** [53]. Figure 2.13 shows the relationship between $\alpha_{n,p}$ and the electric field value, for the cited models.

As anticipated in the introduction of this section, the behavior of the detector is strongly dependent on the gain value. In particular, when the gain value is finite, the detector works in linear mode, while going to an electric field higher than $\sim$ 400-500 kV/cm, the gain tends to infinite and the detector starts to work in a Geiger mode, going in a condition of uncontrolled multiplication called breakdown.

Chapter 3

Low Gain Avalanche Detectors (LGADs)

Low Gain Avalanche Detectors (LGADs) represent an innovative type of pixelated silicon sensors exhibiting an excellent time resolution. They are an evolution of n-in-p planar silicon sensors, based on the implantation of a heavily doped layer beneath the $n-p$ junction. LGADs specifically optimized for timing, also known as **Ultra-Fast Silicon Detectors (UFSD)**, offer a time resolution of around 30 ps by employing thinner sensors to shorten signal collection time and incorporating internal gain to amplify the initial charge, enabling operation with a smaller collected charge. Key features of LGADs optimized for timing include large and fast signals for excellent timing performance, minimal noise increase, reduced Landau fluctuations, and a very uniform weighting field. Some particular types of implementations, e.g. AC-LGAD [54] can provide also excellent space resolutions of the order of 10 µm, by combining a moderate intrinsic gain (from 10 to 70), with a fine sensor segmentation.

This section discusses the operating principles of LGADs, including how the signal is formed, their properties, expected performance, and a small overview of radiation effects, including how these sensors are affected by radiation. In the end, some designs will be presented together with different usage of this kind of technology spanning from high-energy physics to space and medical applications.

3.1 LGAD technology

A simple sketch of the LGAD schematics is reported in Figure 3.1 (right) in comparison to a standard n-in-p diode (left). Here a n-in-p ($n^{++}/p^{+}/p^{-}/p^{++}$) junction scheme is reported, but also a p-on-n design could be used.

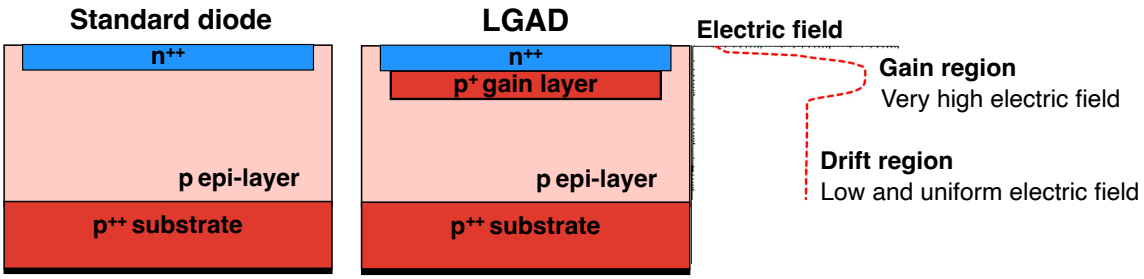

Figure 3.1: Cross-section of a standard silicon diode (left) compared to a Low-Gain Avalanche Detector (right). The additional p+ layer below the n-p junction allow the creation of a localized very high electric field, where the charge multiplication occurs.

The **p-type silicon substrate** is usually highly doped with acceptor impurities, such as boron, with a doping concentration typically in the range of 10^{13} to 10^{15}cm^{-3}. This acts as the bulk material, providing the necessary base for creating the depletion region.

An **epitaxial p-type layer** (p-epi layer) forms on top of the p^{++} layer. This layer has a low doping concentration and represents the drift region of the sensor. By carefully controlling the doping concentration and thickness of this layer, the electric field can be maintained uniform to minimize the noise contribution and assure a more uniform shape of signals.

The main difference with the standard diode regards the additional p^{+}-doped thin layer, or **Gain Layer (GL)**, just below the p-n junction formed with the highly doped n^{++} electrode on the top. This layer, heavily doped with donor impurities, for example, boron (B) or gallium (Ga), has a doping concentration in the range of $\sim 10^{16}\ cm^{-3}$ and it is crucial to generate a strong electric field under reverse bias conditions, which is

essential to accelerate the electrons enough and start the avalanche multiplication process. As shown before, the avalanche mechanism happens when charge carriers drift in a region where the electric field is higher than about 300 kV/cm, and it is important that it happens when the reverse bias on the sensor exceeds the depletion voltage to have this mechanism only when the sensor is fully depleted, but far from the **breakdown (BD)** so that the sensor can be operated in a region in which the gain can be controlled. In a standard silicon sensors, the necessary value of electric field can be obtained only applying a very high external bias voltage, a condition that is prone to cause an early breakdown of the sensor because of the high electric field on the device periphery. The big advantage of the gain layer present in the LGAD design is the generation of this electric field, high enough to obtain the avalanche process in a very narrow region of the sensor, just underneath the n^{++} implant which does not extend to the sensor periphery. So, as shown in Figure 3.1, the electric field results to be divided in two parts: a very high part (E $\sim$ 300 kV/cm) situated along the p-n junction in which the multiplications happens, and a moderate and uniform one along the rest of the depletion zone, of the order of 30 kV/cm, that allows the charges to saturate their drift velocity without starts the multiplication.

Typically, in addition to the basic structure, other elements are presents. Pads can be electrically isolated by a narrow p^{+} ring, called **p-stop**, which separates the n^{++} electrodes, preventing the diffusion of electrons through adjacent pads. At the pad (pixel) edge, an additional **Guard Ring (GR)** and a **Junction Termination Extension (JTE)** can be implemented to prevent premature breakdown at the pad borders and to ensure the uniformity of the electric field [55]. The GR consists of a deep implant between the end of the gain layer and the n^{++} edges (can also be virtual, meaning that it is just a gap between these two elements), while the JTE is a deep, low-concentration n-type region at the junction edge. These termination structures occupy some of the sensor's area and consequently create an inter-pad region where the gain is completely suppressed. This is known as the **no-gain region**, defined as the distance between two adjacent gain regions. Moreover, **metal contacts** could be deposited on the electrode regions to allow external electrical connections. These contacts are usually made of metals such

as aluminum or gold. The precise placement and quality of these contacts are essential for the sensor overall performance, as they facilitate the collection of multiplied charge carriers and their transmission to the external readout electronics. Usually at the top an **anti-reflective coating** (e.g. silicon nitrite), which helps to reduce the reflection of light from the surface allowing more light to enter the silicon, and an **insulator** like silicon dioxide, crucial to prevent electrical shorts or passage of currents, are present.

3.2 Signal formation in LGADs

As shown in Section 2.3.1, when the carriers velocity saturates, the interplay between the sensor thickness and the electric field does not have an impact on the maximum current, resulting, from equation 2.38, in a maximum current $I_{max} = 1.5\ \mu A$. The fact that the current can not exceed this value, poses a strict limit in the design of a sensor for timing measurements, limiting its resolution. Thanks to the introduction of the gain layer, this doesn't represents a problem in the LGAD design, since the formation of the signal happens in a relatively different way. As it is for the standard silicon diodes, the primary carriers drift towards the respective electrodes, but the primary electrons reach the gain layer and start the multiplication mechanism producing secondary *e-h* couples. The **secondary electrons (gain electrons)**, having a drift velocity much higher than holes and because of the proximity to the cathode, are collected almost instantaneously, while the **secondary holes (gain holes)** have to drift the whole bulk thickness in order to reach the anode, making them the ones that generate the greatest part of the signal. In particular, when the last primary electron reaches the cathode the first secondary hole is still drifting. This reflects on the shape of the signal, which increases up to the collection of the last primary electron, remains constant up to the moment in which the first secondary hole is collected by the anode and decreases with a falling time governed by the drift velocity of the holes. Due to the constant electric field in the bulk of the sensor, the drift of the gain holes to the anode produces a large induced current. The different contributions to the signal aredepicted in Figure 3.2. From the plot, it is evident that the signal generated inside an LGAD is really different with respect to the one generated in a standard silicon diode.

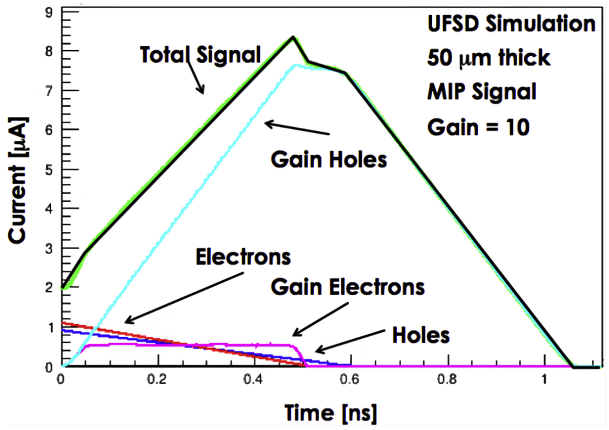

Figure 3.2: Different contributions to the signal current as a function of time [56].

Using considerations similar to the ones made for generic silicon sensors in Section 2.3.1 it is possible to obtain the total current generated in an LGAD structure. In particular, assuming a saturated drift velocity of the carriers v_{sat}, the current due to the multiplication mechanism is related to the electrons which enter in the gain layer in a given interval of time dt: $n_{e-h}v_{sat}dt$, generating a number of secondary e-h pairs of

$$dN_{gain} \propto n_{e-h}v_{sat}dtG \tag{3.1}$$

Assuming, as before, a parallel plate geometry and making use of the Shockley-Ramo's theorem 2.26, the current generated by the secondary charges results:

$$di_{gain} = qv_{sat}E_w dN_{gain} = qv_{sat}\frac{1}{d}dN_{gain} \tag{3.2}$$

from which, equivalently to what done for standard silicon sensor, it is possible to calculate the maximum current of an LGAD sensor. Taking into account that each primary electron generates $G \cdot n_{e-h}$ pairs, i_{max} results in this case:

$$i_{max} \propto N_{max}q\frac{1}{d}v_{sat} = (n_{e-h}dG)\frac{1}{d}qv_{sat} = Gn_{e-h}qv_{sat}. \tag{3.3}$$

Some consequences of this relation related to the time resolution are discussed in the following section.

3.3 Optimization for timing

LGAD principle of operation is an exceptionally effective method for having a detectable signal exceeding the noise in silicon sensors. This approach can be used across various designs, enhancing the sensor and electronics signal-to-noise (S/N) ratio. Nevertheless, just having and increased signal amplitude is not sufficient to achieve a precise determination of the arrival time of an incoming particle. To design a silicon detector optimized for timing a lot of parameters must be taken into account and finely chosen to have the best possible features. As shown in the next paragraphs a timing optimized LGAD must have a very fast signal, achievable through a thin design, a weighting field strong enough to saturate electron drift velocity and uniform in the whole sensitive area, attainable with a parallel plate geometry, and a small internal noise. In addition a high Fill Factor (FF), i.e. the ratio of the active area to the total sensor area, the possibility to work with high bias voltage in order to have an high gain, and the depth of the gain layer are parameters which must be considered.

3.3.1 Gain and thickness

In order to have the best possible time resolution, a large signal to noise ratio is needed. This may suggest to prefer a thicker detector, in which the number of generated charges is higher. However, as a direct consequence of the relations introduced in Section 3.2, which describes the total current induced by secondary charge carriers, it is possible to obtain the relation of this current with the gain and thickness of the detector:

$$di_{gain} \propto \frac{G}{d} dt \ , \tag{3.4}$$

meaning that

$$\frac{di_{gain}}{dt} \sim \frac{dV}{dt} \propto \frac{G}{d} \tag{3.5}$$

which underlines a key feature of LGADs that the signal **slew rate** di/dt is directly proportional to the sensor gain and inversely proportional to its thickness. This implies that in order to have a detector suitable for precise timing measurements, the best option

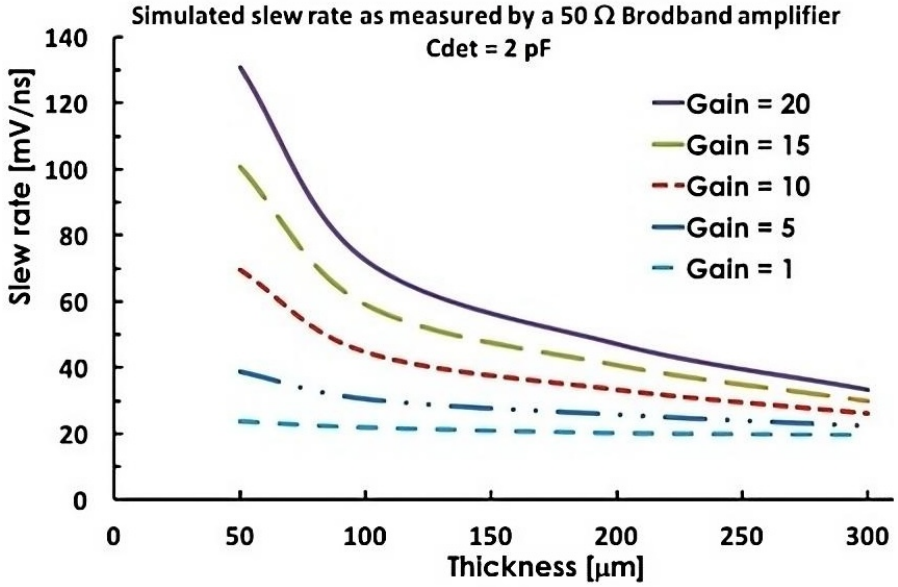

Figure 3.3: Simulated relationship between the signal slew rate and the LGAD thickness for different values of gain. In standard sensors (G=1) the slew rate is almost constant for all the thicknesses, while for higher gain it increases going to thinner sensors [29].

is to have a **thin design** combined with an **high gain**. A simulation reporting the slew rate for different LGAD thicknesses and gains is reported in Figure 3.3.

In addition, from the Shockley-Ramo theorem (2.26), each charge generates a lower initial current (since the weighting field is inversely proportional to the sensor thickness d) and, as described with Equation 3.3, once the drift velocity is saturated the signal peak current does not depend on the sensor thickness, but only on its internal gain. The sensor thickness instead determines the rise time of the signal shape. The shape of signals generated by LGADs with different thicknesses are schematically shown in Figure 3.4. Simulations and results for LGAD with very thin thicknesses will be shown in the next chapter.

3.3.2 Depth of the gain implant

Another important parameter to be considered in the design of LGADs is the depth of the gain implant. The electric field in fact has to be carefully tuned on this parameter,

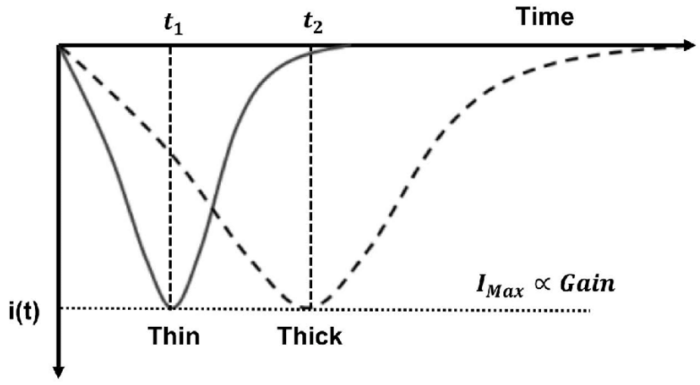

Figure 3.4: Current generated by LGADs with different thickness and the same internal gain, as a function of time. Thinner LGADs shows a larger slew rate [56].

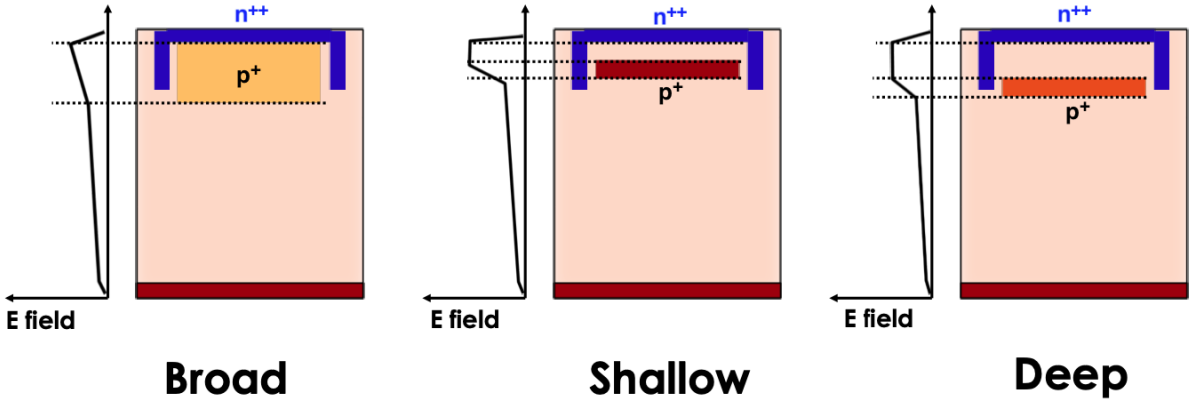

Figure 3.5: LGADs with different depths of the gain implant: broad (left), shallow (middle), and deep (right) designs, with the respective electric field behavior [56].

because the deeper the implant, the higher the number of mean free path contained in the gain layer, having as a consequence a higher gain. The field has to decrease as a function of the gain layer depth, in order to have in the end the same gain value. Three common design are shown in Figure 3.5: an LGAD with a very broad gain layer implant, directly in contact with the n^{++} electrode (left), one with a gain layer near to the n^{++} electrode, but separated from it (middle) and a third with a very deep implant (right), usually called in literature, respectively, **broad, shallow and deep designs**.

In the broad design, the greater part of the avalanche process is confined very near the

pn junction, for this reason small process variations can lead to very different gain values. In shallow and deep design, on the other hand, the avalanche is generated thanks to the electrons that are drifting in a region with the flat electric field, so these two designs are less sensitive to the actual shape of the gain layer implant. In general, considering the same electric field in the three designs, the gain results higher in the deep design since the number of mean free paths contained in the gain layer is higher. For this reason, to obtain the same gain in the three cases, one has to apply higher voltages to the broad and shallow designs. In order to have a detector with a good time resolution, strictly related to the internal gain, it is fundamental to chose the most appropriate depth of this layer.

3.4 LGAD applications

In the last decades, there has been increasing interest in silicon detectors able to provide an excellent time resolution combined with very high spatial precision in high energy physics (HEP) experiments and other areas beyond it. The excellent timing accuracy provided by LGADs constitutes a major advancement, unlocking many new possibilities for applications in a very wide range of disciplines.

PID with Time-Of-Flight technique in HEP

The identity of a particle can be determined by knowing its rest mass. However, the mass cannot be measured directly has to be obtained by correlating other quantities. Two different kinematic variables must be measured simultaneously and independently, with at least one variable depending on the particle's mass. This can be done exploiting the fact that the curvature of a particle in a magnetic field depends on its momentum but also on its electric charge. A magnetic spectrometer can be used to measure the rigidity $R = \frac{p}{z}$, where z is the charge of the particle. In high-energy physics experiments, charged particles are typically bent in a magnetic field to measure their momenta. One of the principal use of timing detectors is related to Particle IDentification (PID) through the Time-Of-Flight (TOF) technique. This allows the separation of particles with momenta

of few GeV/c. Knowing the velocity and the momentum of a particle it is possible to obtain its mass. Measuring the time interval t in which a particle travels inside the detector material L, its velocity is known $v = \frac{L}{t}$ and its mass can be obtained using:

$$m = \frac{p}{c}\sqrt{\frac{c^2t^2}{L^2} - 1} \tag{3.6}$$

which resolution is the sum in quadrature of different terms:

$$\left(\frac{\delta m}{m}\right)^2 = \left(\frac{\delta p}{p}\right)^2 + \left(\gamma^2\frac{\delta L}{L}\right)^2 + \left(\gamma^2\frac{\delta t}{t}\right)^2 \tag{3.7}$$

In particular, considering two particles with the same momentum p and masses m_1 and m_2, travelling the same track length L, the difference of their Time-Of-Flights is

$$\Delta t = t_1 - t_2 \simeq \frac{Lc}{2p^2}(m_1^2 - m_2^2) \tag{3.8}$$

The particle-identification capability of a TOF detector is determined by the number of standard deviations in the time-of-flight difference between two particles so that the separation power n_σ can be defined as

$$n_\sigma = \frac{\Delta t}{\sigma_{TOF}} \simeq \frac{Lc}{2p^2\sigma_{TOF}}|m_1^2 - m_2^2| \tag{3.9}$$

where σ_{TOF} is the time resolution of the detector. This means that increasing the path length L improves the TOF separation power linearly, but the detector area to be covered increases as L^2, making it essential to design detectors that can cover large areas cost-effectively. In the high momentum range, the primary factor influencing mass resolution - and thus separation power - is the detector's time resolution. Therefore, detectors with excellent time resolution are essential for PID scopes.

Timing layers and 4-Dimensional (4D) tracking

Thinking at the substantial increase in hadron colliders luminosity expected over the next years, resulting in a significantly high pile-up rate, there has been a growing interest

in developing silicon detectors with an excellent time resolution also for tracking purposes. Already at the HL-LHC the situation will substantially change [57], arriving to a number of events per bunch crossing of the order of 150-200 with an average distance of 500 microns, in a time window of around 150 ps, so with density so high to have 10-15% [58] of primary vertices composed with two overlapping events, where multiple primary interactions occur within the same time interval during high-energy collisions. This phenomenon, known as pile-up, results in multiple primary vertices and can generate intermediate secondary vertices whose attribution to a specific primary event is extremely complex with the foreseen tracking resolution. These secondary vertices may arise from the decay of particles with characteristic lifetimes, such as hadrons containing heavy-flavor quarks or tau leptons, which decay via weak interactions. This will lead to a loss of events and cause the degradation in the precision of the reconstructed variables. This situation can dramatically improve with the inclusion of the timing information, enabling the full potential of future colliders' luminosity capability.

The inclusion of timing information associated to individual tracks in the structure of a recorded event can significantly transform experimental design and dramatically enhance the reconstruction process. Having the time information allows one to group tracks belonging to different primary interactions, which occur at different times.

For the most accurate option, timing would be associated with each point of the track, consenting to discard all the hits that cannot be associated with a given track due to excessive time difference and use only time-compatible hits in the pattern recognition phase. This requires electronics capable of precisely measuring the time of each hit in every pixel; this option is very challenging due to the substantial increase in power consumption for the necessary readout circuits. An interesting approach to manage the increased power consumption is to reduce the granularity of the timing information. To retain the full benefits of timing information for event reconstruction and maximize the precision of the reconstructed kinematic quantities, it is sufficient to assign a time to each track rather than each hit. This method is more feasible than assigning time to every hit, as it can be achieved with a single dedicated timing layer either inside or outside the tracking detectors.

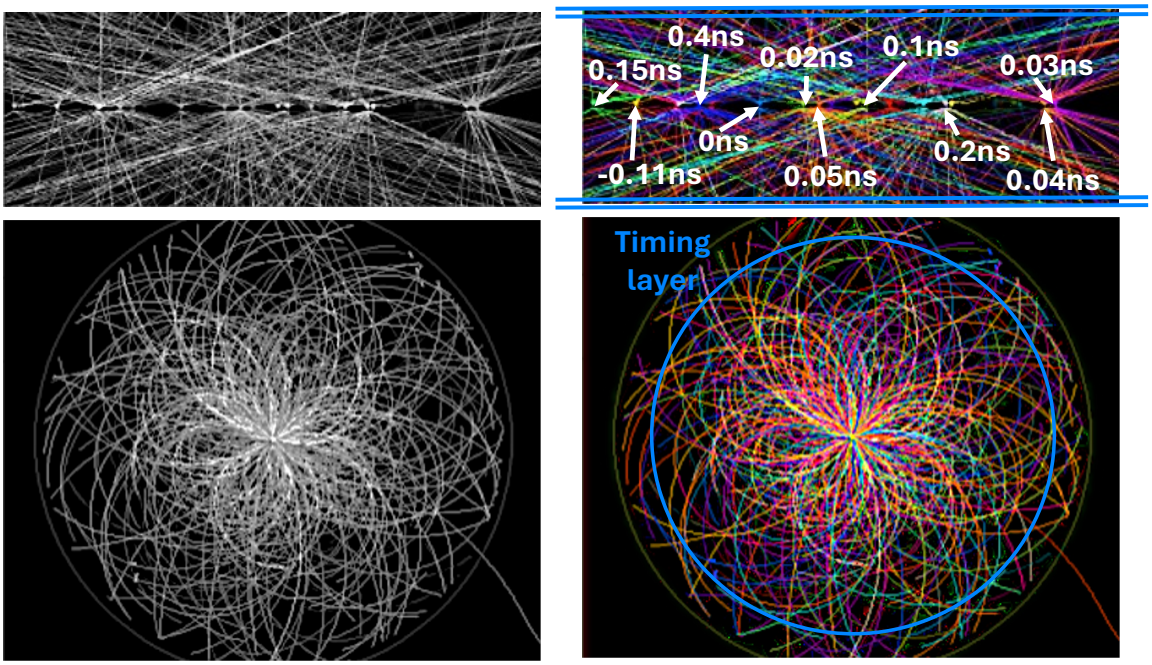

Figure 3.6: Longitudinal and transverse scheme showing how the time information is exploited to distinguish two overlapping events.

In Figure 3.6 an illustration from the longitudinal and transverse planes of how the time measurements is used to disentangle the two overlapping events is reported.

Calorimetry

The fast timing capability can be leveraged to improve energy resolution and reduce pile-up in calorimeters, particularly in high-luminosity experiments [59]. Beyond finer segmentation for both tracking devices and calorimeters, precision timing is emerging as a powerful tool to enhance calorimeters performance. A key approach to mitigate pileup confusion, complementary to precision tracking, is measuring the time of arrival at a specific calorimeter layer, enabling precise time assignment for charged particles and photons. A timing resolution of approximately 20–30 ps, when reliably paired with energy measurements, can reduce effective pileup by a factor of 10. This critical integration of time and energy measurements necessitates a detector design where both are

performed within the same element. By doing so, energy deposits identified as originating from pileup interactions can be effectively removed from event reconstruction. Silicon-based calorimeters are increasingly favored for future colliders due to their radiation hardness and capacity for highly granular detection.

Applications in other fields

The R&D of thin silicon sensors with excellent tracking and timing resolution, capable of covering large areas, will be extremely beneficial also in contexts outside the physics realm. Specific projects are ongoing to use LGADs in single particle counting applications, where they can offer unprecedented rate capabilities. LGADs are particularly well-suited for **hadrotherapy and beam monitoring**, enabling the measurement of particle range and dose profile with millimeter resolution during clinical treatments [60]. By directly counting the number of hadrons, LGADs provide precise control over the energy delivered to the patient and can also utilize the emission of prompt gammas [61]. In this context, time-of-flight measurements can be employed to obtain indirect information on ion ranges [62, 63], or to mitigate neutron-induced background noise. A thin detector with a minimal material budget is crucial for applications like this one where reducing material interactions is essential. Conventional LGADs generally feature substrate thicknesses between 300 and 500 µm, with an active layer of less than 50 µm. So these sensors, once thinned down, can have a naturally low material budget.

More in general, silicon sensors capable to provide an excellent position and time resolution can be extremely beneficial also in the medical field and for many industrial applications. As for medical applications, an example is **Positron Emission Tomography (PET)**. This involves the injection of a radionuclide into the body, which is absorbed by the diseased tissue or organ. The radionuclide undergoes β^+ decay, resulting in the creation of an electron-positron pair. The positron annihilates after approximately 10^{-9} seconds, producing a pair of 0.511 MeV back-to-back photons. This annihilation event can be precisely reconstructed using advanced timing detectors, providing detailed information about the location where the radionuclide have accumulated. Improving the time resolution of silicon detectors reduces background noise by increasing the accuracy

of photon arrival time measurements, thus decreasing the number of spurious events. Dedicated R&D focused on improving the efficiency of LGAD in this photon energy range is needed [64] An LGAD-based system could offers a position resolution more than ten times better than that of current PET systems, while maintaining comparable time resolution. This significant enhancement in resolution can either greatly improve image quality or allow for a reduced radiation dose to the patient [65].

In the industrial context, an example are **LiDAR applications**. LiDAR stands for Light Detection And Ranging and is a remote sensing method that uses light in the form of a pulsed laser to measure variable distances. These light pulses, combined with other information, generate precise, three-dimensional images. The ability to perform precise measurements of light pulses reflected by objects at unknown distances is fundamental. Many applications based on this technique can profit of sensors optimized for timing, including many monitoring systems in the energetic, construction and engineering, as well as tools for archaeological and environmental research or imaging and robotic vision. In this case the development of LGAD with a good geometrical efficiency is pivotal.

Chapter 4

Characterization and Laboratory Measurements

This chapter focuses on the specific R&D efforts on the state-of-the-art LGADs, mainly aimed at improving their timing performance to meet the demanding requirements of next-generation experiments, aiming in large-area systems with an excellent time resolution. In particular the present study is carried out in the context of the design of the Time-Of-Flight (TOF) detector of the ALICE 3 experiment (see Chapter 1), which will play a key role in the PID of the experiment. To achieve design PID capabilities, it will need to provide an outstanding time resolution of 20 ps, including the full front-end and readout electronic chain. Several silicon technologies are under investigation to achieve this goal: in this thesis the whole R&D campaign done on LGADs is presented, leading to the development of sensors capable to reach a time resolution below 20 ps. Overall, the results successfully validated the LGAD option, demonstrating that LGADs can achieve the performance required by the ALICE 3 TOF detector and establishing them also as strong candidates for future-generation experiments.

4.1 Study motivations and R&D development

Conventional LGAD with a thickness of 50 µm have been deeply studied in the last decades. Thanks to the already very good time resolution of around 30 ps [66], this

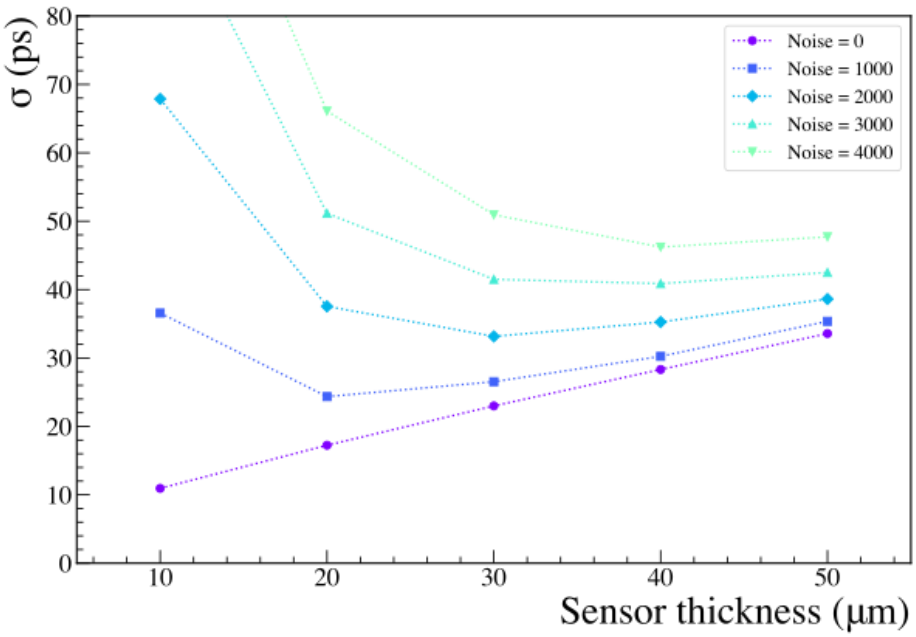

Figure 4.1: Garfield++ [67] simulation of the LGAD time resolution as a function of the sensor thickness for different levels of noise [68].

technology is planned to be used in many detector upgrades, for example, at the HL-LHC (e.g. ATLAS [69] and CMS [70]) for 2030.

Despite their impressive performances, the increasingly demanding requirements of future experiments, such as ALICE 3, coupled with the fact these studies could have a significant impact on various future scenarios, such for example FCCee [71], have motivated significant R&D efforts aimed at pushing current standards further forward;

Simulations have shown the potentiality of LGADs with a thinner layout to achieve better timing performance (Figure 4.1). For this reason, the present study focuses on evaluating the performance of the first very thin LGAD prototypes produced by FBK (Fondazione Bruno Kessler, Italy), with a thickness of 15, 20, 25 and 35 µm, in comparison to standard 50 µm sensors. All the sensors were fully characterized and then studied first with a laser setup and subsequently using charged particle beams at CERN facilities.

While reducing thickness can improve timing performance, it also results in a lower signal at the input of the amplifiers, which may negatively affect the performance of the

front-end electronics. In order to address this problem the new concept of double-LGAD 5.3 was introduced, and tested for the first time in a beam test setup. Pairs of LGADs, both with a standard thickness of 50 µm and belonging to this new generation of thin sensors, have been tested. Indeed, this implementation is expected to generate a higher signal than the individual LGADs in the pair, which is advantageous for the electronics, while keeping the advantages of an ultra-thin sensor with regards to the time resolution.

Furthermore, an investigation was done on how time resolution depends on the incidence angle of the particle on the sensor 5.4. This is important to investigate the changes in the response of sensors placed at the edge of the barrel layer of the TOF detector or in case the sensor is traversed by low transverse momentum particles.

The results obtained with the different configurations are discussed in this chapter, while some very recent measurements are reported in the appendices (Appendix C) regarding a study of the sensors connected to a full front-end and readout chain, in order to obtain the time resolution and the response of LGADs in a condition very similar to that of the real experiment.

4.2 Tested detectors

LGADs of five different thicknesses were studied: 15, 20, 25, 35 and 50 µm. All the four thinner designs are part of the very first production of such thin structures by FBK. Many of these sensors were studied, both single channel and matrices, with different layouts and inter-pad designs, and compared with sensors with the same design but without a gain layer (PIN), when available. LGADs with a standard thickness of 50 µm, measured for comparison with the thinner layout and for the tests of double-LGADs concept, comes instead from different productions of both FBK and HPK (Hamamatsu Photonics K.K., Japan).

4.2.1 15 and 20 µm-thick prototypes

LGAD detectors of 15 and 20 µm thickness, part of the very first FBK production of such thin LGADs, called EXFLU1 [72], were studied. These sensors have an area of 1.3×1.3 mm^2 and appertain to two different wafers: W17 with a nominal thickness of

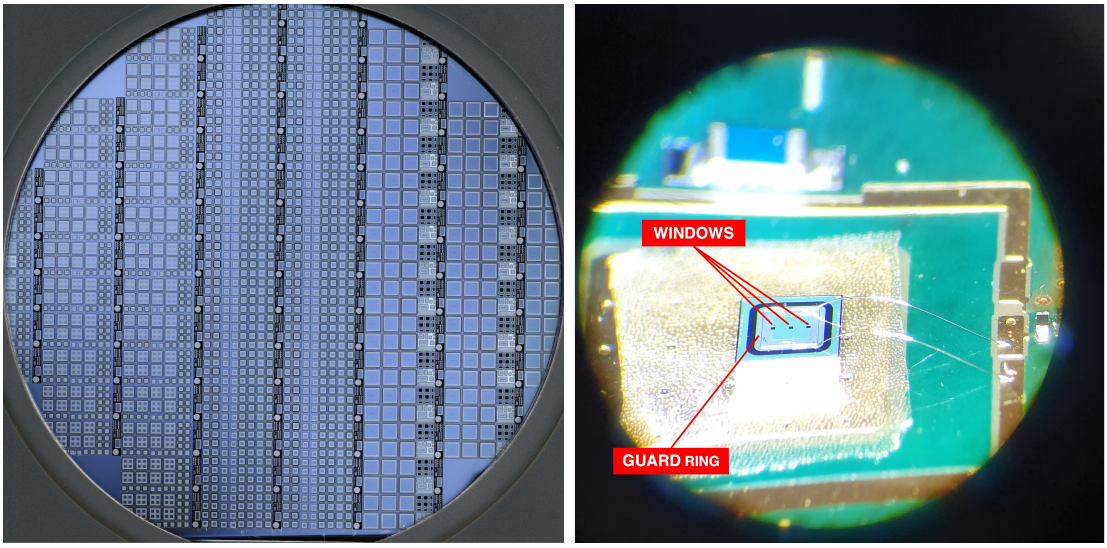

Figure 4.2: Production reticulum for wafer W18 (left) and 15 µm-thick LGAD (from W18) bonded to the front-end board (right). Guard ring and the three windows on the metallization are well visible in the photo. 20 µm-thick LGADs have a similar layout.

20 µm (**FBK20**) and W18 with a nominal thickness of 15 µm (**FBK15**). The photo of one of these structures, bonded to the front-end board, is reported in Figure 4.2. All the LGADs tested have an n-in-p structure, with a p^+ doped gain layer and are single channel (only one pad), totally covered by a metallization with three 35×35 μm^2 (see Section 4.4.2.1) windows (non-covered areas) on the top, to allow testing the chip with a laser setup.

Table 4.1 summarizes all the tested 15 and 20 µm-thick LGADs.

4.2.2 25 µm- and 35 µm-thick prototypes

Both single sensors and matrices with a nominal thickness of 25 µm (**FBK25**) and 35 µm (**FBK35**) thickness from the production called UFSD3.2 [73] were studied. The sensors have different thickness and doping concentration of both the bulk and the multiplication layer and also in this case, the sensors have an n-in-p structure, with a p^+ doped gain layer. Some difficulties in the production of such thin sensors brought to a difference in the doping concentration of both two wafers, as shown in Figure 4.3.

In particular, the 25 µm-thick wafer (W5) has highly doped bulk and gain layer, while

Sensor	Layout	Area (mm^2)	Wafer	Thickness (µm)
FBK15_1.3x1.3_13D FBK15_1.3×1.3_14D FBK15_1.3×1.3_15D FBK15_1.3×1.3_16D FBK15_1.3×1.3_17D FBK15_1.3×1.3_18D	Single	1.3×1.3	W18	15
FBK20_1.3×1.3_15D FBK20_1.3×1.3_16D FBK20_1.3×1.3_17D FBK20_1.3×1.3_18D	Single	1.3×1.3	W17	20

Table 4.1: Main characteristics of the 15 and 20 µm-thick LGADs tested.

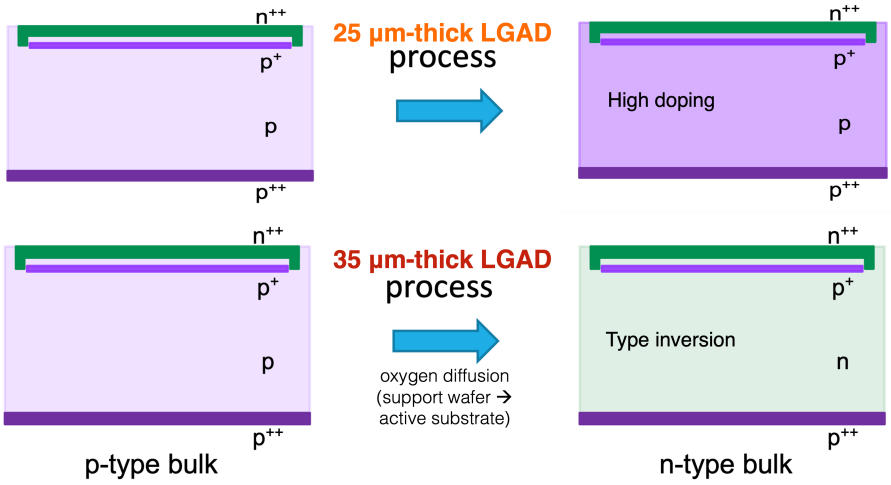

Figure 4.3: Differences in the doping concentration of wafers W5 (25 µm) resulting in a highly doped bulk and gain layer and W6 (35 µm) in which a type inversion occurred due to oxygen diffusion from wafer to the bulk [73].

in the 35 µm one (W6) a type inversion occurred (due to oxygen diffusion from wafer to the bulk: oxygen defects in silicon behave like n defects), resulting in a n-doped bulk. This inversion of the bulk causes depletion to begin from the bottom of the sensor rather than the top, making it impossible to obtain useful information from capacitance-voltage measurements. However, once the entire active thickness is depleted, this inversion does not impact the electric field within the sensor, meaning its overall operation remains unaffected.

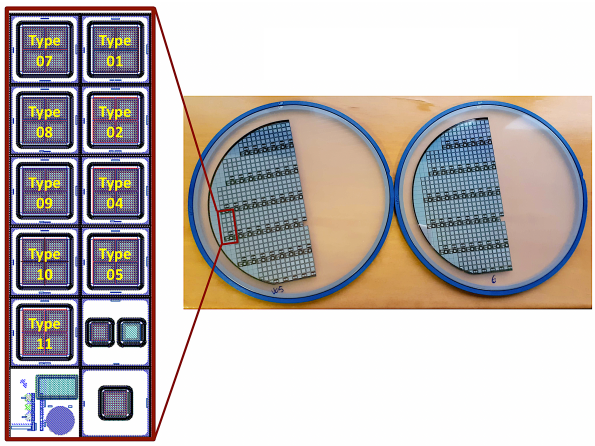

Figure 4.4: Part of the UFSD3.2 production reticulum for wafer W5 and wafer W6, made of 9 types of matrices, PIN and LGAD pairs and single pads. Different samples of PIN and LGAD pairs and of two different matrix layouts (Type 4 and 10) were tested, for both wafer thicknesses.

The basic reticulum and wafer layouts are shown in Figure 4.4. The reticulum was composed by single channel LGADs, PIN and LGAD pairs and different types of matrices. The 2×2 matrices were characterized by different types of pads insulation approaches, and produced with various Inter-Pad (IP) configurations of the gain layer distance and p-stop design. Only samples of PIN and LGAD pairs and of Type 4 and Type 10 matrix layouts were tested and among the eighteen structures analyzed, nine have a thickness of 25 µm and nine have thickness of 35 µm:

- **PIN and LGAD structures** are shown in figure 4.5. The LGAD (left) has an area of 1×1 mm^2 and is surrounded by five concentric Guard Rings (GR), where

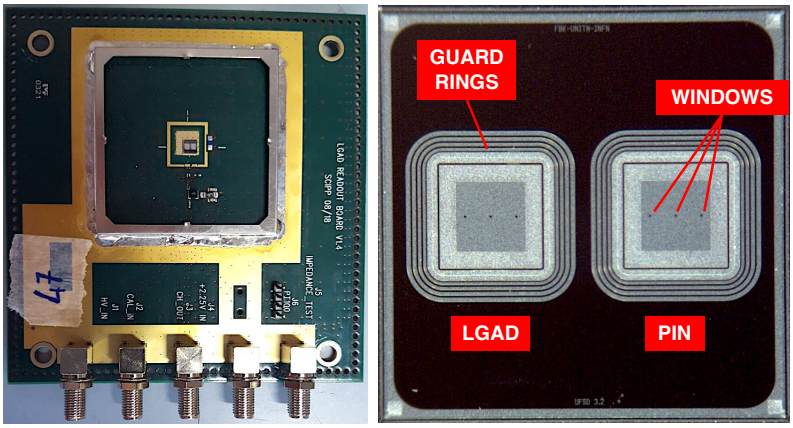

Figure 4.5: 25 µm-thick LGAD connected to the front-end board (left) with a zoom on the PIN and LGAD pair (right); on the left side of the structure there is a single 1×1 mm^2 LGAD and on the right an equivalent detector but without any gain layer. 35 µm-thick LGADs have the same layout.

the inner one is the biasing ring. Like for the other sensors, the whole surface is covered by a metallization, except for three 20×20 µm^2 windows. The PIN (right) has exactly the same design of the LGAD, but without the gain layer.

- **LGAD matrices** of Type 4 and Type 10, characterized by different inter-pad design, are shown in Figure 4.6. Four 1.3×1.3 mm^2 pads with the same layout are present, each one with three windows. Two additionally non-covered areas, one between the two pads on the top and one between the two pads on the bottom (IP windows), are visible; these are needed to investigate the edge effects (see Section 4.4.2.2). The pads are surrounded by the five guard rings.

  - **Type 4 LGAD matrix** is characterized by a biasing ring that is external to the pads, which are separated by a nominal width of only 24 µm. In this configuration only one p-stop is present, forming a grid around the pads. Given their layouts, Type 4 is expected to exhibit good uniformity in terms of current levels among pads. However given the separation between pads done only with a p-stop, this is more prone to premature breakdown, particularly under conditions with floating pads, where the electric field near the p-stop can be really high, leading to an abrupt current rise.

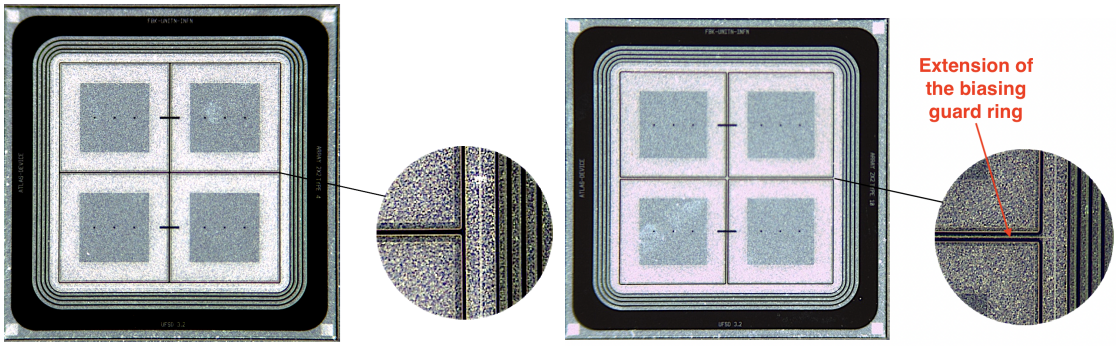

Figure 4.6: Type 4 LGAD matrix (left) and Type 10 (right), with a zoom on the inter-pad area. In the Type 10 one, an extension of the biasing guard ring is present between the four pads.

– **Type 10 LGAD matrix** is characterized by an extension of the biasing ring, called bias grid, present between the pads and all of them have their own p-stop. Thanks to this layout, Type 10 matrices are expected to show better resilience to floating pads, owing to the guard ring between pads that helps maintain a more uniform electric field. This design could ensure more stable breakdown and current behavior and similar breakdown voltage across all pads. The guard ring isolation properties in fact can prevent premature breakdown, providing consistent performance across the matrix [74]. On the other hand, such a layout is characterized by a larger no-gain area, resulting in a lower efficiency at the edges of the sensor.

All the 25 and 35 µm-thick LGADs tested are reported in the Tables 4.2 (single) and 4.3 (matrices).

4.2.3 50 µm-thick prototypes

Different LGADs with a standard thickness of 50 µm were tested, as a comparison with the thinner layout to validate the analysis procedures and results:

- **HPK50_1×3_4S** is a matrix of four 1×3 mm^2 pads (see Figure 4.7), produced by HPK. A metallization covers the pads, and two 25×25 μm^2 windows are present,

Sensor	Layout	Area (mm^2)	Wafer	Thickness (µm)
FBK25_1×1_8-3				
FBK25_1×1_9-3				
FBK25_1×1_10-3				
FBK25_1×1_4-2				
FBK25_1×1_5-2	Single	1×1	W5	25
FBK25_1×1_7-5				
FBK25_1×1_8-5				
FBK25_1×1_9-5				
FBK25_1×1_10-5				
FBK35_1×1_8-3				
FBK35_1×1_9-3				
FBK35_1×1_10-3				
FBK35_1×1_5-5				
FBK35_1×1_6-5	Single	1×1	W6	35
FBK35_1×1_7-5				
FBK35_1×1_8-5				
FBK35_1×1_9-5				
FBK35_1×1_10-5				

Table 4.2: Main characteristics of the 25 and 35 µm-thick LGADs tested.

with two additional ones crossing the neighbors pads edges. A corresponding PIN (HPK_5S) was used only for the evaluation of the gain (see Section 4.4.3).

- Four **HPK2** sensors produced by HPK are single channel LGADs with an area of 1.3×1.3 mm^2 appertaining to two different wafers, namely W36 and W42. The only difference between the two wafers is the doping of the gain layer, slightly higher for W36. Two sensors were tested for each wafer, especially to investigate the double-LGAD concept with very uniform couples of sensors (see Section 5.3 for details). From the photo in Figure 4.8 it can be seen the metallization covering

Sensor	Layout	Type	Area (mm^2)	Wafer	Thickness (µm)
FBK25_T4_1.3×1.3_8-3 FBK25_T4_1.3×1.3_9-3 FBK25_T4_1.3×1.3_10-3 FBK25_T4_1.3×1.3_6-1 FBK25_T4_1.3×1.3_7-1 FBK25_T4_1.3×1.3_8-1 FBK25_T4_1.3×1.3_9-1 FBK25_T4_1.3×1.3_10-1	Matrix	T4	1.3×1.3	W5	25
FBK35_T4_1.3×1.3_8-3 FBK35_T4_1.3×1.3_9-3 FBK35_T4_1.3×1.3_10-3 FBK35_T4_1.3×1.3_6-5 FBK35_T4_1.3×1.3_7-5 FBK35_T4_1.3×1.3_8-5 FBK35_T4_1.3×1.3_9-5 FBK35_T4_1.3×1.3_10-5	Matrix	T4	1.3×1.3	W6	35
FBK25_T10_1.3×1.3_8-3 FBK25_T10_1.3×1.3_9-3 FBK25_T10_1.3×1.3_10-3	Matrix	T10	1.3×1.3	W5	25
FBK35_T10_1.3×1.3_8-3 FBK35_T10_1.3×1.3_9-3 FBK35_T10_1.3×1.3_10-3	Matrix	T10	1.3×1.3	W6	35

Table 4.3: Main characteristics of the 25 and 35 µm-thick LGAD matrices tested.

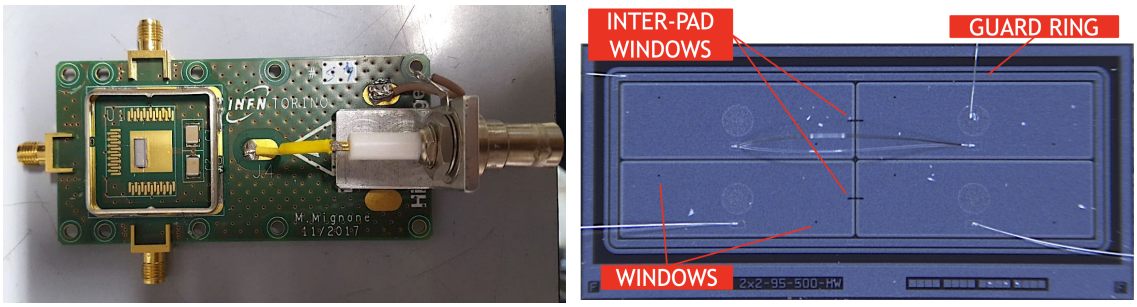

Figure 4.7: HPK50_1×3_4S connected to the front-end board (left) with a zoom on the matrix (right) with the four 1×3 mm^2 LGAD pads visible; only the bottom left was measured in this theses. The pad and inter-pad windows are visible, as well as the connections to the front-end board.

the sensors, and the small windows for the laser measurements.

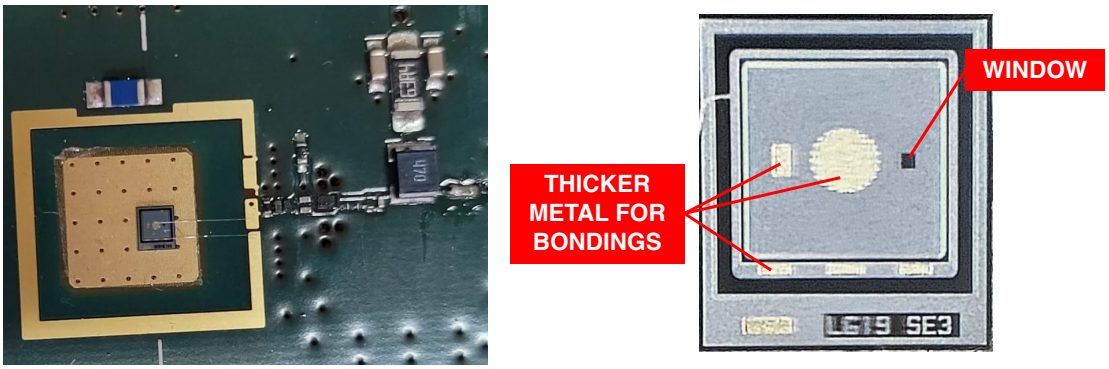

Figure 4.8: HPK2 sensor with the connection to the front-end board (left) and photo of the sensor taken with a microscope.

All the 50 µm-thick LGADs tested are reported in the Table 4.4.

4.3 Characterization measurements

A fully electrical characterization of an LGAD sensor can be done performing current and capacitance measurements at different bias voltages, to obtain current-voltage (IV) and capacitance-voltage (CV) characteristic. In this section, the IV and CV curves and

Sensor	Layout	Area (mm^2)	Wafer	Thickness (µm)
HPK50_1×3_4S	Matrix	1×3	-	50
HPK50_W42_1.3×1.3_A HPK50_W42_1.3×1.3_B	Single	1.3×1.3	W42	50
HPK50_W36_1.3×1.3_E HPK50_W36_1.3×1.3_F	Single	1.3×1.3	W36	50

Table 4.4: Main characteristics of the 50 µm-thick LGADs tested.

the main extracted parameters are reported, together with the experimental setups and an analysis of the results. Comparisons are done between an LGAD and the respective PIN, among LGADs of the same thickness, or among different wafer thicknesses and matrix layouts. Final measurements are done with LGADs attached to the front-end boards.

4.3.1 IV measurements

Firstly, the current as a function of the reversed voltage applied has been measured. The primary goal of IV characteristic is to evaluate the breakdown voltage V_{BD}. This measurement also gives information on the voltage interval in which the sensor can be operated. Moreover, it helps to evaluate the different inter-pad configuration; indeed, some aggressive designs can lead to a premature breakdown of the pads.

4.3.1.1 IV Laboratory Setup

The IV measurements on bare silicon sensors were conducted using a probe station. The bare sensors were placed on a gold-plated chuck. Thin needles were brought into precise contact with the surface of the sensor pads or Guard Ring (GR). A negative high voltage (HV) was applied to the chuck, where the p-type backplane of the LGADs was positioned. This created a reverse bias condition, with the needles held at ground potential.

The entire setup is shown in Figure 4.9. The negative HV on the chuck is supplied

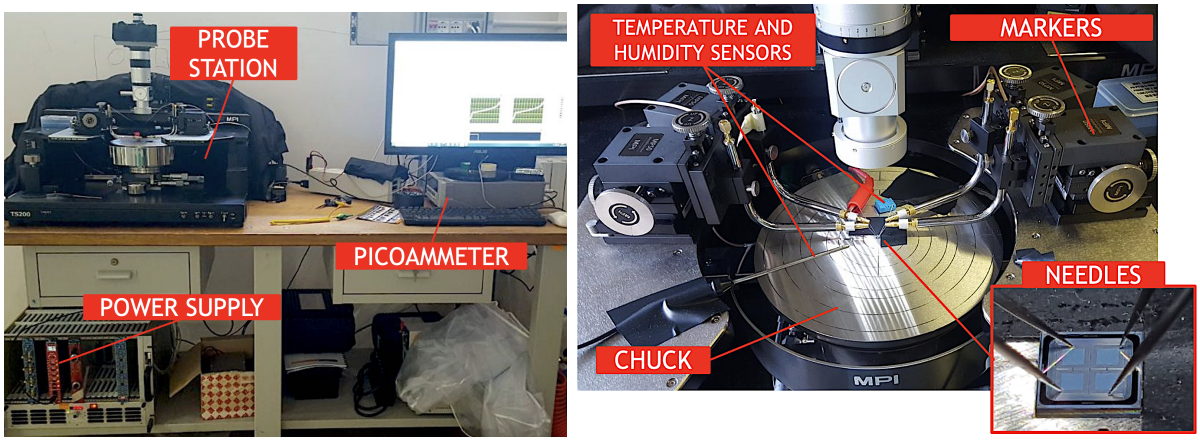

Figure 4.9: Experimental setup for measuring the IV characteristics, comprising the probe station, a power supply, a picoammeter, and a computer. The system is controlled through a LabVIEW program (left). The sensor is positioned on the chuck of the probe station, with four needles (in the case of matrix tests) connected to different elements (right). The needle with the red crocodile clip is connected to the picoammeter for current measurements. Sensors for temperature and humidity monitoring are visible in the photo.

by a CAEN power supply [75]. The current is measured on one element (a pad or the guard ring) at a time through a Keithley 6487 picoammeter [76]. This is connected via the red crocodile clip to the needle in contact with the surface of the element under measurement. All the other pads and the common guard ring are contacted by needles at ground potential, to bias the whole structure. All instruments are controlled through a LabVIEW [77] program, allowing real-time adjustment of parameters. The tests were conducted in a dark environment, and temperature and humidity values were recorded for each IV curve using a sensor placed near the chuck, as these factors can influence the IV characteristics.

For the measurements on PIN and LGAD structures, two needles were used: one in contact with the internal pad and another with the guard ring. This configuration ensures a more uniform electric field within the sensor depletion region and replicates conditions similar to those when the sensor is attached to a front-end board. This setup is referred to as the "2-needle configuration". The measurement was performed twice: first, with the picoammeter connected to the needle in contact with the internal pad,

and second, with it connected to the guard ring.

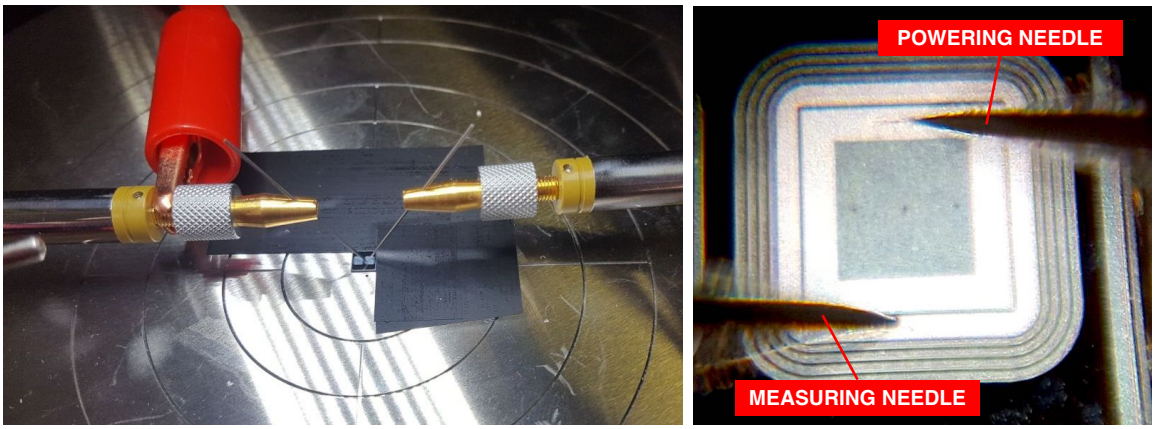

Figure 4.10: 2-needle setup: the measuring needle (connected to the picoammeter) in contact to the element (LGAD pad or GR) where the current measurement is taken, while the other needle powers the second element (left). Image from the microscope of the probe station (right).

A similar setup was used for matrices. Since the probe station gives the possibility to use only four needles simultaneously, one needle was placed on the GR and three on the pads. The floating pad (the one not directly powered) was located opposite to the pad being measured. This "4-needle setup" is illustrated in Figure 4.11.

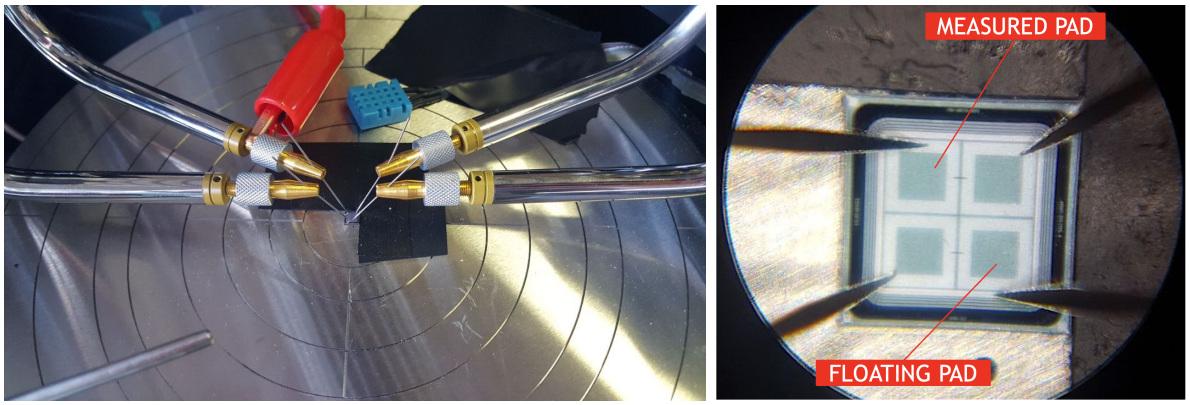

Figure 4.11: 4-needle setup: the measuring needle (connected to the picoammeter) touches the pad where the current measurement is performed, while the other needles power the neighboring pads and the guard ring (left). Image from the microscope of the probe station (right).

For LGADs bonded to the front-end boards, a similar setup was employed, but without the need for the probe station, as the powering and signal readout were done through specific channels on the front-end boards. The sensor was connected to the power supply, picoammeter, and computer in the same configuration as before: applying a negative value on the back and having the top at ground voltage. Also in this case the measurements were taken in a dark environment, with the sensor inside a small box, as shown in Figure 4.12.

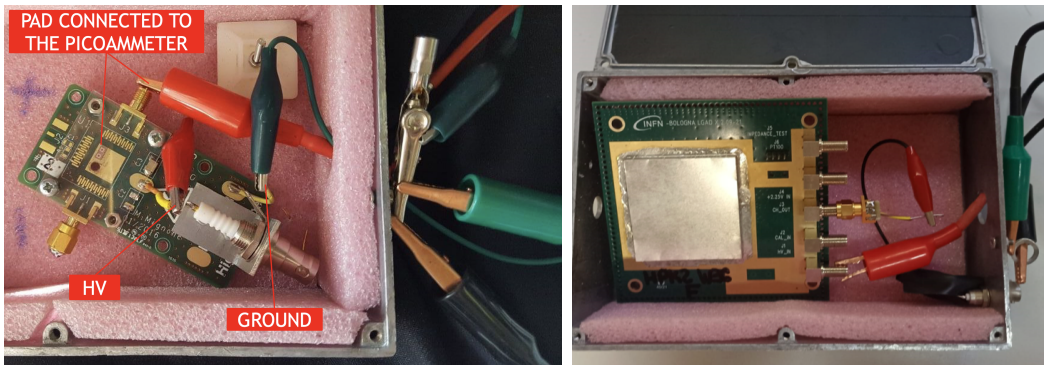

Figure 4.12: Part of the experimental setup for the measurements of sensors connected to two different front-end boards. The sensor is placed inside a box that remains closed and covered with a black cloth during measurements.

4.3.1.2 Characterization of bare silicon prototypes through IV measurements using a probe station

The IV characteristics are always measured on the sensors inversely polarized, and they are primarily used to evaluate the breakdown voltage V_{BD}. Knowing V_{BD} is crucial, as the bias voltage for LGAD sensors must be fine-tuned to achieve an optimal gain value. In addition, this can be used also to assess the sensor design, for both single LGADs and matrices. More aggressive designs can lead to premature breakdown of the pads; if it occurs at too low voltage, it prevent reaching a sufficient gain.

Measurements of the IV characteristics were conducted under the same conditions on both LGADs and their corresponding PIN sensors. Figure 4.13 presents an example of

IV curves measured on bare PIN and LGAD structures for the 25 µm- and 35 µm-thick LGADs.

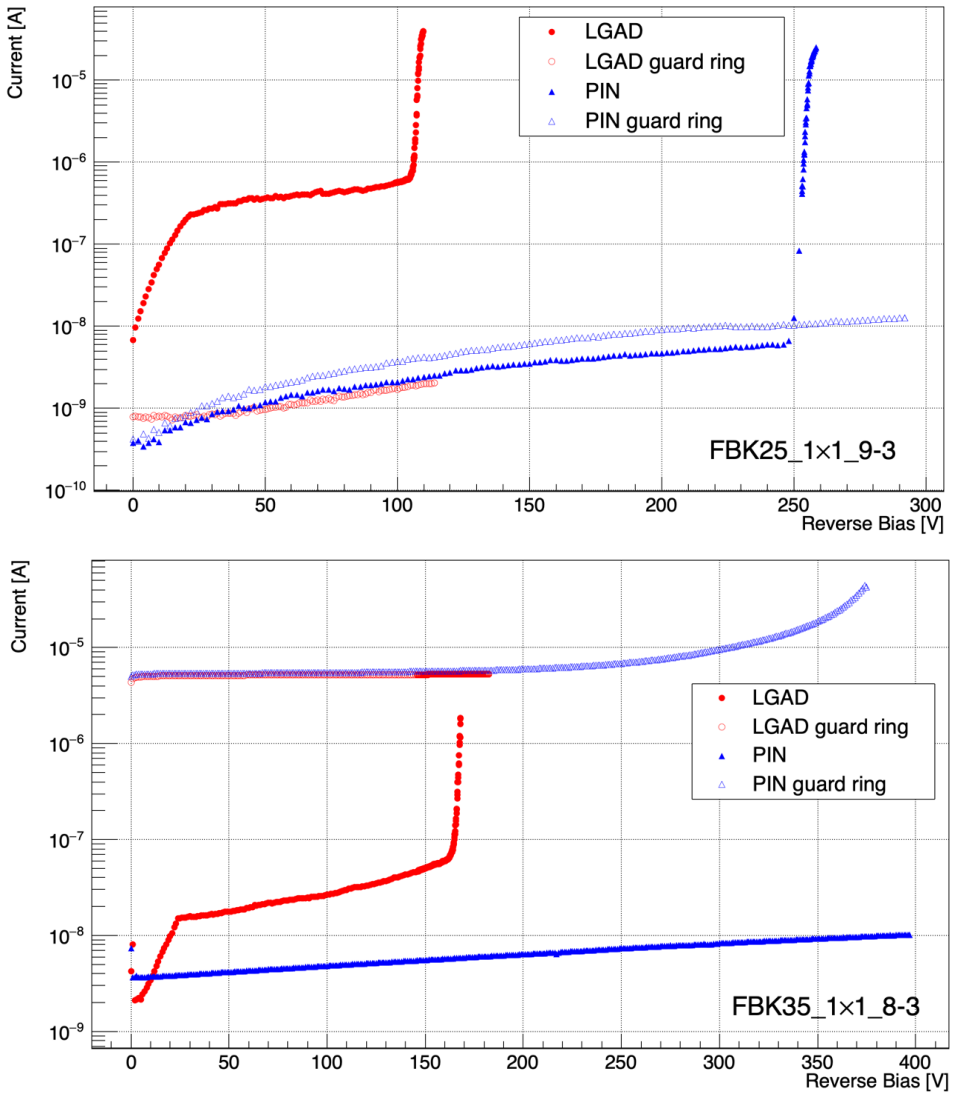

Figure 4.13: Example of measured IV characteristics of PIN and LGAD structure. All measurements were taken using a 2-needle setup. The top plot corresponds to 25 µm-thick LGADs and the bottom plot corresponds to the 35 µm-thick LGADs.

As expected, the IV characteristics of the LGAD and PIN sensors differ significantly. For the PIN, the leakage current remains low, fluctuating, as described by Equation

(2.38), around the saturation current due to noise, until the junction reaches breakdown (around 250 V in the upper figure), where the current rapidly increases.

Instead, the presence of the gain layer significantly alters the IV characteristics of LGAD sensors. The LGAD IV curve exhibits two distinct changes in the behavior: the first is associated with the complete depletion of the gain layer (around 22 V in Figure 4.13), and the second corresponds to the breakdown, as observed in the PIN. The gain also exhibits exponential growth as a function of bias voltage (see Section 4.4.3), which contributes to the exponential rise in leakage current observed in LGAD sensors.

Looking at the guard ring of both PIN and LGAD, a key difference between the 25 µm- and 35 µm-thick sensors is the higher leakage current of the guard ring of the 35 µm-thick LGADs, due to type inversion in the wafer. This type inversion does not affect the electric field inside the depletion region, but, as visible, it does increase the GR leakage current because in this doping condition the GR acts as an n-implant inside an n-doped bulk, collecting charges from the entire bulk.

All measurements were performed using the 2-needle setup. Each measurement was first done on the LGAD with the GR biased, and then on the GR with the LGAD biased. The same process was applied to the PIN. In both cases, the internal pad and GR are in parallel, so the total current is the sum of the currents from both the pad and GR. A current limit was imposed via the LabVIEW program to prevent damage to the silicon. This limit causes the measurement to stop when one of the two elements reaches breakdown, preventing the other from reaching it. As a result, only the breakdown of the first element is visible in the curves. For the LGAD, the internal pad always reaches breakdown first, while for the PIN, either the pad or GR may reach breakdown first.

Two key values can be extracted from these curves: the voltage at which the gain layer depletes completely (approximately 22 V for both thicknesses in this example) and the breakdown voltage (BD). The BD voltage can be determined by calculating the Logarithmic Derivative (LD) and/or the Inverse Logarithmic Derivative (ILD) which are defined as

$$LD = \frac{d\ln(|I|)}{dV} \tag{4.1}$$

$$ILD = \left(\frac{d \ln(|I|)}{dV} \right)^{-1} \tag{4.2}$$

and shown in Figure 4.14 and defined as [78].

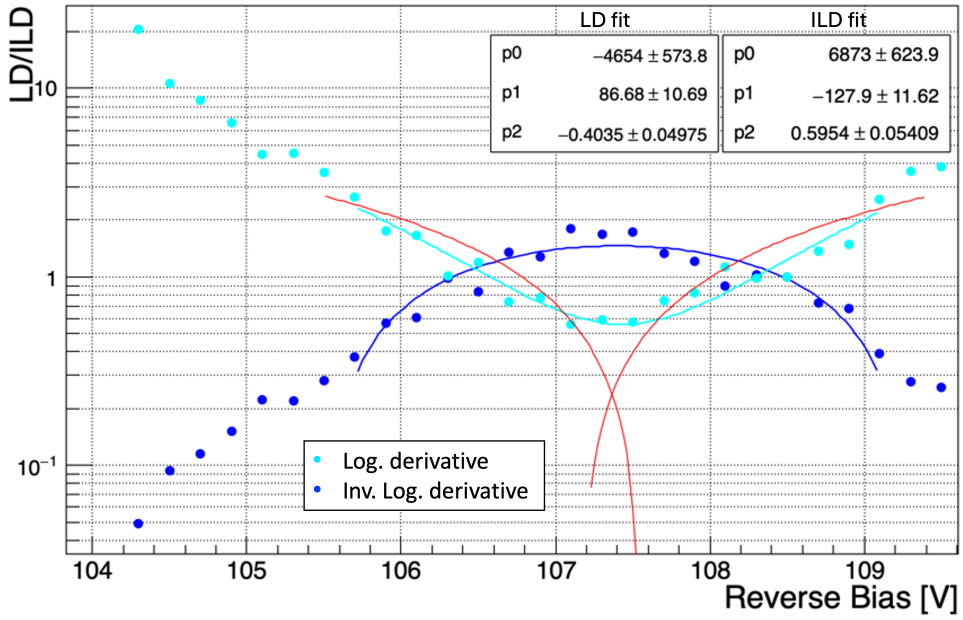

Figure 4.14: Example of using the logarithmic derivative (light blue), inverse logarithmic derivative (blue) and intersection (red) methods to extract the breakdown voltage from IV curves. The vertical axis is in logarithmic scale.

Below the breakdown voltage, the LD increases with the voltage, while above breakdown, it decreases exhibiting a trend which can be fitted as a quadratic dependence on the voltage. The maximum value corresponds to the BD voltage. The ILD shows the opposite trend. To precisely determine the breakdown voltage, a parabolic fit is applied to the data points around the maximum (or minimum in the ILD) values, complemented by the intersection of two linear fits before and after the peak. The final breakdown voltage is obtained by averaging the results of these methods.

4.3.1.3 Uniformity check on 15, 20, 25, 35 µm-thick LGADs

A comparison between more sensors of the same production and thickness was done for the 15, 20, 25 and 35 µm-thick sensors to check the uniformity.

- **15 and 20 µm LGADs**

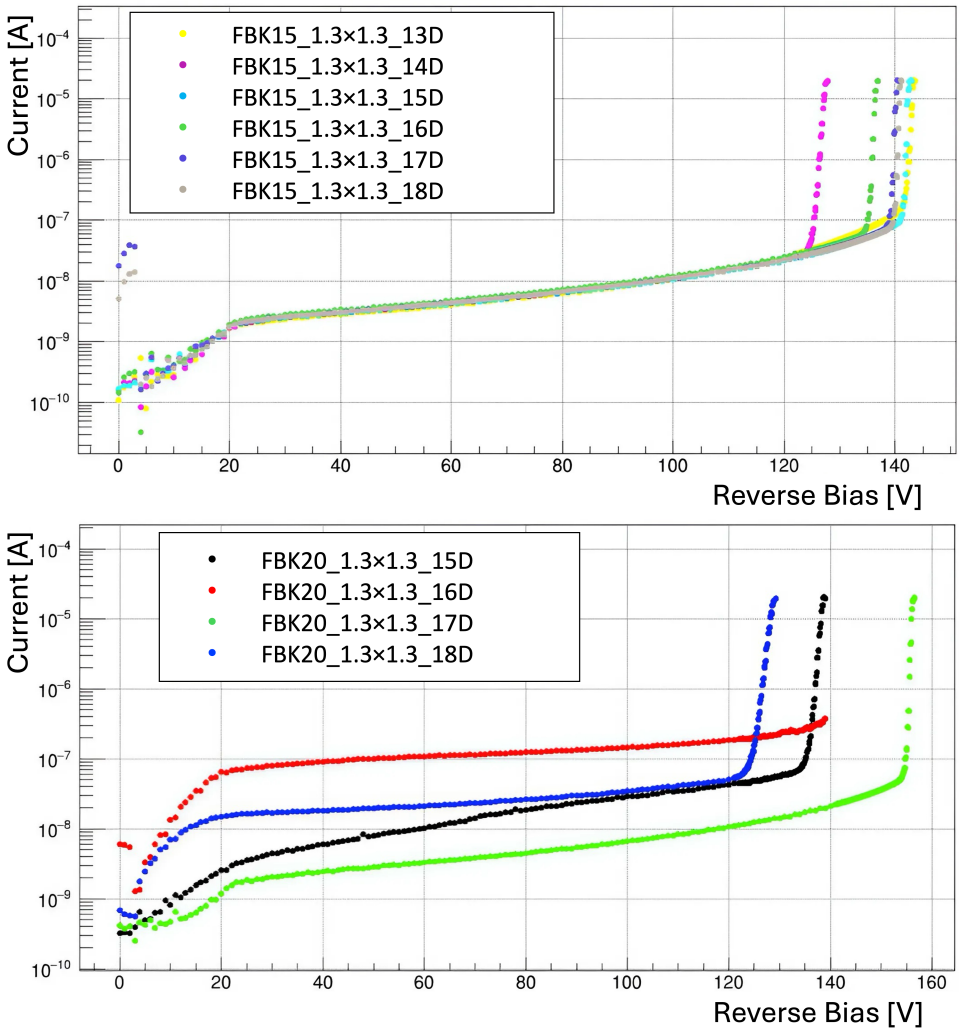

Figure 4.15: 15 µm-(top) and 20 µm-thick (bottom) LGADs IV curves.

All the measured IV curves for the LGADs of 15 and 20 µm thicknesses are reported in Figure 4.15 (top and bottom, respectively).

For the 15 µm sensors it can be observed that the current values at the same voltage are really uniform, while for the 20 µm LGADs, there is a difference, with higher current for some of the prototypes. However for both the thicknesses the voltage value at which the gain layer completely depletes looks similar, at around 20 V, but a more quantitative study is reported in Section 4.3.2. For all the sensors, the breakdown voltage value was extracted, all the values are reported in the Table 4.5. A dispersion is present between the measured values for the different sensors

Sensor	Breakdown voltage V_{BD} (V)
FBK15_1.3x1.3_13D	142.9 ± 0.1
FBK15_1.3×1.3_14D	126.4 ± 0.1
FBK15_1.3×1.3_15D	142.0 ± 0.1
FBK15_1.3×1.3_16D	136.1 ± 0.3
FBK15_1.3×1.3_17D	139.7 ± 0.1
FBK15_1.3×1.3_18D	140.3 ± 0.1
FBK20_1.3×1.3_15D	137.4 ± 0.1
FBK20_1.3×1.3_16D	155.6 ± 0.2
FBK20_1.3×1.3_17D	155.6 ± 0.1
FBK20_1.3×1.3_18D	126.9 ± 0.1

Table 4.5: Breakdown voltage V_{BD} of the 15 (W17) and 20 (W18) µm-thick LGADs tested.

- **25 and 35 µm LGADs**

Some of the measured IV curves for the LGADs of 25 and 35 µm thickness are reported in Figure 4.16 (top and bottom, respectively).

As a general observation, the value at which the gain layer completely depletes, corresponding to the first flex on the curve, is around 22 V for both the thicknesses,

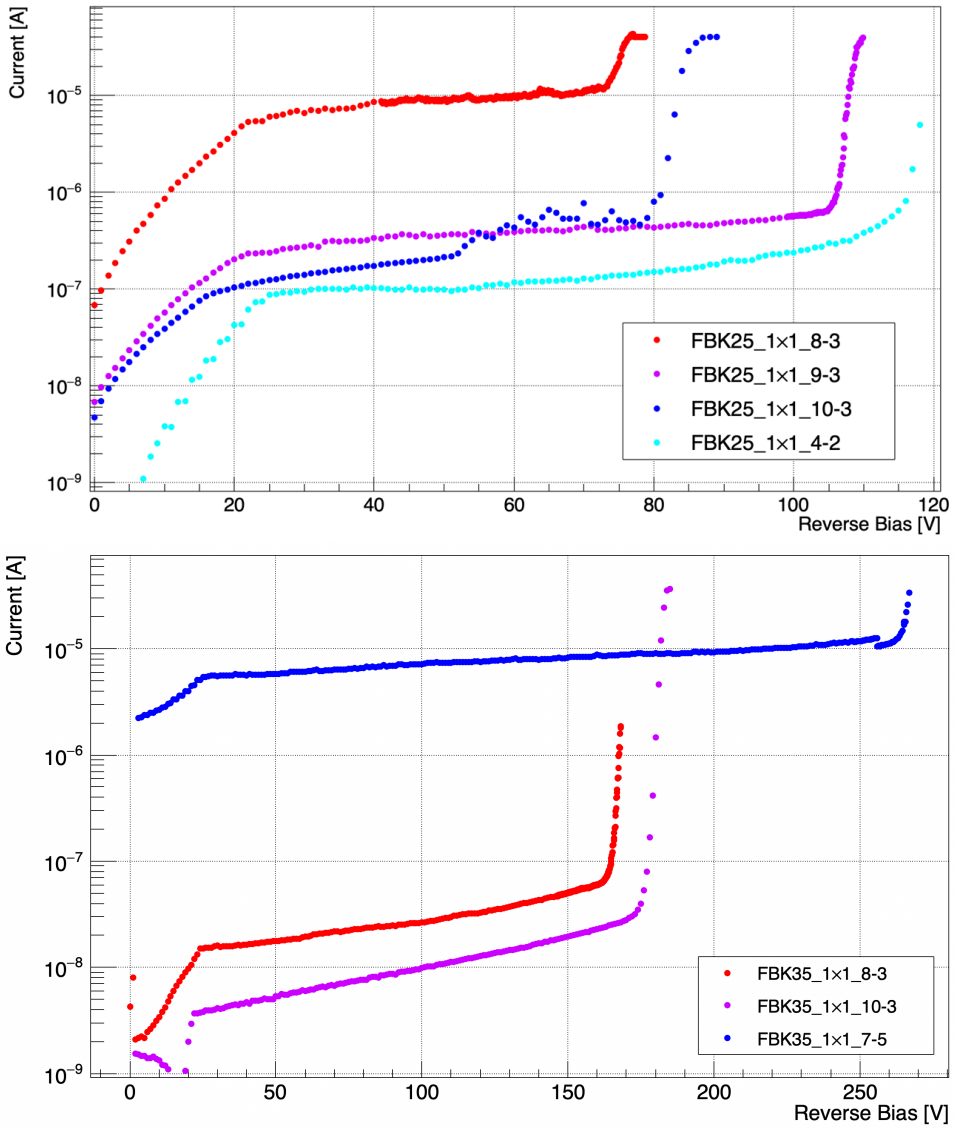

Figure 4.16: 25 µm-(top) and 35 µm-thick (bottom) LGADs IV curves.

while the breakdown voltage for the 25 µm thickness is always lower then the one of 35 µm-thick sensors.

In general the behavior of sensors of 25 µm thickness are similar, while the 35 µm-thick LGADs show more dispersion. It must be said that, in some cases, the measurements may have been affected by the non-optimal dark conditions, which were difficult to keep under control when using the probe station. More reliable considerations on the leakage current can be done once the sensors are connected to a front-end board (see Section 4.3.1.5).

The breakdown voltage for all the tested LGADs is reported in Table 4.6. A dispersion in the values is observed. The parameters exhibit a distribution, probably affected also by different measurement conditions, such as temperature, humidity and light exposure or differences in the sensor production processes that can influence the values. Nevertheless, as a general observation, the breakdown voltages are roughly consistent for the same wafer thickness. From a comparison between the two thicknesses, it can be observed that the V_{BD} is consistently higher for the 35 µm-thick sensors with respect to the 25 µm ones. Indeed, as shown in Section 3.2, a silicon sensor can be treated as a parallel plate capacitor and from the Equation (2.29) it is clear that the same electric field is reached at lower voltages for smaller distances. Therefore, a smaller thickness corresponds to a smaller voltage applied to reach the junction breakdown.

Similar considerations made for the individual LGAD sensors also apply to the tested matrices. For each of the two wafer thicknesses, examples of the measured IV curves are shown in Figures 4.17 and 4.18, for the Type 4 and Type 10 matrices, respectively. These measurements were conducted using the 4-needle setup explained above, with one floating pad. Since the pads were connected in parallel, when the breakdown rising was too steep, the first pad to reach breakdown caused the current to hit the maximum limit that could be supplied to the sensor, thus stopping the measurement before the other pads could reach this condition. Ideally, all pads should exhibit the same breakdown voltage, but slight variations among them must be considered due to production uncertainties.

Also in the case of the matrices, for both types and thicknesses, the depletion of the gain layer occurs at around 22 V and a higher current in the guard ring of the 35 µm-thick LGADs, caused by type inversion in the bulk, is clearly visible in the plots. In comparing

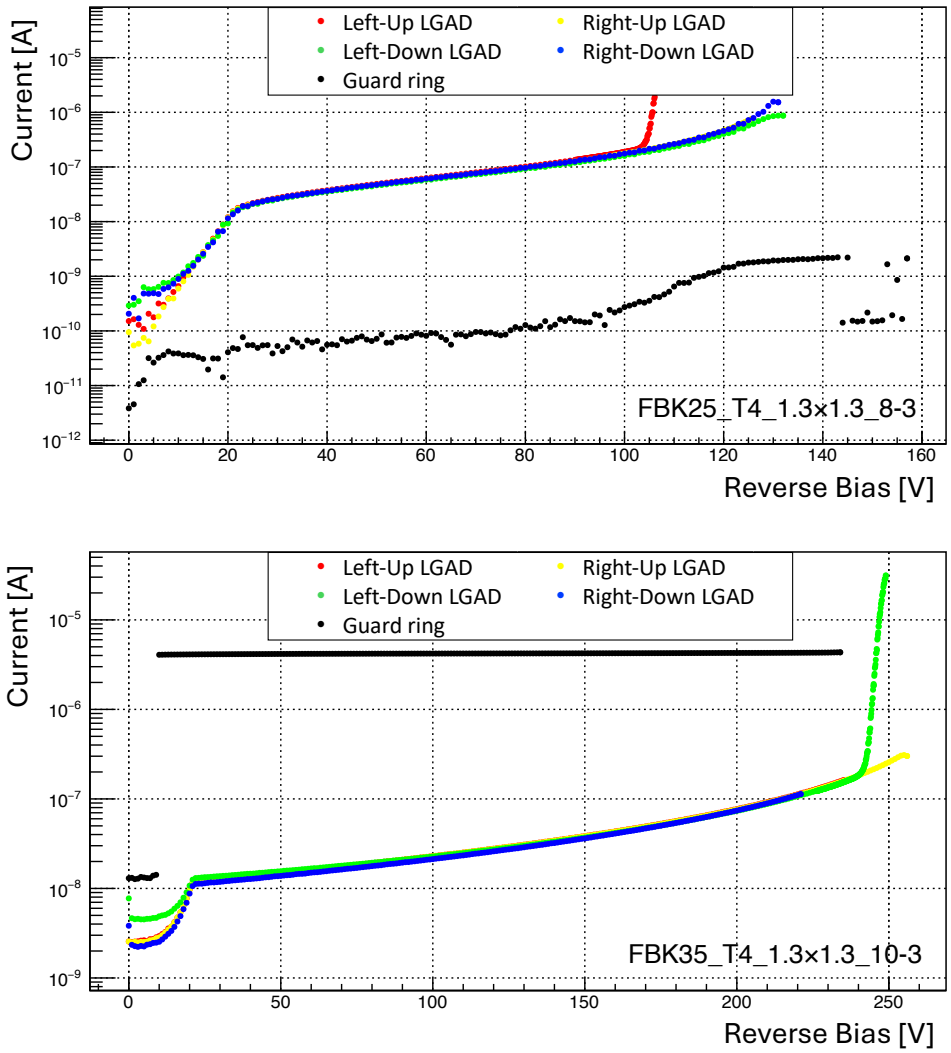

Figure 4.17: Example of measured IV characteristics for 25 µm-thick (top) and 35 µm-thick (bottom) Type 4 matrices. In each graph, five different IV curves are plotted: four corresponding to the pads, and the black one corresponding to the biasing guard ring. All measurements were performed using a 4-needle setup.

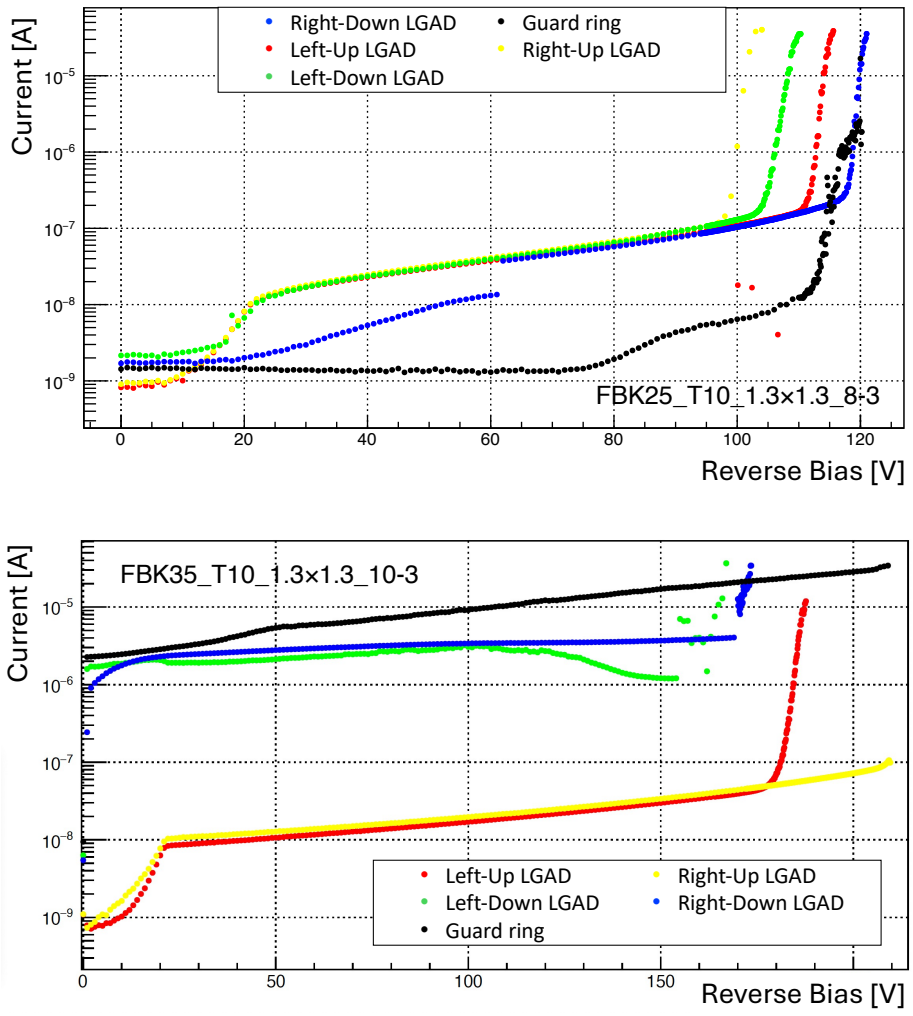

Figure 4.18: Example of measured IV characteristics for 25 µm-thick (top) and 35 µm-thick (bottom) Type 10 matrices. In each graph, five different IV curves are plotted: four corresponding to the pads, and the black one corresponding to the biasing guard ring. All measurements were performed using a 4-needle setup. The gap in the blue curve of the plot in the top, can be due to a non-ideal contact between the needle and the pad.

Sensor	Breakdown voltage V_{BD} (V)
FBK25_1×1_8-3	72 ± 1
FBK25_1×1_9-3	108.2 ± 0.1
FBK25_1×1_10-3	84.1 ± 0.1
FBK25_1×1_4-2	115.4 ± 0.1
FBK25_1×1_5-2	120.1 ± 0.1
FBK25_1×1_7-5	120.6 ± 0.1
FBK25_1×1_8-5	119.2 ± 0.1
FBK25_1×1_9-5	119.2 ± 0.1
FBK25_1×1_10-5	119.0 ± 0.1
FBK35_1×1_8-3	167.1 ± 0.1
FBK35_1×1_9-3	233 ± 1
FBK35_1×1_10-3	175.2 ± 0.2
FBK35_1×1_5-5	-
FBK35_1×1_6-5	-
FBK35_1×1_7-5	262 ± 1
FBK35_1×1_8-5	243.4 ± 0.1
FBK35_1×1_9-5	260.6 ± 0.2
FBK35_1×1_10-5	236.6 ± 0.1

Table 4.6: Breakdown voltage V_{BD} of the 25 (W5) and 35 (W6) µm-thick LGADs tested. The dash corresponds to the LGADs which didn't reach the breakdown, because of the limitation in the total delivered current to the sensor.

the matrices of Type 4 and Type 10, key differences arise in terms of breakdown voltage and uniformity among pads. Type 4, with pads near to each-other, tends to have a very good uniformity in terms of current level among pads. However, it is more sensitive to floating pads and high p-stop doping, which can reduce its breakdown voltage and cause premature breakdown due to the increased electric fields in the inter-pad region. This premature breakdown can be observed in the IV measurements of Figure 4.17, where the curves exhibit an abrupt current rise that in many cases was so steep to be not

measured by the setup. Indeed, the p-stop, in standard working conditions, floats to a potential given by the ground level of the neighboring pads and the negative potential of the backplane. If one of the neighboring pads is not connected to ground, also the p-stop floats to a negative potential because of the influence of the backplane, thus reaching a negative potential higher than the standard condition and increasing the electric field in the inter-pad, potentially causing an early breakdown.

This issue was less evident in the Type 10 matrices, where the presence of a guard ring between the pads offers greater resilience to floating pads and helps maintaining a more uniform electric field, giving excellent uniformity among pads breakdown voltage, thanks to the better isolation, which prevents premature breakdown. As a result, Type 10 exhibits smoother IV characteristics in the region of the breakdown. This can be clearly seen in the top plot of Figure 4.18, where the four pads reach breakdown at more similar voltages value with respect to the Type 4 layout, although also in this case a dispersion can be observed, and have a smoother increasing of the current in the end.

4.3.1.4 From bare sensor to functional device: chip bonding and integration

After the measurements with the probe station, thanks to a Wire bonder TPT HB05, the most performing structures [1] were attached and bonded to the Santacruz V1.4-SCIPP-08/18 front-end board containing a low-noise inverting amplifier, to perform all the measurements with the laser and beam test setups.

The **attachment** of all sensors to the front-end boards was the first step of the process. Isotropic conductive tape was chosen instead of glue due to its reliability in securing different materials with minimal risk of breakage or displacement. Additionally, it allowed for the possibility of removing the sensor from the PCB in the case of incorrect positioning or prototype changes, without damaging either the sensor or the PCB. A small square of tape was attached to the PCB, and the protective layer was then removed. The sensors were manually attached using a micro-aspirator to handle the structure, with the aid of a microscope (Leica S9i). The microscope was connected to a computer where reference lines were drawn on the screen to guide the correct positioning of the sensor.

[1] i.e. all the ones showing an IV characteristics for both the pad and the guard ring, with a reliable value of current and reaching the breakdown at the expected voltage

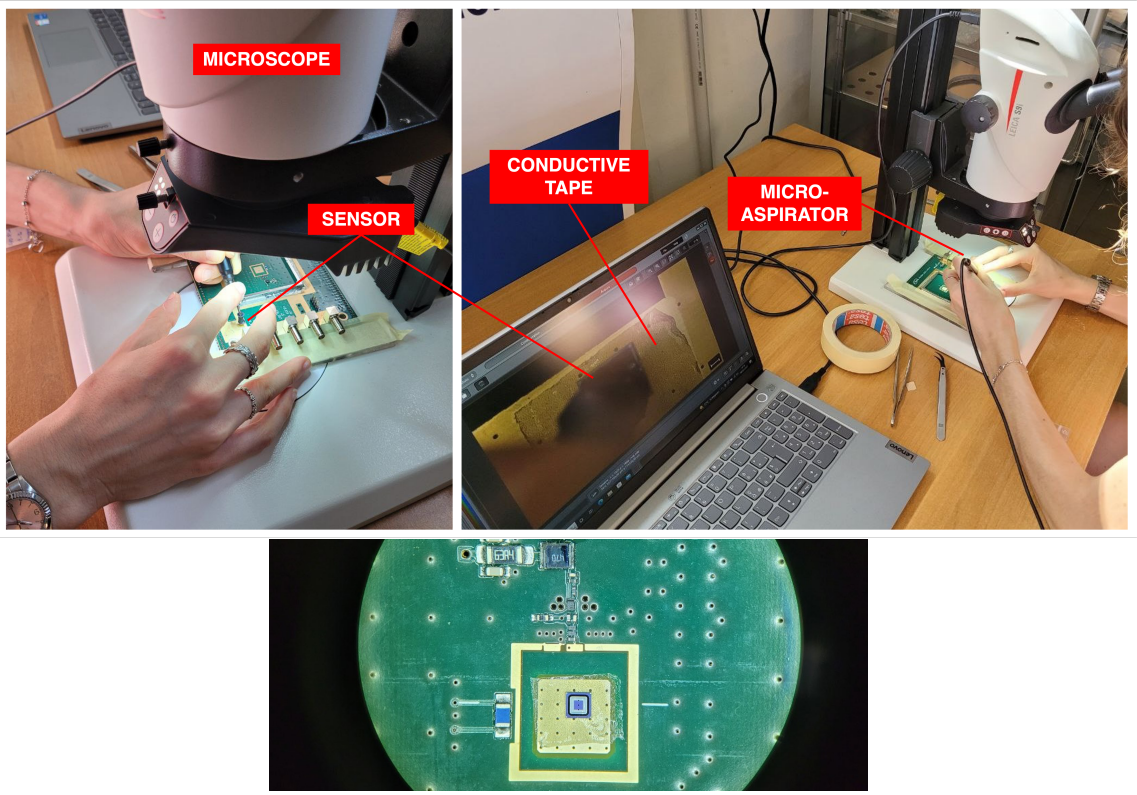

Figure 4.19: Sensor under attachment during the curing (top), and already attached to the front-end board (bottom).

Photos of the attachment procedure are shown in Figure 4.19.

Once the sensors were correctly positioned on the front-end boards, they were electrically connected using the **wire bonding interconnection** technique. Various bonding methods (ball–wedge or wedge–wedge) and bonding mechanisms (thermo-compression, ultrasonic, or thermosonic) were considered [79]. Each method and mechanism comes with its own set of advantages and drawbacks, with the most appropriate one chosen based on the application. After testing different combinations of strength, pressure, and processing time, the wedge-wedge bonding process with ultrasonic interconnection was selected for this type of LGADs and PCBs.

The steps of this technique are illustrated in Figure 4.20. The system rotates to position and weld the wire to the surface, forming the first bond. The clamp then opens, allowing the system to draw out the wire path towards the second bond location on

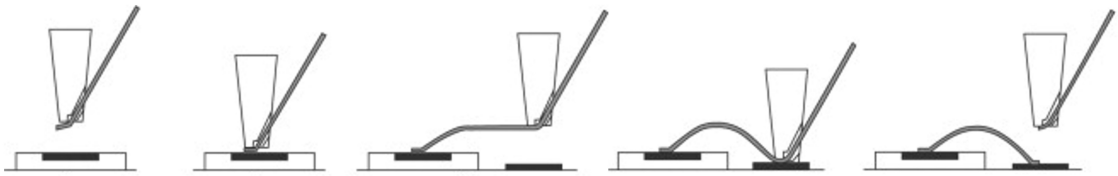

Figure 4.20: Steps of the wedge-wedge bonding process.

the front-end board. It then creates the second bond and terminates the wire with the clamp closed, leaving a small tail of wire below the tool for the next bond. This method was chosen because it allows for a smaller bonding pitch, and the bonding tool does not touch the bond pads, reducing the risk of sensor damage.

A 25 µm diameter gold alloy wire (over 90% Au) was used, and all the bonding was done at room temperature to prevent damage to the sensors. For all prototypes, the pads were bonded to the amplifier of the front-end board, while the guard ring was connected to ground.

During the bonding process, it was crucial to ensure that the wire was centered on the bonding pad, and the wire length was neither too short, which could cause it to touch the border of the prototype, nor too long, which could cause it to touch the sensor cover and create a short circuit. Indeed, if the bonding was not well done, with a wire causing a short circuit, uncontrolled increases in current were observed as soon as 5 Volts were applied to the sensors. For this reason, IV curves were measured again for all sensors after bonding, as an initial check of the bonding quality. Some photos of the bonding operations are reported in Figure 4.21, together with some sensors on-board. Once a sensor was wire-bonded to the substrate, the delicate wires had to be protected to prevent adjacent wires from touching or being damaged during handling.

4.3.1.5 On-board IV characterization of LGAD prototypes

The IV curve for all the attached sensors was measured in order to have the precise operating parameters also when the sensor is integrated with its electronics. A comparison between the IV curve measured on a bare sensor with the probe station and to the same one attached to the front-end board is shown in Figure 4.22. The main difference with respect to measurements performed with the probe station (where the guard ring was

Figure 4.21: Wire bonder (top) and sensor bonded to the front-end board (bottom).

biased, but only the pad was measured) is that with sensors attached to the front-end boards, also the guard ring is connected, and the measure is the sum of both the pad and the guard ring. The full depletion voltage is comparable, while the difference in the leakage current and in the breakdown voltage, which was higher for all the sensors in a range between 2 and 15 V, is probably due to circuitry elements in the board which can alter the measurements.

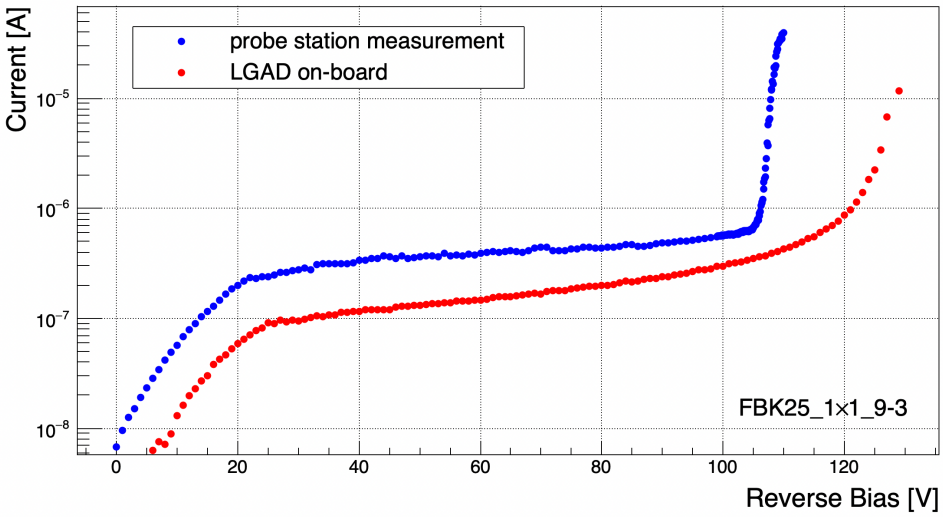

Figure 4.22: Comparison between IV characteristic of FBK25_1×1_9-3, measured on the bare sensor with the probe station and the one on sensor connected to the front-end board.

15, 20, 25, 35 and 50 µm-thick LGADs comparison

A comparison between the measured IV curved for different thicknesses, 15, 20, 25, 35 and 50 µm, is shown in Figure 4.23. The measurement is done for all the sensors connected to the same electronics. As expected, the breakdown has a strong dependence on sensor thickness and layout, for this reason it is meaningless to make a comparison between all the LGAD thicknesses, however, considering the same layout, so comparing for example, 15 and 20, or 25 and 35 µm-thick LGADs, for thicker sensors the breakdown voltage is higher as expected. The higher current of FBK25 is probably due to the higher doping, while for FBK35, this trend is expected. Indeed, as described in Section 4.3.1.2, because of the type inversion, the guard ring, which in the case of the on-board tests is measured, is collecting charges from the entire bulk.

4.3.1.6 Double-LGADs

Thin silicon sensors generate smaller signals at the input of the amplifier, which cannot adequately being managed by standard sensor electronics. This limitation necessitates a more power-consuming front-end design to maintain the time resolution of the detector.

To deal with the small signals generated by thin LGADs, the double-LGAD (d-

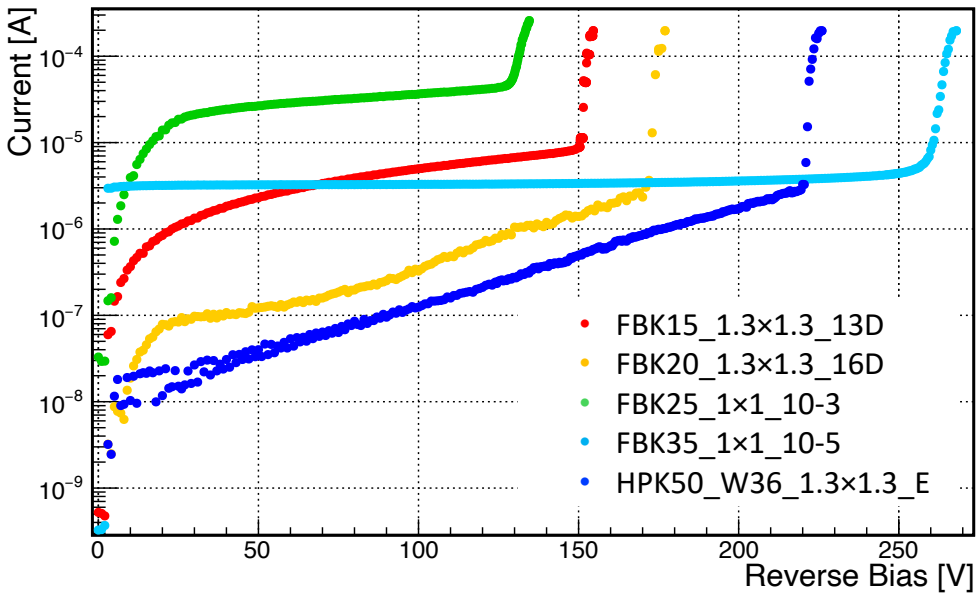

Figure 4.23: IV comparison between LGADs of different thicknesses connected to the same electronics.

LGAD) concept was introduced and tested for the first time. The concept of the double-LGAD is inspired by the Multigap Resistive Plate Chambers (MRPC) [80]. Essentially, the idea is to sum up the signals taken from a double-layer of LGADs and send it to a single front-end amplifier. This is implemented by means of a specific Printed Circuit front-end Board (PCB) design where one sensor is mounted on one side of the board (front) and one on the other side (back).

In Figure 4.24 a schematic of a d-LGAD and a photo of the two sensors attached to the same PCB are reported. This is currently just a proof of concept, but the natural next step would be a better integration of such a concept either in the board containing the electronics or in the detector itself (by having two gain layers in the same wafer or e.g. using Through-Silicon Via, TSV, technique). The possibility to implement the d-LGAD in the detector could allow an easy extension to multi-layer LGADs, although an ad-hoc study and simulation in collaboration with the producer would be required.

In the proposed scheme, given by the sum of two LGADs each with a certain thickness t, the charge of the d-LGAD is expected to be double if compared with a single LGAD of same thickness t. The time resolution of such a d-LGAD is expected to be largely

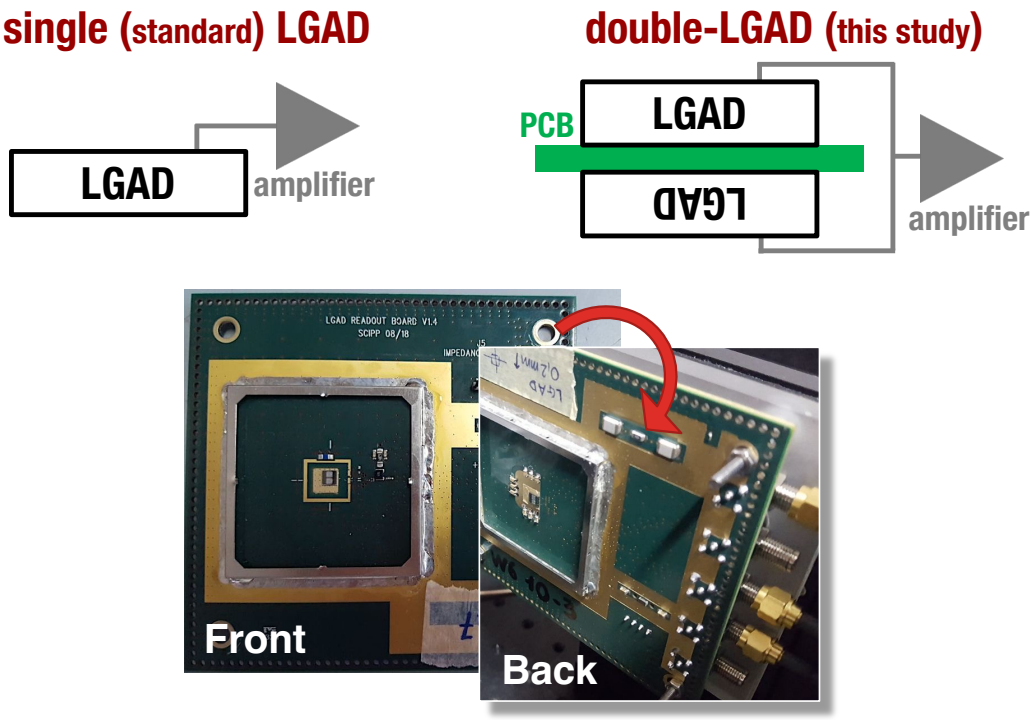

Figure 4.24: Schematic of the single (standard) and double LGAD concept (top) and photo a couple of sensors attached on the two sides of the same front-end board (bottom).

better than that of an equivalent single LGAD of thickness 2t [81]. Similarly to MRPC [82], the time resolution of a d-LGAD is foreseen to improve also w.r.t. to a single LGAD of thickness t; however, due to different signal amplitudes in the d-LGADs, this improvement is less of what expected from simple scaling (i.e. a factor of $\sqrt{2}$). As stated in Ref. [82], the time resolution will be dominated by the LGAD with the largest signal. The largest signal gives the earliest threshold crossing time, so the timing of the d-LGAD is approximately given by the earliest LGAD. In other words, in d-LGAD, the LGAD with the largest signal always dominates the time resolution.

The tests were conducted on the same LGADs used for the previous study. One couple of sensor for each thicknesses available was tested.

All the LGADs tested have been mounted on a front-end board V1.4-SCIPP-08/18, modified in order to place one LGAD on each side of the front-end board and, thanks to a via in the PCB itself, the output of the two LGADs were connected together and sent

to the amplifier described above, realizing a first prototype of d-LGAD.

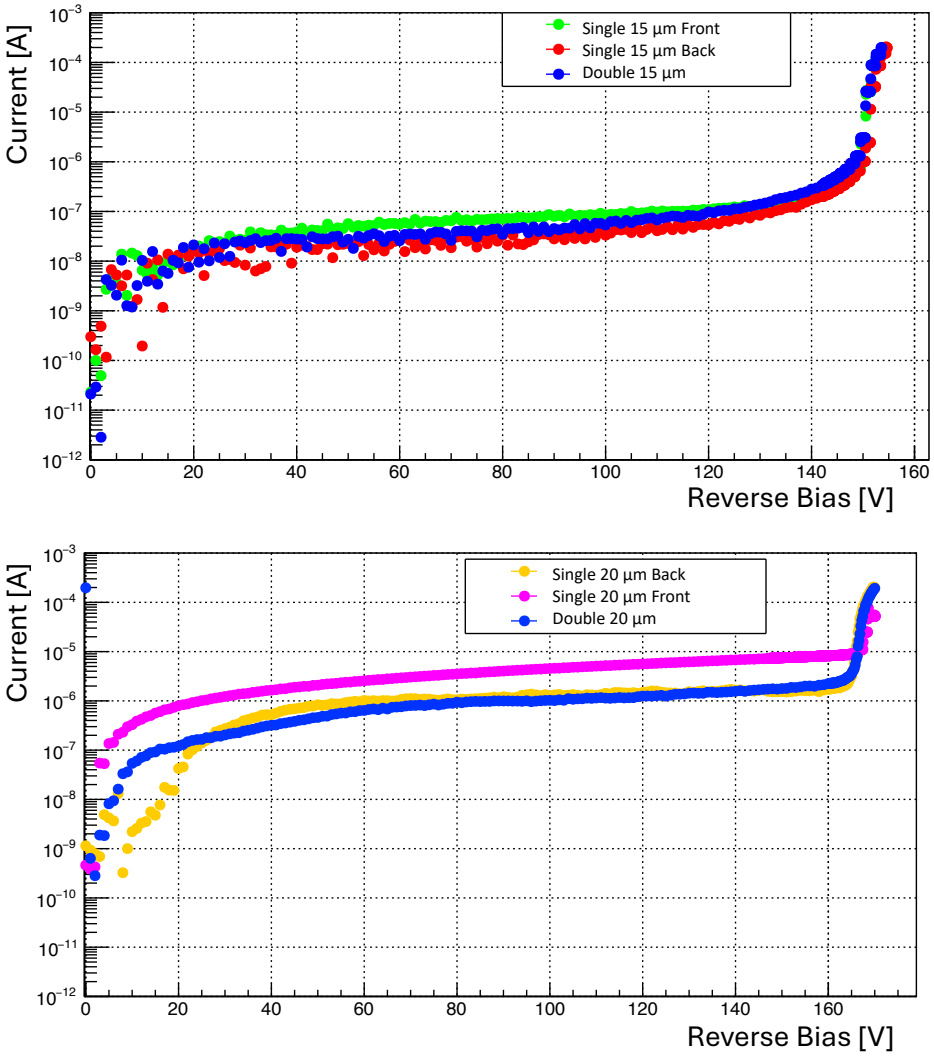

Figure 4.25: Examples of measurements done for the sensors attached to two front-end boards for a 15 and 20 µm-thick LGADs couples. The measurements were repeated in the same setup and under the same electronic conditions on the d-LGADs and on each of the two LGADs of the pairs.

The sensor pairs were carefully selected from all available samples by analyzing the key characteristics measured with the probe station on bare sensors; couples of sensors with IV curves as similar as possible were mounted on the same front-end board. All the

IV curves were then measured having the sensors attached to the electronics. The main objective was to observe the uniformity between the two sensors of each pair, as they are mounted on the same front-end board and powered by the same voltage. It is therefore important to have two sensors that work in an interval and go to breakdown at very similar voltages. To obtain a direct comparison, the measurements were repeated in the same setup and under the same electronic conditions on the d-LGADs and on each of the two LGADs of the pairs. First, the d-LGAD was tested. Then, the bottom LGAD was un-bonded in order to test the top one. Lastly, the top LGAD was un-bonded, followed by bonding and testing the bottom one. As a result, each d-LGAD thickness has three different measurements: two from each LGAD composing the d-LGAD, and one from the d-LGAD itself.

An example of measurements done for the sensors attached to two front-end boards is reported in Figure 4.25. For the two reported plots and in general for all the bonded couples, an excellent overlap is observed for the IV curves of the single sensors and the double sensors for each of the front-end boards. The breakdown voltages are practically the same for the single LGADs and the double LGADs, with a maximum difference of 3 V.

4.3.2 CV measurements

The CV characteristic is another important measurement for the sensors characterization. The value of the capacitance at different bias voltages can be used to extract the gain layer depletion voltage and the full depletion voltage. Furthermore, the shape of the CV curve is directly connected to the doping profile of the sensor, so its measurement is crucial to ensure uniformity between sensors of the same design (especially when used in a large experiment).

4.3.2.1 CV Laboratory setup

The measurement of the CV characteristics was performed through an impedance analyzer [83]. Also in this case the probe station was used, in order to connect the instrument probes to the cathode and the anode of the sensors, through a needle on the top, in contact with the pad and the chuck in contact with the backplane. The experimental setup

is shown in Figure 4.26. In this case just one needle was directly connected to the LGAD, the other two, visible on the right, were used just to maintain the sensor in good contact with the chuck. The same setup, was used to test the sensors once connected to a front-end board, except for the probe station, since in this case the impedance analyzer probes were directly connected to the front-end board.

Figure 4.26: Experimental setup for the measurement of the capacitance-voltage characteristics composed by an impedance analyzer and the probe station (left), with a zoom on the sensor positioned on the chuck (right). The needle connected to the grey probe is the only one directly in touch with the LGAD, the other just apply a pressure on the sensor, and are positioned on the edges of the silicon structure.

4.3.2.2 Uniformity and comparison between different thicknesses

The CV analysis was done only on the 15, 20, 25 and 50 µm-thick LGADs, since the type inversion of the 35 µm-thick LGADs makes it impossible to perform this measurement and extract useful information. A first evaluation was done considering sensors of the same thickness, in order to spot any differences between sensors belonging to the same wafer. The plots reporting the superimposition of some curves related to each thickness are shown in Figure 4.27. First of all, all the curves have the expected behavior. In particular, two main regions can be identified: the first one, where the CV curve decreases slowly, is related to the depletion of the gain layer, and the second one, characterized by a substantial fall-off, is related to the depletion of the lightly doped bulk. The voltage

at which the knee appears is the point in which the gain layer depletes (V_{GL}). The shape of the curve from 0 to this value allow to study the uniformity of the gain layer. There is a very good uniformity among same thicknesses. The only exception is related to 25 µm-thick LGADs, showing an offset of 0.4 V of this value, corresponding to 1.8% of non-uniformity of the doping profile.

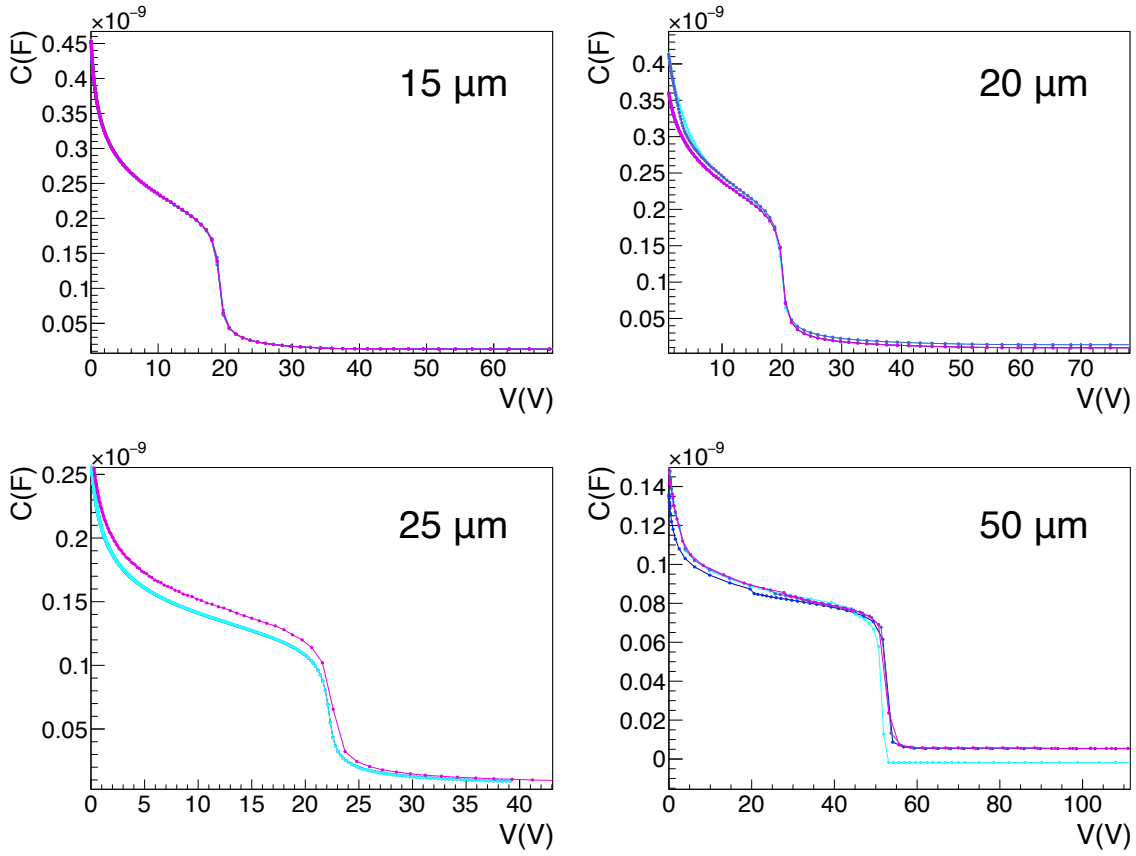

Figure 4.27: Comparison between the CV of different sensors of the same thickness to evaluate the uniformity of each wafer.

A direct comparison between the CV characteristics of LGADs with different thicknesses is then reported in Figure 4.28. The behavior is the same for all the sensors, but it can be seen that the depletion of the gain layer is different for the different productions due to the different implementations of the gain layer implant regarding its thickness, doping level and depth. The gain layer depletion voltages are compatible with the first

change of slope of the IV curves in Section 4.3.1.2.

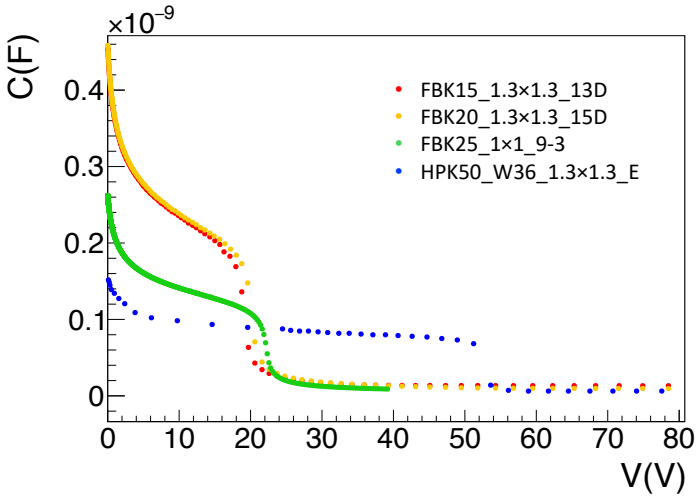

Figure 4.28: Comparison between the CV of one sensor of each thickness.

4.3.2.3 Extraction of the main parameters for the 15, 20, 25 and 50 µm-thick LGADs

Many parameters can be extracted from the measurement of the CV curve. These allows to obtain information about the layout of LGAD sensors, their doping profiles, the electric field trend, and the depletion voltage. Indeed, all these values are useful to understand the response of the sensor under different operating conditions. The behavior of the main extracted ones are reported for one sensor of each thickness in Figure 4.29.

The first value that can be extracted directly from the CV curve is **the full depletion capacitance** C_{FD} of the sensor.

Indeed, after the gain layer depletion, characterized by the slowly decreasing of the CV curve, there is a substantial fall-off related to the depletion of the lightly doped bulk until the curve reaches an asymptotic behavior to the value of the capacitance of the sensor when it is fully depleted C_{FD}. As described in Equation (2.24) this capacitance depends only on the sensor thickness and area.

For all the thicknesses the mean value of the measured C_{FD} is reported in Table 4.7 together with the other extracted parameters.

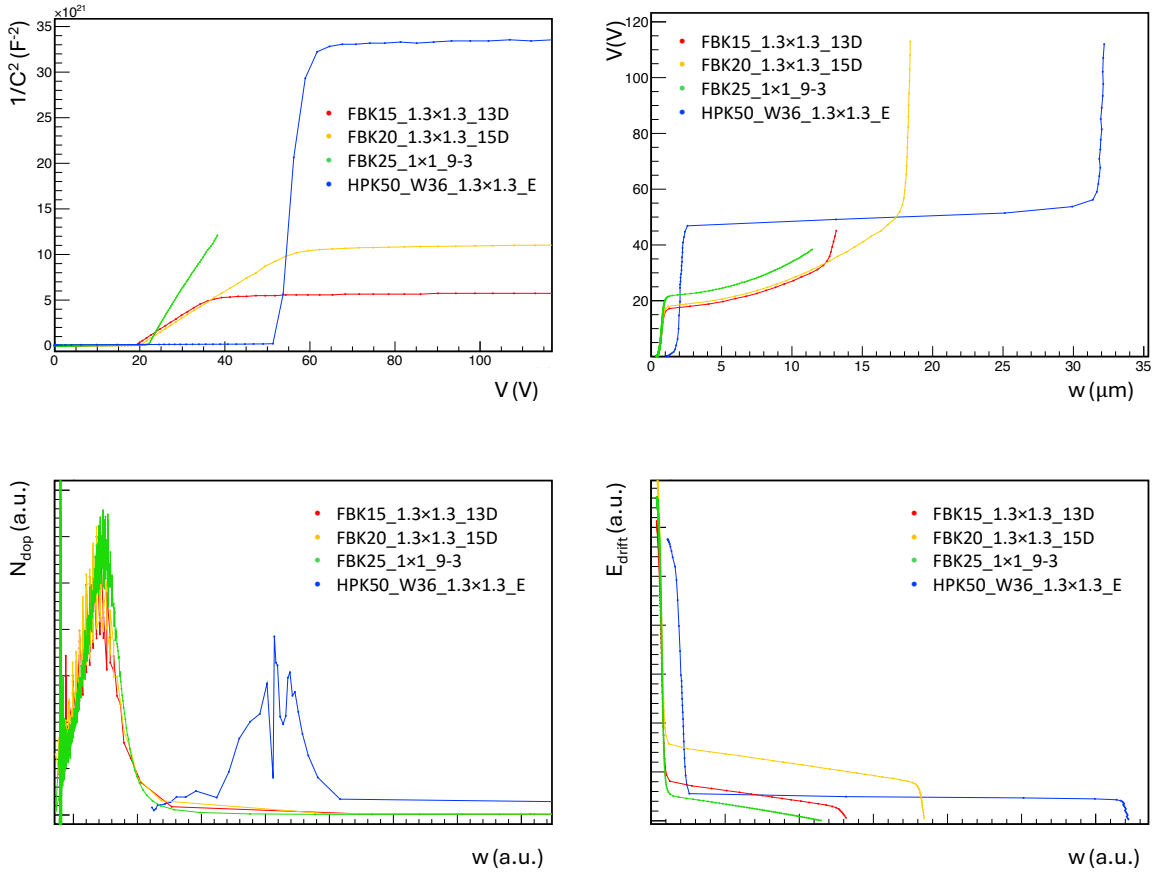

Figure 4.29: Example of the behaviors of the main parameters extracted from CV characteristics for one sensor of each thickness: $1/C^2$ as a function of the applied voltage (top-left), relation between the voltage and the sensor thickness (top-right), doping profile with the dopant concentration per cm^{-3}) atoms (bottom-left) and electric field (bottom-right) as a function of the thickness. The last two plots are in arbitrary units because the doping profiles can't be disclosed. The measurements for the 25 mu-thick LGADs were with an Hameg 8118 impedance analyzer [84] which could not reach values higher than 40 V. For this reason, the full depletion of the sensor was not be reached.

Sensor	C_{FD}	V_{dep}	w (µm)
FBK15	13.2 ± 0.5	39.5 ± 0.9	15.1 ± 0.1
FBK20	9.5 ± 0.5	58.4 ± 0.4	15.2 ± 2.5
FBK25	8.9 ± 0.5	38.9 ± 0.1	22.7 ± 1.8
HPK50	5.4 ± 0.5	61.8 ± 0.9	32.9 ± 0.5

Table 4.7: Main extracted parameters for each LGAD thickness. In the table the values reported are the mean between the ones found for the different sensors of that thickness, and the error is the semi-dispersion of these values. The values for the 25 µm-thick LGAD were simulated using WF2.

The **full depletion voltage** V_{dep}, namely the minimum voltage at which the sensor depletes completely, was then extracted. To achieve this, the inverse of the capacitance squared was plotted as a function of the voltage applied to the sensor (Figure 4.29, top-left). A double linear fit was performed on the points before and after the second inflection point and the full depletion voltage was taken as the intersection point between the two fits.

Since the values of the depleted thickness is related to the capacitance by Equation (2.24), it was then possible to plot the depleted thickness as a function of the applied voltage (Figure 4.29, top-right). This curve is useful to obtain also the real **thickness** w of the sensors by performing a linear fit on the final points of the voltage curve and extracting the asymptotic value to which the curve tends. As a general observation, FBK15 and FBK25 sensors have a thickness very close to the nominal ones with values of around 15 and 23 µm, while for HPK50 (50 µm) sensors the measurements indicate a much lower thickness of around 33 µm. FBK20 showed different values, having two LGADs of around 18 µm of thickness and other two of around 13 µm. The 18 µm-thick sensors were chosen to be tested at the beam test. The thickness values were calculated from the CV measurements considering the nominal areas of the sensors, but various factors (such as the guard ring layout) can influence the actual area, and small variations can lead to significantly different thickness results. For this reason, all considerations in the thesis are based on nominal thickness. However, this uncertainty only affects this value, which is derived from the absolute value of the measured capacitance. Indeed,

all other measurements derived from CV curves are related to the capacitance variation, which in this case is not impacted by the aforementioned factors.

The extracted **doping profile**, found as

$$N_{dop} = \frac{2}{q_e \epsilon_{Si} A_{LGAD}^2} \frac{d}{dV} \left(\frac{1}{C^2} \right), \tag{4.3}$$

is then reported as a function of depth with a zoom on the first peak corresponding to the gain layer (Figure 4.29, bottom-left). As visible in the plot the gain layer shows a doping peak for all the sensors, with a similar depth for the thin sensors, and an higher one for the 50 µm-thick LGADs. As expected a constant and very low doping level is present in the rest of the sensor.

Finally, the **electric field** was extracted and plotted as a function of the depth (Figure 4.29, bottom-right). Since the doping in the gain layer is much higher, we expect a peak in the electric field corresponding to this region. As expected, the electric field is very high at the beginning of the curve, in correspondence of the highly doped gain layer and lower and uniform in the rest of the sensor. Just for completeness, the drift electric field that is quoted in Chapter 5, refers to the electric field inside the silicon bulk (drift region), not to the electric field in the gain region. This has been calculated at the specific voltages applied, for all the sensors, as the difference between the applied voltage and the voltage used to deplete the gain layer, divided for the LGAD thickness. Instead for FBK25, because of the non uniformity of the electric field due to the high doping, a mean value has been extracted using a Weightfield2 (WF2) [85] simulation. WF2 is a simulation program, which allow to study the performance of silicon detectors, simulating the energy released by an incoming particle and the induced signal current. All the input parameters, such as the incident particle, sensor geometry, gain and doping, can be considered, so the performed simulation to obtain the mean value of the electric field was ad hoc tuned on the layout of the sensors and values of the measured data. An example of simulated parameters for a 25 µm-thick LGAD at some applied voltages is shown in Figure 4.30.

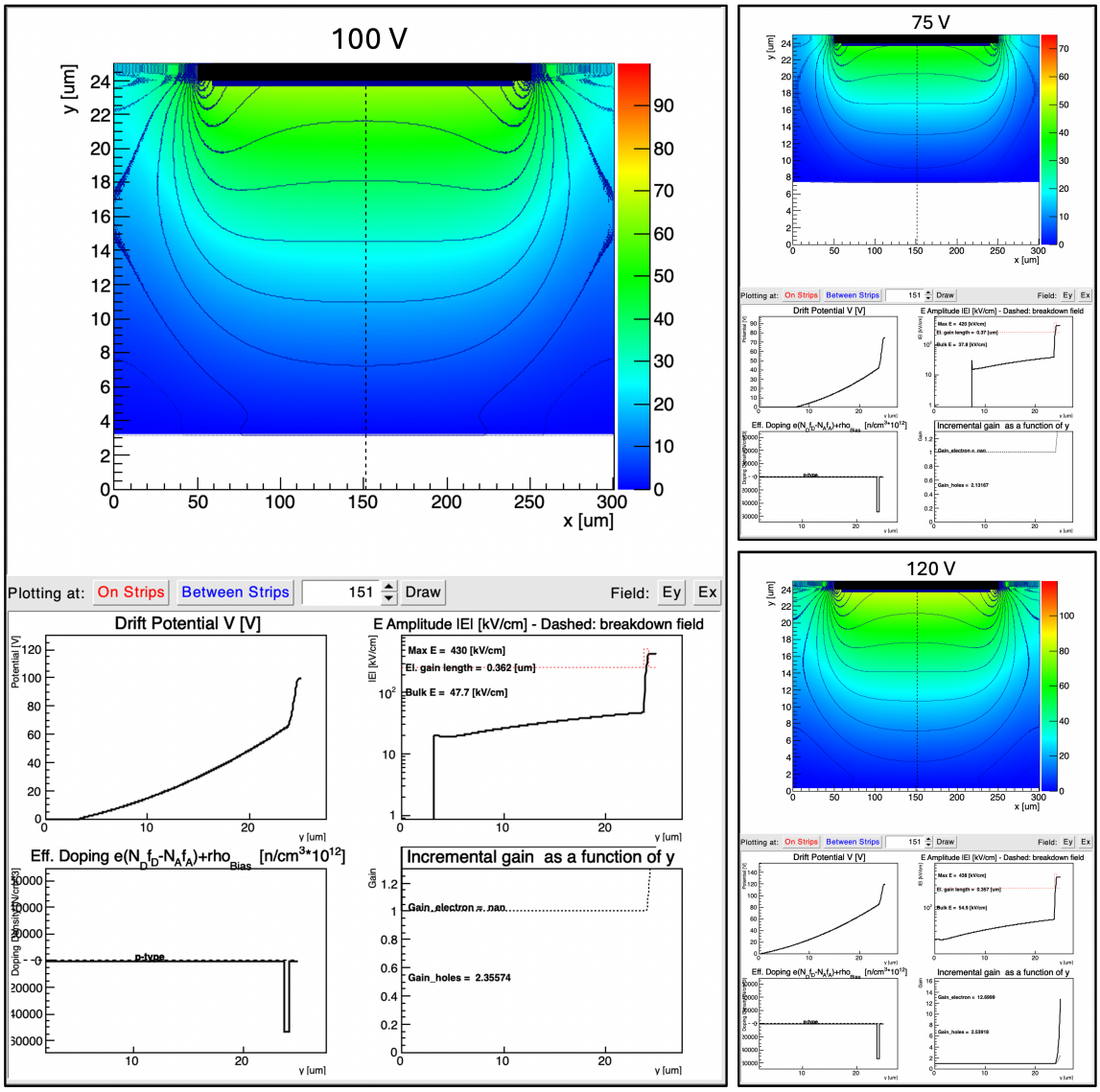

Figure 4.30: Weightfield2 simulation of the depletion and active thickness of 25 µm thick sensors for three different voltages: 75 V, 100 V and 120 V. In each panel is present a visual representation of the depletion of the sensor along the thickness on the y axis with the value of the electric field quoted by the color graduation for the whole central section of the sensor on the x axis. In the plots at the bottom, the simulated drift potential, electric field, effective doping and gain are plotted as a function of the depleted thickness of the sensor.

4.4 Laser measurements

This section presents all the measurements performed using the laser setup. Preliminary studies were conducted on the sensors to assess the light-sensitive areas in terms of efficiency, response uniformity, and edge effects. By scanning the sensors, the window dimensions and laser beam diameter were determined to ensure the entire laser light enters the sensor, enabling reliable comparisons with the PIN. After evaluating the gain of each sensor, initial studies on the time resolution were carried out.

4.4.1 Infrared Laser Setup

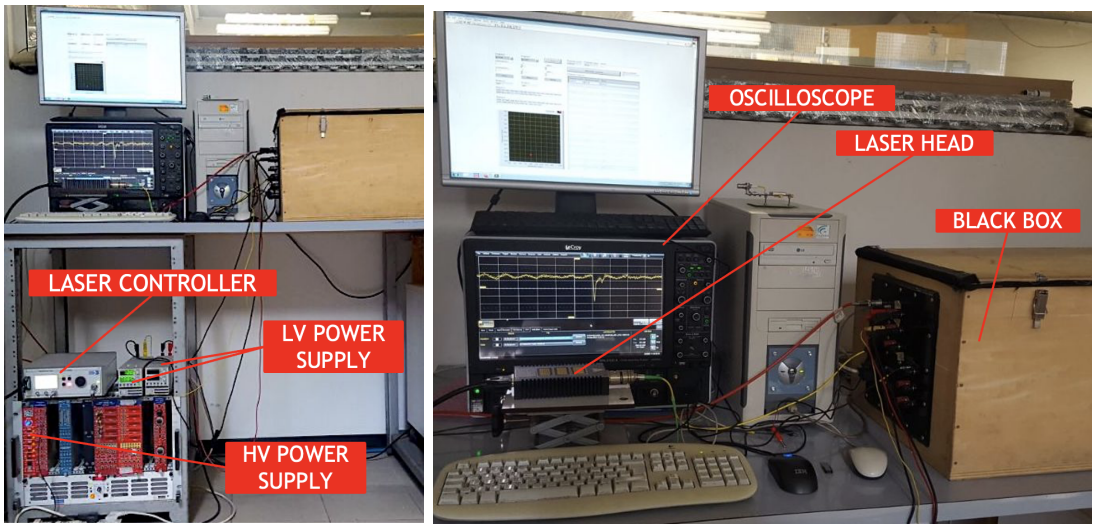

Figure 4.31: Laser measurement setup. The key components comprehend the oscilloscope, the computer running the LabVIEW software to control the micro position stage and the laser head connected to its controller. The laser light is transmitted into the dark box through the yellow optical fiber. Power supplies for the devices inside the box are connected externally to minimize external light exposure.

The main components of the setup are depicted in Figure 4.31. A picosecond pulsed laser with a wavelength of 1054 nm (PiLas PiL036XSM [86]), controlled by an EIG2000DX controller, provides the light. The laser head is connected to a 1-meter single-mode optical fiber (Thorlabs P3-980A-FC-1), which transmits the infrared photons directly into

the black box where the LGAD is positioned (see Figure 4.32).

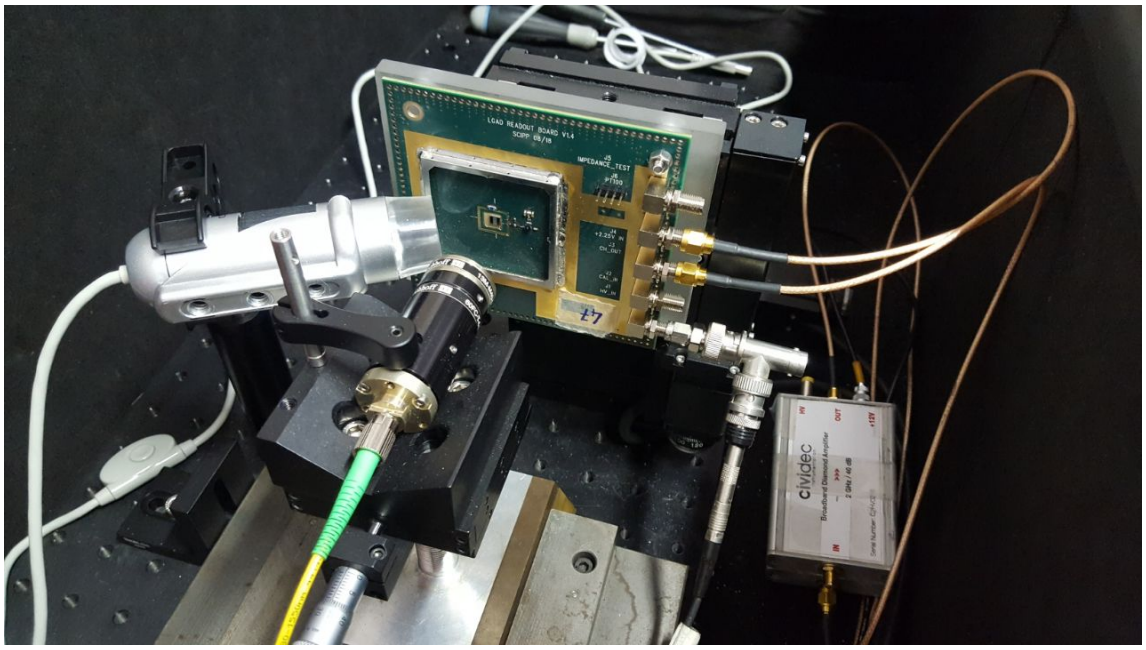

Figure 4.32: Components inside the black box. The LGAD, mounted on a front-end board, is attached to the micro position stage. The top and bottom connectors on the right supply high voltage to the LGAD and low voltage (+2.25 V) to the front-end board. The central SMA connects the output channel to a CIVIDEC, which sends the amplified signal outside the box to the oscilloscope. The single-mode optical fiber enters a micro-focus optics system, mounted on a manually controlled micro positioners stage, allowing precise z-axis adjustments. A camera on the left aids in coarse laser spot positioning on the sensor.

Before reaching the sensor, the laser light is collimated and focused using a collimator-lens combination (Schafter & Kirchhoff 60FC-T-4-M40-54, Micro Focus Optics 13M-M40-54-S). This setup is mounted on a manual micrometer positioning stage, which enables z-axis movement with an accuracy of 20 µm, ensuring precise focusing of the laser spot on the sensor. The front-end board, which holds the LGAD, is mounted on a two-axis Standa 8MT167-25LS micrometer positioning stage [87], controlled via the LabVIEW software. This allows micrometric x-y positioning of the sensor, ensuring the laser spot is accurately aligned with the sensor's active area. The system can be programmed to perform automatic scans of selected areas. To perform the alignment in the x-y plane, a

camera (shown in the figure) connected to the computer was used for coarse positioning.

The LGAD signal is captured by a Teledyne LeCroy digital oscilloscope (WaveMaster SDA 816Zi-A [88]). To ensure measurable signals, an additional amplifier is connected to the front-end board output. Various amplifiers were employed, including CIVIDEC amplifier (visible in the figure [89]), LEE39 [90], Gali5 [91] and Gali52 [92]. While the CIVIDEC is a broadband non-inverting, bipolar current amplifier with high gain, all the others are wideband amplifier offering high dynamic range with a smaller amplification factor. The value of the amplification is specified for the different measurements reported in the thesis. The sensor high voltage is supplied by a CAEN power supply module, while the amplifiers and the front-end board are powered by two Z100-8-TDK-LAMBDA [93] power supplies, as shown in the figure.

4.4.2 Investigation of sensors design, uniformity and edge effects

Using the laser setup, it is possible to perform automated scans across various regions of the sensors allowing the evaluation the dimension of light-sensitive areas, focusing on efficiency, response uniformity, and edge effects.

4.4.2.1 Uniformity of light sensitive area

All the tested prototypes are covered by a metallization on the top, useful to avoid random photons to get into the active thickness, and assure more accurate measurements. To allow the measurements with a laser setup some micrometric windows are present in different positions on the metallization. One of the preliminary measurements done on the sensors consisted in determine the dimensions of these not-covered areas, to ensures that the laser spot is entirely within them, guaranteeing that all photons enter the silicon rather than being reflected by the metallization. This is important especially for the gain evaluation, in which the comparison between sensors with and without the gain layer must be done with the same amount of light and also for performance studies, in order to be sure to inject the right number of photons, necessary to simulate in the sensor the same response it would give with an impinging charged particle.

To conduct these studies, scans were performed inside and around the windows, acquiring the sensor response signal at each step. Figure 4.33 shows an example of the scan results for the area around one of the central windows for a 25 µm (analogous to 35 µm) and a 50 µm-thick LGAD.

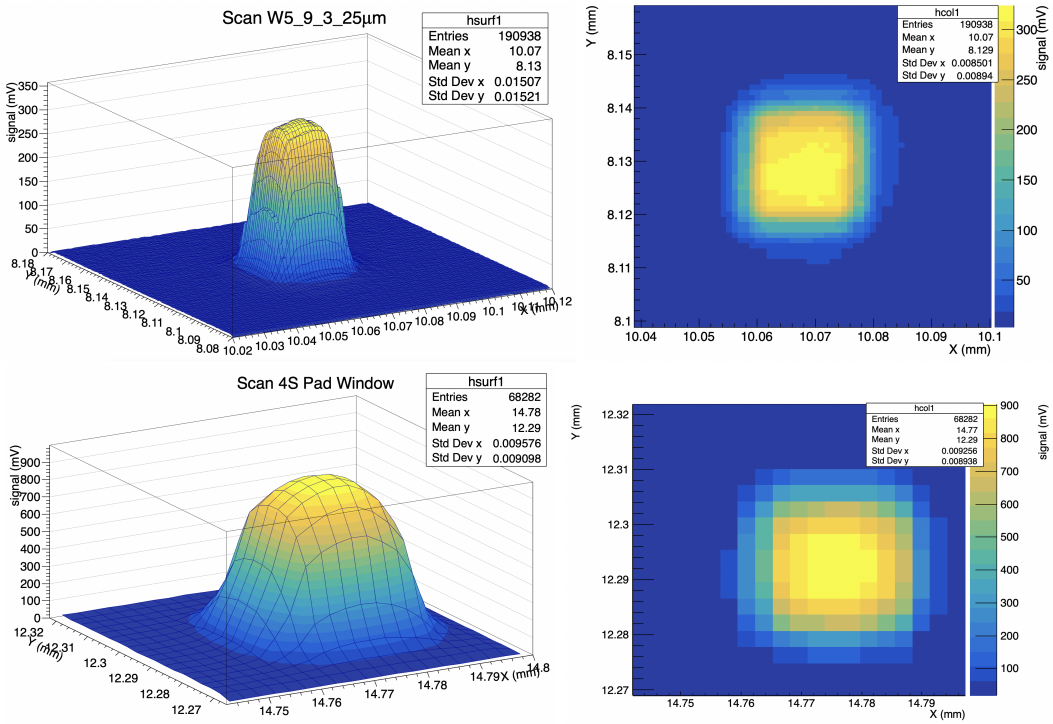

Figure 4.33: Laser scan of FBK25_1×1_9-3 (left) and HPK50_1×3_4S (right) around one of the central windows. A 3D view of the absolute value of the signals (left) and a 2D zoom on the windows (right) are shown. The measurements were performed on FBK25_1×1_9-3 amplified by a LEE39, while HPK50_1×3_4S was amplified by a CIVIDEC, with step sizes of 1 µm in both x and y directions.

The left plot shows a 3D view of the absolute signal values registered by the oscilloscope for each point, while the right plot shows a 2D zoom on the windows. From these it is possible to appreciate the transition between the non-metallized zone of the sensor pad and the laser-blind area. As the laser moves from one region to the other, the signal decreases until it vanishes, indicating that the photons are stopped by the metallization. This transition is not sharp due to the finite size of the laser spot, which has a Gaussian

distribution, with the highest photon density in the core and lower density in the tails. Therefore, as the laser approaches the metallized area, the number of photons entering the window rapidly decreases. It can be observed that in the center of the window, the signal remains uniform, giving confidence that the laser spot size is smaller than the window dimensions. This ensures that, when properly positioned, all photons enter the sensor. The coordinates of the central point, which are essential for gain and time resolution evaluations, are extracted from the plots on the right.

By fixing one of the coordinates during the scan, the signal on the window (negative) can be modeled with respect to the to the other coordinate as a step function, with a constant negative signal in the sensitive area and zero signal in the metallized area. Due to the circular Gaussian intensity distribution of the laser spot, the signal at the window edges transitions smoothly. Considering this behavior, the LGAD signal, as it crosses the transition zone between the metallized and non-metallized areas, is expected to follow the function:

$$Signal = -\frac{A_1}{2}\left[1 + \text{erf}\left(\frac{x - x_{0_1}}{\sqrt{2}\sigma_{G_1}}\right)\right] - \frac{A_2}{2}\left[1 - \text{erf}\left(\frac{x - x_{0_2}}{\sqrt{2}\sigma_{G_2}}\right)\right] + \text{Constant} \qquad (4.4)$$

This is the sum of two error functions, corresponding to the transition between the metallized and non-metallized regions, convoluted with Gaussian distributions representing the laser spot intensity. The parameters A_1 and A_2 correspond to the signal amplitudes, x_{0_1} and x_{0_2} are the transition points, and σ_{G_1} and σ_{G_2} are the standard deviations of the Gaussian distributions.

Examples of fits for the same two LGADs are shown in Figure 4.34. From these measurement a windows dimension of around 35×35, 20×20 and 25×25 µm was found respectively for the 15 (and 20), 25 (and 35) and 50 (HPK50_1×3_4S) µm-thick sensors. Since LGADs require a large number of photons to generate a significant signal, they are primarily sensitive to the core of the laser spot, where photon intensity is highest. Under high-intensity light conditions, the spot size estimated from the fit may differ from the actual size, due to the less populated tails of the Gaussian distribution. In the worst case, the spot sigma was measured to be less than 8.5 µm, which is smaller than the window dimensions in all the analyzed sensors.

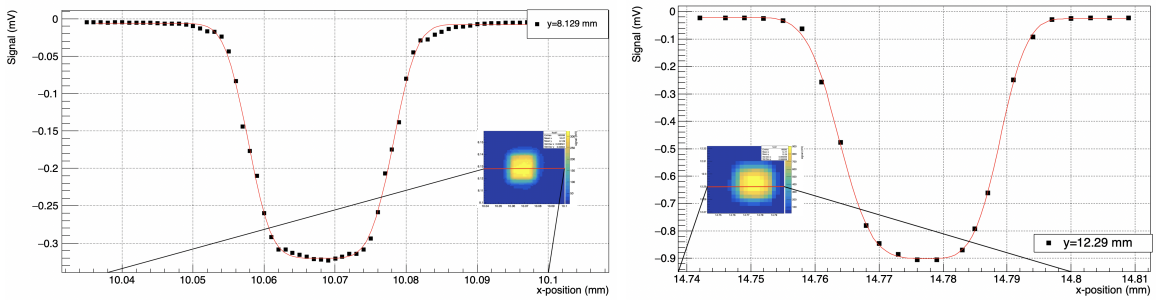

Figure 4.34: Horizontal scan performed on FBK25_1×1_9-3 (25 µm, left) and HPK50_1×3_4S (50 µm, right) around one of the central windows with the y-coordinate fixed at 8.129 mm and 12.29 mm, respectively. The points are fitted with the function (4.4) to determine the dimensions of the window and the laser spot size. The sensors are connected as in Figure 4.33.

4.4.2.2 Edge effects

Using the same setup, the edge effects were studied on some of the LGAD matrices. For the tested samples, a scan was performed in the inter-pad region between two adjacent pads. A dedicated window is present to evaluate any potential differences in the signal at the edges of the active area. Figure 4.35 shows a scan for theHPK50_1×3_4S matrix LGAD matrix, similar to the previous ones. For the reported example, the maximum of the signal is, as expected toward the center of the LGAD-pad and the signal decreases as it moves into the inter-pad region. Some non-uniformities are visible in the outermost part. This window is very useful to evaluate the dead area between the pads. This can be done through the measurement of the Inter-Pad (IP) gap, which is defined as the distance between the multiplication regions of adjacent pads. This value can be determined by identifying the region between pads where the pulse height drops below 50% of the central pad pulse height [94].

Examples of this scan are reported in Figure 4.36 for two different types of 25 µm-thick LGAD matrices (Type 4 and Type 10, the same two layouts gave analogue results for the 35 µm) and for the HPK50_1×3_4S matrix (50 µm). Matrices instead were not present for the 15 and 20 µm. For the 25 µm (35 µm) thick LGADs the results showed IP regions of 30 µm (32 µm) and 60 µm (62 µm) wide for the Type 4 and Type 10 matrices, respectively and of 120 µm for the HPK50_1×3_4S at the maximum applied voltage.

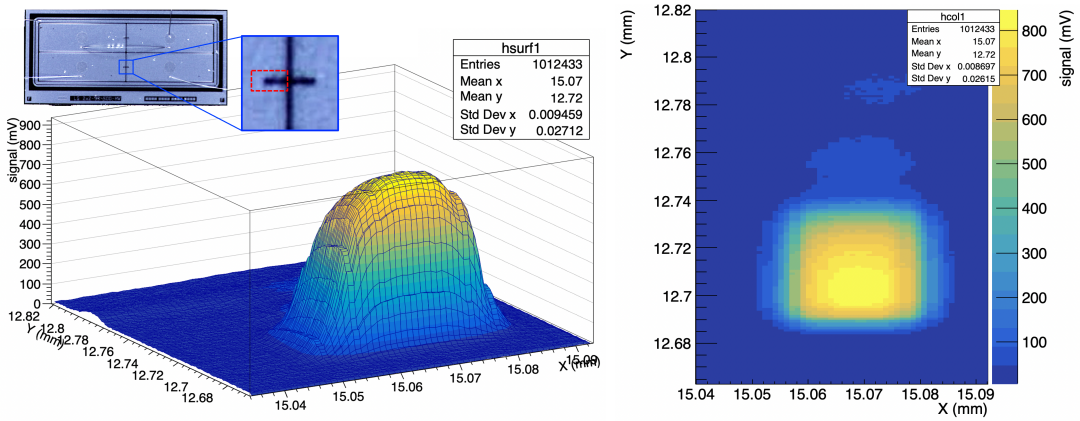

Figure 4.35: Laser scan of the HPK50_1×3_4S (50 µm) LGAD on the left side area of the inter-pad region between two adjacent pads. Only the signal coming from the Left-Bottom pad was read by the oscilloscope. A 3D view of the absolute value of the signals (left) and a 2D zoom on the windows (right) are shown. The measurements were performed with the sensor amplified by a CIVIDEC, with step sizes of 1 µm in both x and y directions.

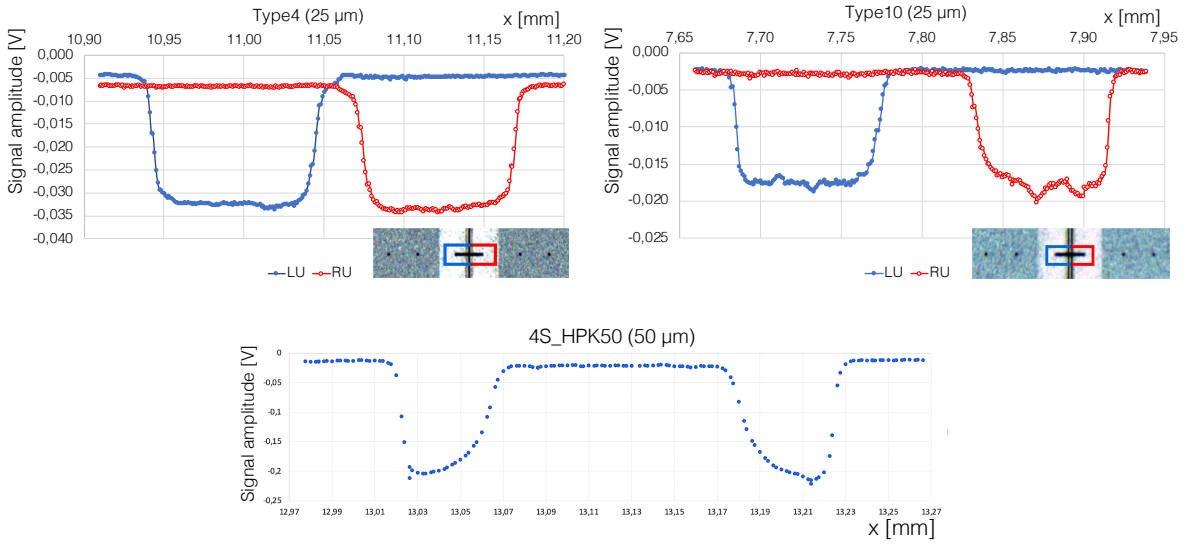

Figure 4.36: Horizontal scan performed on the two different types of 25 µm-thick LGAD matrices (Type 4 and Type 10) and for the HPK50_1×3_4S matrix (50 µm) around the IP gap region. LU (full bullets) and RU (empty bullets) in the images refers to the Left-Up and Right-Up pad of the 2×2 matrices, respectively.

Considering the measured inter-pad gap values a dead area of 0.15 mm^2 (2.2% of the matrix area) and 0.31 mm^2 (4.6% of the matrix area) is present in the Type 4 and Type 10 matrices, respectively. This confirms the layout expectations reported in Section 4.2. A dead area of 0.99 mm^2 (8.3% of the matrix area), is present for HPK50_1×3_4S matrix.

A final comparison was done on a Type 10 matrix, using different applied voltages to investigate any change in the IP region. Scans at different voltages are reported in Figure 4.37.

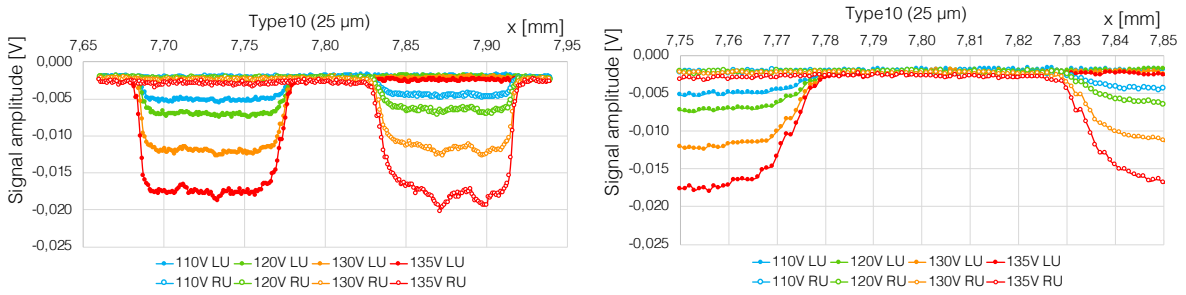

Figure 4.37: Horizontal scan performed on Type 10 25 µm-thick LGAD matrix around the IP gap region at different applied voltages. LU and RU in the images refers to the Left-Up and Right-Up pad of the 4×4 matrices, respectively.

A slightly reduction of the IP region can be observed going to higher voltages, having values ranging from 60 to 65 µm for the 25 µm- and, from 62 to 66 µm, for the 35 µm-thick LGAD matrix, going from the maximum applied voltage to the minimum necessary to appreciate a clear signal.

4.4.3 Gain evaluation

The first measurement performed was the gain of the sensors under consideration. The gain of an LGAD provides significant information, as it is related to various parameters, and in particular to the time resolution versus the applied bias voltage of the detector. The gain evaluation was carried out by comparing each LGAD with a reference PIN of the same thickness, but without a multiplication layer, when available.

Measurements were performed on both the LGAD and the PIN under identical light conditions, ensuring the same focus for the spot. For each pair of sensors, after selecting

a given frequency of the laser pulses and tuning, measurements were taken on both elements without changing any parameters. The spot was consistently well-focused and totally within the windows to ensure the same number of photons reached each sensor and consequently reliable gain values, unaffected by differing amounts of light entering the sensors.

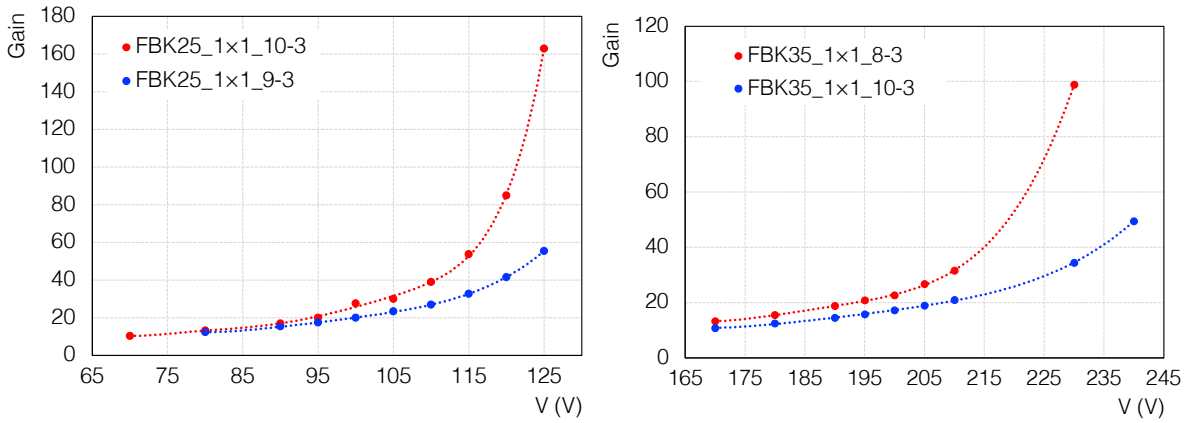

Figure 4.38: Gain curves as a function of the bias voltage for different LGAD-PIN couples for the 25 µm (left) and 35 µm (right) thick LGADs.

The gain was calculated as the ratio of the charge produced by the LGAD to that produced by the reference PIN:

$$\text{Gain} = \frac{\text{LGAD charge}}{\text{Reference PIN charge}} \tag{4.5}$$

The mean charge was determined by subtracting the area under the baseline from the area under the signal (with the same time interval used for both). In the calculation, the internal impedance of the oscilloscope ($R = 50\,\Omega$), the Trans-Impedance of the SantaCruz front-end board ($TI_{SC} = 470\,\Omega$), when present, and any second stage amplifier gain ($G_{\text{amplifier}}$, the same for the LGAD and the respective PIN) connected to the sensor outputs were also considered:

$$\text{Charge} = \frac{A_{\text{Signal}} - A_{\text{Baseline}}}{R \cdot (TI_{SC} \cdot G_{\text{amplifier}})} \tag{4.6}$$

To determine the gain for the 25 and 35 µm-thick sensors, the LGAD-PIN structures were used. For the HPK50_1×3_4S (50 µm) LGADs, HPK_5S PIN was utilized as the

reference. Instead, since for the 15 and 20 µm sensors, no reference PINs were available, the laser tuned to have the light simulating a MIP (based on previous beam test data) was used. In this case, the gain was calculated by comparing the measured charge, to the theoretical charge of a PIN with the same thickness. The calculations by considering the theoretical charge were repeated also for the sensors where a PIN was present and the results were compatible to the PIN and LGAD comparison, validating the reliability of this method. All measurements were conducted under the same electronic conditions and with the same laser light parameters (same tuning, frequency, and intensity) to enable direct comparisons.

The gain curves as a function of the bias voltage, calculated as described, are reported for the 25 and 35 µm-thick LGADs in Figure 4.38. As expected, the curves exhibit exponential behavior as the breakdown voltage is approached. At low voltages, the gain for all sensors of the same thickness is similar, though greater dispersion is observed at higher voltages.

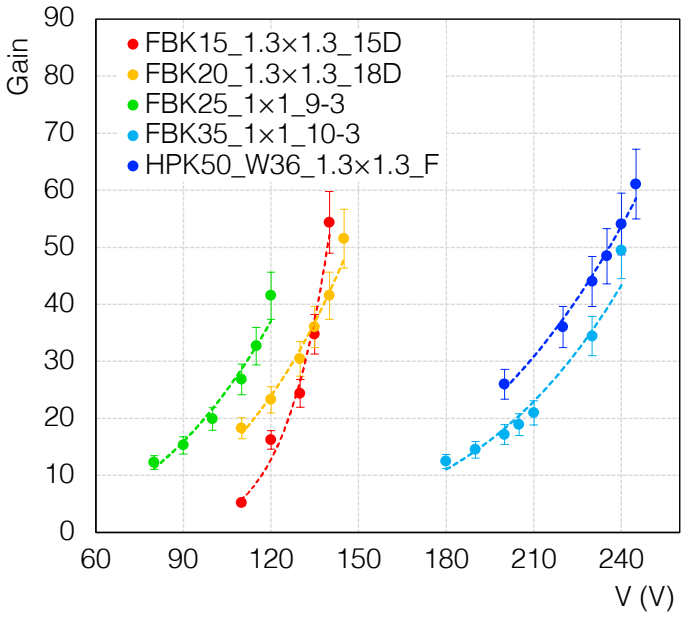

Figure 4.39: Gain curves as a function of the bias voltage for sensors of various thicknesses.

A comparison of the gain for sensors of different thicknesses is shown in Figure 4.39.

Even though at different voltages, the gain generally ranges from a minimum of 10 to a maximum of around 60, as expected for this technology.

4.4.4 Time resolution with a laser setup

A first study of the time resolution through the laser setup was performed before the beam tests on different LGADs. The time resolution was measured using the same laboratory setup described in Section 4.4.1. The aim was to simulate conditions in which the sensors are traversed by a Minimum Ionizing Particle (MIP). As discussed in the previous chapter, a MIP can traverse the entire sensor, producing about 73 electron-hole pairs per µm along its path. IR light can penetrate several tens of µm into the silicon, interacting at various depths after passing through different paths, thus, when correctly tuned it can reproduce the energy deposition of a MIP, simulating its behavior inside the detector. This was done by adjusting the light intensity from maximum to full attenuation, and by mechanically adjusting the laser head optics to reduce the light entering the single-mode optical fiber. In particular, the laser was tuned such that the charge produced by a known LGAD (previously tested in a beam test setup) at a given voltage matched the charge produced during the beam test by using the oscilloscope real-time measurements of $A_{\text{Signal}} - A_{\text{Baseline}}$. All data were collected using the full bandwidth of the oscilloscope (16 GHz for the Wave-Master SDA 816Zi-A), then reduced to 2 GHz during the analysis to filter-out the high-frequency noise. The trigger for the timing measurements was provided by the laser power supply, which adds a contribution in quadrature of 12 ps to the RMS of the distribution of the time response.

Before data acquisition, the laser was precisely focused. Scans of the window area, as described in Section 4.4.2.1, were performed to measure the spot size and determine the exact coordinates of the window center. Approximately 15k events were recorded for each chosen voltage value. Specifically, the oscilloscope recorded the full waveform of the signal for each event.

To reduce noise, several cuts were applied to the data, based on the following criteria:

- the maximum amplitude must fall within a given timing range (specific for each voltage) within a time window of ± 0.75 ns around the maximum of the signal distribution;

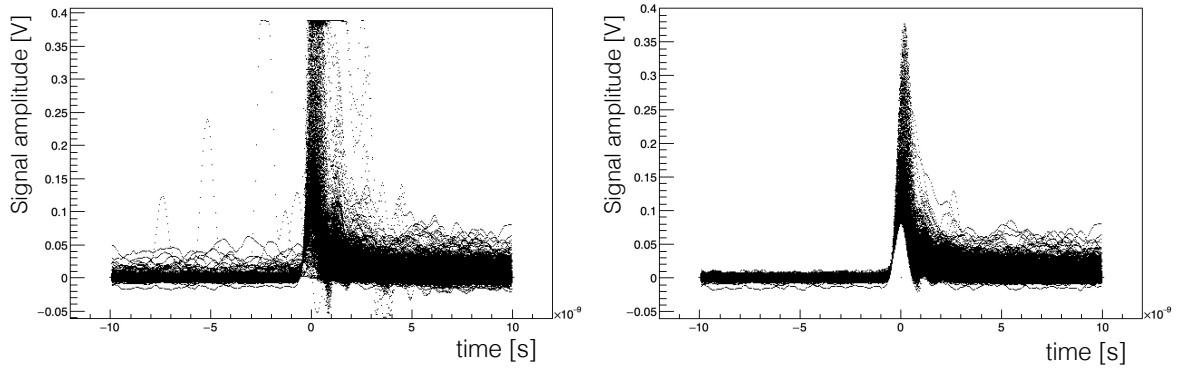

Figure 4.40: Example of signal selection. All events recorded by the oscilloscope based on the trigger condition (left) and selected events after applying the cuts described in the text (right).

- a given amplitude threshold (th_{cut}), chosen to eliminate noise events, must be reached inside the selected signal window;
- noise amplitude outside the selected signal window below th_{cut}, in order to exclude events with significant electronic noise.

An example of the signals surviving the cuts is shown in Figure 4.40.

The time resolution was evaluated offline using the Constant Fraction Discrimination (CFD) technique [95].

The time resolution of the tested LGADs was studied for several values of the CFD percentages at different applied bias voltages. The measured time resolution in this context includes both the intrinsic resolution of the sensor and the additional contribution from the front-end electronics (front-end board and eventual second stage amplifier). An example of the time resolution as a function of the CFD threshold is shown in Figure 4.41, for 25 µm- and 35 µm-thick LGADs at different values of applied voltage. From the plots, it can be observed that at low CFD values, the time resolution worsens. As discussed in the previous chapter, in this region, this is due to the higher contribution of jitter noise.

For all the LGADs, the time resolution improves at higher voltage (gain). This is because each applied voltage corresponds to a specific gain value characteristic of each

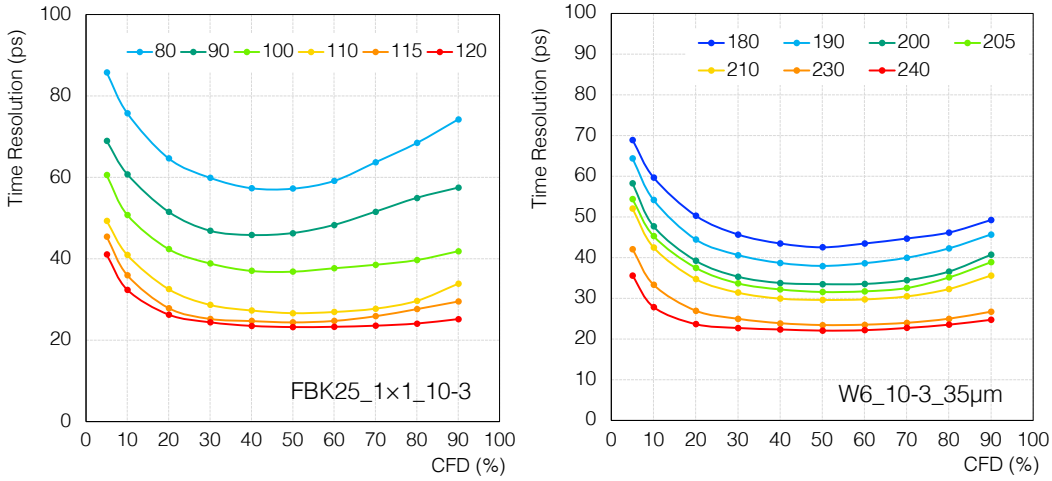

Figure 4.41: Time resolution measured with the laser setup versus the CFD threshold for several applied voltages for 25 µm (left) and 35 µm (right) thick LGADs. The errors have been estimated to be around 10% of the measured value for CFD between 20% and 80% (not shown in the plots for better visibility).

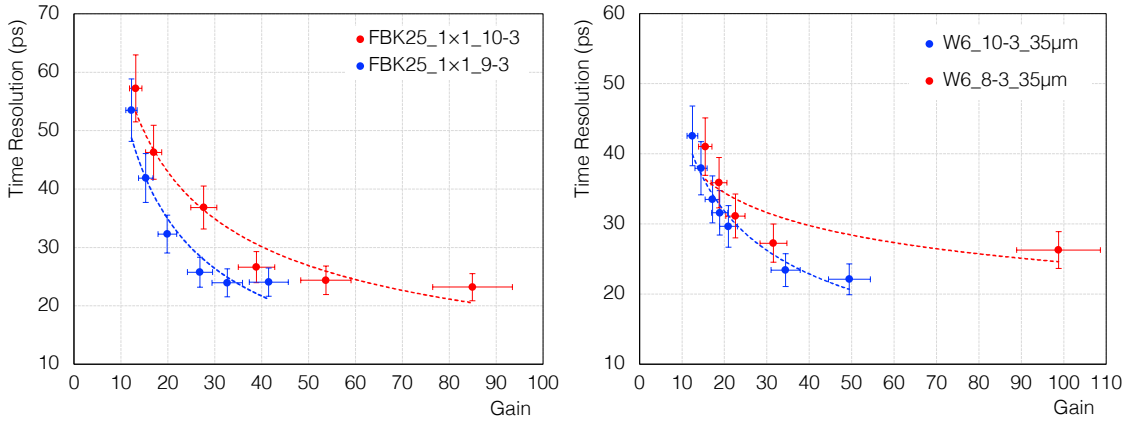

Figure 4.42: Comparison of the time resolution found with the laser setup for two 25 µm- and two 35 µm-thick LGADs as a function of the gain for a CFD of 50%. The lines are included to guide the eye.

sensor. Differently to what happens with particles in the case of a laser setup the Landau effects are absent, since the charge deposit is uniform along depth, resulting in a slightly better time resolution that the one which would be obtained with particles.

From these plots, the optimal CFD value, i.e., the one that minimizes the time resolution, was extracted. The best time resolution for the same two 25 µm- and two 35 µm-thick LGADs of Figure 4.38 is reported as a function of the measured gain in Figure 4.42. As expected, the time resolution values are consistent for LGADs of the same thickness.

A comparison was done also between the time resolutions of pads of a same matrix, for both Type 4 and Type 10 LGAD matrices, and between the results focusing the spot on one of the central and on the Inter-Pad window of the same pad. An example for each type of matrix is reported in Figure 4.43.

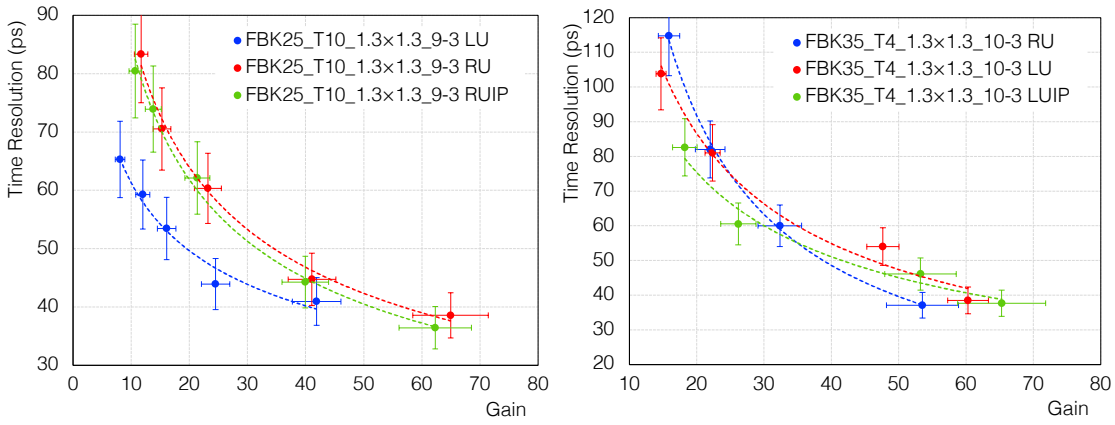

Figure 4.43: Comparison of the time resolution found with the laser setup for two pads of the same matrix in red and blue and for the center of the pad and the edge, as a function of the gain for a CFD of 50%. Type 10 matrix of 25 µm (left) and Type 4 matrix of 35 µm (right) were measured. The lines are included to guide the eye. (LU = Left-Up pad, RU = RightUp pad, LUIP = Left-Up Inter-Pad region, RUIP = Right-Up Inter-Pad region).

The results showed for all the types (4 and 10) and thicknesses (25 and 35 µm) a very good agreement between the resolution in the center and at the edge of the pad. Instead, for both thicknesses the comparison between different pads showed results in agreement for the Type 4 matrices, while some differences in the Type 10 matrices are visible, in accordance with fact that this last layout has pads totally separated by each-other.

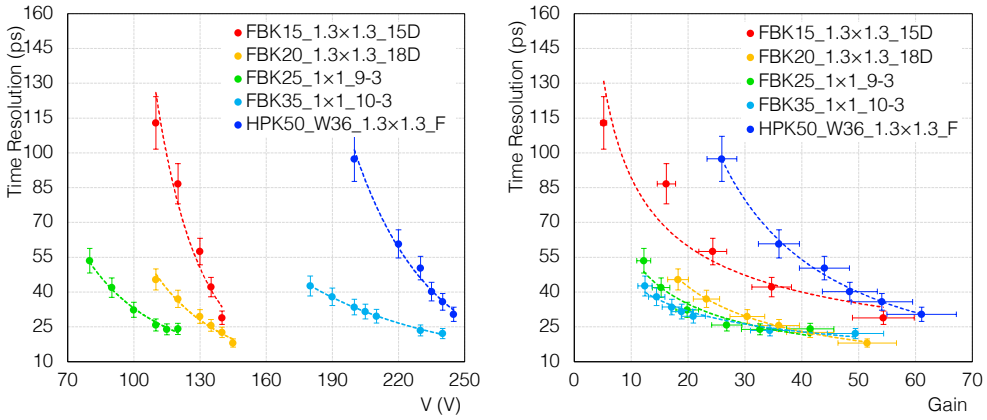

Figure 4.44: Comparison of the time resolution found with the laser setup for all thicknesses: 15, 20, 25, 35, and 50 µm as a function of the applied voltage (left) and gain (right) for a CFD of 50%. The errors for the measured time resolution and gain have been estimated as 10% of the value. The lines are included to guide the eye.

Finally, a comparison among sensors of different thickness (a single one for each thickness, i.e. the same prototypes of Figure 4.39) is shown in Figure 4.44. When comparing sensors of different thicknesses at the same gain, it can be observed that thinner detectors achieve better time resolution in respect to the standard 50 µm-thick LGAD, for all gain values.

4.5 Summary

A comprehensive electrical characterization of LGAD sensors was carried out through current and capacitance measurements at different bias voltages. This allowed us to extract the current-voltage and capacitance-voltage characteristics of the sensors, which are essential for evaluating the breakdown voltage and the operating voltage range of the devices. Additionally, these measurements provided valuable insights into the inter-pad configurations and sensor uniformity.

A comparative study was conducted on LGAD sensors with different thicknesses (15, 20, 25, 35 and 50 mu m) to assess uniformity across sensors of the same production. The results revealed that the 15 mu sensors exhibited consistent current values at the

same voltage, whereas the 20 mu sensors showed slight variations with some prototypes exhibiting higher currents. The 25 mu sensors displayed generally consistent behavior, while the 35 mu sensors showed more variability. Despite these differences, the breakdown voltages remained relatively consistent within the same wafer thickness.

Further comparisons between different sensor matrices, specifically Type 4 and Type 10, highlighted key differences in breakdown voltage and uniformity among pads. Type 4 matrices, with closely spaced pads, demonstrated excellent current uniformity but more sensibility to floating pads and high p-stop doping, which could lead to premature breakdown. On the other hand, Type 10 matrices, which featured a guard ring between the pads, showed improved resilience to floating pads and better isolation, leading to more uniform breakdown voltages and greater overall performance.

After the initial probe station measurements, the most promising sensors were bonded to a front-end board, and the IV curves for these sensors were measured to determine their precise operating parameters when integrated with the electronics. The full depletion voltage was consistent across sensors, but variations in leakage current and breakdown voltage were observed, likely due to the influence of circuitry elements on the board.

The study also investigated the impact of sensor thickness on breakdown voltage, confirming that thicker sensors generally exhibited higher breakdown voltages. Additionally, the introduction of the double-LGAD concept marked an important advancement, with sensor pairs selected based on key characteristics measured on bare sensors.

From the capacitance measurements, the gain layer depletion voltage and full depletion voltage were extracted, providing crucial information about the sensors performance. The shape of the CV curve, which is closely related to the doping profile of the sensor, was analyzed to ensure uniformity across sensors of the same design. Moreover, the full depletion voltage, real sensor thickness, electric field and doping profile were extracted.

Preliminary studies on the light-sensitive areas of the sensors assessed their efficiency, response uniformity, and edge effects. Moreover the gain was extracted using a laser setup: all the curves exhibit exponential behavior as the breakdown voltage is approached. At low voltages, the gain for all sensors of the same thickness is similar, though greater dispersion is observed at higher voltages.

Additionally, time resolution studies were performed using a laser setup before beam

tests, showing that time resolution improved at higher voltages due to increased gain. The time resolution was also compared for pads within the same matrix for both Type 4 and Type 10 matrices. The results showed excellent agreement between the time resolution at the center and the edge of the pad for all thicknesses (25 and 35 mu) and types (4 and 10). While the Type 4 matrices exhibited consistent time resolution across pads, some differences were observed in the Type 10 matrices.

Overall, when comparing results obtained with the laser setup on sensors of different thicknesses at the same gain, thinner detectors were found to achieve better time resolution in respect to the standard 50 mu-thick LGADs.

Chapter 5

Test Beam results

The time resolution of LGAD sensors was studied in seven different beam test campaigns between 2021 and 2024. All the tests were carried out at the T10 beamline at PS-CERN with a positive hadron beam mainly composed of protons and pions with a momentum of 10 GeV/c. Some of the examined LGADs are the same studied in the laboratory tests.

The firsts beam test measurements of 25 µm and 35 µm compared to 50 µm-thick sensors highlighted the potential of a thinner design for improved time resolution. Consequently, comprehensive studies were conducted on progressively thinner sensors, arriving to test the first 15 µm-thick LGADs ever produced by FBK. Moreover, to address the small signal at the input of the electronics, the innovative concept of double-LGAD was introduced and tested for the first time. Notably, this innovative approach not only yields the significant benefit of an enhancement of the charge at the input of electronics but also translates into an improvement in overall time resolution. Finally, a study was conducted to determine the effect on the time resolution due to the angle of incidence of the particles with respect to the normal to the surface of the sensor.

5.1 Test beam setup

For each data acquisition up to four sensors were aligned in a telescope frame and the whole setup was enclosed in a dark environment box and exposed to the beam. In Figure 5.1 photos of the experimental setup at the T10 beam test facility at CERN are reported.

The top pictures refer to a setup (A) used in beam tests during 2021 and early 2022, while the bottom highlights the improved setup (D) from mid-2022 onward. In particular, in the first photo the sensors were blocked in fixed position within the frame (B, C), while in the second, independent micro-moving stages (E) in the x and y directions, remotely controlled and with a precision of $\sim$ 10 µm, were used for the different sensors. In addition, a chiller was added to keep a constant temperature around 20°C inside the box during the whole beam test.

The LGADs have been mounted on different front-end boards, followed by second stage external amplifiers. The electronics used is reported in each section for the corresponding tested sensors. All the instruments were remotely controlled from a PC, connected through Ethernet cables. LabVIEW applications were used for the data transfer and storage, for setting up and monitoring of bias voltages and currents and to run a fast online analysis in order to have a quick real-time quality check on the acquired data.

The trigger for the data acquisition was given by the coincidence of the four LGADs after a given threshold was applied. In Figure 5.2 a schematics of the four sensors in the setup together with the display of a single acquired event, with the four waveforms. More details of specific configurations regarding each setup will be given at the beginning of each section.

The same telescope aforedescribed was also used to test SiPM [96] during the beam tests (see Appendix B). In this case, LGADs were placed at both ends to provide both the trigger for data acquisition and as a temporal reference for the time resolution measurements of the devices under test. The SiPMs were inserted into the two central slots of the telescope [97].

5.1.1 Detectors under test

All the sensors tested during the beam test campaigns are reported in Table 5.1, with the applied voltage and gain ranges (more specifics about the wafer and layout are reported in Section 4.2):

- 25µm- and 35 µm-thick sensors, in Section 5.2.1 referred as FBK25 and FBK35, respectively, were firstly studied in comparison to an HPK LGAD of a standard

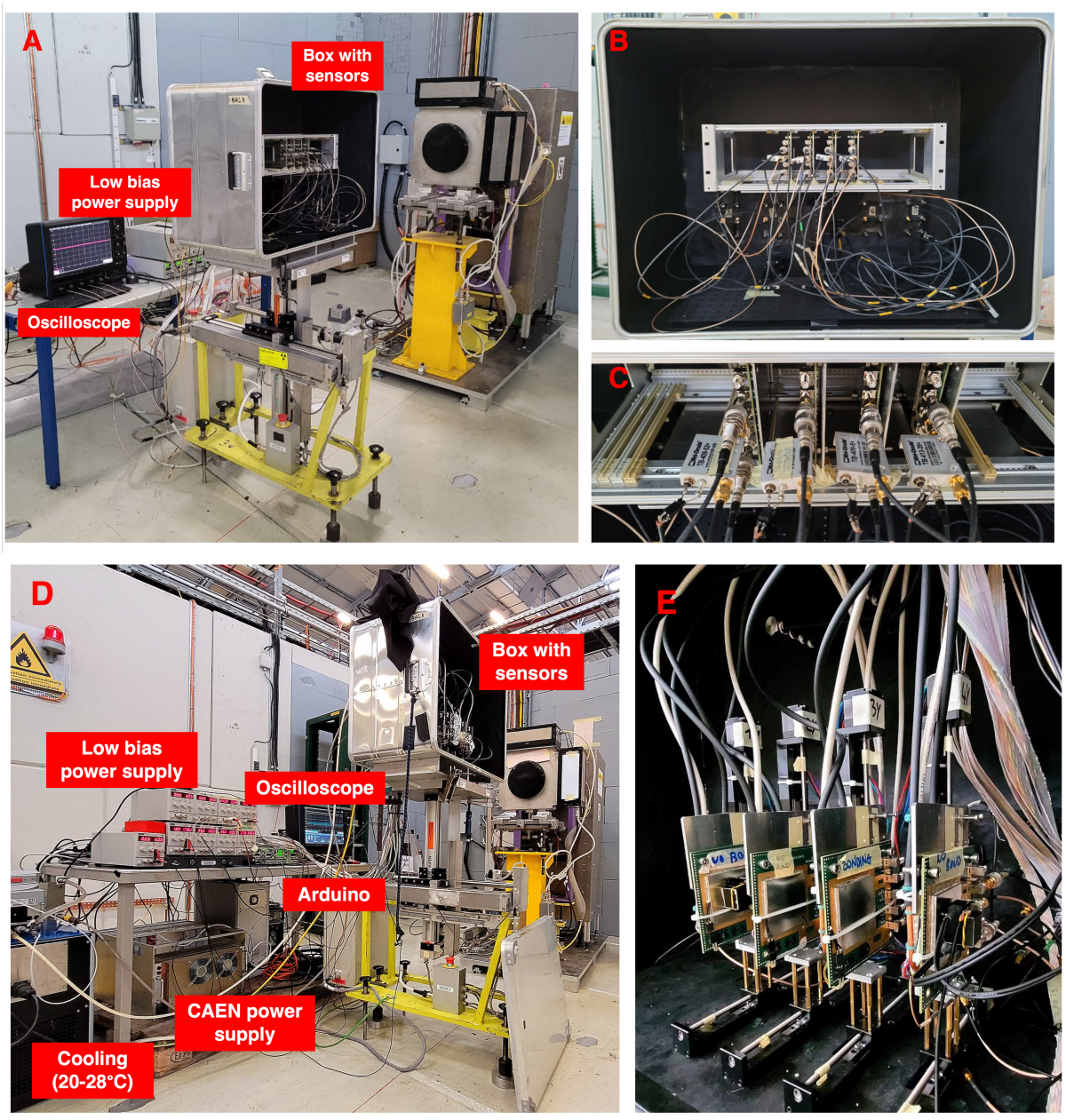

Figure 5.1: Setup in the T10 beam test facility at CERN, together with a zoom on the sensors aligned inside the box, used in the beam tests carried out during 2021 and early 2022 (top), and the setup adopted from mid.-2022 onward (bottom).

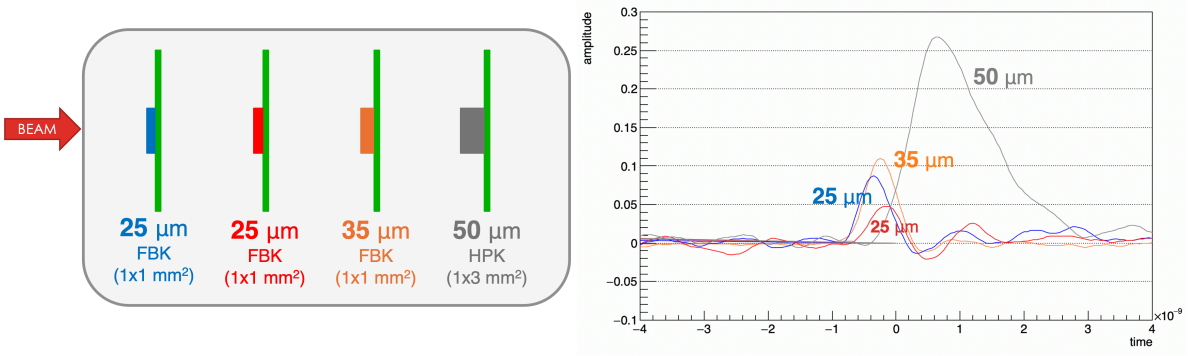

Figure 5.2: Schematics of one run with four sensors aligned in the setup (left) and a single event acquired (right). The acquisition is done when the request of the coincidence of the self-trigger from the LGADs, each one with its own threshold, is satisfied.

thickness of 50 µm (HPK50). Note that the 50 µm-thick LGAD used for this study, has a deeper gain layer implant in respect to the others reported in the table; this can be one of the motivations (see Section 4.3.2) for the higher reached gain.

- few sensors from all the thicknesses, from the standard 50 µm down to 15 µm, were tested and compared; all the sensors with a same thickness have the same layout, area and characteristics, except for 50 µm-thick sensors, which belong to two different wafers, with two different doping profiles;

- one pad of a 25 µm-thick LGAD matrix with a Type 4 design was studied in comparison to a single LGAD; all the pads and the guard ring were biased, but only one pad of the matrix was read out.

Sensors in the table not divided by lines, belong to the same wafer and have the same layout. LGADs used to implement the double-LGAD concept are specified in the table as Double, Single Back and Single Front.

5.1.2 Front-end and readout electronics

All FBK and HPK sensors, both single and matrices, have been mounted on a V1.4-SCIPP-08/18 SantaCruz front-end board, containing a wide bandwidth (2 GHz) and low-noise inverting trans-impedance amplifier with a Trans-Impedance (TI_{SC}) of 470

Sensor	Tests name	A (mm^2)	T (µm)	V (V)	Gain
FBK15_1.3×1.3_15D	Single 15µm Front	1.3×1.3	15	100-140	31-52
FBK15_1.3×1.3_13D	Single 15µm Back			100-140	39-67
FBK15_1.3×1.3_17D				110-140	18-32
FBK15_1.3×1.3_18D				110-145	11-43
FBK20_1.3×1.3_18D	Single 20µm Front	1.3×1.3	20	110-150	20-51
FBK20_1.3×1.3_15D	Single 20µm Back			110-150	28-56
FBK25_1×1_5-2	Single 25µm Front	1×1	25	80-120	11-24
FBK25_1×1_10-5	Single 25µm Back			80-120	12-43
FBK25_1×1_9-3	FBK25			80-120	14-40
FBK25_1×1_10-3				90-125	7-23
FBK25_T4_1.3×1.3_10-1		1.3×1.3	25	80-120	25-49
FBK35_1×1_8-5	Single 35µm Front	1×1	35	180-240	9-17
FBK35_1×1_7-5	Single 35µm Back			190-240	11-27
FBK35_1×1_10-3	FBK35			165-240	7-30
HPK50_W36_1.3×1.3_E	Single 50µm Front	1.3×1.3	50	170-220	24-63
HPK50_W36_1.3×1.3_F	Single 50µm Back			170-220	25-64
HPK50_W42_1.3×1.3_A		1.3×1.3	50	180-240	13-32
HPK50_W42_1.3×1.3_B				190-240	25-67
HPK50_1×3_4S	HPK50	1×3	50	200-245	45-118

Table 5.1: Characteristics of all the LGADs used during the beam tests.

Ω. The front-end board was followed by a second amplification stage, or a mini-circuit LEE39+[90] or Gali52+[92], with a gain factor of around 12 and 13, respectively, having an output charge calculated as in Equation (4.6).

The only exception was the HPK50, which was placed on a front-end board without internal amplification, followed by a C2 [89] broadband (2 GHz) and low-noise current amplifier with a gain factor of 190.

The LGADs used to implement the double-LGAD concept have been mounted on the

Sensor	front-end board	Second stage amplifier
FBK15_1.3×1.3_15D FBK15_1.3×1.3_13D FBK15_1.3×1.3_17D FBK15_1.3×1.3_18D	V1.4-SCIPP-08/18	mini-circuit LEE39+
FBK20_1.3×1.3_18D FBK20_1.3×1.3_15D	V1.4-SCIPP-08/18	mini-circuit LEE39+
FBK25_1×1_5-2 FBK25_1×1_10-5 FBK25_1×1_9-3 FBK25_1×1_10-3	V1.4-SCIPP-08/18	mini-circuit Gali52+
FBK25_T4_1.3×1.3_10-1	V1.4-SCIPP-08/18	mini-circuit LEE39+
FBK35_1×1_8-5 FBK35_1×1_7-5 FBK35_1×1_10-3	V1.4-SCIPP-08/18	mini-circuit Gali52+
HPK50_W36_1.3×1.3_E HPK50_W36_1.3×1.3_F	V1.4-SCIPP-08/18	mini-circuit LEE39+
HPK50_W42_1.3×1.3_A HPK50_W42_1.3×1.3_B	V1.4-SCIPP-08/18	mini-circuit LEE39+
HPK50_1×3_4S	board w/o amplific.	C2

Table 5.2: Front-end board and amplifier used to test each LGAD.

same front-end board used for single LGADs, modified in order to place one LGAD on each side of the front-end board and, thanks to a via in the PCB itself, the output of the two LGADs were connected together and sent to the amplifier of the board followed by a mini-circuit, like it was for single sensors. The specific front-end board and amplifiers used for each LGAD are reported in Table 5.2.

For all the beam tests, a digital oscilloscope readout was used (see Section 5.1.2). Up to four amplified signals were sent to a Teledine LeCroy WaveRunner 9404M-MS

oscilloscope [88], with 20Gs/s sampling rate, 4 GHz of analog bandwidth and 8-bit vertical resolution. The whole signal waveforms were acquired and the digitization was done at the analysis level. The contribution of the oscilloscope time resolution to the measured one was negligible, allowing the direct study of the resolution of the sensors coupled to the front-end electronics. In some very recent tests, the oscilloscope readout was substitute by a full electronic chain, in order to study the performance of the sensors connected to the front-end and readout system, more details are reported in Appendix C.

5.2 Thin sensors

After the preliminary tests in the laboratory 4.4.4, all the thin detectors were tested using a particle beam in order to measure their performance. 25 µm- and 35 µm-thick sensors were initially tested and compared to a standard 50 µm-thick sensor mainly to observe the timing response of thinner LGADs with respect to a standard one 5.2.1. Following the encouraging results, even thinner sensors of a more recent production with a thickness of 15 µm and 20 µm were subsequently tested, and a comparison between the results obtained with sensors of all thicknesses is reported in Section 5.2.2. Many important quantities were extracted, including charge distributions, gain, electronics noise and jitter. A comprehensive analysis of the timing performance was finally carried out.

5.2.1 Going thinner: 25 µm- and 35 µm-thick FBK LGAD prototypes compared to a standard 50 µm-thick sensor

To investigate the potential of a thinner design for improved time resolution, a comprehensive study was done on 25µm- and 35 µm-thick sensors. Additionally, an HPK LGAD of a standard thickness of 50 µm was tested for comparison purposes with the thinner layouts [98].

Thanks to the oscilloscope readout, the completed signal waveforms were recorded and analyzed. For each taken run, the Constant Fraction Discriminator (CFD) method

was used to extract the Detectors Under Test (DUTs) time resolutions. Moreover, an offline study of the bandwidth has been released in order to optimize the time resolution; to filter-out the high-frequency noise, a smoothing of the LGAD signal was applied with a four-point moving average, thus reducing the effective bandwidth to 1 GHz (from the 4 GHz of the oscilloscope).

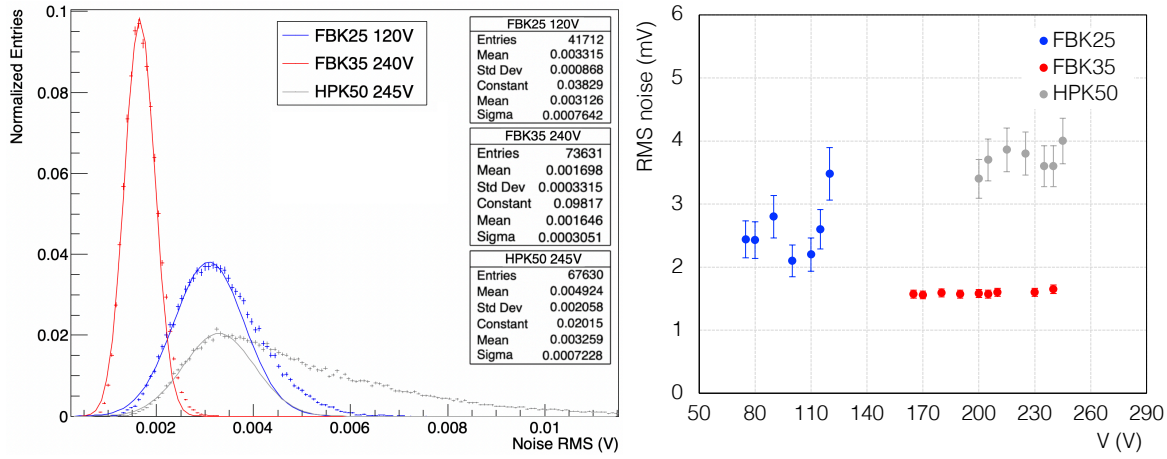

Figure 5.3: RMS noise spectra for the three different LGADs tested, where the distributions have been fitted with a Gaussian function (left). Mean values of the RMS noise as a function of the applied voltage (right). (External gain amplification factors not removed).

To evaluate the noise of each DUT, its RMS has been evaluated; in particular for the analysis offline a time window before the signals has been considered in order to have a direct measurement of the noise in the beam test setup. In Figure 5.3 (left) the RMS spectra are reported for sensors of different thickness. As can be seen, FBK35 has a lower noise with respect to FBK25. The distribution reported in the figure for FBK25 and FBK35 have a Gaussian shape, with only a moderate non-gaussian right tail that instead is much more pronounced for HPK50 [99]. The distribution mean of the three DUTs is quite stable throughout all the data taking, ranging between 1 mV and 4 mV (Figure 5.3 (right)).

In Figure 5.4 the measured charge distributions are shown for particles traversing perpendicularly to the detector surface. The ratio between the width of the distributions and the Most Probable Values (MPVs) decreases as a function of the thickness. Instead, as expected, the amplitude increases both as a function of the thickness and voltage;

moreover the decreasing ratio between the width and the MPV of the distributions, indicates that the fluctuations in the number of electrons-holes created in the silicon detector decrease with larger thickness, in accordance with results obtained in Refs [100, 101].

To extract the time resolution of a single LGAD ($\sigma_{i=1,3}$), a system with three sensors and three differences between the arrival time of each pair of detectors has been considered. In particular, the sigma values extracted from the q-Gaussian functions used to fit the measured time difference distributions between each LGADs pair (σ_{12}, σ_{23}, σ_{13}) were used following the relations:

$$\begin{cases} \sigma_{12}^2 = \sigma_1^2 + \sigma_2^2 \\ \sigma_{23}^2 = \sigma_2^2 + \sigma_3^2 \\ \sigma_{13}^2 = \sigma_1^2 + \sigma_3^2 \end{cases} \implies \begin{cases} \sigma_1 = \sqrt{\dfrac{\sigma_{12}^2 + \sigma_{13}^2 - \sigma_{23}^2}{2}} \\ \sigma_2 = \sqrt{\dfrac{\sigma_{12}^2 + \sigma_{23}^2 - \sigma_{13}^2}{2}} \\ \sigma_3 = \sqrt{\dfrac{\sigma_{13}^2 + \sigma_{23}^2 - \sigma_{12}^2}{2}} \end{cases} \tag{5.1}$$

In Figure 5.5 an example of the time difference between FBK35 and FBK25 is reported with a CFD of 70%. The distribution has been fitted with an asymmetric q-Gaussian function to take into account that the arrival time distribution for a single sensor has a Gaussian shape with a small tail towards late times. The sigma (σ_{12}, σ_{23}, σ_{13}) extracted from the fit has then been used to obtain the final time resolution (σ_1, σ_2, σ_3) of the three LGADs at a given voltage and CFD.

Since our experimental setup allows measuring four sensors at a time, it is possible to build four different systems with three equations having as unknowns the time resolutions of the four sensors under test, thus the final results were obtained considering all the possible triplets of sensors and the mean of the four values obtained was used to asses the time resolution of each sensor.

An example of the values extracted for four sensors in a given run configuration can be seen in Figure 5.6, where the three values obtained for each point are reported.

Figure 5.7 reports the final measured time resolutions for 25 µm- and 35 µm-thick

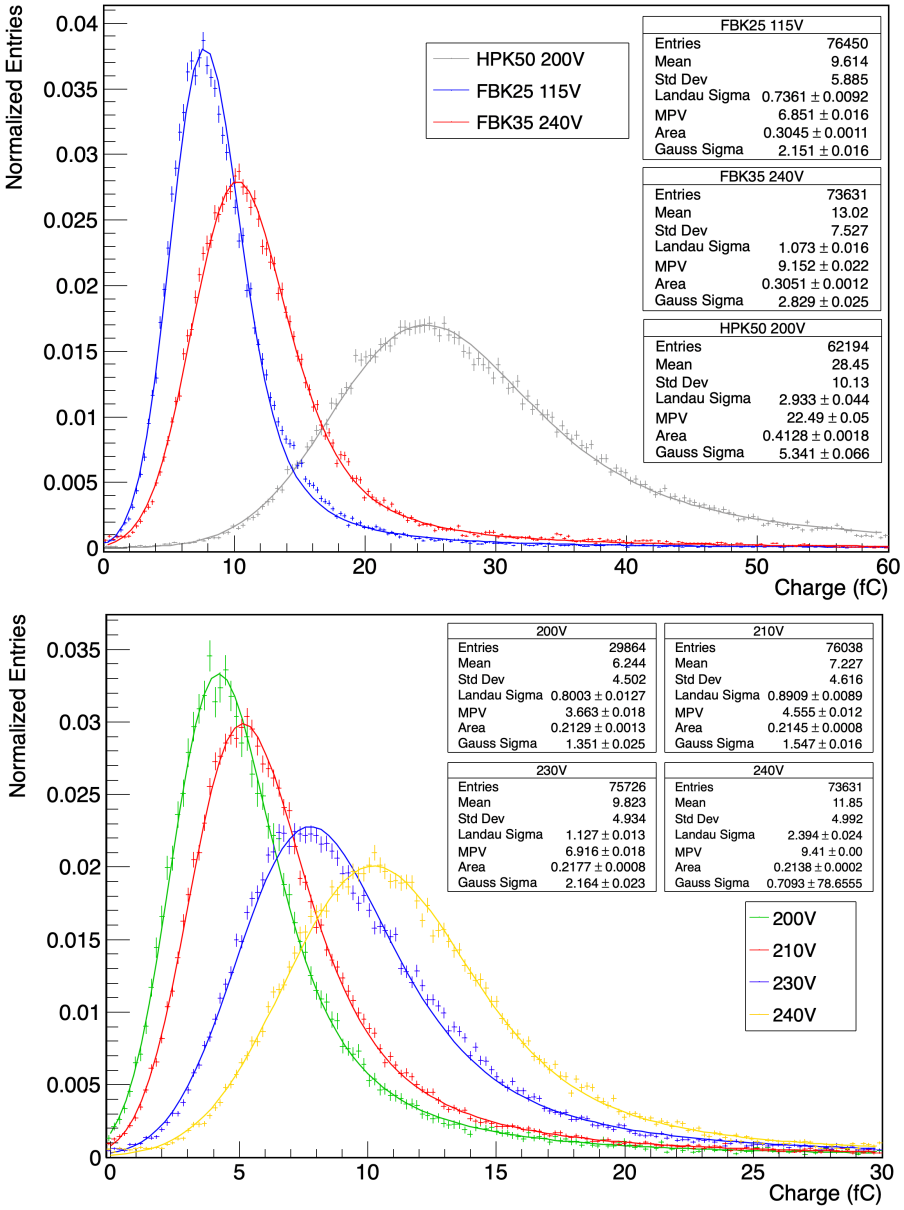

Figure 5.4: Charge distributions obtained for the three thicknesses at a similar gain of $\sim$ 30 for FBK25 and FBK35 and $\sim$ 45 for HPK50 (top). Charge distribution for FBK35 as a function of different applied voltages (bottom). All the amplifications factors were removed from the distributions. The distributions are fitted with a convolution of a Gaussian and a Landau functions.

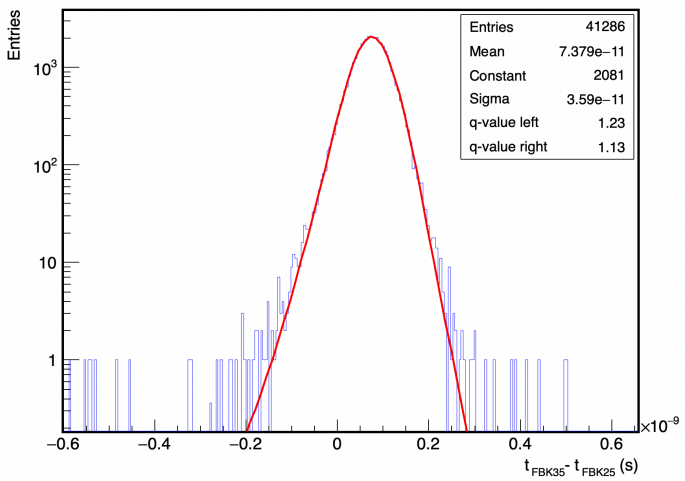

Figure 5.5: Time difference distribution between FBK35 and FBK25 samples, operated respectively at 240 V and 120 V, and with a CFD of 70%. The extracted time resolutions is in this case around 25 ps for both the LGAD sensors. The distribution has been fitted with a q-Gaussian function. In this example, the tails account for the 2.5% of the measures.

LGADs as a function of the CFD threshold for all the applied voltages. For HPK50 the trend and values are totally in agreement with the ones reported in [102, 103] for a 50 µm-thick LGAD.

As expected, the time resolution improves with higher voltages [81]. The trend as a function of the CFD reflects the higher jitter contribution for very low CFD (smaller slew rates) [81]. At higher CFD instead the time resolution is dominated by the Landau term, which is due to the non-uniform creation of electron–hole pairs along the particle path and which is expected to be smaller for thinner detectors. These contributions, in turn, depend on the thickness, S/N and slew rate; these contributions are affected both by electronics and detector, but also by their coupling and their shielding against outer noise [81]. The trend of the measured values as a function of the CFD flattens for values larger than around 30% and 20%, respectively for FBK25 and FBK35 sensors. The S/N ratio has then been evaluated for all the DUTs considering the MPV of the distribution obtained by taking for each acquired waveform the maximum amplitude of the signal divided by the noise RMS evaluated in a window before the signal; values between 6-24 and 16-63 (at low and high applied voltage) for FBK25 and FBK35 sensors have been

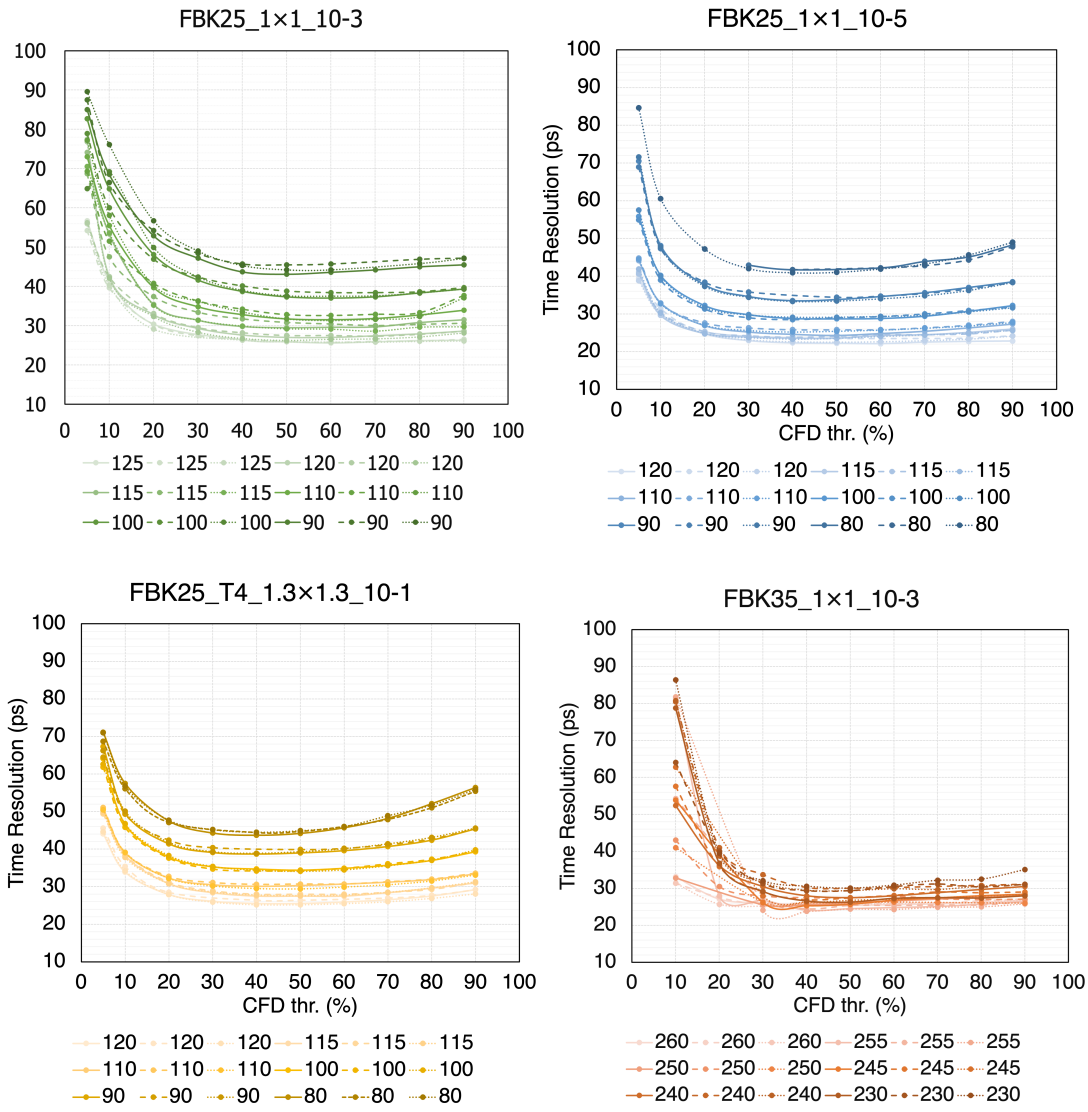

Figure 5.6: Example of sigma values extracted for four sensors (σ_1, σ_2, σ_3, σ_4) in a given run configuration. 3 values were obtained for each point by considering all possible triplets of sensors (e.g. the σ_1 could be extracted considering sensor triplets {1-2-3}, {1-2-4}, {1-3-4}). The values corresponding to different systems are connected by solid, dashed, and dotted lines. The mean (Figure 5.7) of these three lines was used to determine the final time resolution of each DUT.

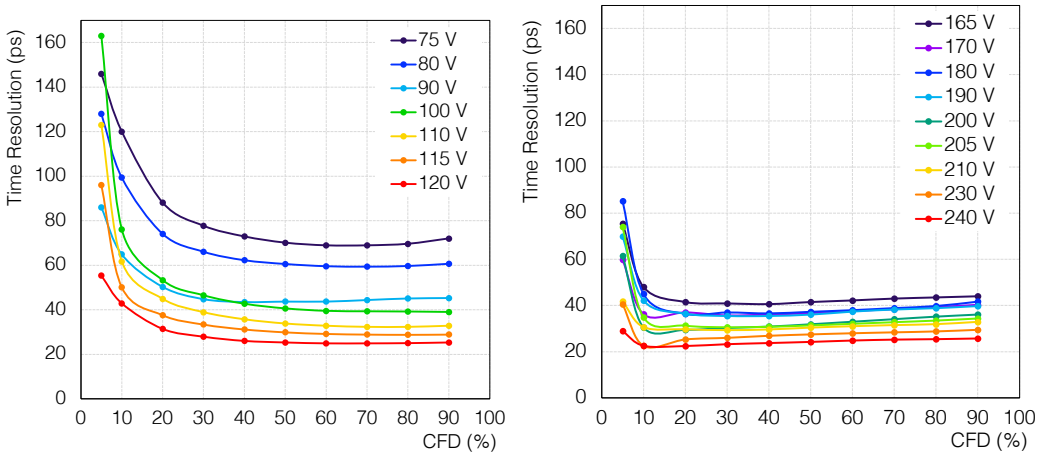

Figure 5.7: Measured time resolution versus the CFD threshold for several applied voltages for FBK25 (left) and FBK35 (right). The errors have been estimated to be around 10% of the measured value for CFD between 20% and 80% (not shown in the plots for better visibility).

found, respectively. The jitter σ_{jitter} has been evaluated for each DUT and each CFD threshold using the Equation (2.36) and the intrinsic time resolution $\sigma_{\text{intrinsic}}$ has been extracted by means of:

$$\sigma^2_{\text{intrinsic}} = \sigma^2_{\text{measured}} - \sigma^2_{\text{jitter}}, \tag{5.2}$$

where the σ_{measured} is the one coming from Equations 5.1. In Figure 5.8 the measured time resolutions for a fixed CFD (the one that optimizes the time resolution) are reported as a function of charge (left) and drift electric field (right) for the three DUTs (see Section 4.3.2) for the drift electric field calculation. The time resolution improves with larger charge (as expected due to larger gain) and drift electric field (as expected due to both larger gain and higher velocity of carriers in the drift region).

In Figure 5.9 the measured and intrinsic time resolutions for a fixed CFD are reported as a function of gain (left) and voltage (right). The upper limit for the percentage error is of 10%[1].

[1]The error was estimated by considering multiple factors. The primary source of uncertainty was determined by analyzing repeated data runs using the same sensors and system - i.e., identical front-end electronics, amplifiers, and setup configuration - while applying a consistent analysis procedure to extract the time resolution and considering the variation between the highest and lowest values of the

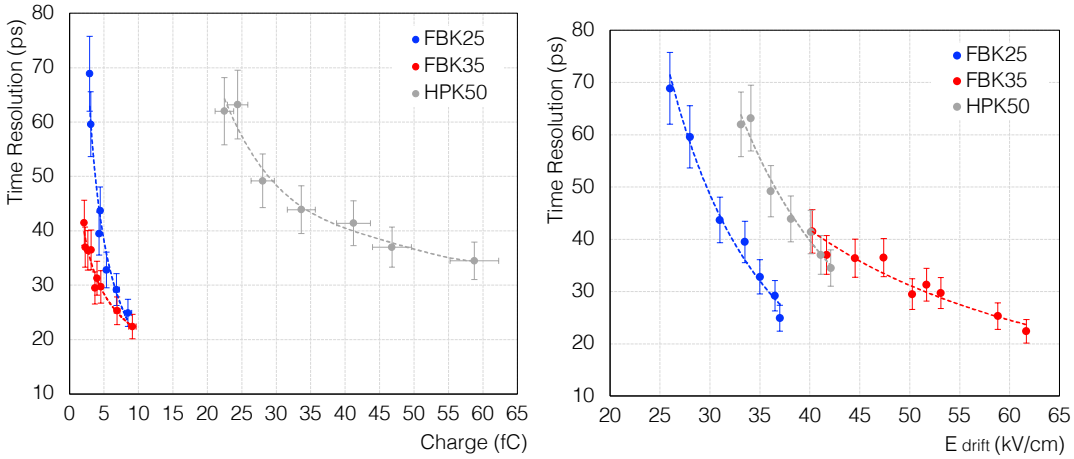

Figure 5.8: Measured time resolution from the beam test as a function of the charge (left) and drift electric field E_{drift} (right) for all the LGADs: FBK25, FBK35 and HPK50 for a CFD of 60%, 20% and 50%, respectively. The errors for the measured time resolution have been estimated as 10% of the value. The lines are included to guide the eye.

In the figure, the three sensors with different thicknesses are compared. As expected, the time resolution improves for higher gain (voltages) for all the detectors.

A time resolution of $\sim$ 34 ps has been measured for HPK50, which confirms previous results [102, 103]. As expected, a better time resolution has been reached with the two thinner LGADs due to a smaller Landau term. FBK35 sensor reaches a time resolution of 22 ps at a bias voltage of 240 V, in agreement with the expectation (see Figure 4.1). FBK25 reaches a time resolution of 25 ps at a bias voltage of 120 V. This result does not show an improvement with respect to FBK35, as FBK25 sensors have been produced

time resolution obtained. Based on this, an error of 3–5% was found for CFD values between 30 and 90%, whereas a larger error, up to 9%, was observed for CFD values between 10 and 20%. Additionally, a systematic error arising from variations in the analysis procedure was added in quadrature. This was assessed by systematically modifying analysis parameters, such as reducing the waveform bandwidth offline and extracting the time resolution using different fitting methods, including Gaussian fits over the full range and in a restricted range, or q-Gaussian fits. Furthermore, the measurements and analysis were repeated using a different beam energy (5–10 GeV). All of these contributed for a maximum of 1% to the overall uncertainty. In the end, the total error was taken as the maximum sum of the individual contributions, among the different CFD, resulting in an upper-bound error of 10%. This procedure was used to estimate the errors for all the measurements reported in this thesis

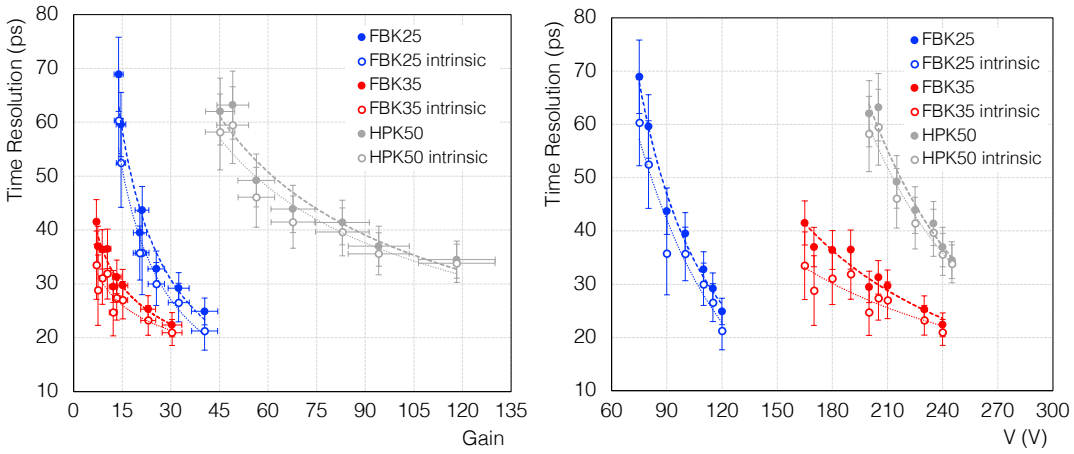

Figure 5.9: Measured (full circle) and intrinsic (empty circle) time resolution from the beam test as a function of the gain (left) and applied voltage (right) for all the LGADs: FBK25, FBK35 and HPK50 for a CFD of 60%, 20% and 50%, respectively. The errors for the measured time resolution are estimated to be around 10% of the value; the error on the gain are estimated to be around the 10% of the value. The lines are to guide the eye.

	Voltage applied	Gain	Time resolution
FBK25	120 V	40 ± 4	(25 ± 3) ps
FBK35	240 V	30 ± 3	(22 ± 2) ps
HPK50	245 V	118 ± 11	(34 ± 3) ps

Table 5.3: Time resolution for FBK25, FBK35 and HPK50 for a given voltage (or gain) obtained in a beam test setup at room temperature.

on a highly doped substrate, not optimized for timing measurements; the low resistivity bulk increases the noise from the sensor, resulting in a worse S/N ratio (see Figure 5.27) worsening the time resolution. However, the measurements of the two samples FBK25 and FBK35, although compatible within the uncertainties, have a trend towards better results for FBK35 w.r.t. FBK25.

In Table 5.3 the best time resolutions reached for the three detectors tested are summarized.

Finally the results have been also compared with simulation from WeightField2 [85]. In Figure 5.10 the measured time resolution obtained for all the LGADs is reported as a

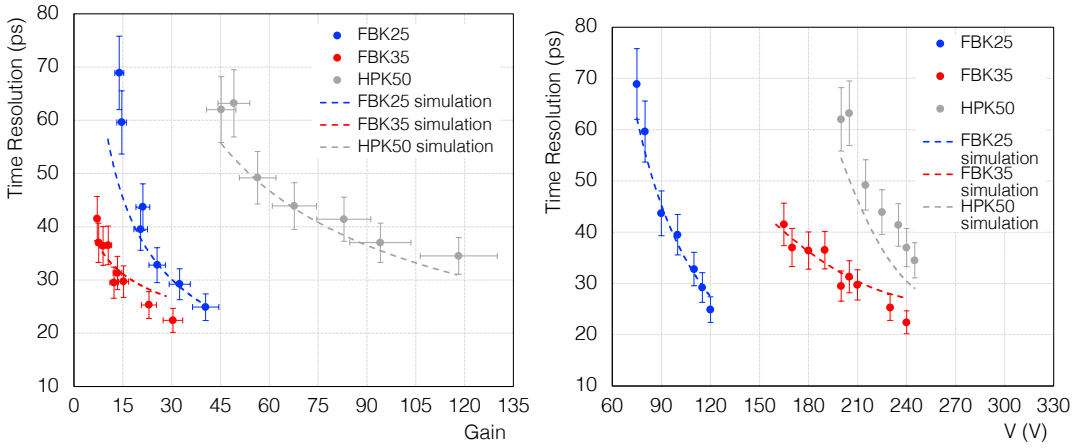

Figure 5.10: Measured (circle) and simulated (dotted lines) time resolution results from the beam test and simulation with WeightField2, as a function of the gain (left) and the applied voltage (right) for all the LGADs: FBK25, FBK35 and HPK50 for a CFD of 60%, 20% and 50%, respectively. The errors for the measured time resolution have been estimated as 10% of the value; the error on the gain has been estimated as the 10% of the value.

function of gain (left) and applied voltage (right) and compared with the one obtained from simulation, using WF2, as reported in Section 4.3.2.3. The timing capabilities were evaluated applying the CFD method, using the same threshold adopted for the measured data. The time resolution of the different LGAD has been calculated by choosing the parameters of the simulation in order to reproduce the signal waveforms obtained at the beam test by the sensors connected to the electronics. This procedure has been tuned for one bias point for each of the three sensors and then extended to the others. Rather than comparing absolute values, in this way it is possible to compare the trend of data with what expected from the simulation with WF2. For all sensors, a good agreement between data and ad hoc tuned simulation has been obtained. As shown in the figure, the simulation reproduces accurately the evolution of the time resolution with gain and bias voltage.

5.2.2 15, 20, 25, 35, 50 µm-thick LGADs: uniformity and comparison

Tests performed so far confirmed that a thinner LGAD design allows to improve the time resolution. For this reason even thinner sensors, with a thickness of 15 µm and 20 µm, were studied. All the sensors were tested in the same conditions. In this section the more important results for all the LGADs tested will be reported. A comparison between sensors with all the thicknesses, from the standard 50 µm down to 15 µm is finally shown.

In Figures from 5.11 to 5.15 the measured time resolutions are reported for each of the different thicknesses as a function of the applied voltage, gain and drift electric field E_{drift} for a fixed CFD. In each plot, different prototypes of the same thickness are compared to each-other. Except for few prototypes, the plots show a similar trend for the sensors belonging to the same wafer between 20 µm, 35 µm and 50 µm of thickness (note that for the 50 µm two different wafers, with a different doping concentration, are reported, so, also in this case, the trend is compatible for sensors of the same wafer). For the 15 µm- and 25 µm-thick sensors instead, the resolutions have a less uniform trends. The differences in the trends can be related to a doping concentrations different from the expectations, it would be interesting repeating the measurements on another production with the same thickness. In the last two plots of each figure, the RMS of the noise and the S/N ratio are also compared as a function of the applied voltage. For all the thicknesses, the RMS of the noise is always between 1 and 4 mV. The S/N ratio is similar between sensors of the same thickness at the same voltage, but it increases with increasing thickness, reaching values between 2 and 20 for the 15 µm-thick LGADs and between 25 and 130 for the 50 µm-thick LGADs. This is expected by having a larger charge production within thicker sensors.

A final comparison between one sensor for each thickness tested (15, 20, 25, 35, 50 µm) is shown in Figure 5.16 as a function of the applied voltage and gain for a fixed CFD, and the best reached time resolution is reported as a function of the sensor thickness in Figure 5.17. The trend of the time resolution is very different between the different thickness, except for the 15 µm: all the sensors thinner that the standard 50 µm show

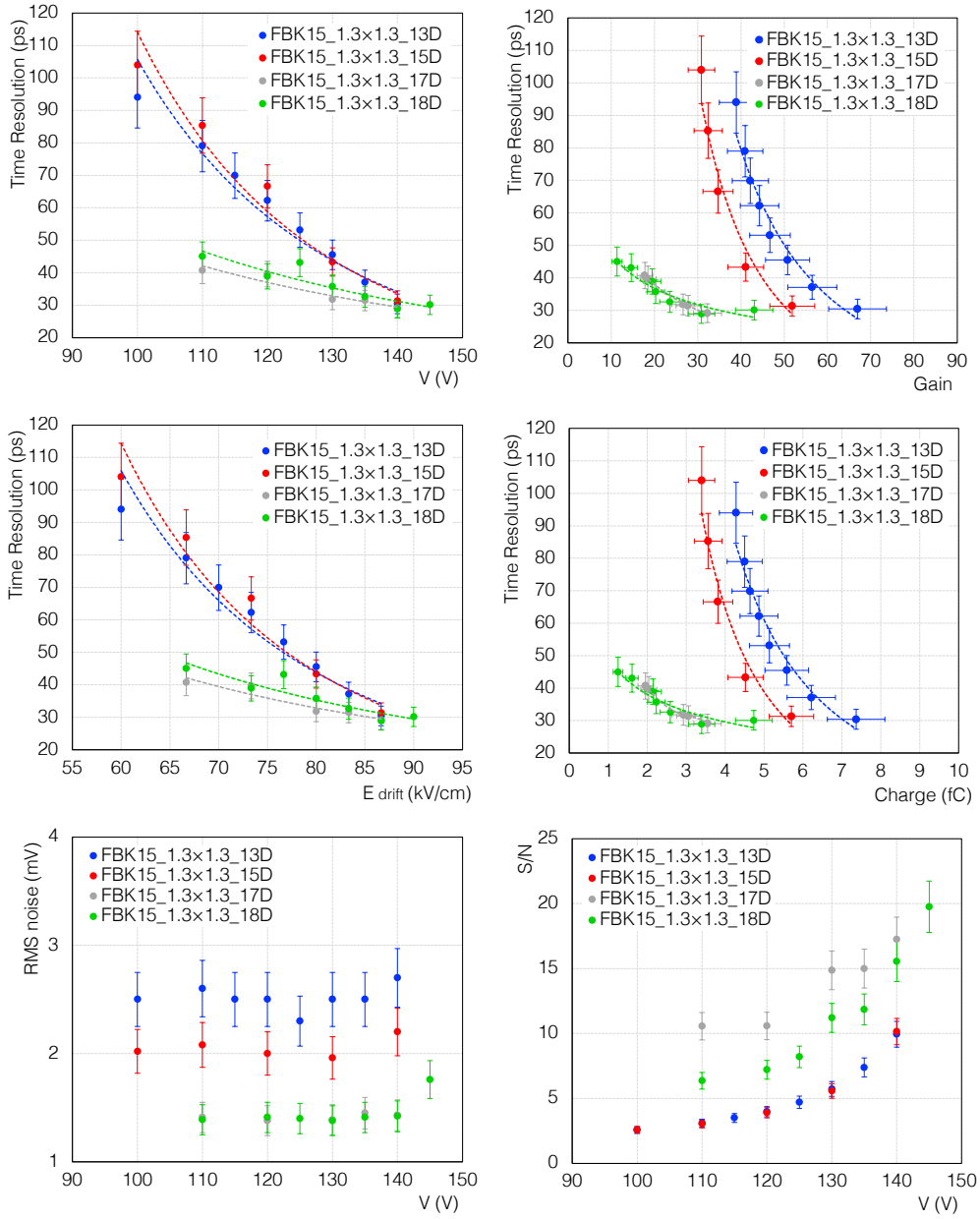

Figure 5.11: Measured time resolution as a function of the applied voltage, gain, drift electric field E_{drift} and charge for different prototypes of 15 µm-thick LGADs for a CFD of 60%, 60%, 50% and 50%, respectively from the first one to the last sensor in the legend. The errors for the measured time resolution, gain and charge have been estimated as 10% of the value. The lines are included to guide the eye. In the last two plots, the RMS of the noise (external gain amplification factors not removed) and the S/N ratio are reported as a function of the applied voltage.

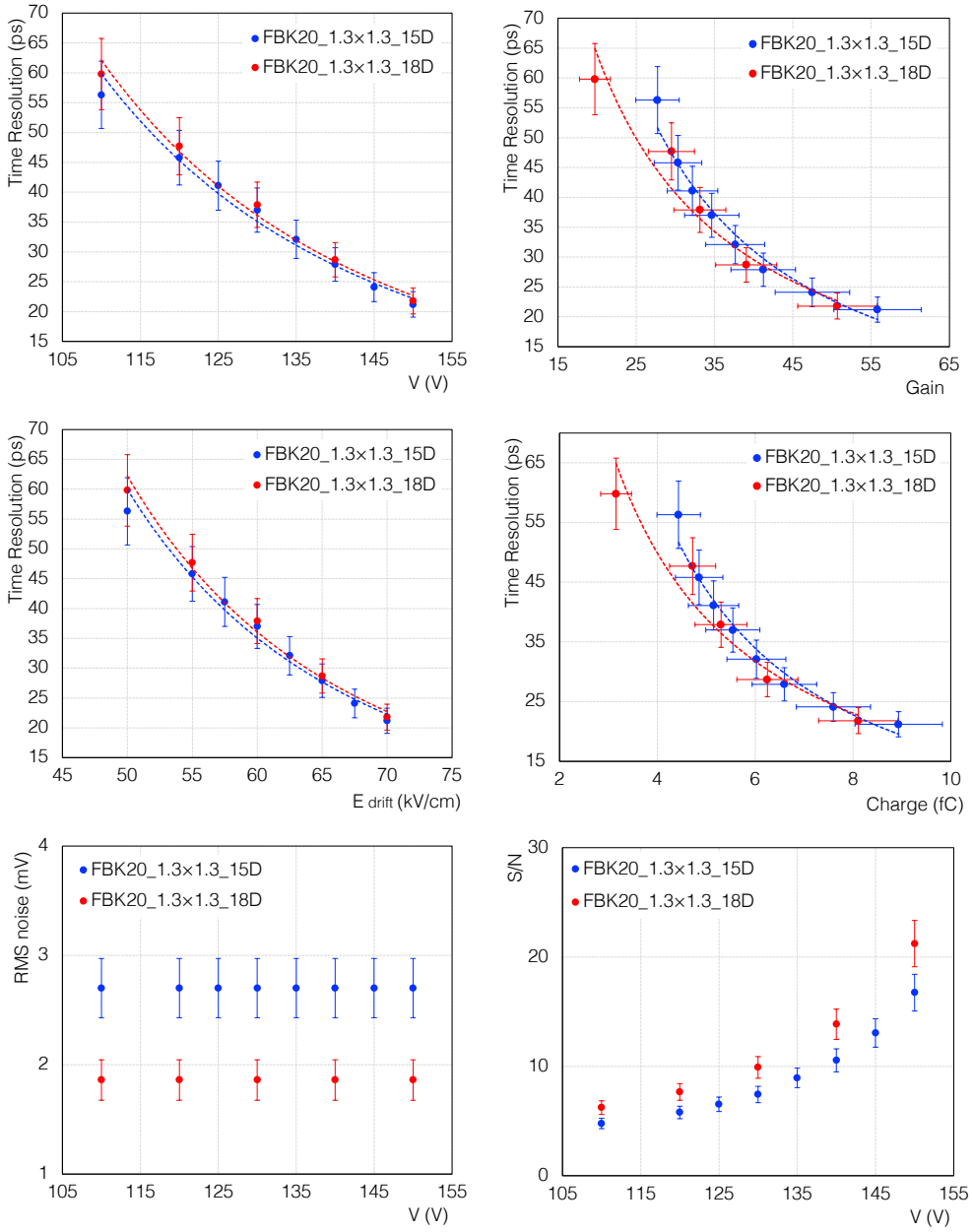

Figure 5.12: Measured time resolution as a function of the applied voltage, gain, drift electric field E_{drift} and charge for different prototypes of 20 µm-thick LGADs for a CFD of 60%. The errors for the measured time resolution, gain and charge have been estimated as 10% of the value. The lines are included to guide the eye. In the last two plots, the RMS of the noise (external gain amplification factors not removed) and the S/N ratio are reported as a function of the applied voltage.

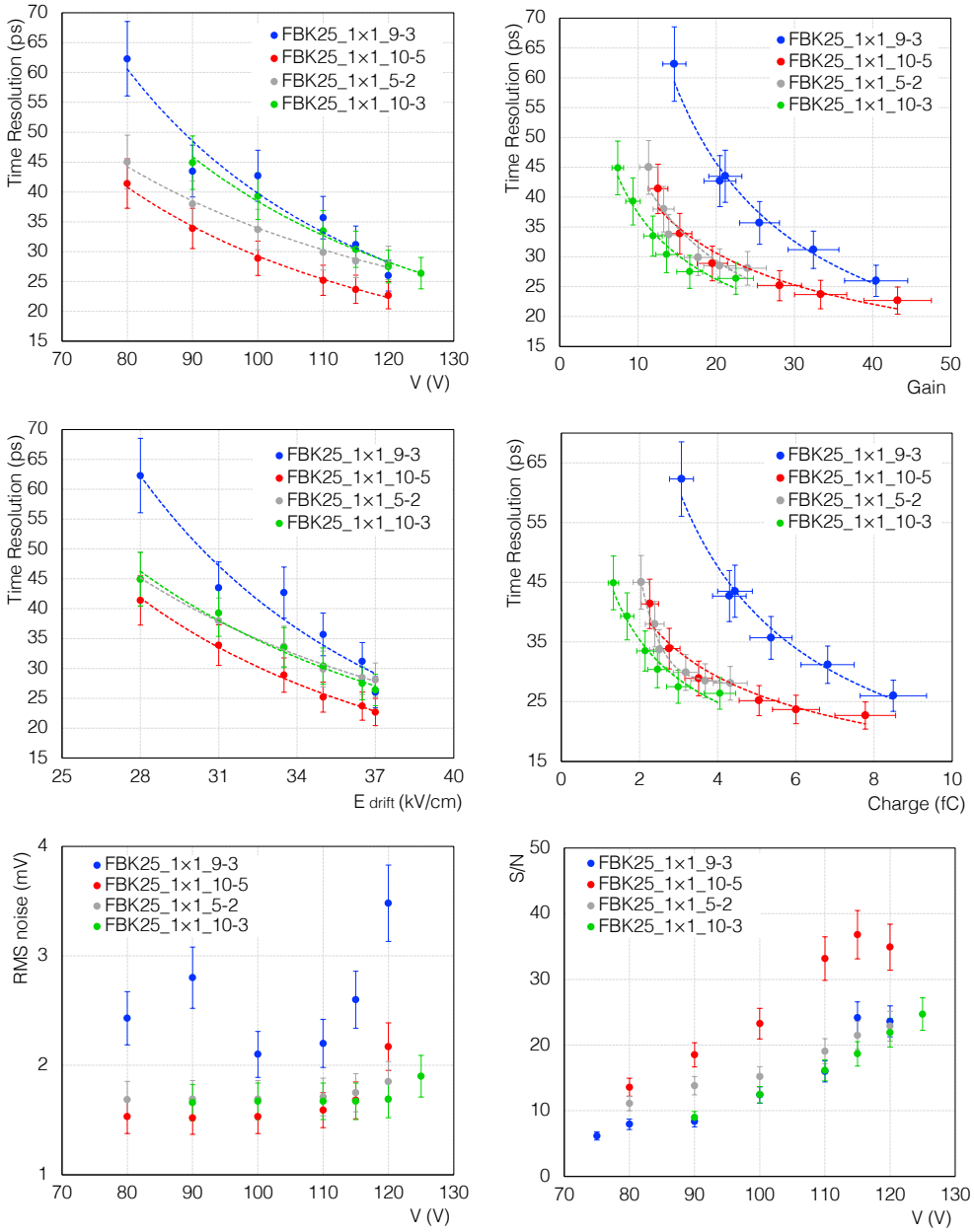

Figure 5.13: Measured time resolution as a function of the applied voltage, gain, drift electric field E_{drift} and charge for different prototypes of 25 µm-thick LGADs for a CFD of 40%. The errors for the measured time resolution, gain and charge have been estimated as 10% of the value. The lines are included to guide the eye. In the last two plots, the RMS of the noise (external gain amplification factors not removed) and the S/N ratio are reported as a function of the applied voltage.

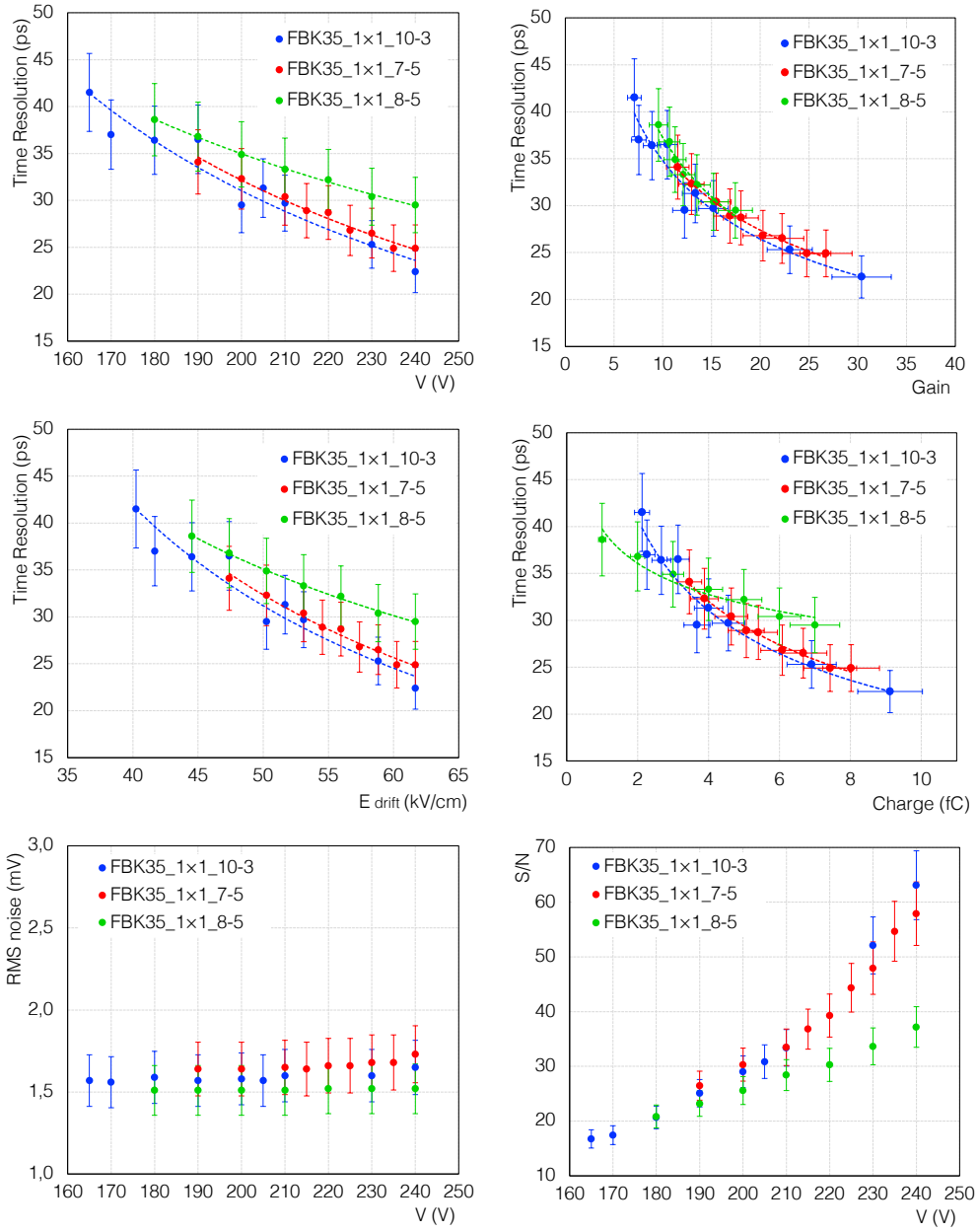

Figure 5.14: Measured time resolution as a function of the applied voltage, gain, drift electric field E_{drift} and charge for different prototypes of 35 µm-thick LGADs for a CFD of 20%, 30%, 30%, respectively from the first one to the last sensor in the legend. The errors for the measured time resolution, gain and charge have been estimated as 10% of the value. The lines are included to guide the eye. In the last two plots, the RMS of the noise (external gain amplification factors not removed) and the S/N ratio are reported as a function of the applied voltage.

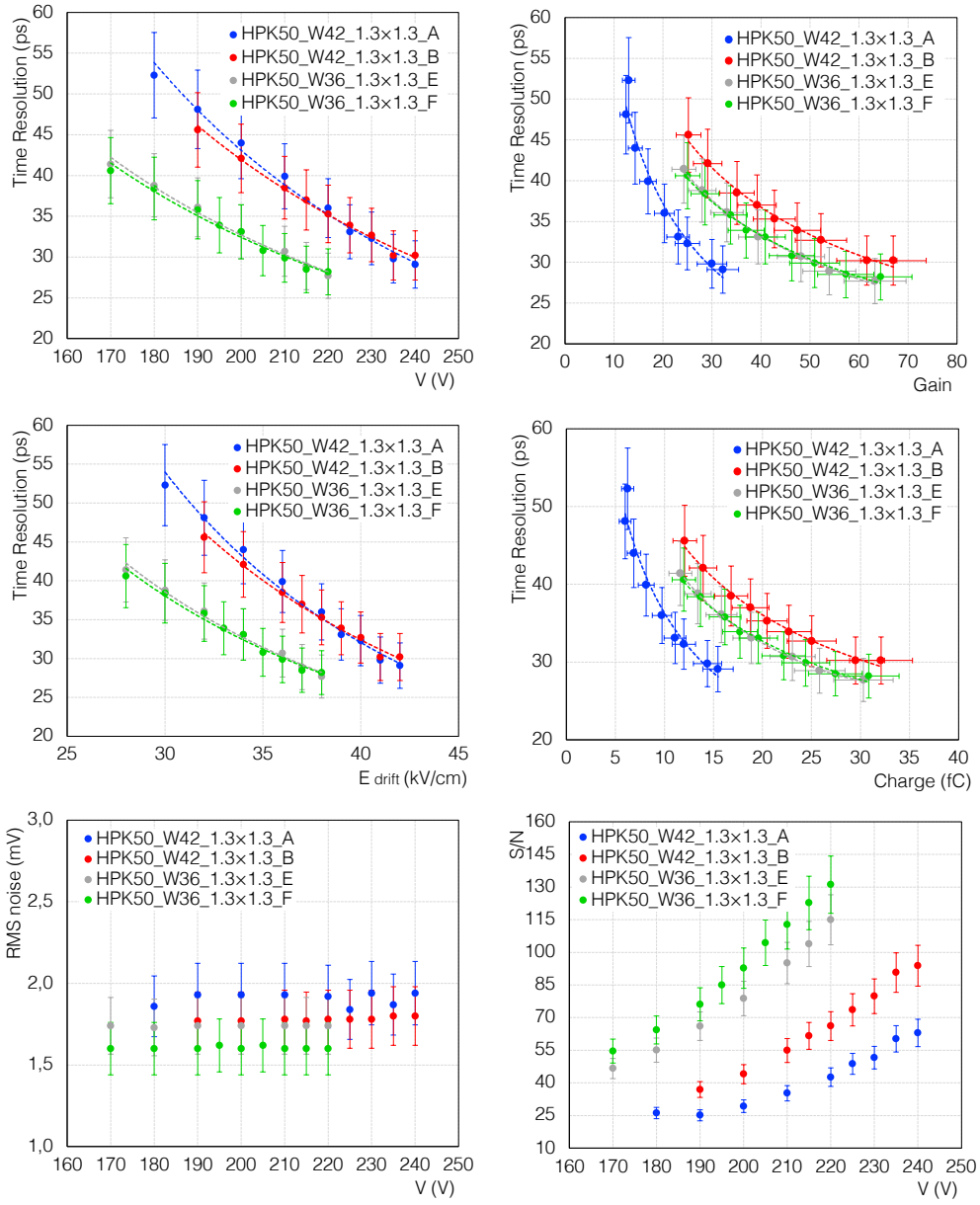

Figure 5.15: Measured time resolution as a function of the applied voltage, gain, drift electric field E_{drift} and charge for different prototypes of 50 µm-thick LGADs for a CFD of 30%, 60%, 30% and 30%, respectively from the first one to the last sensor in the legend. The errors for the measured time resolution, gain and charge have been estimated as 10% of the value. The lines are included to guide the eye. In the last two plots, the RMS of the noise (external gain amplification factors not removed) and the S/N ratio are reported as a function of the applied voltage.

a better time resolution. The behavior of the 15 µm-thick LGAD might be affected by that of the front-end board, which was not optimized individually for the different thicknesses. Indeed, with such small and fast signals, the contribution of the electronics and so its optimization, becomes more and more important.

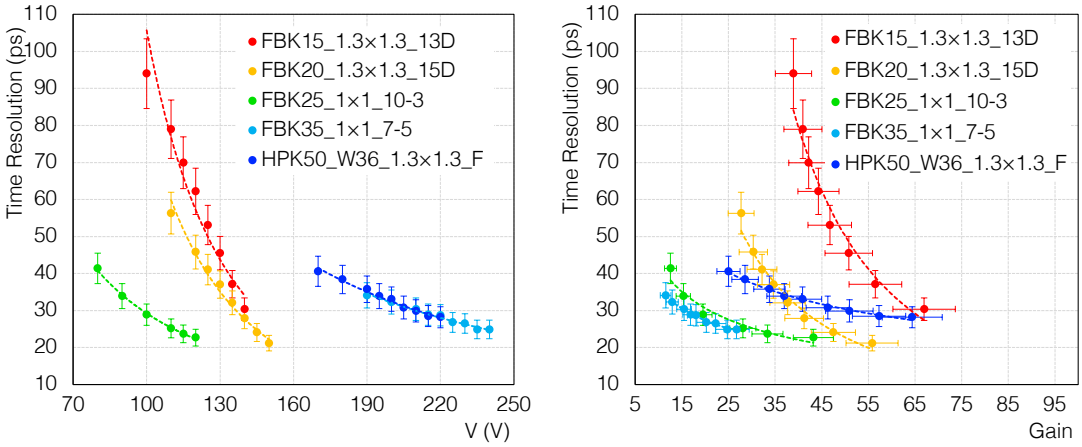

Figure 5.16: Comparison between the measured time resolution of all the thickness: 15, 20, 25, 35, 50 µm as a function of the applied voltage and gain for a CFD of 60%, 60%, 50%, 30% and 30%, respectively. The errors for the measured time resolution and gain have been estimated as 10% of the value. The lines are included to guide the eye.

Finally, a summary plot of time resolution as a function of both gain and drift electric field is reported in Figure 5.18 for the LGADs tested. As expected [104], it indicates that to obtain a good time resolution a combination of both gain and drift electric field is necessary.

For completeness, comparing these results with the time resolution found with the laser setup (Section 4.4.4), trends are in a good agreement. Indeed, while some differences are present considering the time resolutions as a function of the gain, for the time resolution as a function of the voltage, the values are almost compatible within the errors, assuring that the laser setup was properly tuned to simulate the passage of a MIP inside the detector.

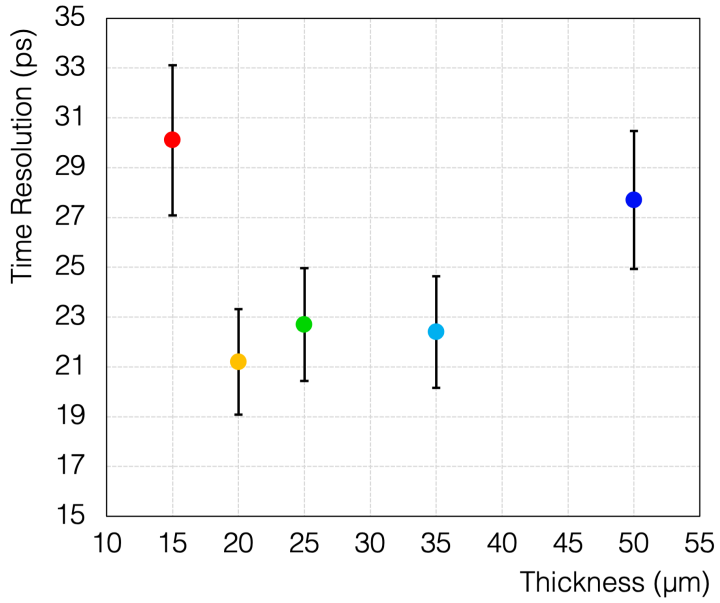

Figure 5.17: Comparison between the best measured time resolution of all the thicknesses: 15, 20, 25, 35, 50 µm. The errors for the measured time resolution have been estimated as 10% of the value.

5.2.3 Thin LGAD matrices

Tests with a particle beam were done also on the FBK25_T4_1.3×1.3_10-1 matrix, in order to understand any possible difference with respect to the single sensors. Here some results are reported in comparison to a single 25 µm-thick LGAD connected and tested in the same conditions.

From Figure 5.19 it can be seen that the noise of the matrix was comparable to the one of the single sensor within the errors. The time resolution of the matrix pad is then reported in Figure 5.20 as a function of the CFD percentage for all the voltages. A final comparison between the matrix and the single sensor is shown in Figure 5.21 where the time resolution is plotted as a function of the applied voltage, gain and electric field. The time resolution for one pad of the matrix is totally comparable with the one of a single sensor. The systematic slightly higher values of the matrix can be due to the higher capacitance (larger area).

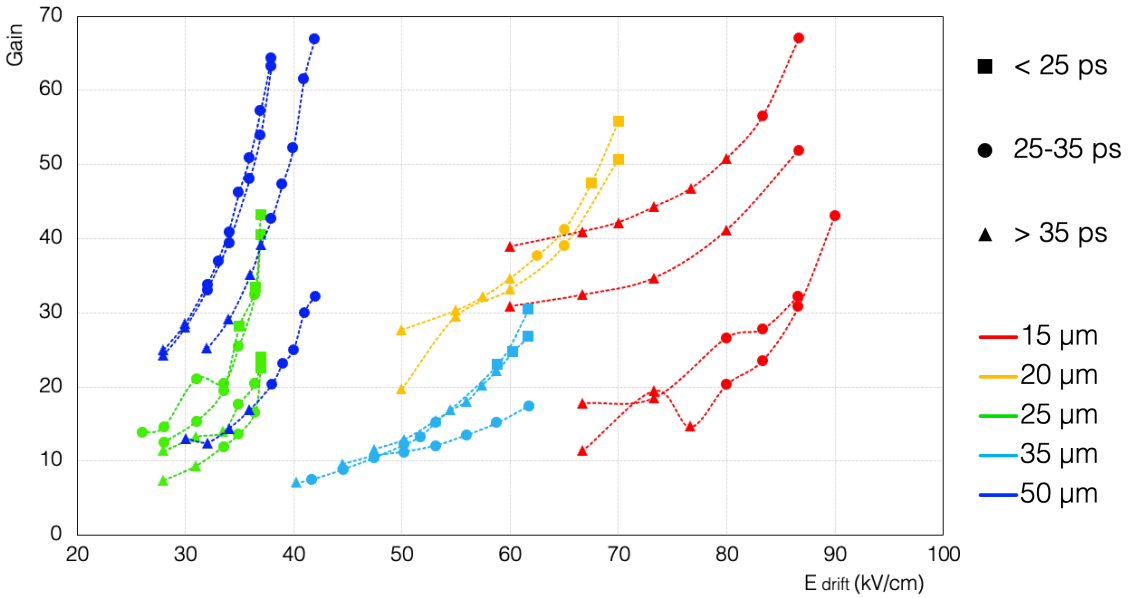

Figure 5.18: Measured time resolution for the chosen CFD as a function of gain and drift electric field E_{drift} for all the sensors and thicknesses. Each line joins the measurements of a given sensor, with the colors indicating the thickness; the marker shapes refer to a given time resolution interval.

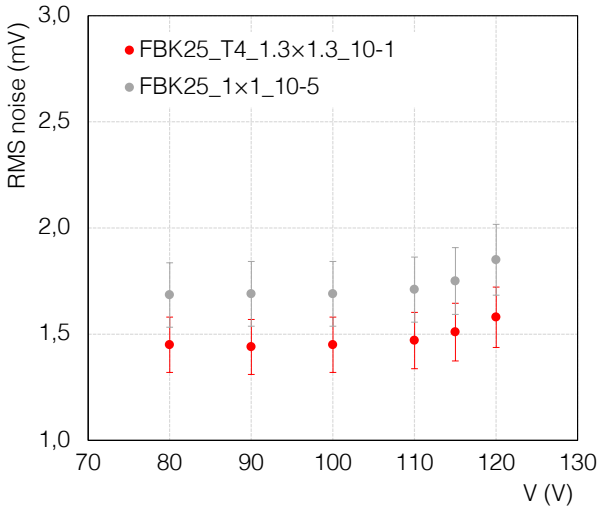

Figure 5.19: RMS of the noise as a function of the applied voltage for a pad of an LGAD matrix in red and for a single LGAD of the same thickness in grey. (External gain amplification factors not removed)

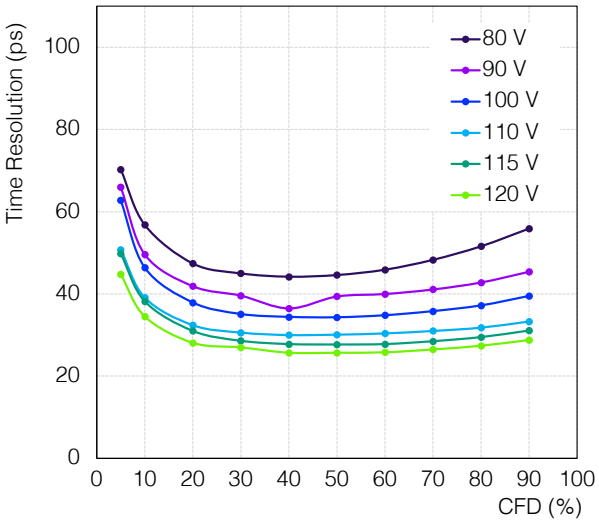

Figure 5.20: Measured time resolution results of FBK25_T4_1.3×1.3_10-1 pad as a function of the CFD percentage for all the applied voltages.

5.3 The double-LGAD concept

The new concept of double-LGAD (see Section 4.3.1.6) was tested in a beam test setup for the first time in July and November 2022 [105]. This approach is expected to bring the significant benefit of an enhancement of the charge at the input of electronics and also an improvement in overall time resolution.

For all the measurements reported hereafter, the double LGAD has always been compared with the performances of the two single LGADs composing the d-LGAD under test.

In Figure 5.22 the measured charge distributions are shown. Notice that, the comparisons between single and the double LGADs have been done at a fixed gain. The d-LGAD always showed a MPV for the charge distribution double that of the single one, as naively expected, demonstrating the success of a so-built detector and, as a consequence, the potentially less demanding electronic front-end that can be used, thanks to the larger charge in input.

From the charge distribution, it was also possible to estimate the quality of the

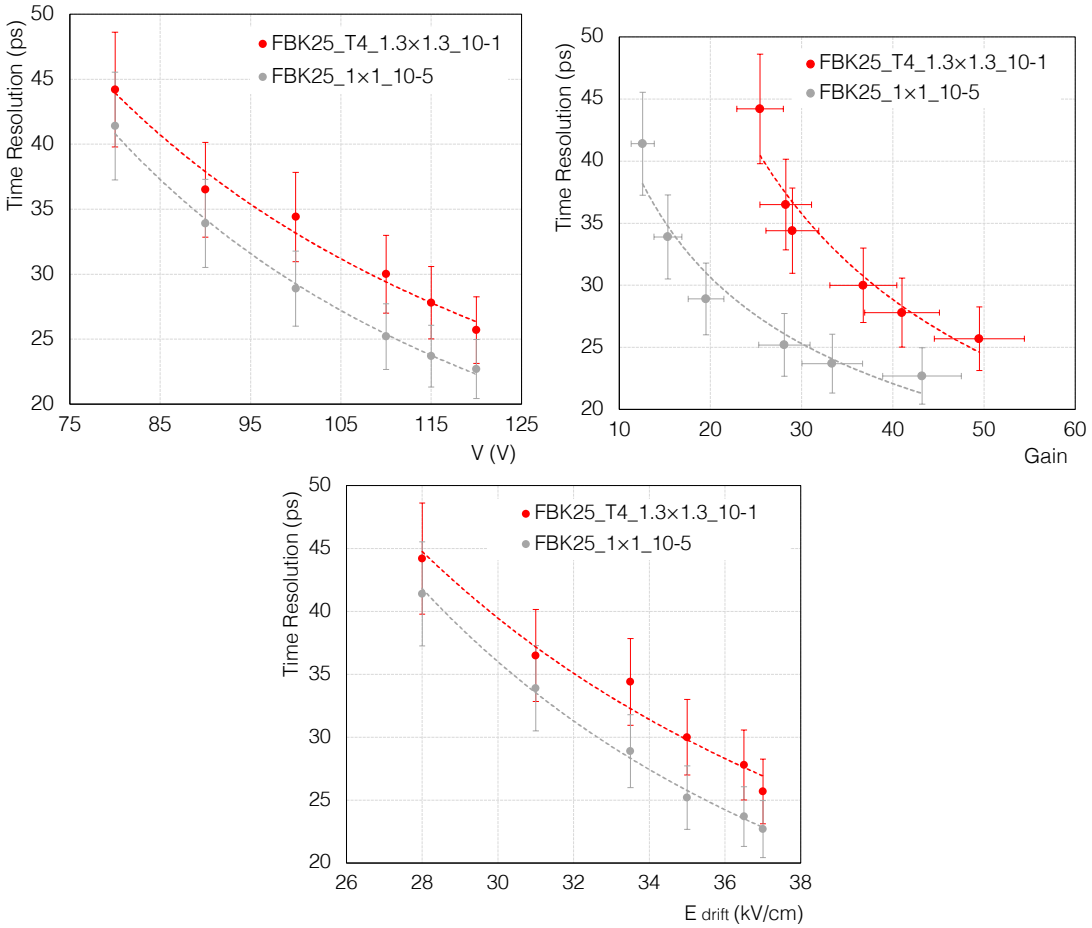

Figure 5.21: Measured time resolution results from the beam test as a function of the voltage, gain and the drift electric field E_{drift} for a pad of an LGAD matrix in red and for a single LGAD in grey of the same thickness with a CFD of 40%. The errors for the measured time resolution have been estimated as 10% of the value. The lines are included to guide the eye.

alignment between the sensors on the two sides of the front-end board.

When attaching the two single sensors, a small misalignment between the two LGADs, as shown in Figure 5.23, can result in particles passing through one sensor without traversing the other in some events. In such cases, the charge deposited by the particles shows a peak corresponding to the charge collected by a single sensor. To study this effect, values were randomly generated following a Landau distribution with the charge MPV taken from the measured data. Different levels of overlap between the two sensors were

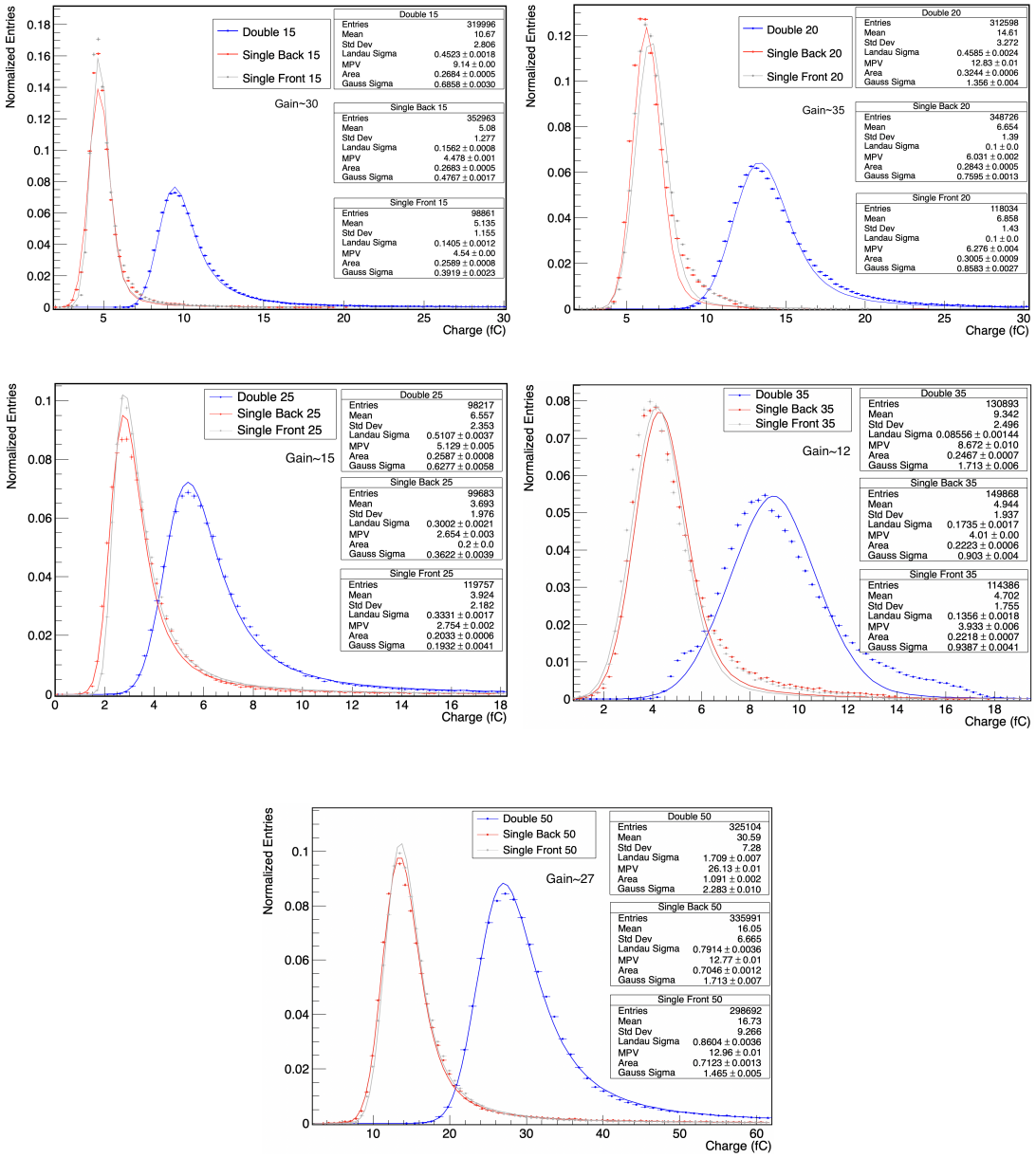

Figure 5.22: Charge distributions for all the DUTs at a gain of 30, 35, 15, 12 and 27 for FBK15, FBK20, FBK25, FBK35 and HPK50 couples, respectively. The values of the gain was chosen in order to have a measured value of voltage corresponding to the same gain for the single LGAD and d-LGAD of each thickness. The distributions are normalized and fitted with a convolution of a Gaussian and a Landau functions.

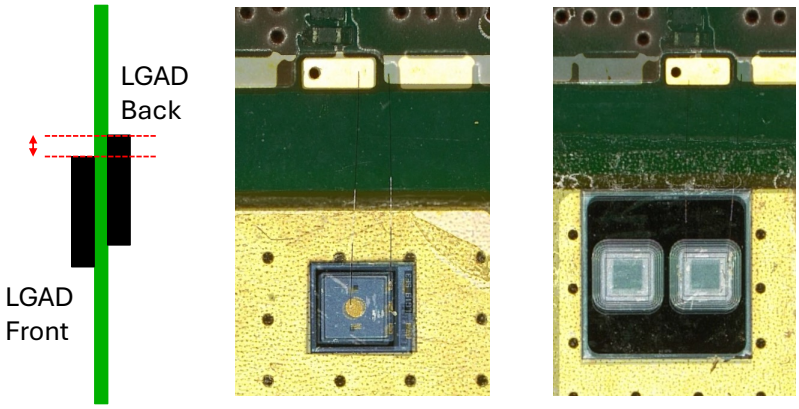

Figure 5.23: Picture showing the misalignment of two sensors (left) and examples of alignment between the sensor in the front and in the back for two different double-LGADs (center and right). In each of the two pictures, two photos taken with the microscope are superimposed to have the same portion of front and back side totally aligned (by considering an hole positioned in the same position in the front and in the back). The misalignment between the two sensors of the couple can be seen from the photos.

simulated. The resulting convoluted distribution was then compared to the measured charge distribution of the double-LGAD. An example is shown in Figure 5.24, with different proportions of events corresponding to the front LGAD, the back LGAD, and the double-LGAD. As the correct percentage of overlap is approached, the simulated and measured normalized distributions align, giving the effective overlap area and the number of single LGAD events.

In particular, from the example reported in Figure 5.24 the two LGADs show to be quite well superimposed for the double 35 µm-thick LGAD, with percentages of single events of 9% (for each one of the two single LGADs) ad 82% of double-LGAD events (particle passing through both sensors). For the double 50 µm-thick LGAD reported in Figure 5.25, the two sensors are almost totally superimposed with a percentage of single events of 2% (1%+1%) and a 98% of double events. As previously written, this implementation is fine for a proof-of-concept, but a better integration of such a concept either in the board containing the electronics or in the detector itself would allow to have a totality of d-LGAD events.

To have a direct comparison between d-LGADs and each one of the two LGADs of

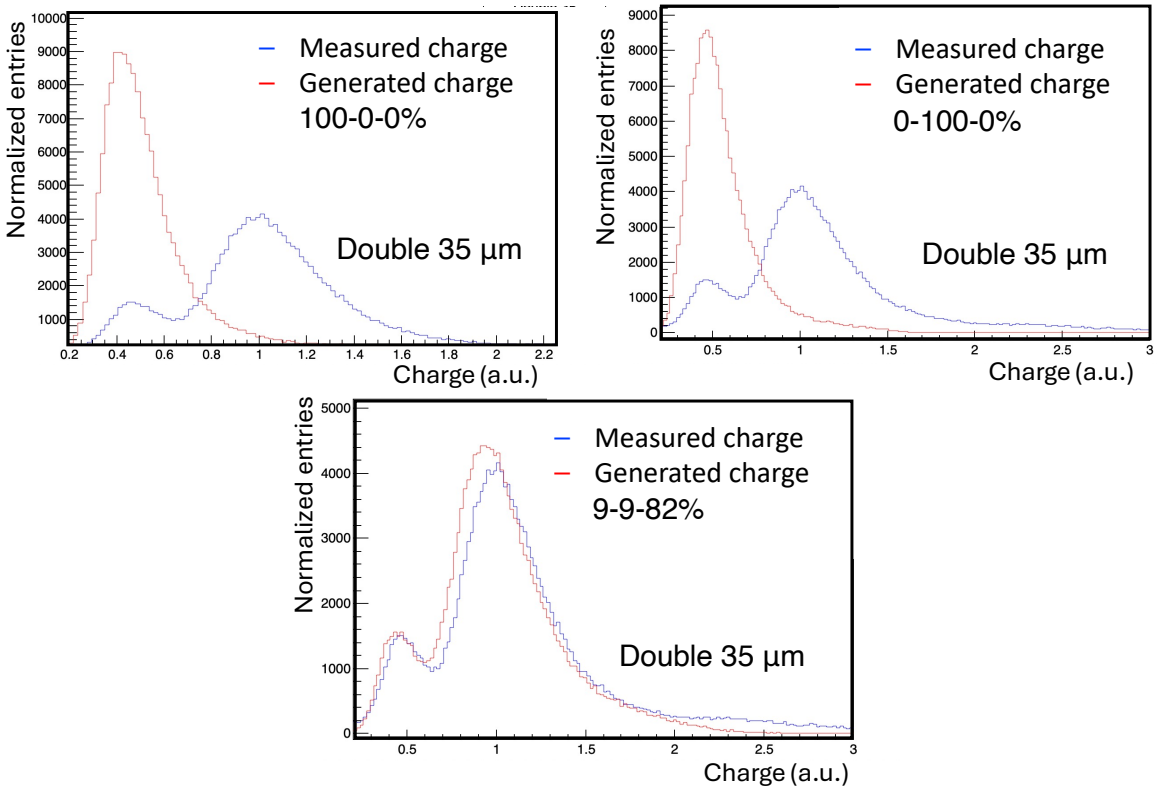

Figure 5.24: Example of comparison of measured double 35 µm-thick LGAD charge distribution and a generated one with different proportions of events corresponding to the front LGAD, the back LGAD, and the double-LGAD. A 100% of the events generated in the front LGAD (100-0-0%); a 100% of the events generated in the back LGAD (0-100-0%), and 9% of the events generated in each one of the single LGADs and an 82% of double-LGAD events (9-9-82%). The last distribution is the one that is better superimposed to the real one.

the pairs, measurements were repeated in the same setup and electronics conditions. A schematic showing an example of the different steps of the tests is reported in Figure 5.26. First we tested always the d-LGAD. Then we un-bonded the bottom LGAD in order to test the top one. Lastly, we un-bonded the top LGAD, bonding and testing the bottom one. Therefore, every LGAD thickness will always have three different measurements: two coming from each of the LGAD composing the d-LGAD, and one from the d-LGAD itself.

The RMS of the noise and the S/N ratio have been evaluated for each sensor (single

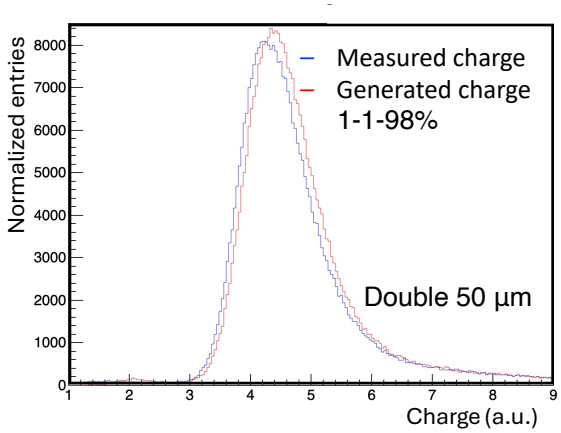

Figure 5.25: Example of comparison of measured double 50 µm-thick LGAD charge distribution and a generated one with different proportions of events corresponding to the front LGAD, the back LGAD, and the double-LGAD. 1% of the events generated in each one of the single LGADs and 98% of double-LGAD events (1-1-98%).

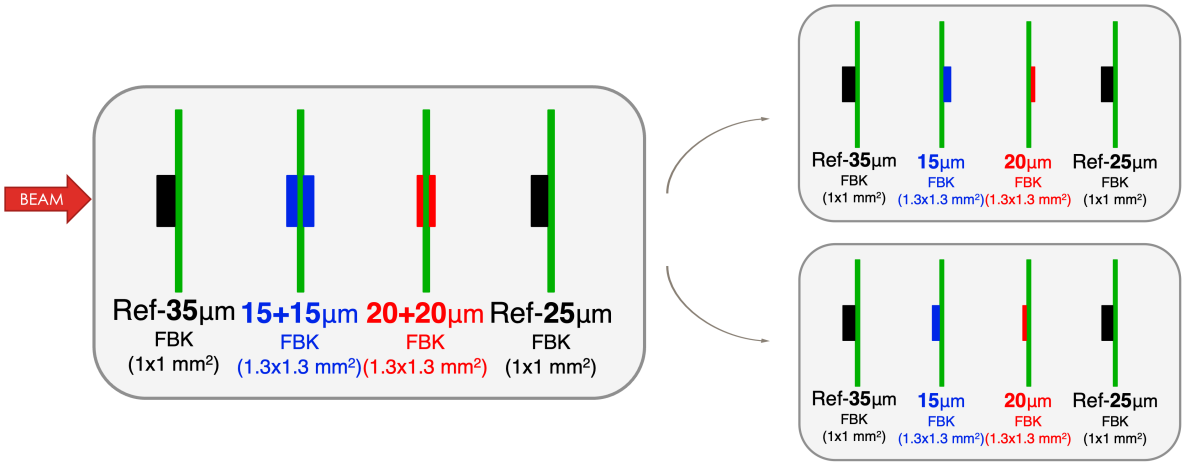

Figure 5.26: Example of schematic representing the different steps of the tests. For each couple the d-LGAD was tested first. Then the bottom LGAD was un-bonded in order to test the top one as a single sensor. Lastly, the top LGAD was un-bonded, and the bottom one bonded for testing.

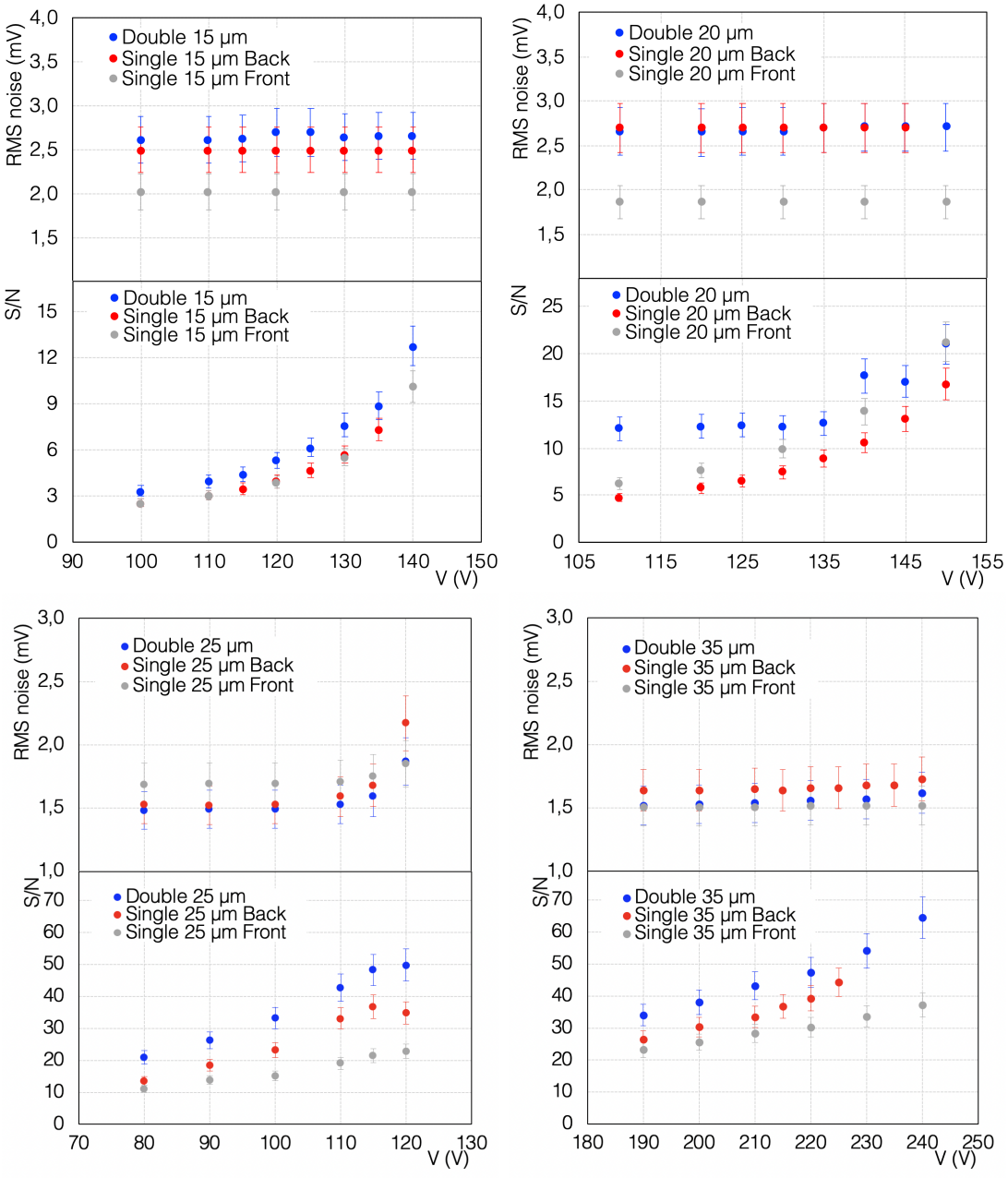
RMS noise (mV)
Double 15 µm
Single 15 µm Back
Single 15 µm Front
S/N
V (V)
RMS noise (mV)
Double 20 µm
Single 20 µm Back
Single 20 µm Front
S/N
V (V)
RMS noise (mV)
Double 25 µm
Single 25 µm Back
Single 25 µm Front
S/N
V (V)
RMS noise (mV)
Double 35 µm
Single 35 µm Back
Single 35 µm Front
S/N
V (V)

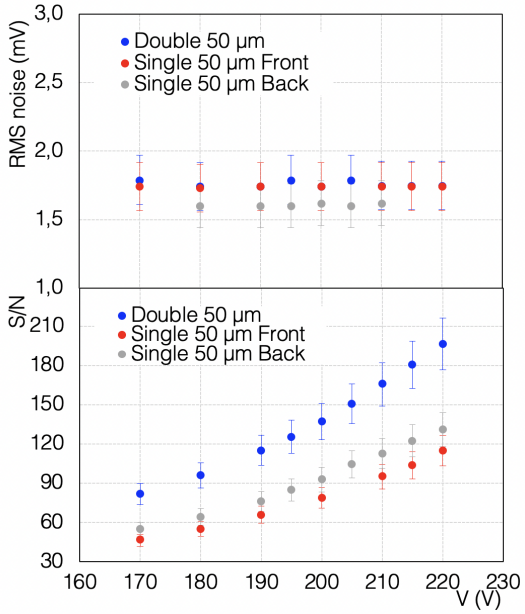

Figure 5.27: RMS of the noise (External gain amplification factors not removed) and S/N ratio for all the tested LGADs.

and double) and voltage. In Figure 5.27 they are reported as a function of the applied voltage.

As can be seen, the noise between single and double sensors is compatible for all thicknesses. The S/N instead is always higher for the d-LGAD, giving already some insight into the better performances reported later.

As in previous tests, a comprehensive analysis of the time resolution was conducted using the CFD method. A smoothing of the LGAD signal was applied with a four-point moving average. The resolution was extracted as done for single LGADs (Sections 5.2.1). The time resolution is reported in Figure 5.28 for all the voltages applied and CFD percentages for the d-LGADs and one of the two single sensors composing the d-LGAD. As can be seen, the time resolution has a similar behavior as a function of the CFD for the single and double LGAD for all the thicknesses.

In Figures 5.29, 5.30 and 5.31 the measured time resolution as a function of the applied voltage, charge and gain is reported for a fixed CFD.

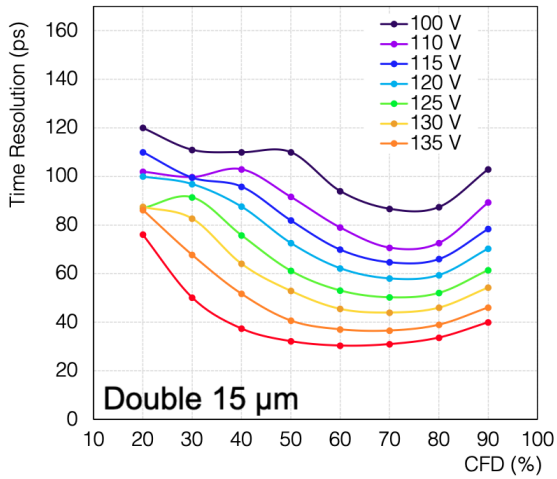
Time Resolution (ps)
CFD (%)
100 V
110 V
115 V
120 V
125 V
130 V
135 V
Double 15 µm

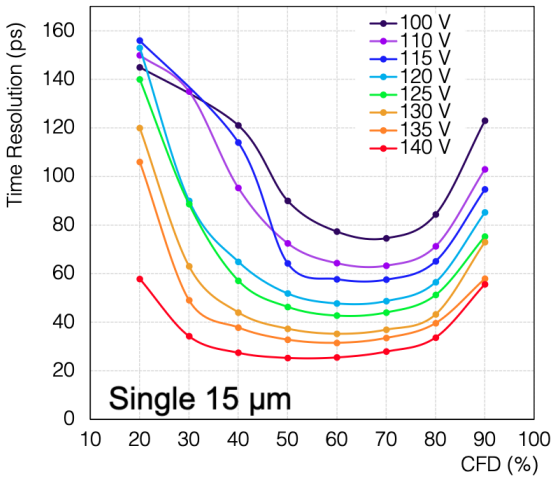
Time Resolution (ps)
CFD (%)
100 V
110 V
115 V
120 V
125 V
130 V
135 V
140 V
Single 15 µm

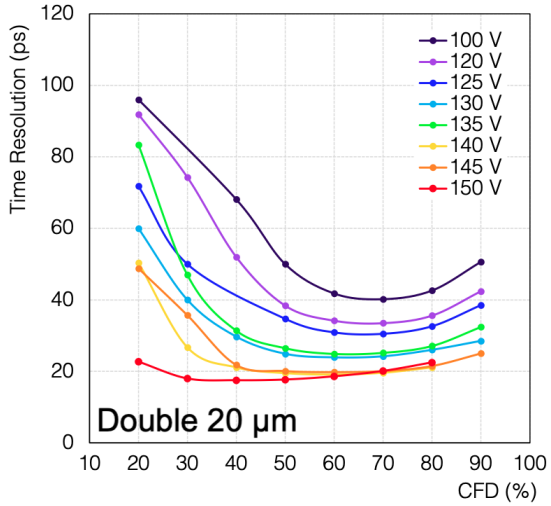
Time Resolution (ps)
CFD (%)
100 V
120 V
125 V
130 V
135 V
140 V
145 V
150 V
Double 20 µm

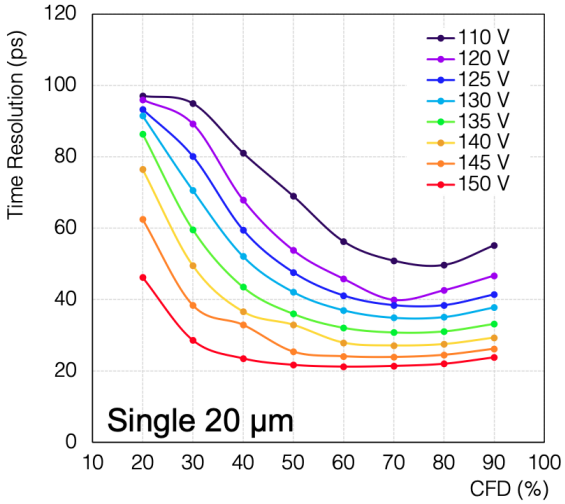
Time Resolution (ps)
CFD (%)
110 V
120 V
125 V
130 V
135 V
140 V
145 V
150 V
Single 20 µm

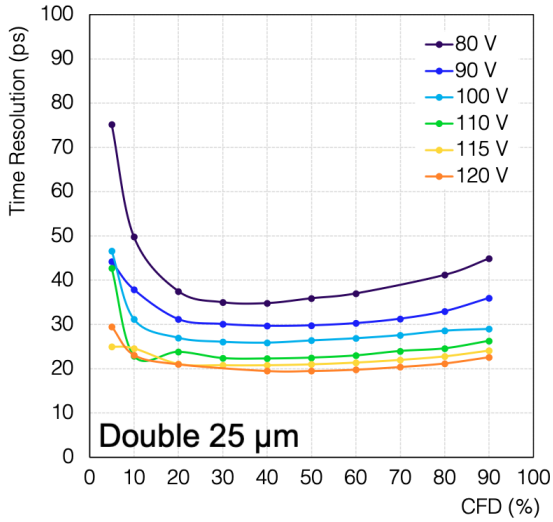
Time Resolution (ps)
CFD (%)
80 V
90 V
100 V
110 V
115 V
120 V
Double 25 µm

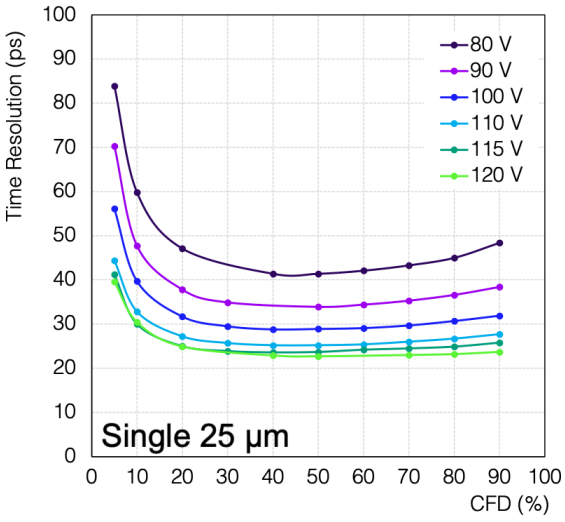
Time Resolution (ps)
CFD (%)
80 V
90 V
100 V
110 V
115 V
120 V
Single 25 µm

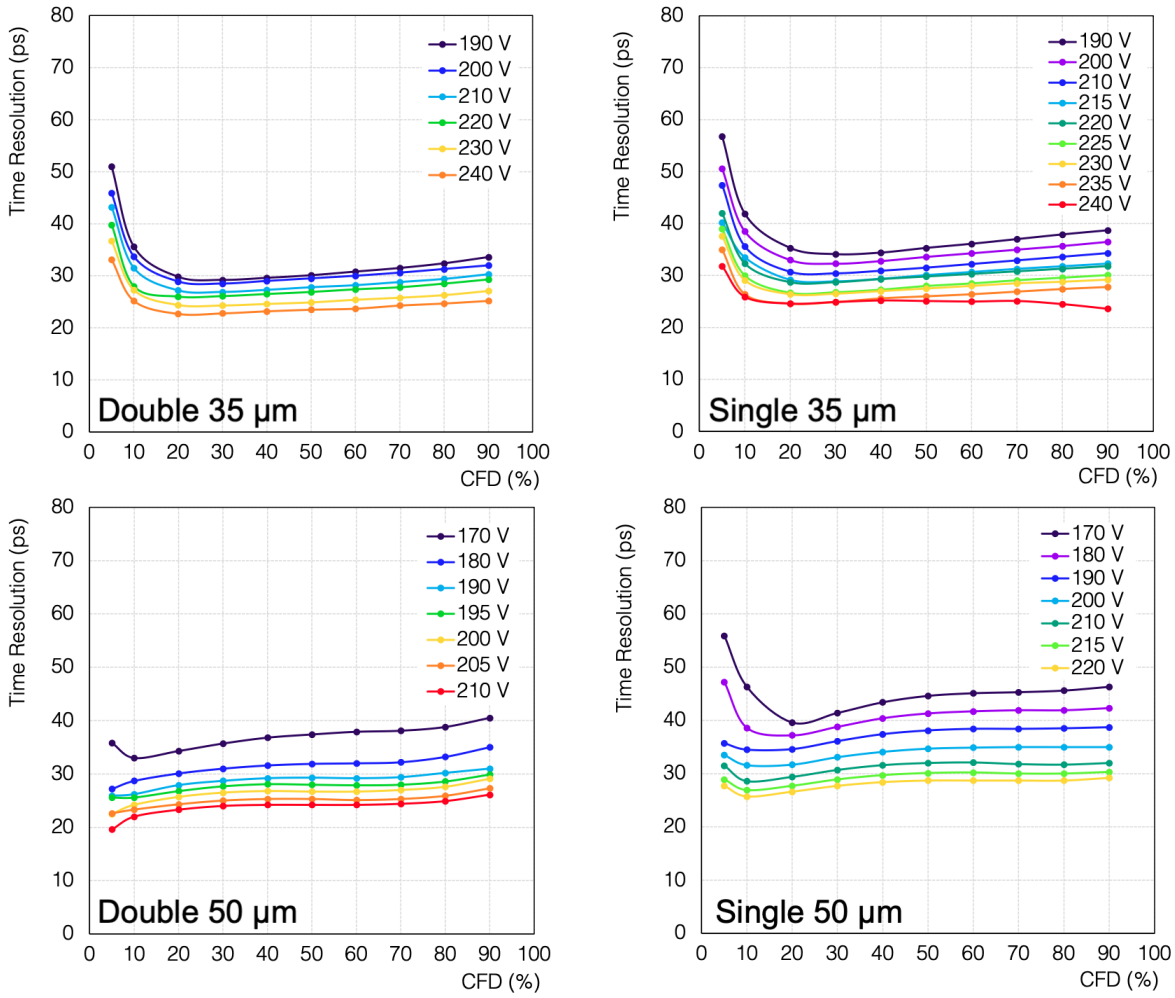

Figure 5.28: Time resolution for all the voltages applied and CFD percentages for the d-LGADs on the left and for one single sensor of the same thickness on the right. The sensor thicknesses are, from the top to the bottom, 15, 20, 25, 35 and 50 µm, respectively.

The results obtained with the single sensors are compatible with the ones found in the previous section. In addition, it can be noticed that the resolutions of the single LGADs of each pair are compatible, and in particular the values are very uniform for the 15 µm-, 20 µm- and 50 µm-thick couples, owing to the more uniform sensor wafers (and specifically to the more similar gains for the two sensors). As main observation, looking at a fixed voltage (or gain) an improvement of the time resolution has been observed with the d-LGADs in respect to the single ones composing the couple, for all the thicknesses.

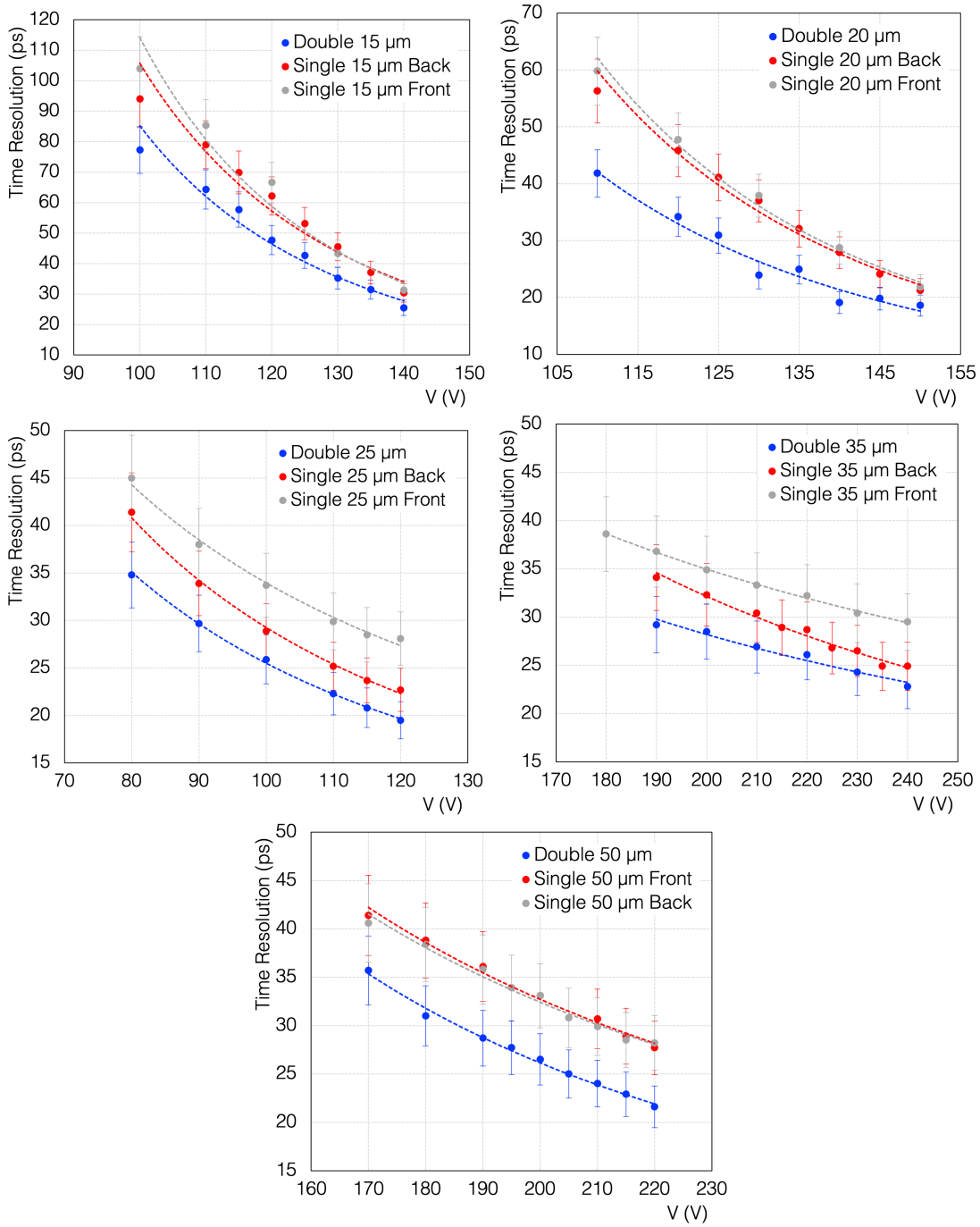

Figure 5.29: Measured time resolution results from the beam test as a function of the voltage applied for all the LGADs with 15, 20, 25, 35 and 50 µm of thickness, and for a CFD of 60%, 60%, 50%, 30% and 30%, respectively. The errors for the measured time resolution have been estimated as 10% of the value. The lines are included to guide the eye.

Moreover, as expected, the d-LGADs always show a larger charge with respect to single LGADs. A time resolution of $\sim$ 20 ps has been reached for all the d-LGAD thicknesses.

Finally, a comparison is done between a 50 µm-thick LGAD and a 25+25 µm-thick d-LGAD. The RMS of the noise and the S/N ratio as a function of the applied voltage are shown in Figure 5.32. In Figure 5.33 the time resolution is reported as a function of the applied voltage and of the charge, together with the noise values and the S/N ratio. A comparison of the charge distribution is reported in the last plot for a similar charge. It is interesting to observe that for a similar charge, the double 25 µm-thick LGAD shows a 50% better time resolution.

In Table 5.4 the best time resolutions reached for the five detectors tested are summarized.

All the single sensors of each pair exhibited a compatible time resolution. For all the thicknesses, an improvement is observed with the d-LGADs compared to the corresponding single sensors, yielding a final time resolution of approximately 20 ps. The results obtained with d-LGADs of different thicknesses are reported in Figure 5.34 and a comparison with single sensors of the same thickness in Figure 5.35.

The overall results show that the time resolution for the d-LGAD, made of two single LGADs, each with thickness t, is significantly better than the one of a single LGAD, both of thickness t and $2t$. Regarding the time resolution for d-LGADs of thickness $t + t$ and single sensors of thickness t, the improvement is less than what is expected from simple scaling (i.e., a factor of $\sqrt{2}$). As stated in Section 4.3.1.6, the time resolution of a d-LGAD will be dominated by the sensor of the pair with the largest signal. It is worth noting that for the 50+50 μm-thick d-LGAD, where the behavior of the front and back sensors is extremely uniform, $\sqrt{2}$ scaling is actually verified and measured.

5.4 LGAD performance with inclined tracks

So far, all the measurements were performed with the sensors perpendicular to the beam, but in the experiment, there will also be different conditions to consider, such as sensors positioned at the edge of the barrel layer of the TOF detector, traversed by inclined tracks of high-momentum particles. Additionally, some sensors will be crossed by inclined tracks

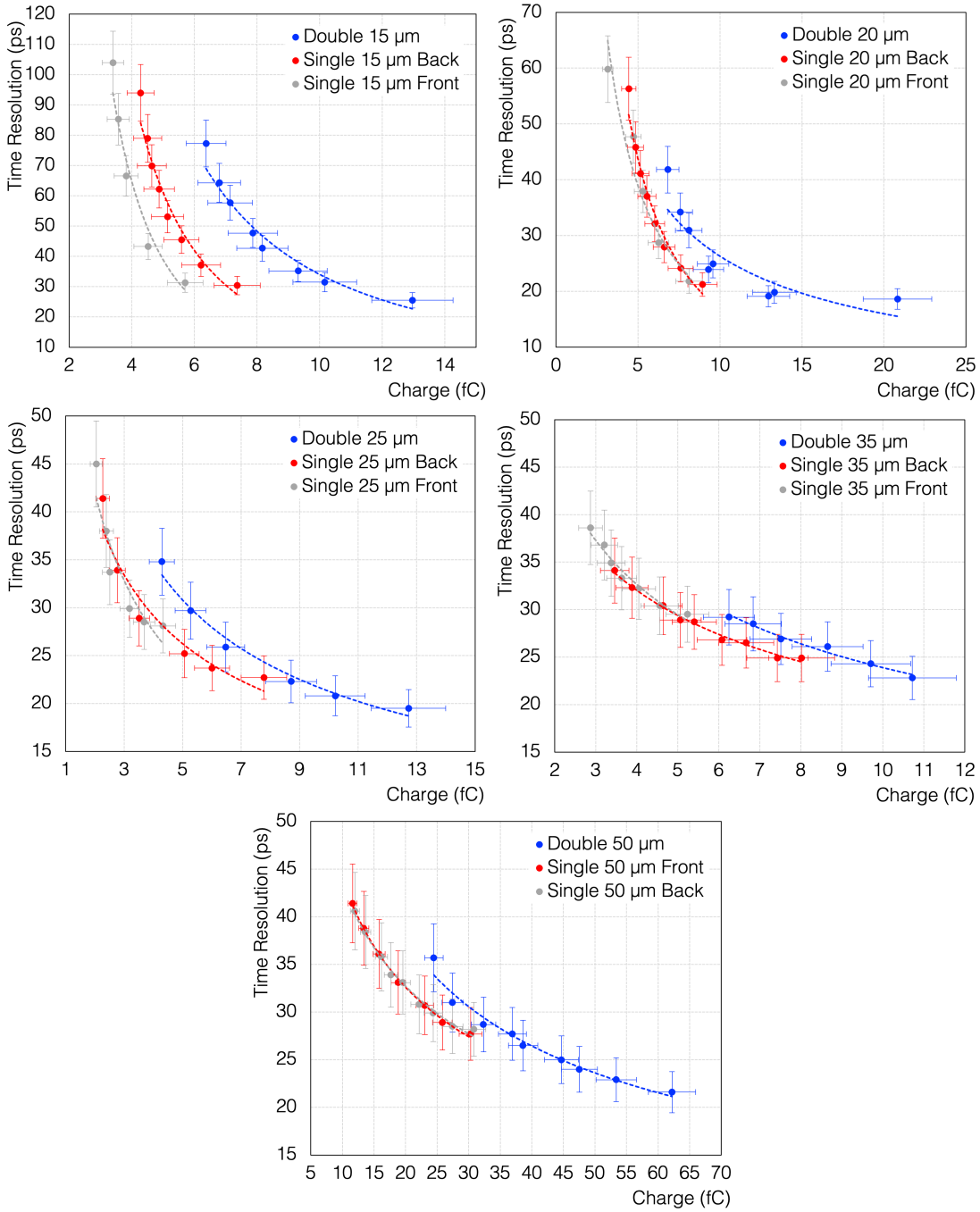

Figure 5.30: Measured time resolution results from the beam test as a function of the charge collected for all the LGADs tested with 15, 20, 25, 35 and 50 µm of thickness, and for a CFD of 60%, 60%, 50%, 30% and 30%, respectively. The errors for the measured time resolution and the charge have been estimated as 10% of the value. The lines are included to guide the eye.

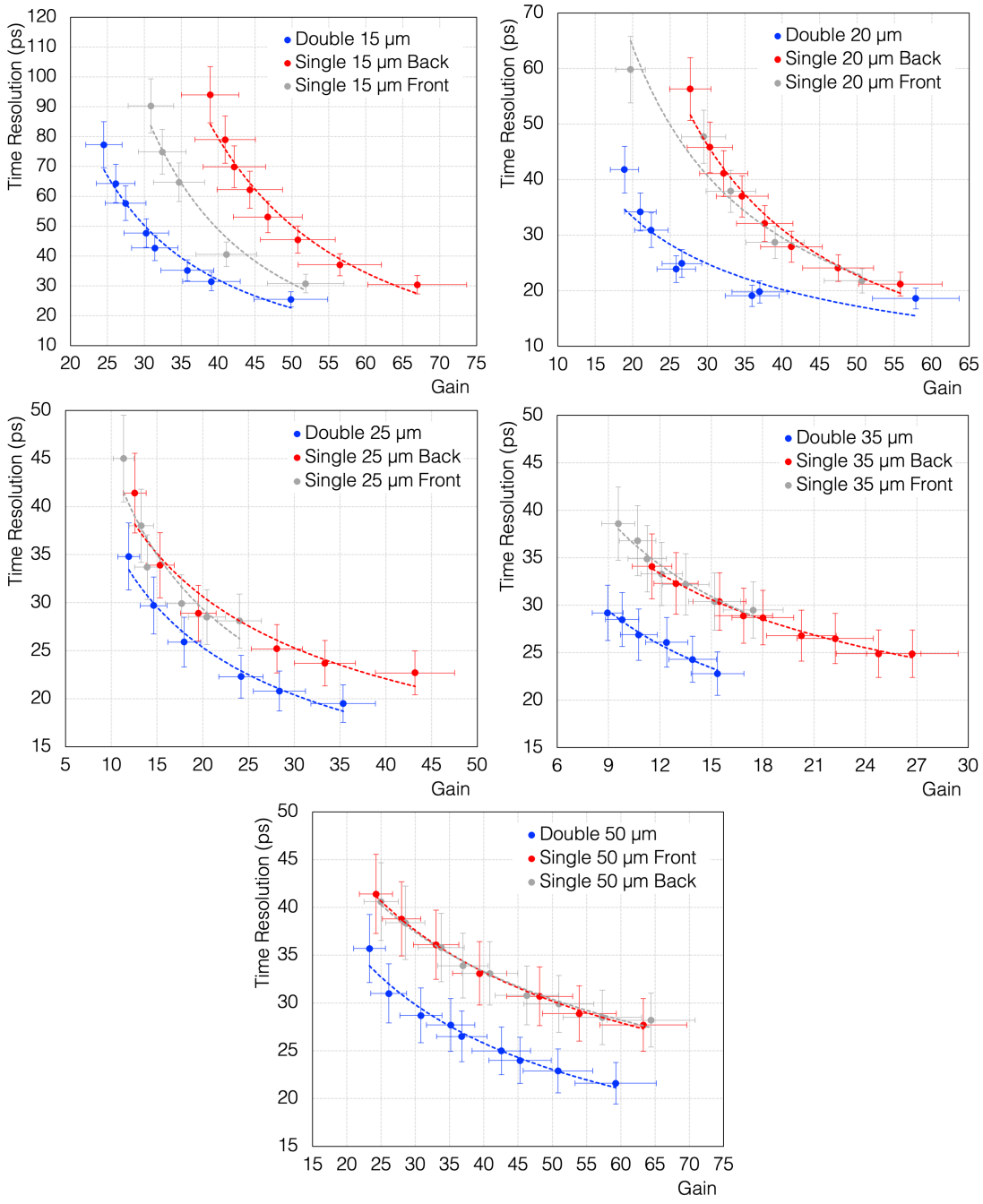

Figure 5.31: Measured time resolution results from the beam test as a function of the gain for all the LGADs tested with 15, 20, 25, 35 and 50 µm of thickness, and for a CFD of 60%, 60%, 50%, 30% and 30%, respectively. The errors for the measured time resolution and the gain have been estimated as 10% of the value. The lines are included to guide the eye.

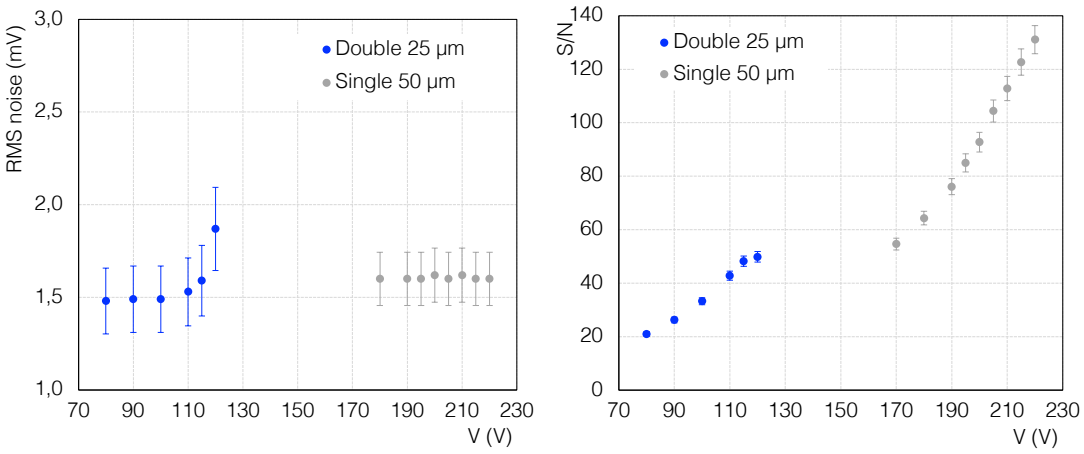

Figure 5.32: Comparison of the RMS of the noise (left) (external gain amplification factors not removed) and the S/N ratio (right) of a 50 µm-thick sensor and a 25+25 µm-thick d-LGAD as a function of the applied voltage.

of low-momentum particles due to bending in the magnetic field, while others may be only partially traversed, as depicted in Figure 5.36. For this reason, a further investigation on the dependence of the time resolution on the particles incidence angle with respect to the normal to the surface of the sensor was performed. Four supports were appositely produced for such purpose.

An LGAD with a thickness of 35 µm, also used in previous studies, was tested at four different angles with respect to the beam's orthogonal axis: 0° (perpendicular to the beam), 30°, 45°, 75° (maximum tilt in respect to the beam), as shown in Figure 5.37.

When a sensor is crossed by a particle with a direction that is different from the perpendicular one, two concurrent effects can affect the time resolution:

- due to the longer path traveled by the particle in the sensor, in principle more charge is produced inside it;
- a part of the charge can be released at the edges of the sensor.

The first effect is expected to be the dominant one. Indeed, the setup was designed to allow to change the angle by rotating the sensor around its center. This ensures that even at the maximum tilt angle of 75° for the 35 µm-thick LGAD with a 1×1 mm^2 area, the entire particle track remains well within the sensor active area. Indeed, assuming

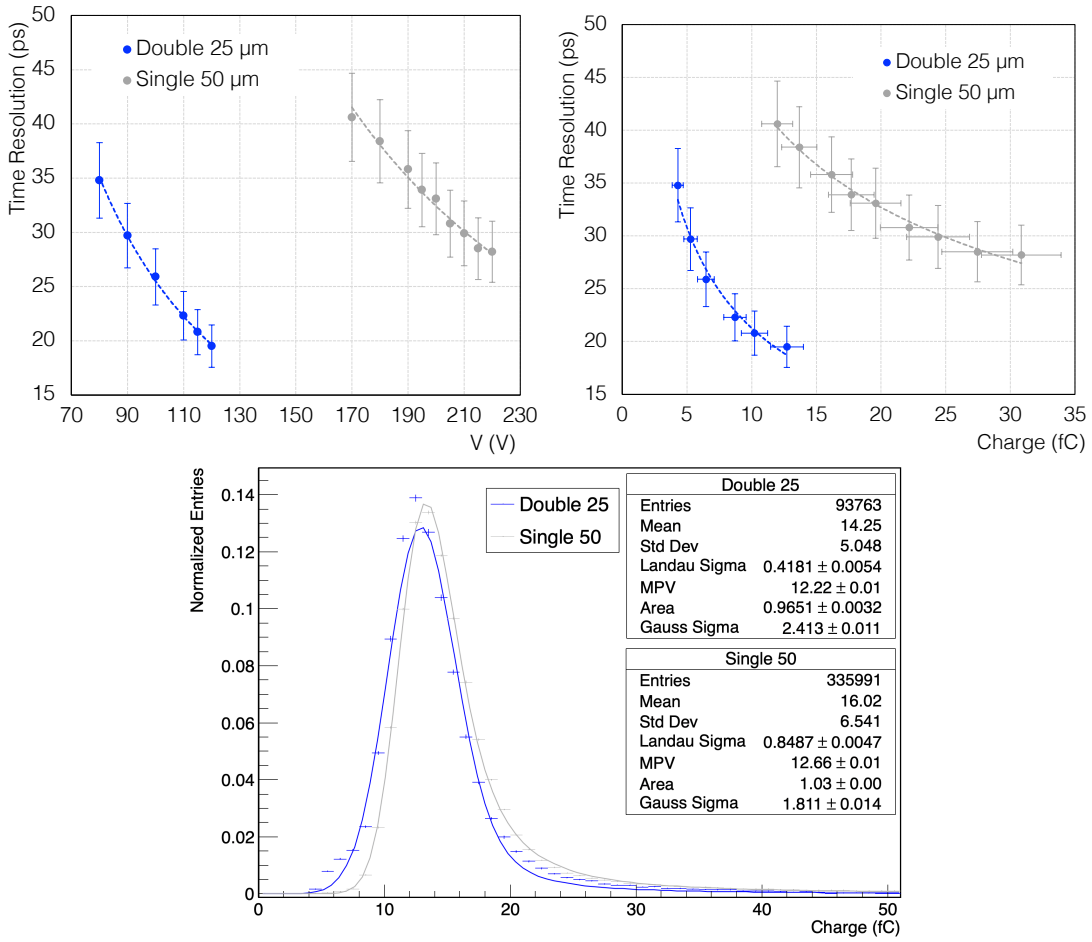

Figure 5.33: Comparison between a 50 µm-thick sensor and a 25+25 µm-thick d-LGAD and. Time resolution is reported as a function of the applied voltage (left) and of the charge (right) in the upper plots, for a CFD of 30% and 40%, respectively. The errors for the measured time resolution, gain and charge have been estimated as 10% of the value. The lines are included to guide the eye. A comparison of the charge distribution is reported in the last plot for a similar charge.

the sensor is aligned with the center of the beam, at 75°, the track is expected to impact the sensor at an average maximum distance of 65 µm from its center, traversing the full thickness of the pad area without approaching the edges.

As shown in Figure 5.38 (left), a larger charge is released at higher tilting angles due to the longer path traveled by the particles inside the sensor. In particular, considering

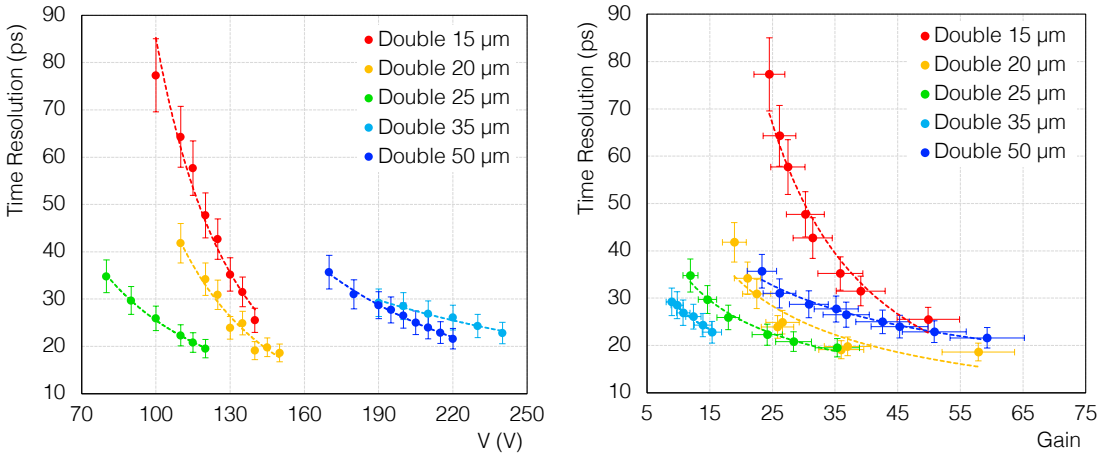

Figure 5.34: Measured time resolution as a function of the applied voltage and gain for d-LGADs composed of pairs of sensors of 15, 20, 25, 35 and 50 µm, with a gain at the maximum applied voltage of, respectively, 50, 58, 35, 15 and 59 and CFD of 60%, 60%, 40%, 30%, 30%, chosen to have the best time resolution.

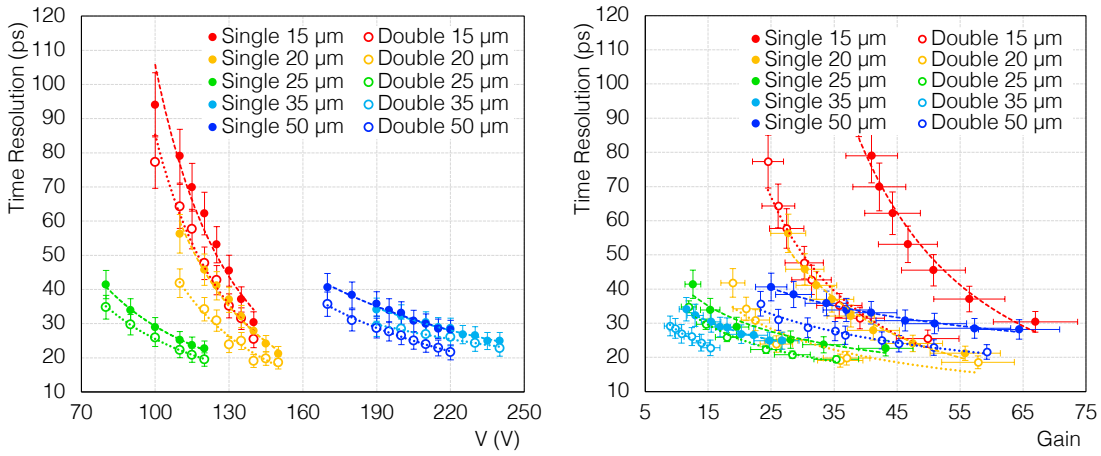

Figure 5.35: Measured time resolution as a function of the applied voltage and gain for d-LGADs composed of pairs of sensors of 15, 20, 25, 35 and 50 µm, compared with the one of one of the two sensors composing the couple. The CFD, chosen to have the best time resolution, is for the double sensors of 60%, 60%, 40%, 30%, 30% and for the single sensors 60%, 60%, 50%, 30%, 30%, respectively from 15 to 50 µm. Here the single sensors shown are the back LGADs of each couple.

	Voltage applied	Gain	Time resolution
FBK15 Front	140 V	52 ± 5	(31 ± 3) ps
FBK15 Back	140 V	67 ± 6	(30 ± 3) ps
d-FBK15	140 V	50 ± 5	(25 ± 2) ps
FBK20 Front	150 V	51 ± 5	(22 ± 2) ps
FBK20 Back	150 V	56 ± 5	(21 ± 2) ps
d-FBK20	150 V	58 ± 5	(19 ± 2) ps
FBK25 Front	120 V	24 ± 2	(23 ± 2) ps
FBK25 Back	120 V	43 ± 4	(28 ± 3) ps
d-FBK25	120 V	35 ± 4	(20 ± 2) ps
FBK35 Front	240 V	17 ± 2	(30 ± 3) ps
FBK35 Back	240 V	27 ± 3	(25 ± 2) ps
d-FBK35	240 V	15 ± 2	(23 ± 2) ps
HPK50 Front	220 V	63 ± 6	(28 ± 3) ps
HPK50 Back	220 V	64 ± 6	(28 ± 3) ps
d-HPK50	220 V	59 ± 6	(22 ± 2) ps

Table 5.4: Time resolution for 15, 10, 25, 35 and 50 µm-thick couples for a given voltage (or gain) obtained in a beam test setup at room temperature.

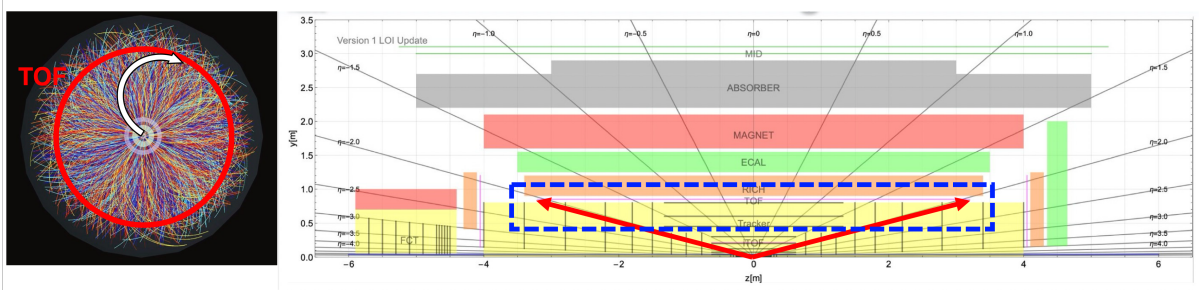

Figure 5.36: The motivation of this study is to investigate the response of sensors to particles not perpendicular to its surface, as in the case of sensors positioned at the edge of the TOF barrel layer or low-momentum particles traversing the sensors non perpendicularly or only partially.

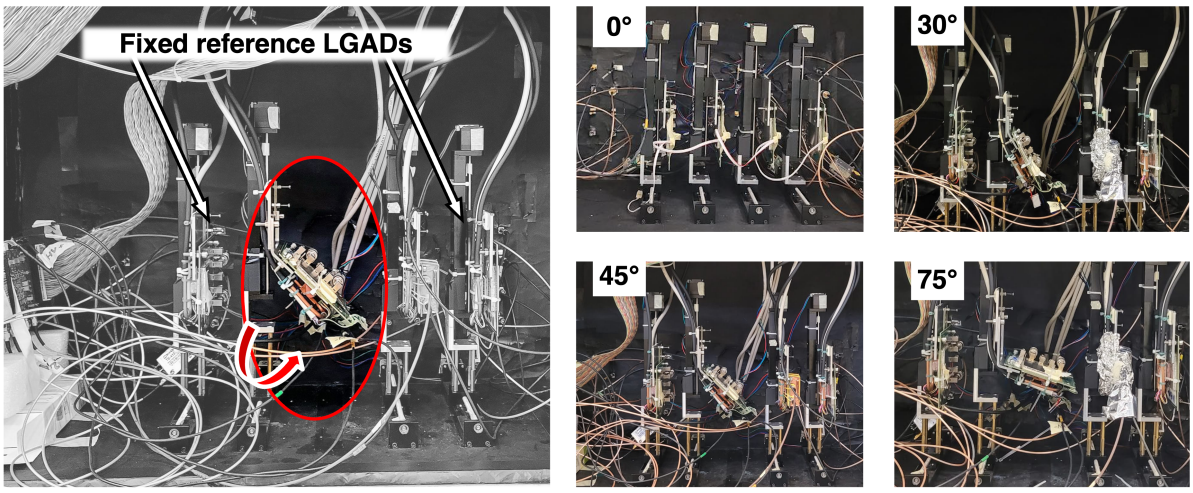

Figure 5.37: Telescope used to test an LGAD at four different angles with respect to the beam's orthogonal axis with reference LGADs and rotated LGAD under test are indicated (left). Telescope with the 4 different rotation angles of the LGAD under test (right): 0° (perpendicular to the beam, top-left) and 30° (top-right), 45° (bottom-left), 75° (maximum tilt in respect to the beam, bottom-right). For all the tests, two other LGAD in the front and in the back of the setup were used as references and trigger.

the effective thickness of silicon traversed by the particle at different angles, and assuming the same gain, the charge corresponds to what would be observed in an LGAD with an equivalent thickness to the traversed path. As expected, for a same sensor thickness (i.e. same drifting volume), the time resolution improves when a larger charge is released in the sensor as shown in Figure 5.38 (right). This is visible also in Figure 5.39, where the time resolution of the 35 µm-thick sensor is reported as a function of the CFD for different tilting angles. Although the benefit on the time resolution is evident, since these studies were done directing the beam to the center of the sensors, future tests with an LGAD matrix and a telescope (See Appendix D) are planned to investigate eventual concurrent effects at the edges and an eventual charge sharing among pixels.

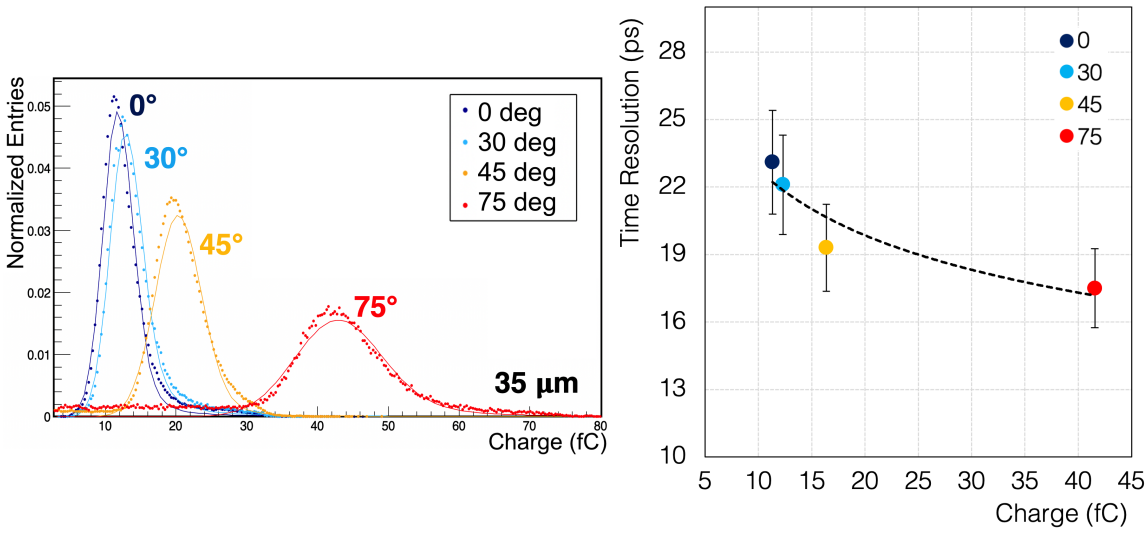

Figure 5.38: Charge distribution (left) and measured time resolution as a function of the charge released in the sensor (right) of a 35 µm-thick LGAD with four different tilting angles for a fixed CFD of 40%.

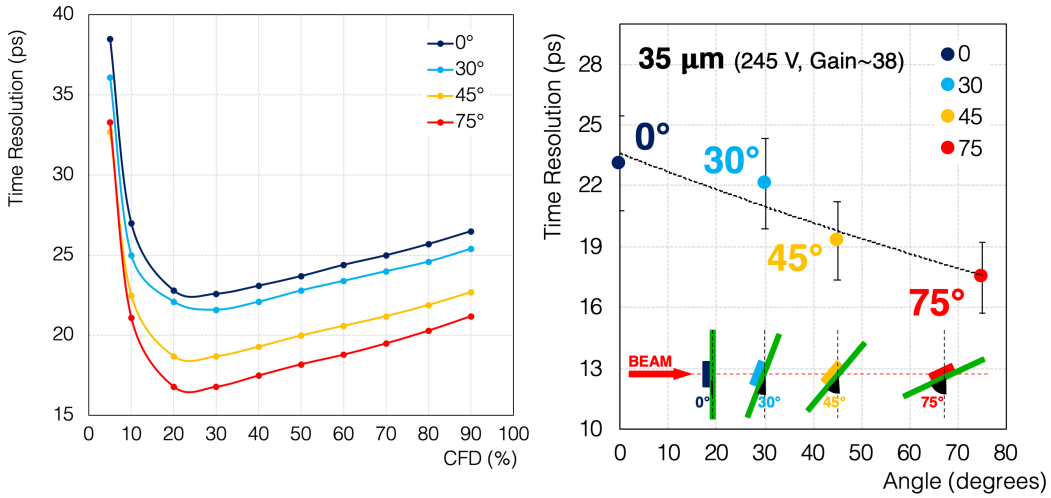

Figure 5.39: Measured time resolution of a 35 µm-thick LGAD with four different tilting angles for all the CFD (left) and for a fixed CFD of 40%.

5.5 Summary and outlook

Extensive beam tests were conducted at the T10 beamline at CERN from 2021 to 2024 to study different LGADs performances. Significant progress has been achieved and the results so far demonstrate the promising potential of LGAD technology to achieve the required 20 ps of time resolution opening the way to many different studies, in order to further improve the capabilities of LGADs.

The future of particle physics, from high-luminosity colliders to underground experiments, demands a new generation of particle identification detectors capable of providing separation power across 4–5 orders of magnitude in momentum. To strategically guide detector R&D efforts in Europe, ECFA has developed a Roadmap that aligns with progress in emerging technologies from adjacent fields [59]. This Roadmap defines a broad range of research efforts designed to improve the performance of particle physics experiments in both the near and long term. In this picture, the development of TOF systems with picosecond-level precision will be a priority. For these systems, high-granularity silicon sensors achieving timing resolutions on the order of 10 ps and the capability to operate under high-rate conditions will be critical.

The tests performed so far confirm that thinner LGAD designs can significantly improve time resolution. While these designs were not originally optimized for timing, they have nonetheless demonstrated the potential to achieve 20 ps of time resolution, with the potential for further improvements in optimized productions. It would be interesting a production of LGADs with such low thicknesses appositely optimized for timing purposes to assess potential improvements. In addition to this, also a front-end optimized for such a fast signal could make a difference; ongoing tests are presently investigating the performances of these sensors with a full front-end and data read-out chain.

Moreover, the innovative concept of double-LGAD was introduced and tested for the first time, showing significant advantages for the electronics and further improvements in overall time resolution. While still at the proof-of-concept stage, the logical progression would involve a more straightforward integration of this concept, either within the electronics board or directly within the detector itself, potentially utilizing techniques such

as through-silicon via (TSV). Overall, this concept presents a promising development for LGAD's performance and paves the way for future implementation of such sensors.

Studies with LGADs tilted at different angles relative to the beam have shown that time resolution remains largely unaffected, with slight improvements observed at higher impinging angles. Since these studies have primarily done directing the beam to the center of the sensors, future tests with an LGAD matrix and a telescope will explore possible effects at the edges, such as partial charge loss and resolution dependence on the impinging point.

For the ALICE 3 studies, given the results achieved so far, the R&D efforts to meet the required specifications will continue with the exploration of monolithic LGADs (a.k.a. CMOS LGADs), which could provide a cost-effective and easily implementable alternative. Combining these two technologies (LGAD and CMOS) would deliver a transformative solution for high-energy physics experiments and other medical applications, fostering innovation across multiple domains. While the current focus has been on achieving excellent time resolution, future research must also address other critical properties of CMOS LGADs, such as radiation hardness, to ensure robust performance in a variety of conditions.

Chapter 6

Conclusions

In conclusion, this thesis has demonstrated that LGAD detectors successfully met the stringent timing requirements of the ALICE 3 Time-Of-Flight (TOF) detector, achieving time resolutions in line with the 20 ps target. As a consequence, the results also establish these sensors as strong candidates for a variety of future high-energy physics experiments [1].

The direction of these studies was initially motivated by the expected improvement in the timing performance of thin LGAD layouts showed by simulations. For this reason, the first very thin LGAD prototypes produced by FBK, with a thickness of 15, 20, 25 and 35 µm, were deeply studied, in comparison to standard 50 µm sensor. Both single channel and matrices, with different layout, doping and characteristics were studied, performing tests on both bare silicon prototypes and with the sensors attached to the electronic boards. In addition, the new concept of double-LGAD, expected to generate a higher signal at the input of the amplifier, resulting in a benefit for both electronics performance and overall time resolution, was introduced, implemented and tested for the first time. A final investigation was done regarding the dependence of the time resolution on the particles incidence angle, in order to study the response of sensors placed at the edge of the barrel layer of the TOF detector to inclined tracks, or of sensor placed at mid-rapidity traversed non-perpendicularly of only partially by low-momentum particles due to the bending in the magnetic field.

All the sensors were fully characterized and studied previously in the laboratory of

my home institute with a laser setup and subsequently using particle beams at CERN facilities.

A thorough electrical characterization was first conducted involving current-voltage (IV) and capacitance-voltage (CV) measurements on both bare silicon sensors and sensors coupled to the front-end:

- IV characterization revealed variability in the breakdown voltages and intervals of operations of sensors of the same thickness, which can be attributed to uncertainties in the production process, but in general, for a same layout, breakdown voltages were higher for thicker sensors as expected. Comparisons between different inter-pad designs indicated that matrices with pads near to each others exhibited good current uniformity, but are more susceptible to premature breakdown. In contrast, the presence of a guard ring between the pads helps maintaining a more uniform electric field resulting in a better uniformity between pads breakdown voltage, thanks to the better isolation, which prevents premature breakdown.

- CV measurements allowed to extract the full depletion voltage and capacitance, the gain layer depletion, the drift electric field and doping profile of all the sensors. The results showed in this case a very good uniformity between sensors with same thickness and layout, a behavior which is essential for consistent performance in large-scale applications.

Tests in a laser setup were used to study the efficiency, response uniformity, and edge effects, leading also to a first evaluations of gain and time resolution. As expected, these performance studies indicated that thinner detectors consistently achieved better time resolution across all gain values.

After laboratory measurements, extensive beam tests were conducted at the T10 beamline at CERN from 2021 to 2024 to study the sensors performances. The first beam test measurements of 25 and 35 µm compared to 50 µm-thick sensors confirmed the potential of a thinner design for improved time resolution. Consequently, comprehensive studies were conducted on progressively thinner sensors, arriving to test the first 15 µm- and 20 µm-thick LGADs ever produced by FBK.

The plot in Figure 6.1, shows the best time resolution achieved for all the LGAD

thicknesses (15, 20, 25, 35, 50 µm), layouts (single and matrices) and specific tests (double-LGADs implementation and studies with different particles incident angles), reported in this thesis.

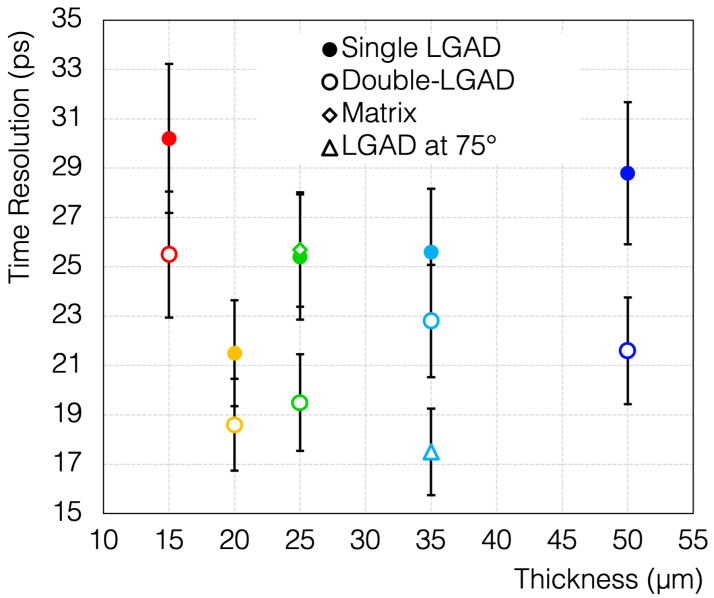

Figure 6.1: Best measured time resolution for all the thicknesses (15, 20, 25, 35, 50 µm), layouts (single and matrices) and specific tests (double-LGADs implementation and studies with different particles incident angles), reported in this thesis. For each thickness, the points for single sensors represent the average of the best results achieved across all tested sensors with that thickness.

The research demonstrated that reducing sensor thickness generally improves time resolution, with the 20 µm-thick sensor exhibiting the best performance. It is important to consider that these were the first production of such thin sensors by FBK when comparing trends across different thicknesses. The data also revealed that, despite the benefits of thinner sensors, the optimization of electronic chain becomes increasingly important as sensor thickness decreases, especially for the very thin 15 µm prototypes, where electronic limitations may have affected the performance.

The double-LGAD concept, implemented and tested for the first time, showed for all thicknesses a higher charge with respect to single LGADs, resulting in a benefit for the electronics. In addition, looking at a fixed voltage (or gain) an improvement of the

time resolution was observed with the double-LGADs in respect to each single LGADs composing the couples. It is important to note that some of the single sensors could reach higher voltages and gain, so this plot should not be viewed as a direct comparison between single and double sensors, but rather as a summary of all the results.

Overall, it can be observed from the plot that double LGADs can achieve values below 19 ps; a matrix was tested, showing a worse time resolutions in respect to single LGADs, probably due to its layout non optimized for timing. A study on a 35 µm-thick sensor positioned at different angles relative to the beam was important to investigate eventual changes in the timing performance for sensors traversed totally or partially by inclined tracks, like the ones placed at the edge of the barrel layer or at mid-rapidity traversed by low-momentum particles bended from the magnetic field. Actually, results indicated improved timing performance at higher angles relative to the beam, thanks to the higher charge released in the sensor, reaching for this sensor a resolution of around 17 ps, at an angle of 75. Although the benefit on the time resolution is evident, future tests with an LGAD matrix and a telescope are planned to investigate eventual concurrent effects when the sensor is only partially traversed by a particle and thus a part of the charge is lost or shared among different pixels.

In conclusion, the data suggest that while reducing sensor thickness improves the time resolution, optimizing electronic signal processing is essential for achieving the best overall performance. This R&D campaign on LGAD detectors finally resulted in sensors with a time resolution in line with the requirements of ALICE 3 Time-Of-Flight detector and also classifies these sensors as excellent candidates for many future-generation experiments. These studies highlight the outstanding performances of these sensors in the different layouts and implementations, opening avenues for further research to unlock their full potential.

Appendix A

Other research activities within the ALICE TOF detector

This appendix describes additional research activities, in which I played a leading role. They concern the ALICE Time-Of-Flight (TOF) detector, which I served as System Run Coordinator, i.e. responsible for the proper working and data quality of the system during the ALICE data taking, and for the maintenance and development of the hardware and software components of the whole system; furthermore, I was appointed as chair of the Paper Committee for the article on the TOF performance in LHC Run 3 currently under internal review. These activities were carried out during the PhD enrollment, although they are not directly related to the main topic of this thesis.

A.1 Performance of the ALICE TOF detector in LHC Run 3

The core physics program of the ALICE experiment at the LHC is the study of the properties of the strongly interacting, dense, and hot matter created in high-energy heavy-ion collisions. Most of the physics analyses rely on the capability to perform Particle IDentification (PID). In the ALICE detector, this is done using different and complementary techniques to ensure a wide coverage in momentum, from approximately $\sim 100\,\mathrm{MeV}/c$ to about $\sim 20\,\mathrm{GeV}/c$. The time-of-flight measurement, provided by the

ALICE Time-Of-Flight (TOF) detector allows particle separation in the intermediate momentum range (from 0.5 to $3 - 4\,\mathrm{GeV}/c$). This is achieved by ensuring a precise determination of the event collision time (t_{ev}), the track length (l) and its momentum (p) along with an accurate measurement of the tracks arrival time at the TOF detector. At the end of Run 2 (2018), the TOF detector successfully completed more than 10 years of operation. During Long Shutdown 2 (LS2), the ALICE Collaboration upgraded its detector to handle a higher interaction rate (50 kHz in Pb–Pb collisions) and to increase the integrated luminosity collected, by adopting a continuous readout scheme. During LS2 , also the TOF DAQ system was adapted to the new data-taking paradigm in ALICE by upgrading its electronics. A refurbishment of its aged components was also performed, along with an upgrade of the offline data processing algorithms (data quality control, reconstruction, calibration, and analysis). An analysis is currently ongoing to study the performance of the upgraded ALICE TOF detector with Run 3 data, focusing on detector resolution and its impact on particle identification. In particular, two different methods are being used: the first is a new approach implemented for the first time, relying purely on the TOF and tracking information, while the second method was previously used and depends on event time determination.

A.1.1 Time Of Flight (TOF) detector

The TOF detector measures the time of arrival of particles to the detector (t_{TOF}), its resolution drives the separation power between particle species. In addition, particle separation in the momentum interval of interest relies on a precise determination of the event collision time (t_{ev}), the track length (l) and its momentum (p). The separation between different particles species can be obtained as $m = |\overline{p}| \cdot \sqrt{\left(\frac{t_{\mathrm{TOF}} - t_{\mathrm{ev}}}{l}\right)^2 - 1}$. The track length and momentum measurement are obtained with the ITS [107] and TPC [108, 109] detectors. The ALICE TOF detector has cylindrical symmetry, covering the pseudorapidity interval $-0.9 < \eta < 0.9$ with full azimuthal acceptance. It is located at an average distance of 3.8 m from the beam pipe spanning an active area of 141 m^2. It is composed by 1593 Multigap Resistive Plate Chambers (MRPC) (see Section A.1.1.1), designed as double–stack strips of 7.4×120 cm^2 active area and arranged in 87 gas-tight modules distributed over 18 azimuthal Super Modules (SM). Each SM is $\sim 9.3\,\mathrm{m}$ long,

covering approximately 20° of azimuthal angle and it is composed by five modules: the two external and two intermediate modules contain 19 MRPCs each, while the central one contains 15 strips, having in total 91 MRPCs per SM. In order to minimize the dead areas and to orient the strips perpendicularly to the interaction point, the MRPCs are slightly rotated with respect to the horizontal direction and positioned to have the active area overlapped by 2 mm. Each MRPC strip is segmented into two–row arrays of 48 pickup pads, for a total of 96 2.5×3.5 cm^2-area pads for each strip and 152928 total readout channels.

A.1.1.1 Multigap Resistive Plate Chambers (MRPC)

Multigap Resistive Plate Chambers are gaseous detectors based on the impact ionization mechanism (2.5).

ALICE TOF MRPC have a double stack structure, where cathode pickup electrodes are located at the top and bottom of the chamber, and the anode in the middle is shared between the two stacks. Each stack consists of 5 equally spaced gas gaps of 250 µm, filled with a non-flammable freon-rich gas mixture containing C2H2F4 (tetrafluoroethane or freon) and SF6 (sulfur hexafluoride) in the concentration of 93% and 7%. The high voltage provides a uniform and high electric field for each gap, allowing a very fast avalanche formation between resistive plates. Ionising particles create independent avalanches in each gap. In this way, the dimension of the avalanches is constrained, and the time resolution is improved. The final signal obtained, as charge induced on both the cathode and anode, has the shape of a Landau distribution and is the analogue sum of the signals given by each avalanche. This configuration was chosen to achieve the best time resolution and a good efficiency in the high charged-particle density environment of Pb–Pb collisions.

A.1.1.2 Front-end and Readout electronic

A schematics of the TOF readout system is shown in Figure A.1. A Front End Analogue card (FEA) mounted on the TOF module provide very fast amplification and signal discrimination. Each FEA contains three NINO ASIC chips, each amplifying and discriminating 8 channels. A total of 4 FEAs and 12 NINO chips read the 96 pads of each

MRPC strip. The discrimination of the signal then provide a Time over Threshold (ToT) output; the leading edge of the ToT provides the time of the hit, and the width of the signal is proportional to the charge deposited during the interval in which the signal is above the threshold. The the shaped signals are then transmitted to dedicated readout boards.

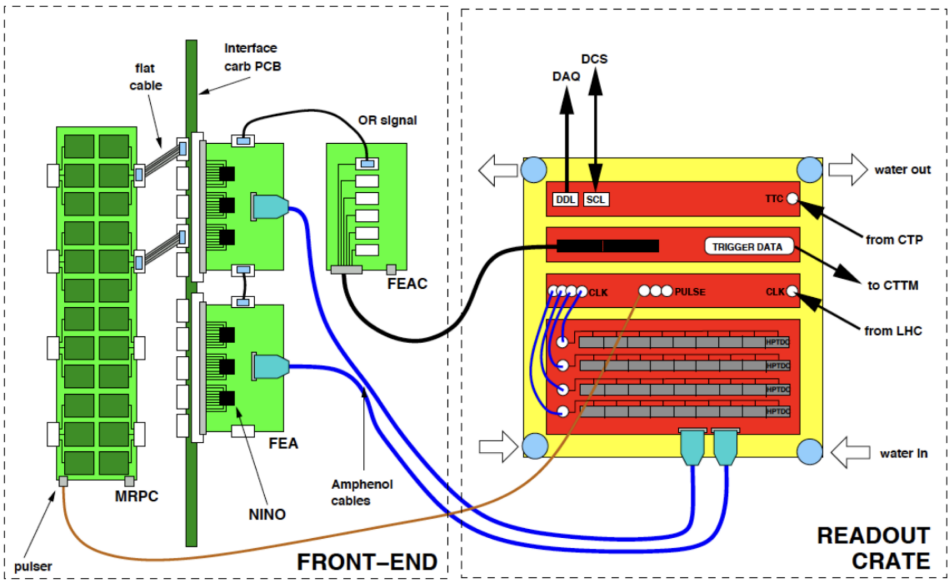

Figure A.1: Schematic picture of the ALICE TOF front-end and readout electronics.

The discriminated output from the Front-End electronics is transferred to a custom VME crate, where the signals are digitized. Each TOF Supermodule provides on either side two VME crates, supporting a DC-to-DC converter for low-voltage power supply and the Supermodule readout electronics. Each crate can contain up to 12 boards:

- **TDC Readout Modules (TRMs)**, 9 in right crates and 10 in left crates, which provide the time-to-digital conversion of the signals coming from the FEAs. Each TRM is equipped with 3 High Performance TDCs (HPTDC) which can read 8 channels.
- **A Local Trigger Module, LTM** which acts as first level of the TOF trigger. It receives the output from the Front End Analogue Control board (FEAC) and

transfer it to the CTTM (Cosmic and Topology Trigger Module), also setting and monitoring low voltages and temperatures of the Front-End electronics.

- **A Data Readout Module, DRM** that is placed in each crate and reads the data from the TRM modules. DRMs constitute the primary interface between the Central ALICE DAQ and the TOF readout electronics, connected through optical links (DDL). For Run 3, a new readout board was designed, the DRM2 (see Section A.1.2).

The extensive upgrade of the TOF detector that was accomplished during LS2 is described in the following section.

A.1.2 The upgraded TOF in Run 3

As described in Chapter 1, after the rich physics program pursued during LHC Run 1 (2009–2013) and Run 2 (2015–2018), the ALICE experiment underwent a series of upgrades during Long Shutdown 2 [9]. The new detector couples improved tracking performance with the capability to sustain data taking under high interaction rate conditions, up to 1 MHz in pp collisions and 50 kHz in Pb–Pb collisions.

Among the different improvements, an extensive upgrade of the TOF detector was carried out, concerning mostly the detector readout electronics and specifically, passing to continuous readout. This was achieved making use of the buffering capabilities for digitized data available in the High Performance TDC (HPTDC) boards [110] and thanks to the small intrinsic dead time ($\sim$10 ns) of the MRPC detector and its front-end electronics.

In Figure A.2, the Run 3 approach is compared to the one used in Run 1 and Run 2. During Runs 1 and 2, since the trigger rate was restricted to a few kHz due to the limited high-rate capacity of the ALICE barrel detectors, the internal HPTDC buffers for the TOF, could collect all hits with a latency window (i.e. latency of the triggers reaching TOF) of 6500 ns and a matching window of 600 ns. Three different trigger levels (L0, L1 and L2a), received from the triggering hardware [112] were used to read hits and match them to the triggered event. In Run 3, Continuous readout was achieved by applying a strictly periodic trigger with frequency f_{T} and matching window $m_{\mathrm{w}} = 1/f_{\mathrm{T}}$. The

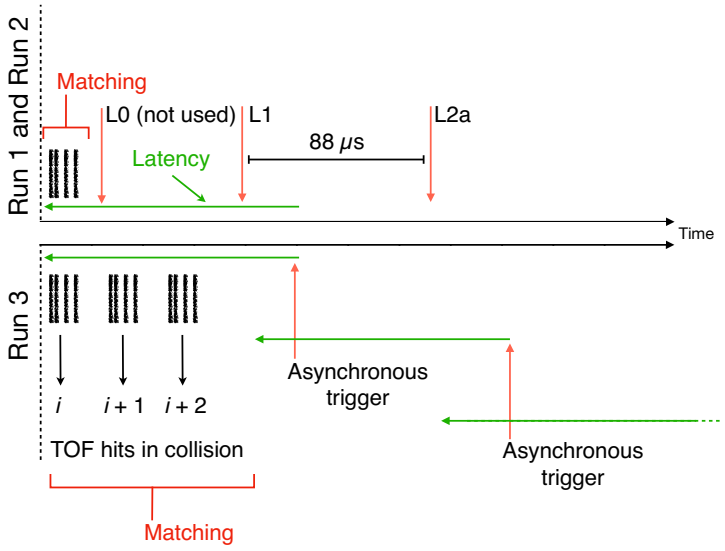

Figure A.2: HPTDC programming in Run 1 and Run 2 operations (top) and in Run 3 (bottom). In Run 3 the trigger levels (L0, L1 and L2a [111]) are replaced by a periodic trigger with a given frequency to achieve a continuous readout. All hits (small black lines) are read out and can be associated to physical events at a later stage.

HPTDC allows the readout trigger latency to be programmable over a large dynamic range and supports overlapping trigger windows. The optimal values were chosen to have a latency window lower than half of an LHC orbit period keeping a trigger frequency not too high. This assure a readout time lower than $1/f_{\mathrm{T}}$. After some optimization and commissioning phase an optimal operation point was fixed at $f_{\mathrm{T}} = 3/t_{\mathrm{LHC-orbit}} \sim 33$ kHz. So, in this configuration, all hits are read-out by using a trigger with a constant frequency, and setting latency and matching windows of 29.8 µs. In addition to this, in order to keep up with the planned increase of luminosity and of the interaction rate, a new Digital Readout Module 2 (DRM2), was designed [113]. This board is equipped with a faster link towards the DAQ system using the GBTx ASIC and the VTRX transceiver. During the Long Shutdown 2, the DRM2 board replaced the old DRM1. Moreover, the VME64 readout (40 MB/s) was also upgraded to VME64 2eSST protocol, yielding a data throughput of 160 MB/s over the VMEbus.

Finally, together with the hardware updates, reconstruction, quality control, and analysis software were also upgraded to meet the new requirements.

A.1.3 TOF performance with the upgraded apparatus

A.1.3.1 Calibrations in continuous readout

TOF calibrations are performed at different stages of data taking and reconstruction to reach the best performance in terms of efficiency, noise rejection and resolution or at the simulation level to reproduce with high accuracy the conditions of the data taking:

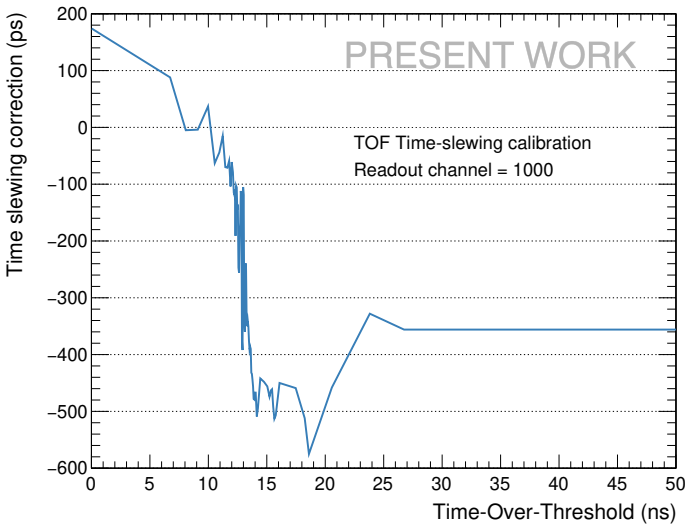

Figure A.3: Example of time slewing correction for one readout channel of the TOF detector (channel = 1000) obtained from the data taken with pp collisions at $\sqrt{s}$ = 13.6 TeV. The correction is extracted from this plot through an interpolation of this curve as done in [114].

1. The first level of calibration (DCS), from the TOF slow control system, consists of storing the TOF active channel map at the beginning of the run. An updated map is eventually sent if some channels are switched off during the run.

2. During the data taking a synchronous reconstruction on Event Processing Nodes (EPNs [115]) provides all the remaining calibrations (except for time slewing corrections, which require higher statistics), including:

   (a) LHC phase drift as a function of time, which is a global offset for all TOF channels;

(b) individual channel offsets;

(c) readout diagnostics looking at the frequency of decoding errors for each readout module.

3. Finally, an offline calibration (async), is performed with a better reconstruction quality and each channel offset is updated with the final time slewing correction, needed to re-absorb the delay in the leading time due to the finite rise time going above the threshold in the discriminator 2.4.2. An example of time slewing calibration for a single channel is reported in Fig. A.3

A.1.3.2 Time resolution extraction with the first Run 3 pp collisions at $\sqrt{s} = 13.6$ TeV

The analysis was carried out on data collected in 2022 with pp collisions at $\sqrt{s} = 13.6$ TeV. Only tracks with a TOF match are considered in the analysis. The expected time-of-flight of a track (t_{exp}) is computed during tracking for every mass hypothesis and $\sim 10^9$ events were used with an average interaction rate of ~ 500 kHz.

Since in the continuous readout scheme, the events are not any more triggered, the definition of the event coincides with the definition of collision vertex reconstructed from tracks. In order to guarantee that the reconstructed collision comes from a genuine pp event, the timing information from the two FT0 arrays must match the timing of the LHC bunch crossing. Good quality tracks were selected by discarding tracks with a $\chi^2/\text{NDF} > 2$, applying the cut separately. In addition, primary tracks, i.e. tracks that point to the primary vertex of the collisions, were selected to avoid the contribution of delayed signals from tracks coming from displaced secondary vertices. A dedicated study using a Monte Carlo simulation was carried out to optimize this selection criteria. Secondary tracks are discarded by requiring the distance of closest approach of the track to the primary vertex to be smaller than 7σ the resolution of primary particles.

The separation of the different particle species achieved with the TOF detector, computed under the mass hypothesis of the kaon, is shown in Fig. A.4 as a function of p. The pion and proton bands are clearly visible and separated at low momenta.

The detector resolution was measured with two methods. The first one is a self-

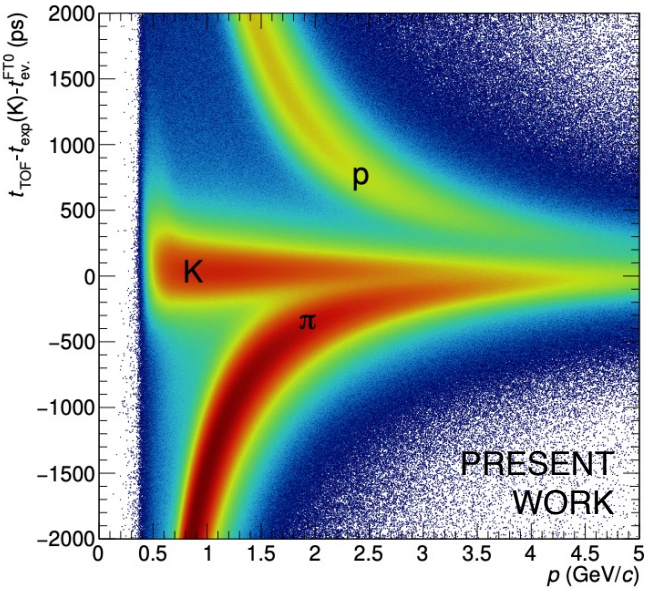

Figure A.4: Separation between particle species as a function of p for the kaon mass hypothesis as obtained with the $t_{\rm ev}^{\rm FT0}$.

consistent measurement by using the variable $\Delta\Delta t_{\rm TOF}$, defined from the difference between the time measured from two tracks matched with TOF in the same event. This strategy has the advantage of being independent on the definition of the collision. The second one, is a measure of the time resolution from $t_{\rm TOF} - t_{\rm exp} - t_{\rm ev}^{\rm FT0}$, by using the event times obtained with the FT0 detector. As previously done in [106], a Gaussian fit on the TOF signal was used to extract the detector timing resolution.

Two-track difference

The first method to obtain the time resolution of the TOF considers a self-consistent measurement based on the difference of two tracks matched to TOF.

A double-delta variable, between two tracks of the same event (i.e. same event time), was defined as:

$$\Delta\Delta t_{\rm TOF} = ((t_{\rm TOF} - t_{\rm exp}(\pi))_2 - t_{\rm ev}) - ((t_{\rm TOF} - t_{\rm exp}(\pi))_1 - t_{\rm ev}) \quad \text{(A.1)}$$

$$= (t_{\rm TOF} - t_{\rm exp}(\pi))_2 - (t_{\rm TOF} - t_{\rm exp}(\pi))_1 \quad \text{(A.2)}$$

The $\Delta\Delta t_{\rm TOF}$ is defined in such a way that it can be used without knowing the event collision time. This makes this variable independent of the event-by-event fluctuations

of the event collision time, which has a spread depending on the size of the colliding bunches.

The method consists in considering one track (1) as a *reference* in a well defined kinematic region and the other one (2) as a probe at a given momentum (p).

The resolution of $\Delta\Delta t_{\rm TOF}$ variable is thus given by two contributions:

$$\sigma_{\Delta\Delta t_{\rm TOF}}\ (p) = \sigma(p) \oplus \sigma(p_{\rm Reference}) = \sigma(p) \oplus \sigma_{\rm Reference} \tag{A.3}$$

Accordingly to Eq. A.1, each term contains a contribution to the time resolution given by the time-of-flight ($\sigma_{\rm TOF}$) measurement and another from the tracking ($\sigma_{\rm Tracking}(p)$):

$$\sigma(p) = \sigma_{\rm TOF} \oplus \sigma_{\rm Tracking}(p) \tag{A.4}$$

In particular, $\sigma_{\rm Reference}$ can be measured choosing a particle in the same kinematic region of the reference particles:

$$\sigma^{\rm Reference}_{\Delta\Delta t_{\rm TOF}} = \sigma_{\rm Reference} \oplus \sigma_{\rm Reference} = \sqrt{2} \cdot \sigma_{\rm Reference} \tag{A.5}$$

$$\sigma_{\rm Reference} = \sigma^{\rm Reference}_{\Delta\Delta t_{\rm TOF}}\ /\sqrt{2} \tag{A.6}$$

Once $\sigma_{\rm reference}$ is known, particles with a momentum different from the reference one can be considered. Taking into account Equation A.4, the calculations done in Eq. A.3 was repeated with particles under study in various p intervals.

The single particle resolution for each p is thus extracted as:

$$\sigma(p) = \sqrt{\sigma^2_{\Delta\Delta}(p) - \sigma^2_{\rm Reference}} \tag{A.7}$$

When the particle momentum is high enough (for pions $p > 1$ GeV/c, see Section A.1.3.3), the contribution from $\sigma_{\rm Tracking}$ becomes negligible, and only the TOF component contributes to the resolution.

In this analysis the *reference* resolution $\sigma_{\rm Reference}$ is extracted considering both tracks ($\rm track_1$ and $\rm track_2$) in a kinematic region of $600 < p < 700$ MeV/c. In Figure A.5, the distribution, fitted with a Gaussian function is reported.

For the dataset considered, the *reference* resolution is

$$\sigma_{\rm Reference} = 89.1 \pm 1.2 \text{ ps}. \tag{A.8}$$

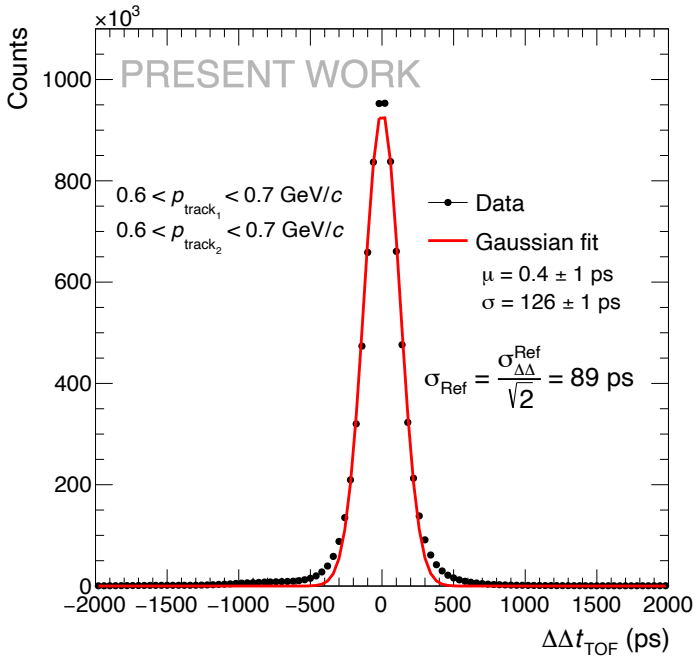

Figure A.5: $\Delta\Delta t_{\mathrm{TOF}}$distribution for the reference tracks, i.e. when both track$_1$ and track$_2$ have a momentum on the range $600 < p < 700$ MeV/c.

The procedure was repeated for particles in different momentum intervals and $\sigma_{\mathrm{Reference}}$ was used to calculate $\sigma_{\mathrm{TOF}} \oplus \sigma_{\mathrm{Tracking}}$ as a function of momentum.

The resolution of the $\Delta\Delta t_{\mathrm{TOF}}$ as a function of φ for the different η regions, considering both tracks in a momentum range of $1.4 < p < 1.5$ GeV/c, is reported in the upper plots of Figure A.6.

The results show a flat behavior as a function of φ in both alignment of the signal and resolution. The resolution instead decreases at larger pseudorapidity (consistently in both hemispheres), possibly due to the track propagation over longer distances. The $\Delta\Delta t_{\mathrm{TOF}}$ mean spread of $\langle\Delta\Delta t_{\mathrm{TOF}}\rangle$ per η intervals is shown in the bottom plot of Figure A.6. The spread of the signal average as a function of η can result in an extra smearing of the distribution when integrating over the full η acceptance. The obtained narrow shape of this plot makes it possible to appreciate the effects of the calibration procedure described in Section A.1.3.1.

Difference with the event collision time

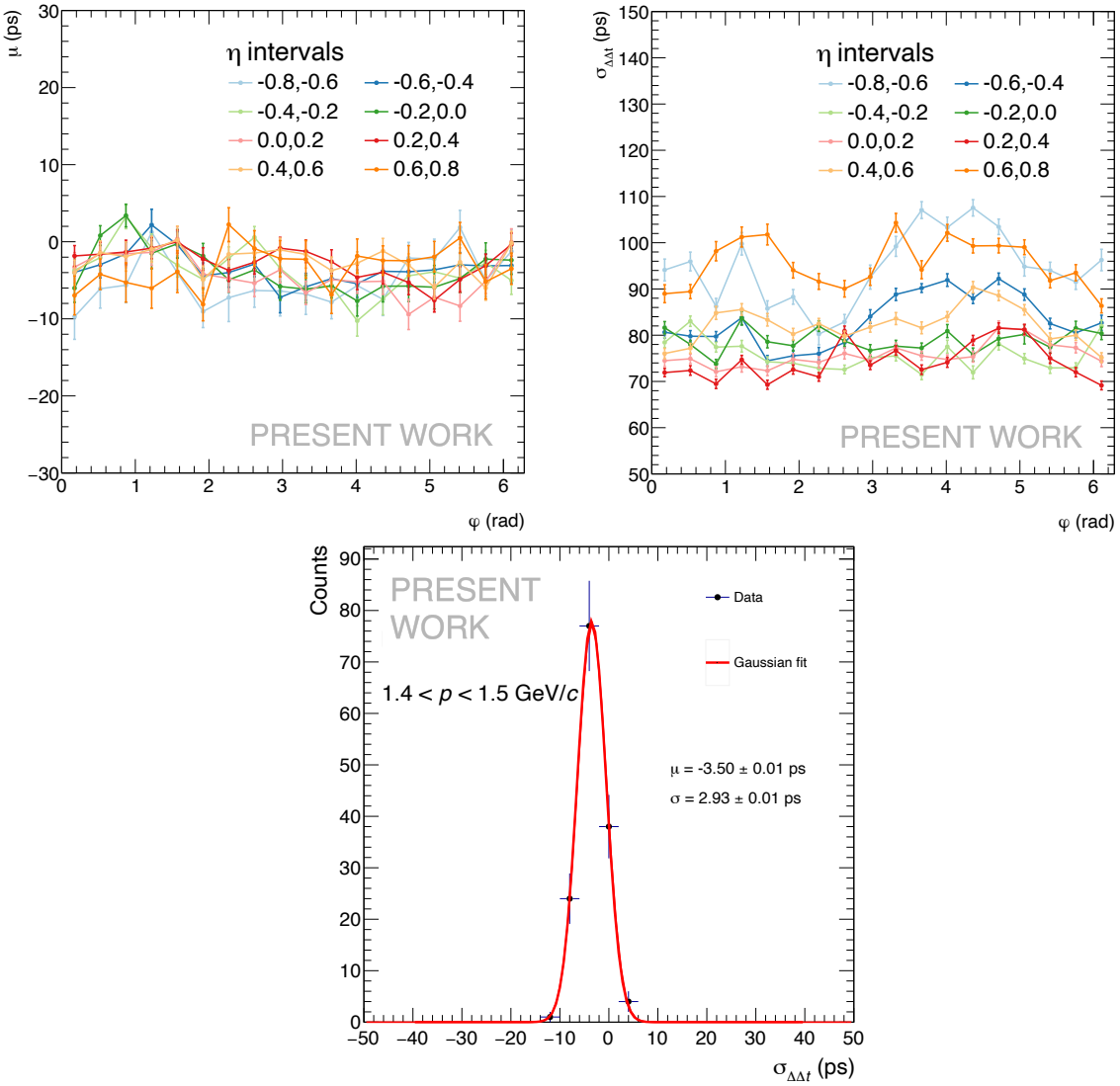

Figure A.6: Distribution of the mean value (up left) and sigma (up right) of the $\Delta\Delta t_{\mathrm{TOF}}$ as a function of φ for different η classes. $\langle\Delta\Delta t_{\mathrm{TOF}}\rangle$ spread of the $\Delta\Delta t_{\mathrm{TOF}}$ split per η intervals fitted with a Gaussian function (bottom).

The second method used to evaluate the TOF resolution is a more classical approach, equivalent to what is done in [106]. Specifically, the measurement of the separation between particle species $t_{\rm TOF} - t_{\rm exp} - t_{\rm ev}$was carried out using event collision times obtained from the FT0 detector. The resolution was extracted at high momenta ($1.4 < p < 1.5$ GeV/c), where the contribution due to tracking is negligible (A.1.3.3). The momentum interval was chosen such that the peaks for pions and kaons resulted well separated. In deriving the final result, the contribution of the FT0, which provides an event time resolution of approximately 17 ps, was subtracted.

A.1.3.3 Results

The overall results on the TOF timing resolution are reported for both methods.

The $\Delta\Delta t_{\rm TOF}$ distribution is reported in Figure A.7 (left) for the momentum range $1.4 < p < 1.5$ GeV/c. This is the highest momentum range, where the peaks relative to pions and kaon can be clearly distinguished, resulting to be the interval in which the best value of the time resolution is found. The plot is fitted with a Gaussian function to extract the $\Delta\Delta t_{\rm TOF}$ time resolution. After removing the contribution of reference A.8 (see Equation Eq. A.7) the TOF resolution in this momentum interval is found to be 83 ± 3 ps.

In Figure A.7 (right) the time resolution extracted for each p interval is reported. In this plot, the effect of the tracking on the TOF resolution ($\sigma_{\rm TOF} \oplus \sigma_{\rm Trk}$) is well visible. The resolution is shown to improve significantly from about 100 ps at around $p \sim 500$ MeV/c to better than 85 ps at higher momenta, where the contribution from tracking becomes almost negligible. Above 1.5 GeV/c the overlap of the bands of pions and kaons becomes significant, affecting the measurement.

As for the previous method, the resolution extracted considering the difference with the event collision time is reported in Figure A.8, for the $1.4 < p < 1.5$ GeV/c interval, where the two peaks for pions and kaons are well separated, and as a function of the momentum interval in which it was calculated.

As anticipated the contribution of the FT0 detector, expected to provide event time resolution with a resolution of $\sim$ 17 ps has been subtracted. This technique led to a TOF resolution of 78 ± 1 ps.

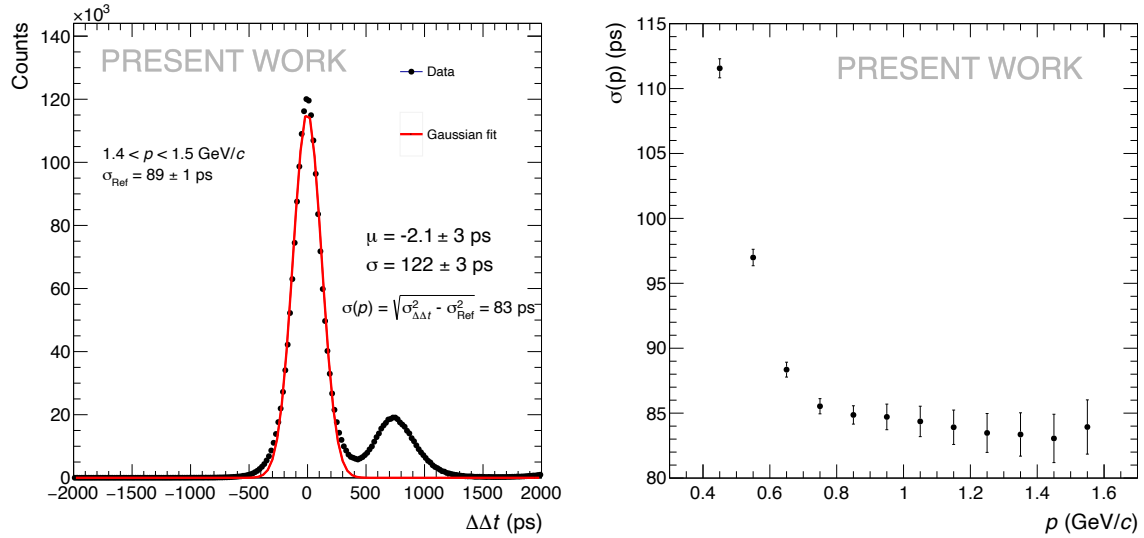

Figure A.7: $\Delta\Delta t_{\mathrm{TOF}}$distribution for both tracks in the momentum range $1.4 < p < 1.5$ GeV/c without removing the contribution of the reference track (left). The plot is fitted with a Gaussian function to extract the $\Delta\Delta t_{\mathrm{TOF}}$ time resolution. Resolution of the double delta distribution as a function of momentum p with $\sigma_{\mathrm{Reference}}$ already subtracted (right).

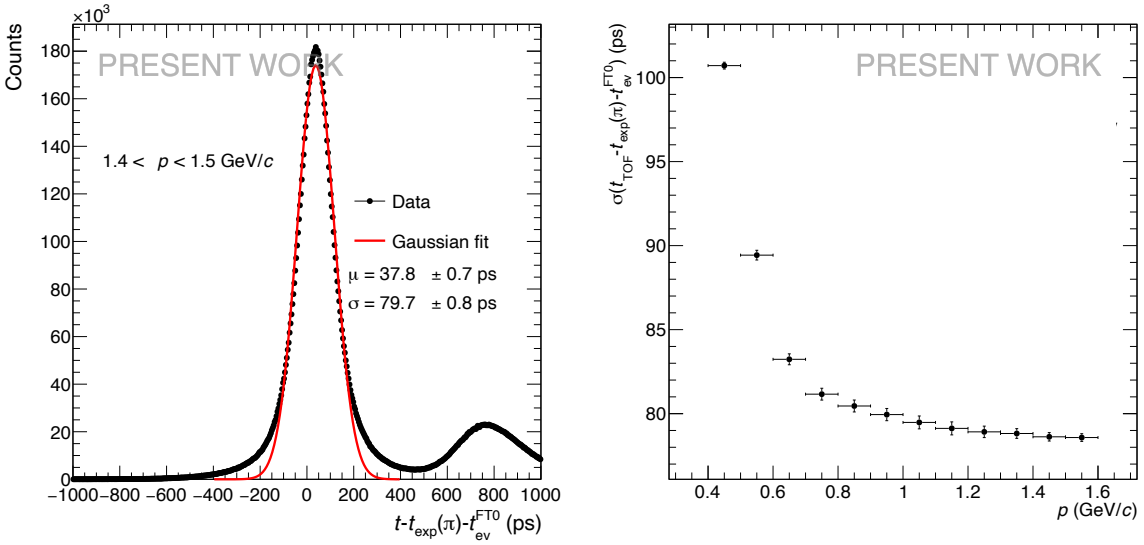

Figure A.8: $t_{\mathrm{TOF}} - t_{\mathrm{exp}}(\pi) - t_{\mathrm{ev}}^{\mathrm{FT0}}$in the momentum range $1.4 < p < 1.5$ GeV/c considering a cut on the event multiplicity (left). Resolution of the $t_{\mathrm{TOF}} - t_{\mathrm{exp}}(\pi) - t_{\mathrm{ev}}^{\mathrm{FT0}}$distribution as a function of p (right).

The two methods show results in agreement, yielding an overall resolution of about 80 ps. The slight difference in the results might be related to the non totally Gaussian behavior of TOF. Indeed relation Eq. A.7 is extracted in a Gaussian approximation, while the TOF signal shape is characterized by non-Gaussian tails. The effect of the non-Gaussian tails might be different for the two techniques, however this constitutes a second-order effect and could be studied in further work.

In conclusion, the results indicate the ALICE TOF detector stability and its reliable particle identification in the continuous readout mode of Run 3.

Appendix B

Time resolution in action: thin LGADs used for Particle IDentification (TOF) at the beam tests

LGADs were used during the beam test campaigns also to test SiPMs [97]. LGADs, placed at both ends of the telescope, were used to provide both the trigger for data acquisition and as a temporal reference for the time resolution measurements of the devices under test. During these tests, the uniformity of the response of SiPMs to different energies and particles has been studied.

The T10 beam facility at CERN-PS has the possibility to provide particles down to 1 GeV/c although the nominal species composition strongly varies: it is dominated by protons and pions (70/20%) at high energies, while a considerable fraction of positron is present at 1 GeV/c [116]. The momentum resolution is estimated to be $\sim$5%.

The ability of the beam test setup in separating particles species at such energies, thanks to the excellent time resolution of LGADs placed 24 cm apart, was exploited.

In Figure B.1 the difference of the measured time between the two LGADs is reported for beam momentum of 1.5 and 1.0 GeV/c respectively. The curve is fitted considering the sum of two q-Gaussian distributions. The peak on the right represents protons

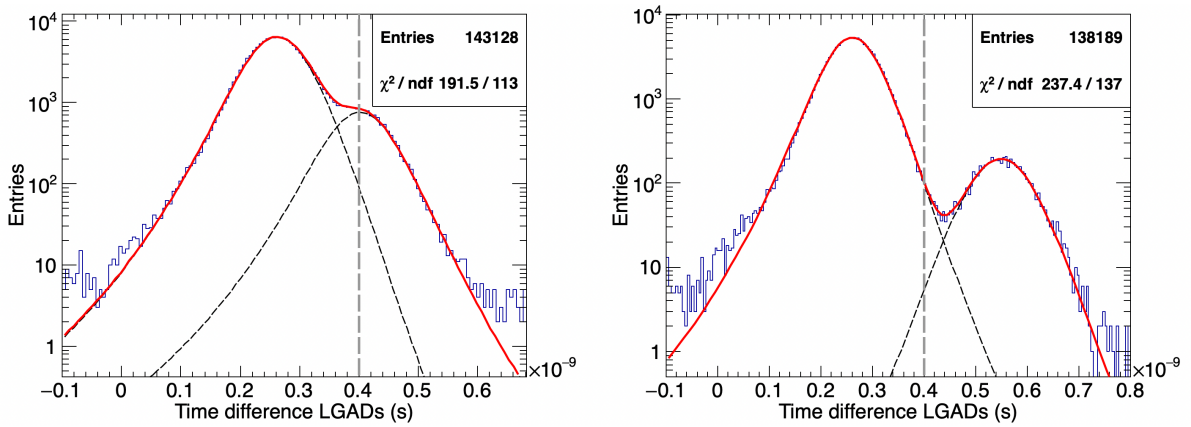

Figure B.1: Measured time differences between first and last LGAD sensor for 1.5 GeV/c (left) and 1.0 GeV/c (right) beam momentum. The fit is performed with the sum of two asymmetric q-Gaussian.

while the peak on the left corresponds to electrons and pions. The cut to discriminate electrons and pions from protons is made considering a distance of 3σ from the mean of the electrons/pions peak. Choosing events with a time difference ≥ 0.40 ns (both at 1 GeV/c and 1.5 GeV/c), it is possible to select protons with an estimated purity of 96% and 91%, respectively.

Appendix C

LGADs coupled to a digital readout electronics

In tests done until the beginning of 2024, sensors have been always studied using an oscilloscope readout (5.1.2), in order to investigate the performance of the sensors itself with negligible contribution of the electronics and to have the possibility to extract much useful information performing an analysis directly on the recorded signal waveforms. Nevertheless in the experiment a readout electronics is needed. For this reason in a beam test conducted this year, a full front-end and readout electronic chain was connected to the sensors in order to test the new electronics chain and start to investigate the contribution of the electronics and the overall resolution of the system composed by the sensor and the full electronic chain.

C.1 Setup with sensors connected to the electronics

In Figure C.1, few photos of the setup are reported. For each data acquisition up to four sensors were aligned to the beam in a telescope frame and the whole setup was enclosed in a dark environment, as explained in section 5.1.2. All FBK and HPK LGADs were mounted on a V1.4-SCIPP-08/18 board, containing a wide bandwidth (2 GHz) and low-noise inverting trans-impedance amplifier with a Trans-Impedance (TI_{SC}) of 470 Ω. The board was followed by a second amplification stage, or a mini-circuit LEE39+[90] or

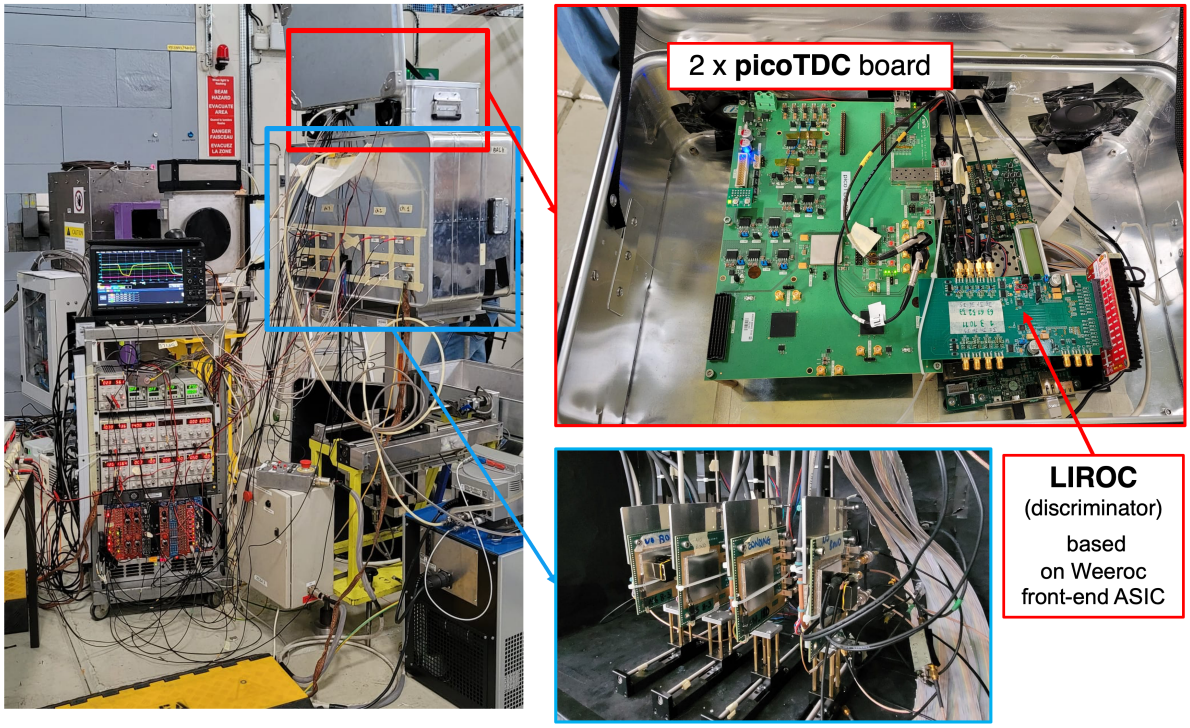

Figure C.1: Setup in the T10 beam test facility at CERN (left), together with a zoom on the Liroc and PicoTDC boards placed in the box at the top of the setup (red square) and on the sensors aligned to the beam (blue square).

Gali52+[92], with a gain factor of around 12 and 13, respectively.

In this case the second stage amplifiers were followed by a Liroc [117] board and a PicoTDC [118] board, placed in the smaller box on the top of the setup.

Liroc is a LIDAR dedicated multi-channel readout chip prototype discriminator, produced by Weeroc [119] , with a high bandwidth, which allow a fast counting and time measurements.

The PicoTDC board provides a PolarFire FPGA to implement the logic that controls two PicoTDC ASICs, hosted on board. In particular, the PicoTDC is a 65 nm CMOS technology ASIC designed by CERN and readapted at INFN of Bologna for the TRM2 of the ALICE TOF upgrade [120], that provides high-resolution measurements with a high channel counts. The two PicoTDCs thus receive sub-LVDS signals through 2 FMC connectors, where the Liroc is plugged, then decode the hit signals received in each input

channel, elaborate the data and collect them into FIFO memories, waiting to be read out. Each PicoTDC provides 64 input channels and a time resolution of 3.05 ps LSB. The board's features were controlled through Ethernet communication protocols.

C.1.1 Trigger configuration and data acquisition

A scheme of the full electronic chain from the detector to the readout, is reported in the top panel of Figure C.2.

In the described setup configuration, the trigger was provided by the first LGAD hit by the beam. The signal from this LGAD, after amplification by the SantaCruz board and a second stage amplifier, was sent to a CAEN discriminator, sending in output a square wave, which remain high for as long as the amplified LGAD signal (negative polarity) is below an appositely set threshold of -10 mV. This output was then stretched and delayed by a CAEN dual delay module [121] to meet the trigger input requirements of the PicoTDC.

The signals of all the LGADs under study were sent directly to the Liroc discriminator and the processed signal was subsequently sent to the PicoTDC board. The PicoTDC, after receiving the trigger signal of the first LGADs records data within a 250 ns matching window starting 600 ns before the trigger. These windows were chosen to ensure optimized data acquisition for the duration of the particle spill delivered by the PS accelerator at the T10 facility. An oscilloscope real-time view of the trigger signal entering in the PicoTDC, an analog signal of one LGAD under test and a representation of the matching an latency windows is shown in the bottom panel of Figure C.2.

C.2 Fast QA analysis and preliminary results

A fast Quality Assurance (QA) analysis was implemented to have a fast check on the taken data. An example of outcome plots generated by the analysis are reported in Figure C.3.

A first check was done on the number of hits for each dataset (1): since the number of hits corresponds to the number of rising and falling edges passing the set threshold from any of the channels, an even number of hits indicate that for the signals both rising

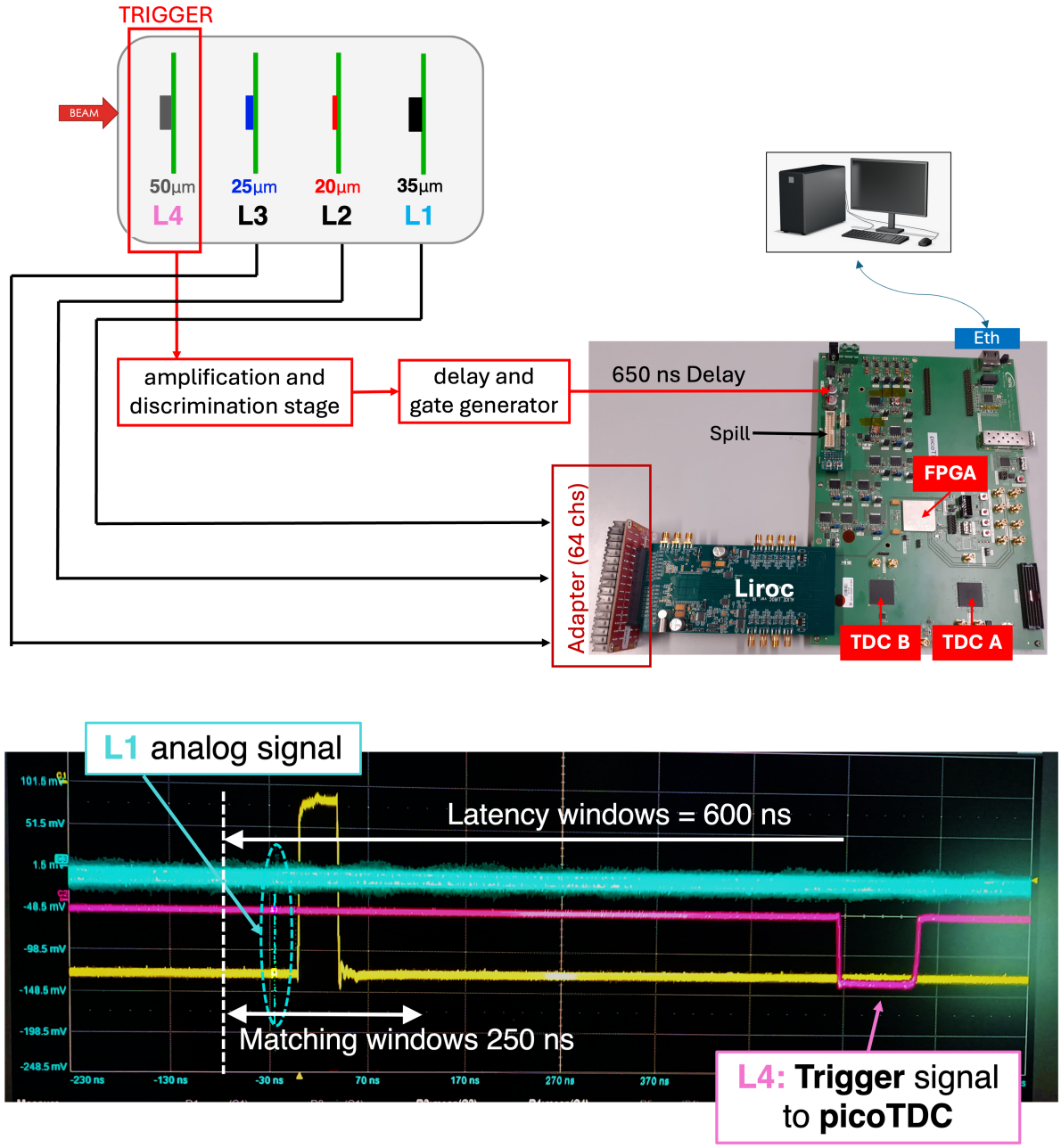

Figure C.2: Scheme of the connection between the sensors and the full electronic chain (top). Oscilloscope real-time view (bottom) of the trigger signal (pink) entering in the PicoTDC, an analog signal of one LGAD under test before entering the Liroc (light blue), with the matching an latency windows (white) superimposed. Just for reference, the yellow waveform corresponds to the trigger signal directly out the CAEN discriminator (-10 mV threshold) before being stretched and delayed to be handled by the PicoTDC.

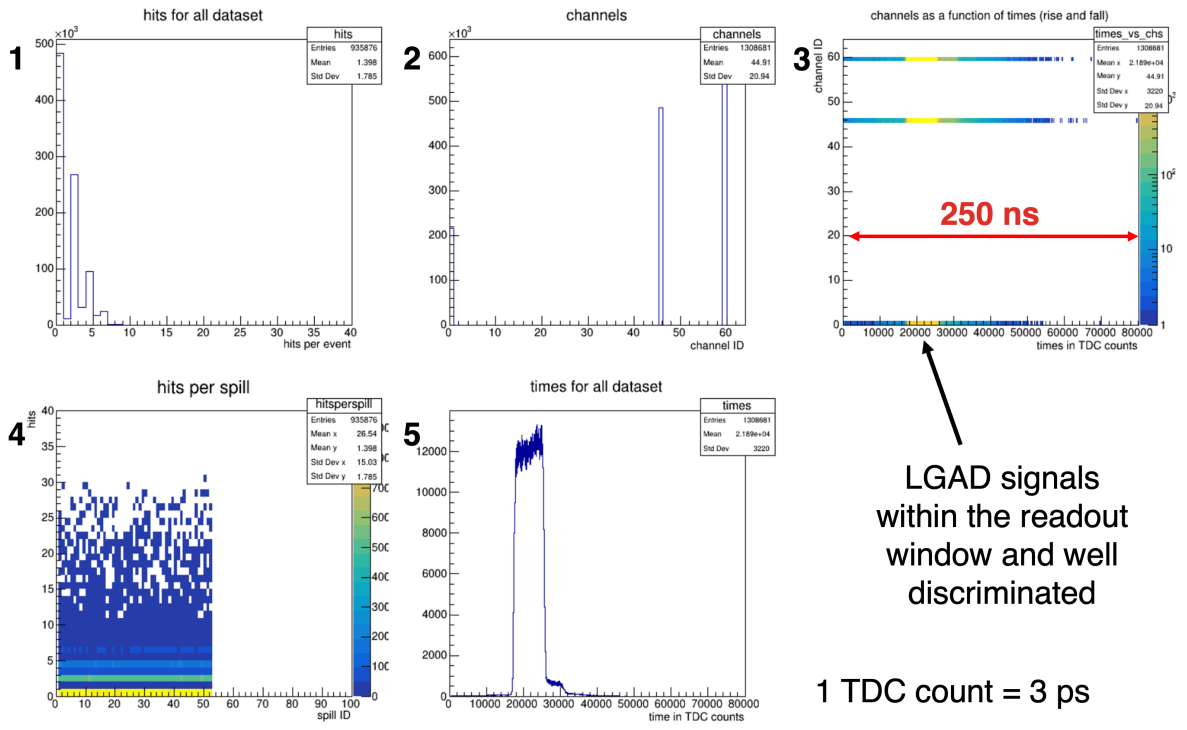

Figure C.3: Example of QA fast analysis outcome (see text for an explanation of each plot).

and falling are recorded and a peak on 8 for example indicate that the sensors are all well aligned to the trigger; on the other hand a peak on zero indicates the inefficiency of the trigger. The signal input channel ID (2), corresponding to the PicoTDC channel number to which each LGAD was connected, was plotted to verify that all connections between the various stages of the electronic chain were correctly established. The distribution of the threshold crossing time of the signals coming from the different channels (3) was particularly important to verify that all signals fell within the readout window and were correctly discriminated (see the yellow region). Indeed if the acquisition window is well defined, the rising and falling times are expected to cumulate in a given interval. Finally, the number of hits per spill (4) and the cumulative threshold crossing times (5), given by the projection of (3) were examined across the entire dataset. This allowed for a quick assessment of any changes in acquisition behavior. In general all these checks were useful to optimize the full data acquisition process.

A very preliminary offline analysis on the data acquired was carried out, mainly to

have a first estimation of the overall time resolution of the sensors coupled to the full electronic chain. As done in previous studies (5.1), to extract the time resolution of a single LGAD, a system with three sensors and three differences between the arrival time of each pair of detectors has been considered. An example of the time difference distributions is reported in Figure C.4.

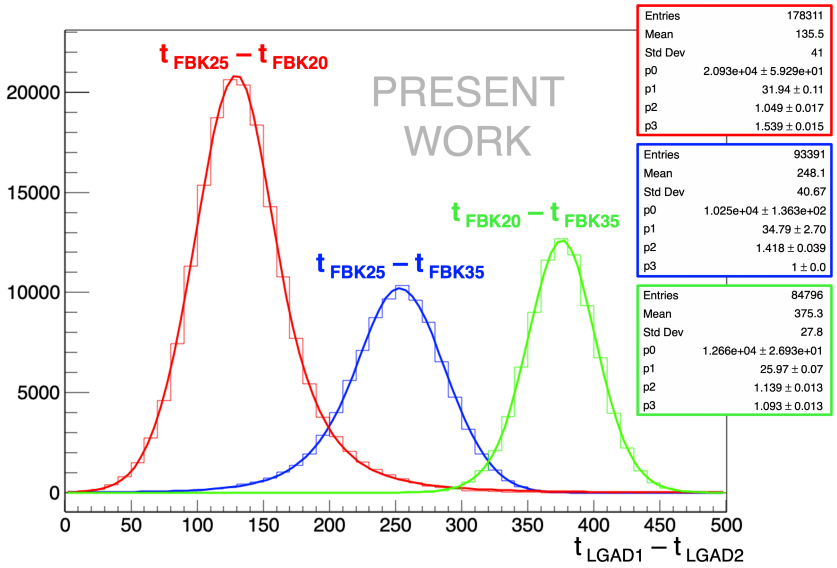

Figure C.4: Example of the distributions of three differences between the arrival time of each pair of detectors. On the horizontal axis of the plot the time is reported in TDC count, where each TDC count corresponds to 3 ps. The distributions are not corrected for time slewing.

Here a cut to consider only the first hit as rising edge and the second hit as falling edge was done, but for a more refined analysis some cuts should be applied considering only hits inside a given window and implementing a Time-Over-Threshold (ToT) correction. In this particular example a resolution of:

$$\begin{aligned} \sigma_{FBK20} &= 46.7 \pm 57\, ps \\ \sigma_{FBK25} &= 83.6 \pm 8\, ps \\ \sigma_{FBK35} &= 62.4 \pm 6\, ps \end{aligned} \tag{C.1}$$

were found. In these values the contributions from all the elements of the electronic chain are present: sensor, amplification, discrimination (Liroc) and digitization

(PicoTDC). While, as already mentioned the one from the PicoTDC is of a few picoseconds, the one from Liroc in this case is substantial. Better results are expected with an ad-hoc discriminator. Note that the values of the voltages here are not the best ones for each detector, so comparison between the different thicknesses can not be done.

In summary, these initial tests conducted with the full electronic chain primarily aimed at testing the functioning of such electronics. However, they allowed us to optimize the data acquisition process, the software to control the whole system, and the trigger system, resulting in a fully operational setup for future beam tests. From these tests, we gained a rough estimation of the detector performance when connected to the electronics. The analysis is still ongoing and a more refined analysis should be done, applying, for example, some more specific cuts to the signals and implementing a time slewing correction. Nevertheless, the Liroc discriminator was found to be a not optimal choice for handling LGAD signals. Based on the outcomes of this test, a new optimized discriminator board is currently being designed at the INFN laboratories in Bologna for this purpose.

Appendix D

Construction of a tracking telescope

As discussed in Section 5.4, future tests with LGAD matrices will require tracking information to, for example, investigate edge effects, evaluate different inter-pad configurations, and assess sensor efficiency. To address this, a tracking telescope is currently being built using ALTAI sensors [123]. An ALTAI is a Monolithic Active Pixel Sensor (MAPS) with a structure similar to the more widely known ALPIDE sensor [124]. Specifically, the ALTAI sensor consists of 512×1024 pixels, each measuring 28×28 µm, covering a total area of 15×30 mm^2. Initial tests were conducted to characterize the sensors and determine their optimal operating ranges. Four sensors were selected for the integration of the telescope, and a complete data acquisition based on EUDAQ [122] software framework was set. The setup was then tested in stages, first using cosmic rays and later with at a beam test facility, to validate its functionality and achieve a fully operational system.

D.1 Laboratory measurements

As a first step, ALTAI sensors composing the telescope were characterized. Figure D.1 shows a photo of one of the sensors during characterization.

The primary objective was to determine the optimal operating range for each sensor, ensuring consistent responses across all sensors and verifying the functionality of both the structures and the front-end electronic boards. A total of five sensors were characterized.

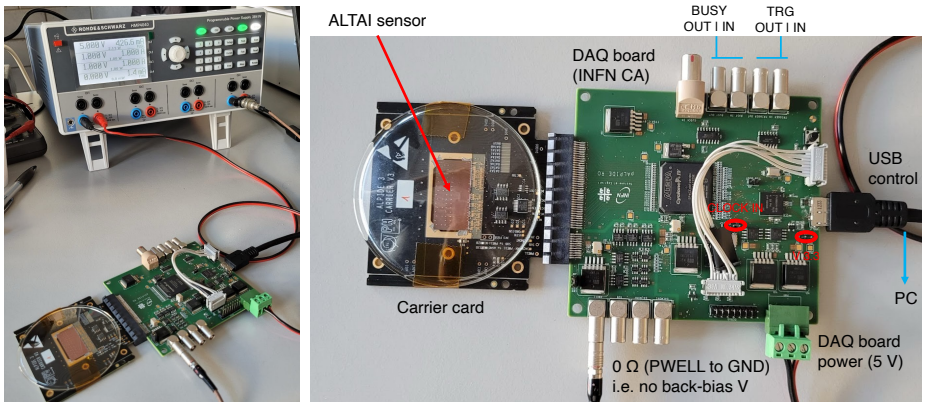

Figure D.1: ALTAI sensor, connected to the carries card and to the DAQ board [124], biased by a power supply during the characterization measurements.

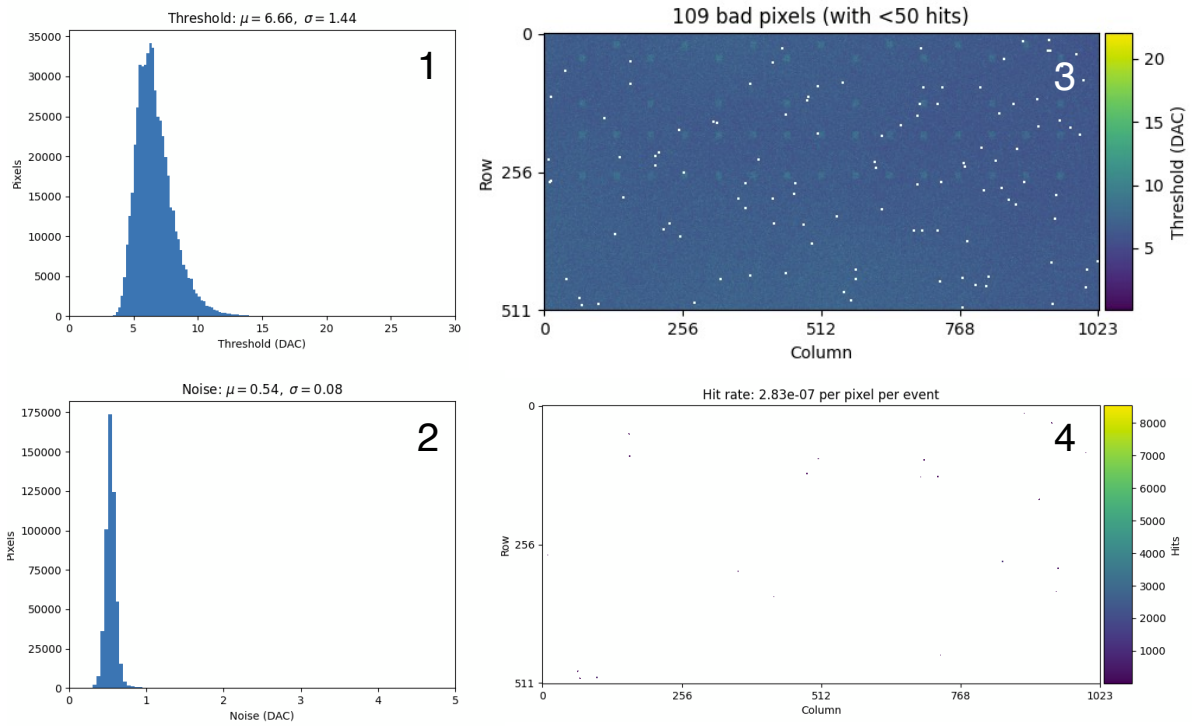

Figure D.2: Example of output plots from the ALTAI characterization measurements. Charge threshold (1) and Temporal Noise (2), distribution of the thresholds per pixel (3), fake-hit rate (4) for one sensor are reported.

Figure D.2 provides an example of some key measurements taken during this process. A threshold scan was performed by pulsing the pixels. Indeed the in-pixel discriminator charge threshold is defined by three front-end biasing parameters and common to all pixels. For a given combination of these three parameters, each pixel charge threshold can be determined via pulsing capacitance C_{inj} on the pixels by injecting N_{inj} times selected test charges Q_{inj}. This was done by applying a negative voltage step on the injection capacitor C_{inj}. For each test charge Q_i, out of N_{inj} total injections, N_i exceed the threshold, resulting in a pixel hit. The charge threshold is finally defined as the charge at which a pixel fires in 50% of the total injections. For each injected charge, the hit-detection probability p_{hit} of the pulsed pixel was then calculated. Assuming a Gaussian distribution of the electronic noise, the response function of the pixel can be written as:

$$p_{\text{hit}}(Q_{\text{inj}}) = \frac{1}{2}\left(1 + \text{Erf}\left[\frac{Q_{\text{inj}} - \mu}{\sqrt{2}\cdot\sigma}\right]\right) \tag{D.1}$$

where μ is the **charge threshold** and σ the **Temporal Noise** [125]. The values for μ and σ were extracted pixel by pixel. An example of distribution of thresholds and noise are shown in Figure D.2 (1) and (2), respectively. The average of the threshold distribution is defined as the chip threshold. This measurement is useful also to assess the response uniformity of the pixels. An example of map with the threshold distribution per pixel is shown in Figure D.2 (3).

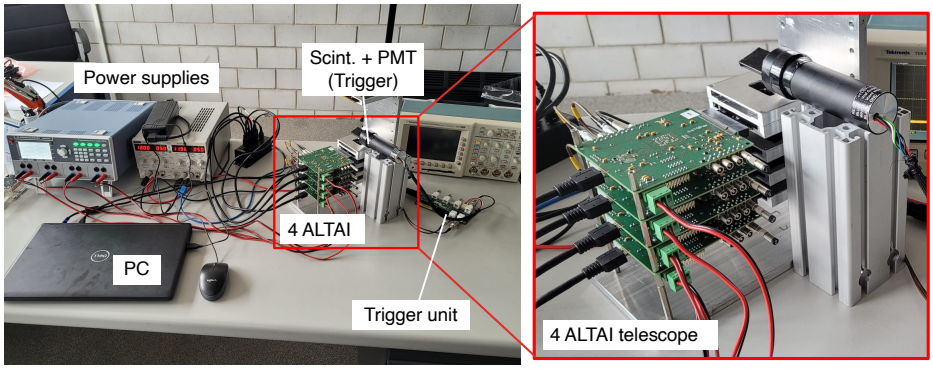

Figure D.3: Cosmic rays setup to test the electronic connections and the DAQ system.

In addition the **Fake-Hit Rate (FHR)** (Figure D.2 (4)) was measured for each

sensor. This is defined as the number of hits per pixel per event (i.e. trigger) in absence of any external stimulus. The fake-hit rate is measured by sending a number of triggers (N_{trg}) to the chip without providing any external pulse, where the number of hits N_{hit} is defined as:

$$\text{FHR}_{\text{meas}} = \frac{N_{\text{hit}}}{N_{\text{pix}} \cdot N_{\text{trg}}} \tag{4.7}$$

where N_{pix} is the number of pixels in the sensor. Increasing the threshold or decreasing the noise lowers the fake-hit probability. The measured fake-hit rate was on the order of 10^{-7} hits per pixel per trigger for all sensors for all the possible thresholds.

Following these tests, the sensors exhibiting the most consistent responses were selected to construct the telescope, which was subsequently tested using a cosmic ray setup. This test primarily aimed to verify the connections and the functionality of the data acquisition system. The setup used for these tests is shown in Figure D.3.

The trigger was given by a scintillator attached to a Photo Multiplier (PM) aligned to the 4 ALTAI sensors and connected to a Trigger Unit giving the trigger signal to all the ALTAIs through a daisy chain. From the data acquisition of about 20 hours, some correlated tracks between the different planes were acquired.

D.2 Preliminary test beam measurement

Some tests were done with particle beam at the T10 beam line at CERN PS facility at the end of June 2024.

The setup, reported in Figure D.4, was totally equivalent to the one in the laboratory, the telescope in this case was placed horizontally on a movable DESY table, in order to align it to the beam.

Preliminary measurements were obtained during the beam test applying various threshold voltages. An example of a hit map, along with the corresponding residuals in both the horizontal and vertical directions, is shown in Figure D.5.

In addition, one ALTAI sensor was selected as the Device Under Test (DUT) to provide a first estimation of the **tracking efficiency** and **spatial resolution** achievable at different thresholds set on the sensors. As shown in Figure D.6, the efficiency was

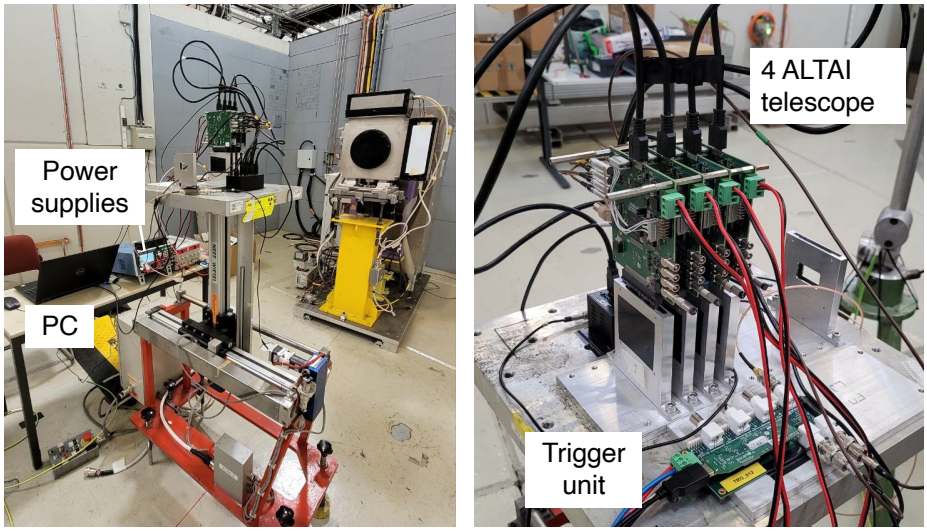

Figure D.4: Test beam setup: the ALTAI telescope is aligned to the beam, the whole DAQ and readout system was inside the experimental room. The PM trigger is not shown in the photo, but was placed in front-of the setup.

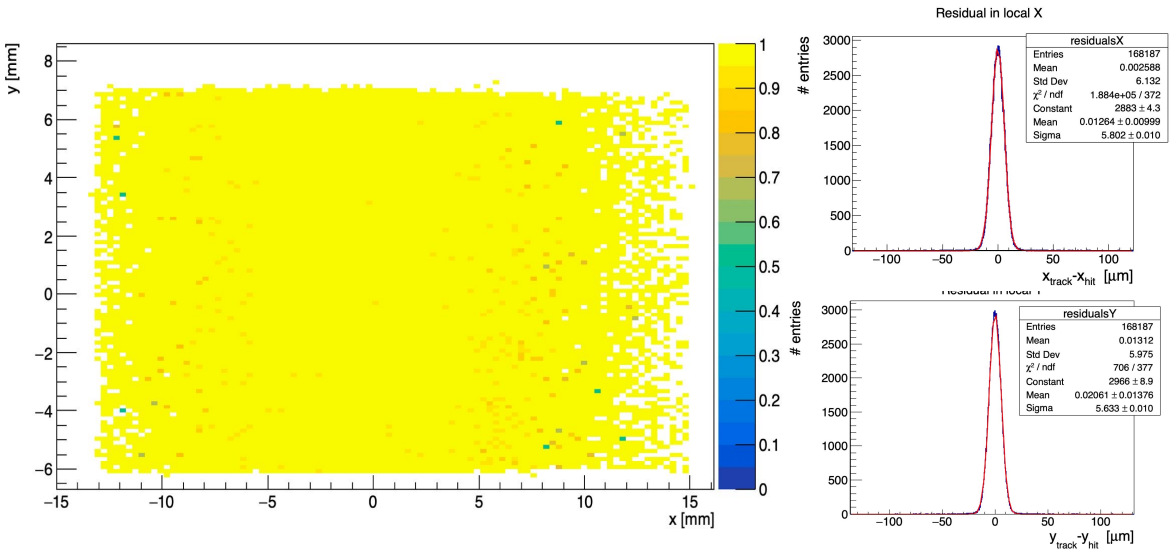

Figure D.5: Example of global efficiency map (left) with the corresponding residuals (right) in both the horizontal and vertical directions.

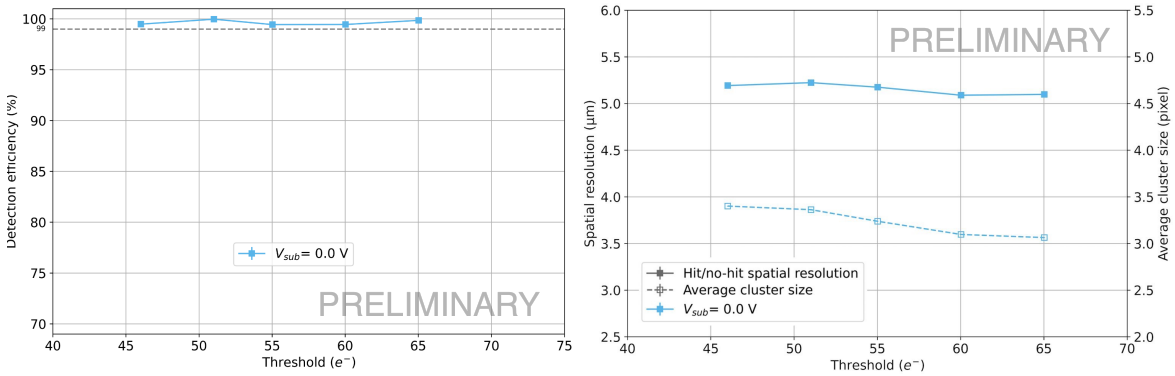

Figure D.6: Preliminary measurement of the detection efficiency (left) and spatial resolution (right) for different chosen thresholds (in electrons).

above 99% for all applied thresholds, and, except for the point at the highest threshold value, the spatial resolution was of the order of 5 µm, with an average cluster size between 6 and 7.

These results are preliminary, and as previously mentioned, the main goal was to validate the sensors, the setup, and the entire DAQ system. The next steps will involve integrating the various sensors to be tested with the telescope into the system.

Bibliography

[1] ECFA Detector R&D Roadmap Process Group, The 2021 ECFA detector research and development roadmap, CERN-ESU-017, Geneva, 2020, https://cds.cern.ch/record/2784893

[2] ALICE Collaboration, K. Aamodt et al., "The ALICE experiment at the CERN LHC", JINST 3 (2008) S08002.

[3] arXiv:1812.06772v2 [hep-ph] 25 Feb 2019

[4] ALICE Collaboration, "Letter of intent for ALICE 3: A next-generation heavy-ion experiment at the LHC, CERN-LHCC-2022-009, LHCC-I-038," arXiv:2211.02491 [physics.ins-det], CERN-LHCC-2022-009, LHCC-I-038, November 2022.

[5] ALICE collaboration. The ALICE experiment - A journey through QCD. 2022,arXiv:2211.04384.

[6] U. W. Heinz and M. Jacob, "Evidence for a new state of matter: An assessment of the results from the CERN lead beam programme," arXiv:nucl-th/0002042.

[7] N. Tsoupas, H. Huang, W. W. MacKay, F. Meot, T. Roser, and D. Trbojevic, "BNL Alternating Gradient Synchrotron with Four Helical Magnets to Minimize the Losses of the Polarized Proton Beam," Phys. Rev. ST Accel. Beams, vol. 16, no. 4, p. 043501, Apr. 2013, doi: 10.1103/PhysRevSTAB.16.043501.

[8] I. Arsene et al., "Quark–gluon plasma and color glass condensate at RHIC? The perspective from the BRAHMS experiment," Nuclear Physics A, vol. 757, no. 1–2, pp. 1–27, Aug. 2005, doi: 10.1016/j.nuclphysa.2005.02.130.

[9] ALICE Collaboration, "Recent results from ALICE at the LHC," arXiv:2305.12345 [hep-ex].

[10] J. D. Bjorken, "Highly relativistic nucleus-nucleus collisions: The central rapidity region," Phys. Rev. D, vol. 27, pp. 140–151, 1983, doi: 10.1103/PhysRevD.27.140.

[11] A. Andronic et al., "Heavy-flavor and quarkonium production in the LHC era: from proton–proton to heavy-ion collisions," Eur. Phys. J. C76 (2016), no. 3, 107, arXiv:1506.03981 [nucl-ex].

[12] A. Beraudo et al., "Heavy flavor production in high-energy nuclear collisions: theory overview," arXiv:1803.03824 [nucl-th].

[13] S. Plumari, V. Minissale, S. K. Das, G. Coci, and V. Greco, "Λ_c enhancement from coalescence and fragmentation in relativistic heavy-ion collisions," Eur. Phys. J. C78 (2018), no. 4, 348, arXiv:1712.00730 [hep-ph].

[14] R. J. Fries, V. Greco, and P. Sorensen, "Coalescence models for hadron formation from quark–gluon plasma," Ann. Rev. Nucl. Part. Sci. 58 (2008), pp. 177–205, arXiv:0807.4939 [nucl-th].

[15] LHCb Collaboration, "Observation of a new exotic hadron in the J/ψ-pair mass spectrum," arXiv:2107.10093 [hep-ex].

[16] J. Zhao, H. He, and P. Zhuang, "Searching for Ξ_{cc} in Relativistic Heavy Ion Collisions," Phys. Lett. B771 (2017), pp. 349–353.

[17] H. He, Y. Liu, and P. Zhuang, "Ω_{ccc} production in high energy nuclear collisions," Phys. Lett. B746 (2015), pp. 59–63.

[18] A. Berezhnoy, V. Kiselev, A. Likhoded, and A. Onishchenko, "Doubly charmed baryon production in hadronic experiments," Phys. Rev. D57 (1998), pp. 4385–4396, arXiv:hep-ph/9710339.

[19] A. Andronic et al., "The thermal model on the verge of the ultimate test: particle production in high-energy nuclear collisions," Phys. Lett. B797 (2021), pp. 134836, arXiv:2001.09947 [hep-ph].

[20] NA38 Collaboration, "J/Ψ suppression in pA and nucleus-nucleus collisions at 200 GeV," Z. Phys. C38 (1988), pp. 117–121.

[21] ALICE Collaboration, J. Adam et al., "Centrality dependence of J/ψ production in p-Pb collisions at $\sqrt{s_{NN}} = 5.02$ TeV," Phys. Lett. B766 (2017), pp. 212–224, arXiv:1606.08197 [nucl-ex].

[22] P. Braun-Munzinger and J. Stachel, "(Non)thermal aspects of charmonium production and a new look at J/Ψ suppression," Phys. Lett. B490 (2000), pp. 196–202.

[23] R. L. Thews, M. Schroedter, and J. Rafelski, "Enhanced J/Ψ production in deconfined quark matter," Phys. Rev. C63 (2001), p. 054905.

[24] J. Adam et al., "Direct photon production in Pb-Pb collisions at $\sqrt{s_{NN}} = 2.76$ TeV," Phys. Lett. B754 (2016), pp. 235–248.

[25] V. Lysov, S. Pasterski, and A. Strominger, "Low's Subleading Soft Theorem as a Symmetry of QED," Phys. Rev. Lett. 113 (2014), no. 11, p. 111601.

[26] F. Bloch and A. Nordsieck, "Note on the Radiation Field of the electron," Phys. Rev. 52 (1937), pp. 54–59.

[27] L. Pancheri et al., "Time-of-flight measurements with monolithic pixel sensors," IEEE Trans. Electron Dev., Vol. 67, No. 6, June 2020, doi: 10.1109/TED.2020.2985639.

[28] W. Snoeys et al., "A large monolithic CMOS pixel sensor for high energy physics applications," NIM A 871 (2017), pp. 90–96, doi:10.1016/j.nima.2017.07.046.

[29] H. F. W. Sadrozinski, A. Seiden, and N. Cartiglia, "4-Dimensional Tracking with Ultra-Fast Silicon Detectors," 2017, arXiv:1704.08666 [physics.ins-det].

[30] S. White et al., "Radiation hardness studies of 3D silicon sensors for the ATLAS upgrade," IEEE Trans. Nucl. Sci., Vol. 64, No. 9, pp. 2345-2352, Sept. 2017, doi: 10.1109/TNS.2017.2714953.

[31] ALICE Collaboration, "Time-of-flight calibration in the ALICE detector," ALICE internal note, 2021.

[32] M. Ferrero et al., "Radiation damage effects on silicon photomultipliers," JINST 14 (2019), no. 07, P07009, doi:10.1088/1748-0221/14/07/P07009.

[33] S. Meroli, F. Corsi, and G. Mazza, "Noise characterization of silicon photomultipliers," NIM A 635 (2011), pp. 101-105, doi:10.1016/j.nima.2011.01.072.

[34] G. Collazuol et al., "Characterization of Silicon Photomultipliers for Time-of-Flight PET," NIM A 581 (2007), pp. 461-464, doi:10.1016/j.nima.2007.08.110.

[35] C. Tenllado, "Data acquisition systems for radiation detectors," Nucl. Instrum. Methods Phys. Res. A, vol. 890, pp. 59-69, 2018, doi: 10.1016/j.nima.2018.02.093.

[36] Passage of Particles Through Matter, Revised August 2023 by D.E. Groom (LBNL) and S.R. Klein (NSD LBNL; UC Berkeley). `https://pdg.lbl.gov/2023/reviews/rpp2023-rev-passage-particles-matter.pdf`

[37] Stopping Powers and Ranges for Protons and Alpha Particles, ICRU Report No. 49 (1993);

[38] D.E. Groom, N.V. Mokhov, and S.I. Striganov, Muon stopping-power and range tables: 10 MeV–100 TeV, Atomic Data and Nuclear Data Tables 78, 183–356 (2001).

[39] W. H. Barkas, W. Birnbaum and F. M. Smith, Phys. Rev. 101, 778 (1956).

[40] Fabjan C.W. and Herwig S. Particle Physics Reference Library, Volume 2: Detectors for Particles and Radiation. Springer, Gewerbestrasse 11, 6330 Cham, Switzerland, 2020.

[41] S. M. Sze and M.-K. Lee. Semiconductor Devices: Physics and Technology. John Wiley Sons, New York, 3rd edition, 2012. ISBN 978-0470-53794-7.

[42] G. Lutz. Semiconductor Radiation Detectors: Device Physics. Springer Berlin Heidelberg, 2007. ISBN 978-3-540-71678-5

[43] G. F. Knoll, Radiation Detection and Measurement, 3rd ed. John Wiley and Sons, New York, 2000. http://www.slac.stanford.edu/spires/find/books/www?cl=QCD915:K55:2000.

[44] W. Shockley, "Currents to conductors induced by a moving point charge," Journal of Applied Physics 9 no. 10, (1938) 635–636. http://dx.doi.org/10.1063/1.1710367

[45] Z. He, "Review of the Shockley-Ramo theorem and its application in semiconductor gamma-ray detectors," Nuclear Instruments and Methods in Physics Research Section A 463 no. 1, (2001) 250 – 267. http://www.sciencedirect.com/science/article/pii/S0168900201002236

[46] J. C. W. Song and L. S. Levitov, "Shockley-ramo theorem and long-range photocurrent response in gapless materials," Phys. Rev. B 90 (Aug, 2014) 075415. https://link.aps.org/doi/10.1103/PhysRevB.90.075415

[47] A. Alberigi Quaranta, M. Martini, and G. Ottaviani, "The pulse shape and the timing problem in solid state detectors - a review paper," IEEE Trans. Nucl. Sci. 16N2 (1969) 35–61.

[48] Seo, DK., Hoffmann, R. Direct and indirect band gap types in one-dimensional conjugated or stacked organic materials. Theor Chem Acc 102, 23–32 (1999). https://doi.org/10.1007/s002140050469

[49] A. G. Chynoweth, Phys. Rev. 109, 1537 (1958).

[50] D. Massey, et al., Temperature dependence of impact ionization in submicrometer silicon devices, IEEE Transactions on Electron Devices 53 (2006) 2328-2334.

[51] E.Curras Rivera, M. Molla, Study of Impact Ionization Coefficients in Silicon With Low Gain Avalanche Diodes, arXiv:2211.16543v1

[52] R. Van Overstraeten, H. De Man, Measurement of the ionization rates in diused silicon p-n junctions, Solid-State Electronics 13 (1970) 583-608.

[53] Y. Okuto, C. Crowell, Threshold energy eect on avalanche breakdown voltage in semiconductor junctions, Solid-State Electronics 18 (1975) 161-168.

[54] S. M. Mazza et al., "Development of AC-LGADs for Large-Scale High-Precision Time and Position Measurements," 2021 IEEE Nuclear Science Symposium and Medical Imaging Conference (NSS/MIC), Piscataway, NJ, USA, 2021, pp. 1-7, doi: 10.1109/NSS/MIC44867.2021.9875583.

[55] P. Fernandez-Martinez, D. Flores, S. Hidalgo, V. Greco, A. Merlos, G. Pellegrini, D. Quirion, "Design and Fabrication of an Optimum Peripheral Region for Low Gain Avalanche Detectors", Nucl. Instrum. Methods Phys. Res. A 821, pp. 93–100, 2016, DOI: 10.1016/j.nima.2016.03.049.

[56] Ferrero, Marco & Arcidiacono, Roberta & Mandurrino, Marco & Sola, Valentina & Cartiglia, Nicolò. (2021). An Introduction to Ultra-Fast Silicon Detectors: Design, Tests, and Performances. 10.1201/9781003131946.

[57] arXiv:1705.08830 [physics.acc-ph]

[58] R. Yohay, Precision timing for the high luminosity upgrade of CMS, in: PoS 028, Pixel, 2017, URL https://pos.sissa.it/309/028/pdf

[59] The 2021 ECFA Detector Research and Development Roadmap, CERN-ESU-017, The ECFA R&D Roadmap Process Group, 2022, https://cds.cern.ch/record/2784893

[60] R. Sacchi et al. Med. Phys., 42 (2015) 3581-3582, doi: https://doi.org/10.1118/1.4925480.

[61] Krimmer, J. et al. NIM A, 878 (2018) 58–73 doi:10.1016/j.nima.2017.07.063.

[62] Golnik, F. et al. Phys. Med. Biol.,59 (2014) 5399–5422 doi: 10.1088/0031-9155/59/18/5399

[63] S. Marcatili, J. et al. Phys. Med. Biol., (2020) doi: 10.1088/1361-6560/ab7a6c

[64] J. Zhang, Development of LGAD sensors with a thin entrance window for soft X-ray detection, Journal of Instrumentation, 2022, 17-11 10.1088/1748-0221/17/11/C11011

[65] Lecoq, Paul. (2022). On the way to the 10 ps time-of-flight PET challenge. The European Physical Journal Plus. 137. 10.1140/epjp/s13360-022-03159-8.

[66] Cartiglia, N., et al.: Beam test results of a 16ps timing system based on ultra-fast silicon detectors. NIMA 850, 83–88 (2017). https://doi.org/10.1016/j.nima.2017.01.021

[67] https://garfieldpp.web.cern.ch/garfieldpp/documentation/UserGuide.pdf

[68] F. Carnesecchi, private communication

[69] Technical Proposal: A High-Granularity Timing Detector for theATLAS Phase-II Upgrade. Technical report, CERN, Geneva (Jun2018). https://cds.cern.ch/record/2623663

[70] CMS, C.: A MIP Timing Detector for the CMS Phase-2 Upgrade. Technical report, CERN, Geneva (Mar 2019). https://cds.cern.ch/record/2667167

[71] https://arxiv.org/abs/2204.10029

[72] https://www.sciencedirect.com/science/article/pii/S0168900224007241

[73] Sola, V., et al.: First results from thin silicon sensors for extreme fluences. 37th RD50 Workshop, Zagreb Online (2020)

[74] https://www.to.infn.it/~cartigli/ufsd_project/ewExternalFiles/1-s2.0-S0168900224000792-main%20%281%29.pdf

[75] https://wikihost.nscl.msu.edu/protondetector/lib/exe/fetch.php?media=n1470_rev19.pdf

[76] https://download.tek.com/manual/6487-901-01(B-Mar2011)(Ref).pdf

[77] LabVIEWTM User Manual, National Instruments, 2003.

[78] arXiv:1605.01692v1 [physics.ins-det] 4 May 2016

[79] Schuettler, Martin & Stieglitz, Thomas. (2013). Microassembly and micropackaging of implantable systems. 10.1533/9780857096289.1.108.

[80] Cerron Zeballos, E., et al.: A New type of resistive plate chamber: The Multigap RPC. NIMA 374, 132–136 (1996). https://doi.org/10.1016/0168-9002(96)00158-1

[81] Sadrozinski, H.F.-W., et al.: 4d tracking with ultra-fast silicon detectors. Reports on Progress in Physics 81(2), 026101(2017). https://doi.org/10

[82] Riegler, W., et al.: Detector physics and simulation of resistive plate chambers. NIMA 500(1), 144–162 (2003). https://doi.org/10.1016/S0168-9002(03)00337-1. NIMA Vol 500

[83] https://www.keysight.com/it/en/assets/7018-04256/data-sheets/5991-3890.pdF

[84] https://www.testequipmenthq.com/product-search/hameg-hm8118

[85] Cenna, F., et al.: Weightfield2: A fast simulator for silicon and diamond solid state detector. NIMA 796, 149–153 (2015). https://doi.org/10.1016/j.nima.2015.04.015

[86] https://contentnktphotonics.s3-eu-central-1.amazonaws.com/Datasheets/PILAS/ALS_Pilas_DX.pdf?1632838010

[87] https://pdf.directindustry.com/pdf/standa/manual-translation-rotation-stages/35170-558253.html

[88] https://docs.rs-online.com/035e/0900766b8127e31c.pdf

[89] https://cividec.at/electronics-C2-HV.html

[90] https://datasheetspdf.com/pdf-file/64399/Mini-Circuits/LEE-39/1

[91] https://datasheetspdf.com/pdf-file/590418/Mini-Circuits/GALI5/1

[92] https://www.minicircuits.com/pdfs/GALI-52+.pdf

[93] https://eu.mouser.com/datasheet/2/400/z_plus_e_low_voltage_10v_to_100v-2581128.pdf

[94] https://doi.org/10.1016/j.nima.2020.164379

[95] McDonald W.J. Gedcke D.A. Design of the constant fraction of pulse height trigger for optimum time resolution. Nuc. Inst. and Meth., 58:253–260, 1968.

[96] https://www.first-sensor.com/cms/upload/appnotes/AN_SiPM_Introduction_E.pdf

[97] Carnesecchi, F., Sabiu, B., Strazzi, S. et al. Measurements of the Cherenkov effect in direct detection of charged particles with SiPMs. Eur. Phys. J. Plus 138, 788 (2023). https://doi.org/10.1140/epjp/s13360-023-04397-0

[98] F. Carnesecchi, S. Strazzi et al., Beam test results of 25 um and 35 um thick FBK ultra fast silicon detectors. Eur. Phys. J. Plus 138(99), 1-8 (2023). https://doi.org/10.1140/epjp/s13360-022-03619-1

[99] Semiconductor Physics and Devices, Basic Principles, Fourth Edition, Donald A. Neamen, University of New Mexico

[100] Meroli, S., et al.: Energy loss measurement for charged particles in very thin silicon layers. JINST 6(06), 06013–06013 (2011). https://doi.org/10.1088/1748-0221/6/06/p06013

[101] Riegler, W., Rinella, G.A.: Time resolution of silicon pixel sensors. JINST 12(11), 11017–11017 (2017). https://doi.org/10.1088/1748-0221/12/11/p11017

[102] Cartiglia, N., et al.: Beam test results of a 16ps timing system based on ultra-fast silicon detectors. NIMA 850, 83–88 (2017). https://doi.org/10.1016/j.nima.2017.01.021

[103] Carnesecchi, F., et al.: Development of ultra fast silicon detector for 4d tracking. NIMA 936, 608–611 (2019). https://doi.org/10.1016/j.nima.2018.09.110

[104] Arcidiacono, R., et al.: State-of-the-art and evolution of ufsd sensors design at fbk. NIMA 978, 164375 (2020). https://doi.org/10.1016/j.nima.2020.164375

[105] F. Carnesecchi, S. Strazzi, et al. A new low gain avalanche diode concept: the double-LGAD. Eur. Phys. J. Plus 138, 990 (2023). https://doi.org/10.1140/\protect\discretionary{\char\hyphenchar\font}{}{}epjp/s13360-023-04621-x

[106] Akindinov, A., et al.: Performance of the ALICE Time-Of-Flight detector at the LHC. Eur. Phys. J. Plus 128, 44 (2013). https://doi.org/10.1140/epjp/i2013-13044-x. Eur. Phys. J. Plus Vol 128.

[107] Abelev, B., et al.: Technical Design Report for the Upgrade of the ALICE Inner Tracking System. J. Phys. G 41, 087002 (2014). https://doi.org/10.1088/0954-3899/41/8/087002. J. Phys. G Vol 41.

[108] Adolfsson, J., et al.: The upgrade of the ALICE TPC with GEMs and continuous readout. JINST 16(03), P03022 (2021). https://doi.org/10.1088/1748-0221/16/03/P03022. JINST Vol 16.

[109] Lippmann, C.: Upgrade of the ALICE Time Projection Chamber. CERN-LHCC-2013-020 (2014).

[110] A.N. Akindinov et al., edited by P. Dupieux, R. Santonico, and E. Vercellin, "Design aspects and prototype test of a very precise TDC system implemented for the multigap RPC of the ALICE-TOF," Nucl. Instrum. Meth. A, vol. 533, pp. 178–182, 2004, doi:10.1016/j.nima.2004.07.023.

[111] ALICE Collaboration, "ALICE upgrades during the LHC Long Shutdown 2," CERN, Tech. Rep. CERN-EP-2023-009, arXiv:2302.01238, Geneva, 2023. https://cds.cern.ch/record/2847599

[112] Abelev, B.B., et al.: Performance of the ALICE Experiment at the CERN LHC. Int. J. Mod. Phys. A 29, 1430044 (2014).

[113] Falchieri, D.: DRM2: the readout board for the ALICE TOF upgrade. PoS TWEPP-17, 081 (2018). https://doi.org/10.22323/1.313.0081. PoSVolTWEPP-17

[114] F. Carnesecchi [ALICE],Performance of the ALICE Time-Of-Flight detector at the LHC, JINST **14** (2019) no.06, C06023, doi:10.1088/1748-0221/14/06/C06023

[115] Richter, Matthias & Krzewicki, Mikolaj & Eulisse, G.. (2019). Data Handling In The Alice O2 Event Processing. EPJ Web of Conferences. 214. 01035. 10.1051/epjconf/201921401035.

[116] Van Dijk, M., et al: Introduction to Secondary Beams (2023) https://indico.cern.ch/event/1254858/

[117] https://satsearch.co/products/weeroc-liroc-read-out-chip-for-lidar

[118] S. Altruda et al., PicoTDC: a flexible 64 channel TDC with picosecond resolution, IOP Publishing 18 n. 07 (2023), DOI: 10.1088/1748-0221/18/07/P07012

[119] https://www.weeroc.com/

[120] ALICE Collaboration, "Time-of-Flight detector", ALICE upgrades during the LHC Long Shutdown 2, CERN Geneva (2023), pages 86-91, [arXiv:2302.01238v1]

[121] https://www.caen.it/products/n108a/

[122] https://eudaq.github.io/manual/EUDAQUserManual_v1.pdf

[123] U. Savino, Expected performance of the High Energy Particle Detector (HEPD-02) tracking system on board of the second China Seismo-Electromagnetic Satellite, Nuclear Instruments and Methods in Physics Research Section A: Accelerators, Spectrometers, Detectors and Associated Equipment, Volume 1063, 2024, 169281, ISSN 0168-9002, https://doi.org/10.1016/j.nima.2024.169281

[124] M. Mager, ALPIDE, the Monolithic Active Pixel Sensor for the ALICE ITS upgrade, Nuclear Instruments and Methods in Physics Research Section A: Accelerators, Spectrometers, Detectors and Associated Equipment, Volume 824, 2016, Pages 434-438, ISSN 0168-9002

[125] Hui Tian, Boyd Fowler, and Abbas El Gamal, Analysis of Temporal Noise in CMOS APS, Information Systems Laboratory, Stanford University Stanford, CA 94305 USA

Acknowledgements

First and foremost, I would like to thank my supervisor Andrea, who, with immense patience, has guided me, thesis after thesis, through all my professional milestones, advising me and guiding me in every choice that has allowed me to achieve far more than I could have ever imagined.

I am grateful to Francesca, who has been by my side at every step of my work, always finding time to help me at any hour of the day (and night), with her unwavering dedication and showing me the beauty of the work we do. Since I met her, she has been a role model and inspiration, someone I aspire to become like one day.

Thanks to Daniele, who made every day in the lab enjoyable and fun, always ready to lend a hand with his creative (if not always photogenic) solutions that always worked, sharing his enthusiasm and teaching me to think outside the box, never giving up.

My thanks go to Manuel, who, since I arrived at CERN, has been a friend and a guide, not only in my work but also in my life there. Always willing, with endless patience, to explain (and re-(re-)explain) me so many things. This past year, he has supported me in everything.

I thank Rosario, whose questions (on average at least five per presentation) always made me reflect on things without taking anything for granted. With his wealth of knowledge, he has always given me invaluable advice, and his unparalleled enthusiasm constantly inspires me to keep learning and understanding more.

I thank my travel companions: Bianca, my adventure accomplice, who, after sharing countless sleepless nights at beam tests, all-out battles with CERN_noise, and data analyses that produced magical peaks, now understands me with just a glance. These years would not have been as wonderful without her; Marco, who patiently imparted all

his knowledge (or at least enough to keep the TOF safe) and served as a steadfast point of reference on many occasions; Riccardo and Giovanni, who accompanied me throughout the journey, forming a friendship with them that transcends time and space. Francesca and Nicola, who welcomed me into the group, making me feel like I truly belonged; Gleb and Sofia, who shared numerous lunch breaks with me, bringing a bit of relaxation and joy even on the busiest of days.

I am grateful to the "TOF Performance" group - Nicolò, Francesco and Pietro - who patiently taught me how to conduct an analysis, allowing me to see how beautiful it is too. And I'm grateful to everyone who is part of the TOF group in Bologna; since I started working with them, they have welcomed and supported me, believed in me, and consistently put me in a position to follow the best path. I couldn't have hoped for a better group to work with.

I thank my "Villa Poma friends", especially Giulia, Lucrezia and Sara, who have been with me for almost 27 years. They have celebrated each milestone with me, and patiently put up with me during stressful days, and I know they are always there, even when we're on opposite sides of the Earth. This journey to where I am now would not have been the same without them. I want to thank as well my friends from Bologna: Chiara, Sara, Martina, and Elisa - my soul sisters. I think they, more than anyone else, have been my confidants and my advisors in life choices, the only people who sometimes seem to read my mind. With them, I spent five wonderful years studying Physics, filled with laughter, exams, pizza nights, and (creative adjustments in) lab reports, all of which have brought me here. I also thank my "Saint-Genis friends", who, throughout my time at CERN, were like family, truly making me feel at home. They were part of this journey, and I hope that, despite the distance, our paths will often cross again. Finally, I thank my friends from the summer camps, who welcome me back each time as if I had never left.

The greatest thanks go to my family - my brother, my grandparents, aunts, uncles and cousins - and especially to my parents, who have always supported and helped me in every choice I've made. From an early age, they encouraged me to follow my dreams, never letting me think anything was out of reach. I admire them immensely; they are my guiding light, and without them, I would never have made it this far.